Stiffening glass structures with laser-bending techniques

A study testing the stiffness of laser-formed glass panels

MSc-Thesis

Rens Hoekstra

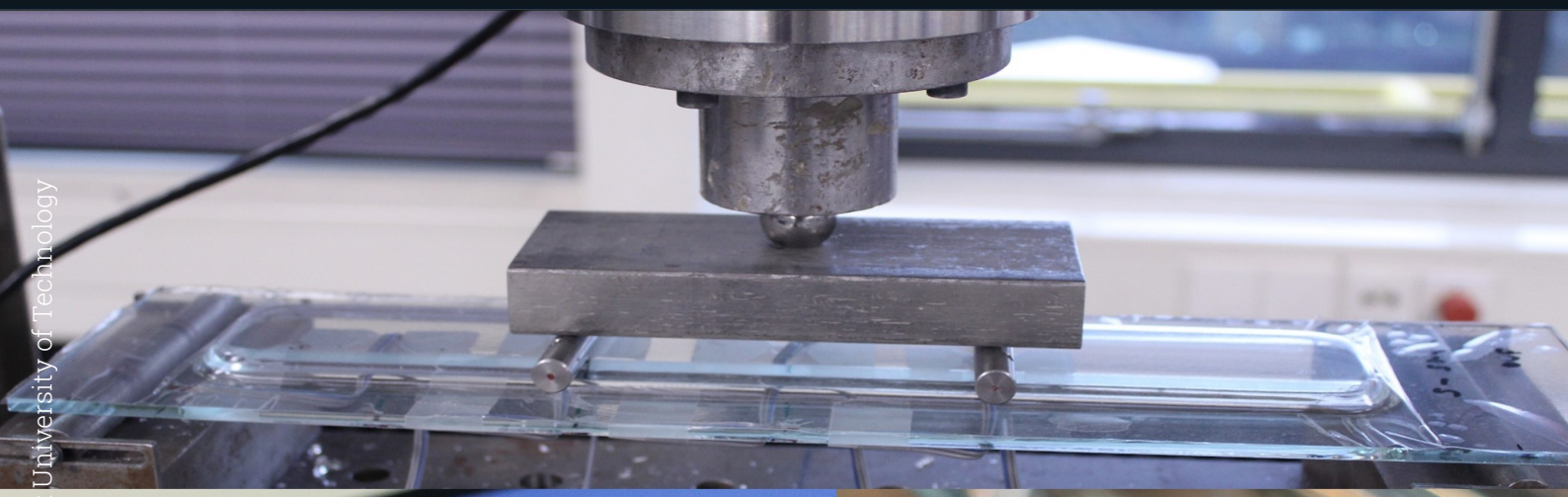

Delft University of Technology

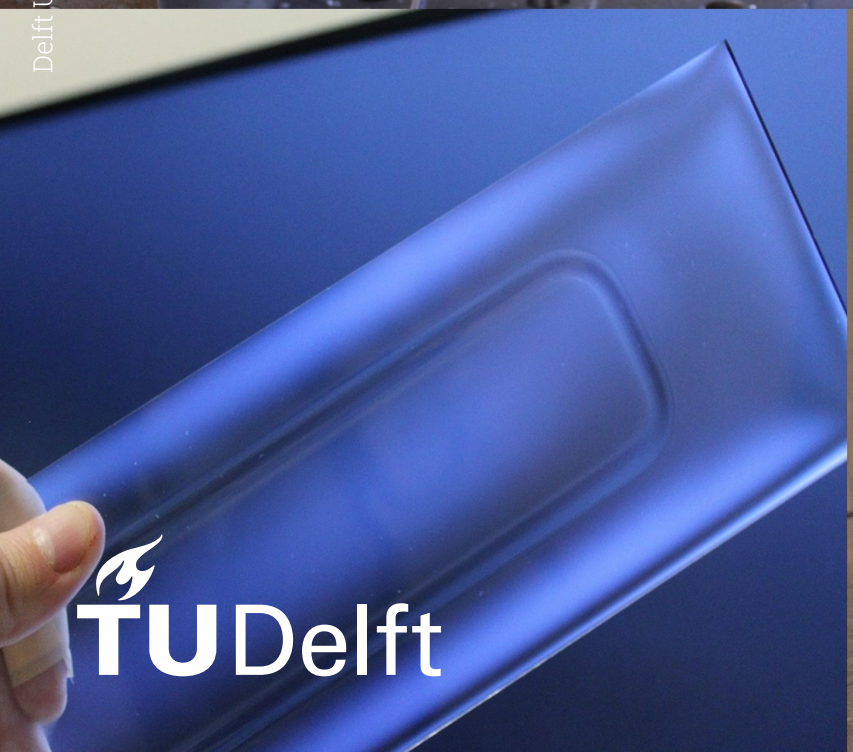

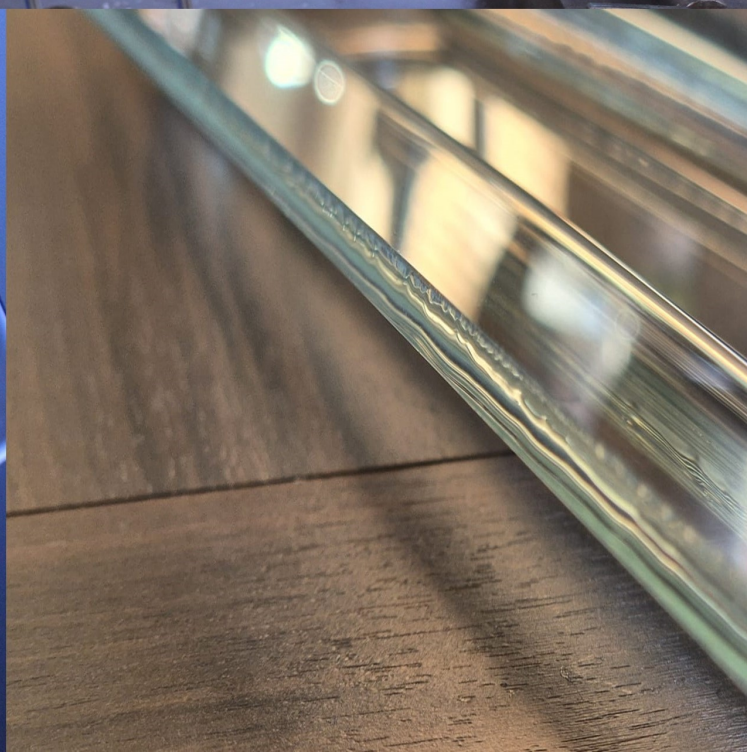

TU Delft

Stiffening glass structures with laser-bending techniques

A study testing the stiffness of laser-formed glass panels

by

Rens Hoekstra

Student Name	Student Number
Rens Christian Hoekstra	5419697

Supervisor TU Delft:	Prof. dr. ir. P.C. Louter
Project Duration:	09.2024 - 05.2025
Committee member(s):	Dr. F. Messali (TU Delft)
Company:	ABT bv.
Company supervisor:	ir. K.J. Haarhuis
Faculty:	Faculty of Civil Engineering and Geosciences, Delft
Glass manufacturer:	Fraunhofer institute for Mechanics of Materials IWM

Date: 02-5-2025

TU Delft abt

Preface

This thesis marks the final part of my Master of Science degree in Civil Engineering at the Delft University of Technology. The specialisation track Structural Engineering with courses in the likes of Building Engineering and Glass Science and Engineering concluded this study programme. With passion, ambition and the usual struggles as well, I researched the innovation of laser-formed glass over the course of September 2024 to May 2025. I would like to express my sincere gratitude to everyone that has been involved in this last chapter of my student-life.

First, I would like to thank my graduation committee: Many thanks to Prof. Dr. ir. Christian Louter for chairing my committee and for his enthusiasm and introduction to the magical world of the engineering and science of glass structures. To be able to conduct my own research topic and having the opportunity to come to you with my own ideas about a topic resulted in a thesis that I enjoyed very much. Your expertise, involvement, availability, feedback, and guidance are greatly appreciated. Secondly, I would like to thank Dr. Francesco Messali for his guidance and expertise in the area of FEM-modelling. Your patience, knowledge and your guidance are very much appreciated. And finally, I would like to thank ir. Kars Haarhuis. Together we searched for an innovative, challenging, and maybe most importantly of all, fun topic for this MSc-Thesis, which at the end I can say worked out perfectly. What started more than a year ago with small coffee talks and brainstorms at ABT resulted in me becoming a colleague of yours after this thesis. Your everyday availability, knowledge, criticism, and guidance have helped me write and conclude a thesis that I am proud of, thank you.

Secondly, I would like to thank ABT bv, at which I was able to work on this thesis. After starting as an intern in 2019 during my hbo-degree, working part-time as a workingstudent during my pre-master programme, I again felt very welcome to start as a graduate-intern. In the end, these collaborations led to a full-time job at ABT after graduating, for which I am more than grateful. To all the colleagues who helped me with the small and bigger challenges, or just for being interested in what I was doing all day: Thank you.

I would like to thank Fraunhofer IWM and especially Dr. Kai Schillinger-Engel for the very much appreciated collaboration. To be able to receive glass samples to test in real-life has been invaluable in concluding this thesis. Thank you for the kind messages, support and feedback and it feels really nice to hear that I was able to help understanding the structural behaviour of laser-formed glass. Let's see what future projects and applications lie ahead.

I would also like to give my thanks to Maiko van Leeuwen for helping me during the lab-tests. Your instrument expertise, quick thinking and good sense of humour led to me enjoying this phase of my thesis very much. Thanks as well to ing. Paul Vermeulen for the patience, guidance, and help with applying and obtaining the results of strain-gauges during the lab-tests.

Lastly, I want to thank my family and friends for their support during this thesis and throughout the whole study programme. The support of my family helped me pursue my dreams of obtaining this degree and without this support this would not have been possible. My friends both back in Enschede and all the new friends I made in Delft, thank you for all the support and fun we had (and will have), and all the hours we had to go through of studying together during exam periods. A special thanks to U-BASE at which I was able to meet new friends, develop myself with new skills in three committees, and all the fun this association was able to provide next to all the hard work.

Thank you!

Rens Hoekstra
Delft, May 2025

Abstract

Flat glass is used in many applications such as window glazing, whereas curved and bent glass is rising in its applications nowadays as well. Innovative ways of bending glass have been further developed in the past 25 years, and bending glass by laser-induced heat has been developed and discovered in 2017. This technique allows, at this moment in time, for bending glass around corners of up to 90 degrees with radii less than 10mm and is able to sag various forms out of plane. The structural properties, such as the stiffness, strength, and failure mechanisms of this laser-formed glass, have not been investigated thoroughly yet. This results in the product still being in the development phase, instead of already being available on the market and applicable in construction projects.

In the search for the use of sustainable and less raw materials in buildings, laser-forming might directly impact the latest goal. Flat geometries are structurally unfavourable, so the hypothesis states that laser-forming flat glass increases the inertia. This thesis aims to confirm the assumption of creating stiffer glass by using laser-forming techniques, the opportunity to reduce material, and to be able to predict the behaviour of laser-formed glass in Finite Element Method (FEM) programmes. Both lab-experiments and numerical analyses were performed to obtain results on these objectives.

The thesis starts with a parameter study on the influence of different cross-sectional parameters on the stiffness. The second moment of area (inertia) relates to the stiffness of the cross-section and four different parameters have been checked by its influence. The thickness of the web is directly related to the total height of the sample, as a deeper elevation induces larger necking of the web, resulting in thinner glass. The influence of this necking phenomenon is, therefore, investigated and described.

Subsequently, a design for a two-sided supported glass panel is manufactured with an implemented laser-formed elevation to perform an experimental study. By implementing this laser-forming technique, the total height of the samples went from 4mm to a maximum of 12mm, while retaining the same amount of material. The laser-formed glass panels were tested in a four-point bending test setup. Four flat samples were first tested to obtain reference values for the stiffness of the glass. Subsequently, the laser-formed sample sets were tested.

A numerical research is performed to simulate and predict the behaviour of the laser-formed glass. FEM-models have been used to compare the numerically derived deformations and therefore the stiffness of the panels, with the results of the four-point bending tests. In addition, the FEM-models were used to obtain numerically derived stresses at the points of failure. Individual and nominal models have been created to obtain insight into the need for individual models.

The results of this research conclude that the increase in stiffness shows nearly the same behaviour as the increase in cross-sectional inertia. The effect of laser-forming is therefore immediately visible in the stiffness properties of the glass. The laser-forming process of glass is able to convert the stiffness properties of an originally 3.87mm panel to meeting the properties of an equivalent thickness of 8.3mm thick flat glass panel. The stiffness showed predictable behaviour in the FEM-models, whereas the (failure) stresses showed a harder predictability. The presence of necking showed to be an influence in predicting the failure behaviour and needs to be taken into account when designing with laser-formed glass. Individual models are needed in order to visualise the different failure mechanisms in the FEM-models.

A comparison-study is performed to theoretically increase the size of a laser-formed glass panel and the stiffness properties and the bending stresses are checked. The stiffness and stresses are compared to regular flat glass panels. For stiffness properties, the laser-formed glass panels are able to reduce the material use by 46%. Laser-formed glass is able to decrease a required equivalent flat thickness of 23.6mm to a laser-formed glass thickness of 14.5mm, when observing the bending stresses. A material reduction of 39%.

Contents

List of Figures

List of Tables

1

Introduction

Glass, the material used to create transparency, is nowadays in every building envelope. Glass is the material that is used to look outside, while creating a barrier between the inner climate of a building and the outer one. The applications of glass are rising, with glass not only creating a barrier, glass can also take up loads and be used as structural elements. Since the late 1980s the use of glass as a structural element has increased [1]. By replacing non-transparent walls and floors with glass, architects are able to create this aesthetic gain.

On the side, the building industry is a major contributor to all the greenhouse emissions, To be able to thrive for a more sustainable industry, material reduction can be a way to reduce these emissions.

Looking at building facades, it can be stated that in most cases the glass is flat. Flat structures are less stiff than corrugated structures. Most of the people will recognize this by adding folds to a flat piece of A4-paper, in this way it acts stiffer than a non-folded piece. So by implying that flat surfaces are less stiff than corrugated surfaces, why can corrugation and/or 3D-shapes not improve the structural behaviour of flat glass panels as well?

Figure 1.1: Glass deformed by laser bending [2].

A new technology that can contribute to these ambitions is laser-bending. This technique is based on heating glass panels in an oven, with a set temperature just before the glass becomes viscous. For soda lime silicate glass this temperature lies just before 600 degrees Celsius. Inside the oven, the glass is heated extra locally by lasers to reach the viscous state in very specific predetermined places. By becoming viscous, this is where these laser-heated areas drop several millimetres by gravity. With this technique bending radii smaller than 10mm can be achieved. This technique is in the early stages of development and investigation. Therefore, many possibilities and ideas have not been explored yet, making this a highly interesting topic to involve in this thesis.

Questions about structural integrity and architectural purposes are examined and researched. This thesis focusses on stiffening glass panels by using these laser-bending techniques and creating 3D-shape patterns.

1.1. Research problem

With glass covering a large part of buildings, reducing materials can have a significant impact on reducing the emissions of a building and the use of raw materials. Looking at the cross section of facade panels, it can be observed that there is no cross-sectional depth, besides the thickness of a flat panel. Visually profitable and reasonable, but structurally it is questionable whether flat panels are the best performing designs. From a structural perspective, it is not the best performing design. By increasing the stiffness of glass panels, less material can be used in comparison to conventional non-formed and flat glass panels. Laser-bending techniques can be used to increase this stiffness. Is this method sufficient to increase the overall stiffness of a glass panel? In theory, the cross section of the glass is improved by adding grooves or a form of depth to the glass. This thesis provides results whether the increase in inertia results in better stiffness performances.

The problem that is tackled during this thesis is that glass facade panels have a minimal stiffness based on their geometry. Laser-bending techniques are used to increase the stiffness of these panels without adding material and to be able to use thinner glass.

1.2. Research objective

With sustainability and the availability of raw materials being major challenges and innovation leading to new insights, the objective of this research is to test new ways to reduce the amount of glass material needed for glass facades. The research is successful when results and knowledge about two structural properties of the laser-formed glass are obtained. These two properties will be the increase in stiffness of laser-formed glass and the bending stress resistance of these panels. The stiffness of the glass is obtained through observing the applied force and the corresponding deformation. The bending stresses are obtained by applying strain gauges, which will provide insight into the present stresses. In addition, the bending stresses are obtained numerically with FEM-models. Conclusions about the bending stress resistance are made by stating the observations, and plotting Weibull distributions to obtain 5% fractile values.

A FEM model is made to predict the behaviour of the laser-formed glass panels and is compared to the real-life behaviour. The goal is to develop a model that is checked in sensitivity regarding geometrical details, mesh sizes and computational time. The influence of parameters like glass thickness, bending angle and necking will be examined and visualised analytically at first. The FEM-models give results regarding the stiffness of all the panels. The comparison between nominal models and unique models needs to give insight into the need for unique models.

A visual relation between the stiffness performance of flat versus laser-formed glass will be another objective. In this way, the use and research of laser-formed glass can be promoted if proven beneficially.

1.3. Research scope

Many properties of laser-formed glass panels have not been researched up until now. To scope this research, the focus lies on the behaviour and properties of single Soda Lime Silica glass panels. Specifically, the behaviour of out-of-plane loaded panels will be researched. One situation will be elaborated on and examined, which contains a two-sided supported laser-formed glass panel. The design of the elevation/3D-shapes will be done in Rhino and Grasshopper and is bound by the manufacturing capabilities.

Four parameters are checked for the sensitivity towards inertia of the two-sided supported panel. This panel is designed with a 3D-shape consisting of an elevation, where the parameters are the elevation depth, the bending angle, the glass thickness, as well as the thickness of the web regarding the influence of necking.

After designing, multiple DIANA-models are built. Rhino-models are directly imported as solids into DIANA FEA to be able to obtain structural analysis.

The designs are tested in the Micro-lab of the Civil Engineering and Geosciences faculty of the TU Delft. The properties that are observed are the deformations with respect to the loading and the strain of the glass. This provides information on the structural integrity of the laser-formed glass panels. The

laser-formed panels are compared to conventional flat panels to see if the stiffness is indeed increased and by what amount. The results of the strain and stresses are used to see if there is any loss or gain in bending strength regarding this unique production process of laser-bending.

The lab-tests deliver the deformation and the strains after certain loading. The data collected from the lab-tests are compared to DIANA-models to see if FEM can correctly predict the behaviour of real-life samples of laser-formed glass panels.

A comparison study is performed to demonstrate if laser-forming glass is structurally beneficial in relation to flat glass. Solutions and recommendations for future research are given to complete the research.

1.4. Research questions

The main research question that will be discussed during this thesis is:

- ”What is the structural performance of laser-formed glass panels, when loaded out-of-plane until failure?”

Follow-up questions supporting this main research questions are:

- ”What is the influence of the shape geometry on the inertia and the stress distribution?”
- ”What is the stiffness and strength capacity of out-of-plane loaded glass panels?”
- ”How can the structural behaviour be modelled in DIANA FEA to resemble real life behaviour?”
- ”Is laser-bending beneficial for reducing the material use of glass panels?”

1.5. Research theory and methods

The research theory is based on the knowledge gained in the CIEM1304 Glass Science and Engineering course. This is the introductory course of the TU Delft for glass structures for civil engineers. During this course, topics in the likes of glass production, -sustainability, -fracture mechanics, -3D-printing and glass testing, -reuse, -connections, and glass engineering projects are discussed. This is the basis of the knowledge of glass before starting this thesis.

Other theory is used from several other courses of the TU Delft Structural Engineering programme. Topics like FEM-modelling, mechanics of (slender) structures, and building engineering are necessary to gain an understanding of the structural behaviour of laser-formed glass panels. Knowledge that is not covered in the curriculum is acquired in the literature study, which is further elaborated in chapter 2.

The research methods are based on designing, FEM modelling and lab-tests. The FEM-programme in which is modelled, is DIANA FEA, since this is based on the availability of the software, the compatibility, and the accessibility to experts of the software.

The lab tests are performed by four-point bending tests for the glass samples. With strain gauges, the strain is obtained, while the deformation is measured within the press. By doing so, the stresses in the glass are determined, and it is checked whether laser-formed glass can be predicted and modelled correctly in FEM as well.

1.6. Thesis outline

This thesis starts with a description of the theoretical background concerning this topic of glass and laser-bending in Chapter 2. Chapter 3 shows the investigation of the influence of different geometry parameters. Subsequently, the lab experiments and the obtained data are described and presented in Chapter 4. The FEM-models and numerically derived results are presented in Chapter 5. The results of comparing laser-bent glass with flat glass in a case-study are described in Chapter 6. Finally, the discussion, conclusions, and recommendations are stated in chapters 7, 8 and 9.

2

Theoretical Background and State of the Art

This chapter describes the background information found in the literature and the state of the art. This chapter is divided into three main sections. First, the material glass in general is discussed, and then the applications and properties of architectural and structural glass are elaborated. To gain knowledge of CO_2-lasers, a separate subchapter describes the principles of this product and process.

2.1. History and production of float glass

2.1.1. History and production of glass

Glass has been around for centuries, even millenniums. The man made glass at least, because glass has always been around in nature in multiple forms. Sand and or rock can be heated naturally due to, for instance, lightning strikes or volcano eruptions. When these materials are rapidly cooled down, a glassy state material such as obsidian or volcanic glass can be formed. These glass like materials were used in ancient times for arrowheads, knives and other crafts [3].

Figure 2.1: Black obsidian volcanic glass [4].

The first glass created by humans was made around 5500 years ago by Egyptians. The first applications with glass produced by men were jewellery and vases. In a later stage, the Romans further developed the application and production of glass products. The first products with clear glass were developed and the application in buildings rose as well. Where glass was first a luxury, in the 14th century the

French developed a method to make flat glass panels to use on larger scale. The so called crown glass was made by blowing glass and rotating it rapidly [5]. The centrifugal force allowed the soft glass to form circular panels. The glass produced with this method is circular and the application in buildings required mostly rectangular shapes, therefore a waste of material was inevitable [6].

The research and development of making flat glass sheets dates from the late 1800s to the early 1900s. Multiple production processes were developed starting with vertically drawn glass in 1901 by Emile Fourcault. The Fourcault process involves the molten glass being pulled in a upward direction. By letting it cool down in the process, a continuous flat piece of glass is made. A single panel is then cut from the continuous glass. Distortions and irregularities were common during this production method, making it likely to have flaws [3].

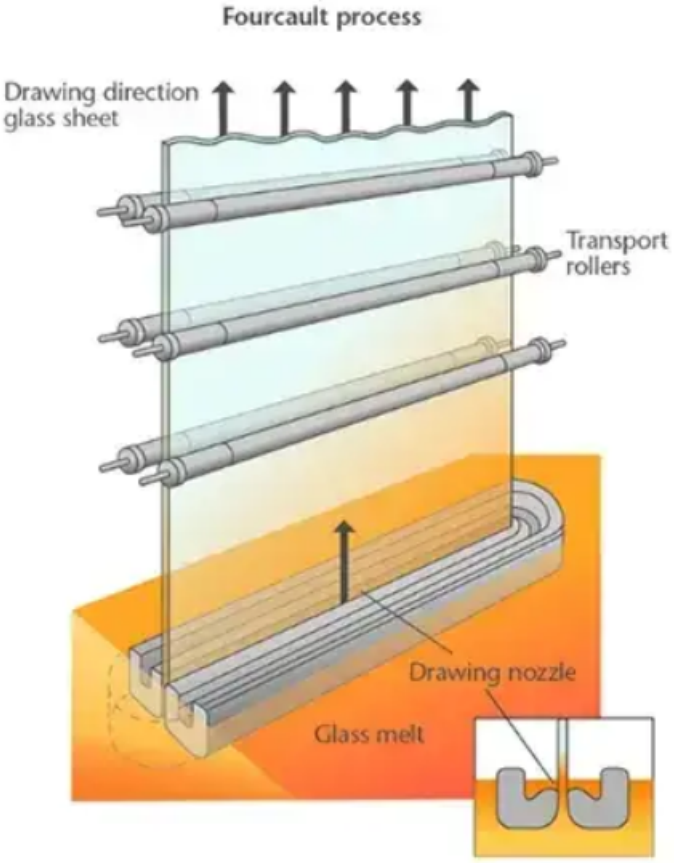

Figure 2.2: The Fourcault process [7].

With irregularities being an issue in previous production methods, a new method needed to be developed. This new method called the float process was developed in the mid 1900s. The production of float glass, as it is used today in the building industry, was introduced to the public market by the Pilkington Brothers in 1959. Sir Alastair Pilkington, a Cambridge University graduate, joined the company in 1947. In 1952 he introduced his idea to form glass by floating melted glass on a bath of liquid tin. Because liquid tin has a density higher than that of the molten glass, the glass floats on top of the tin. A great benefit of this process is the fact that liquid tin has a flat surface. Therefore, the glass floating on top will end up having a flat surface as well [3].

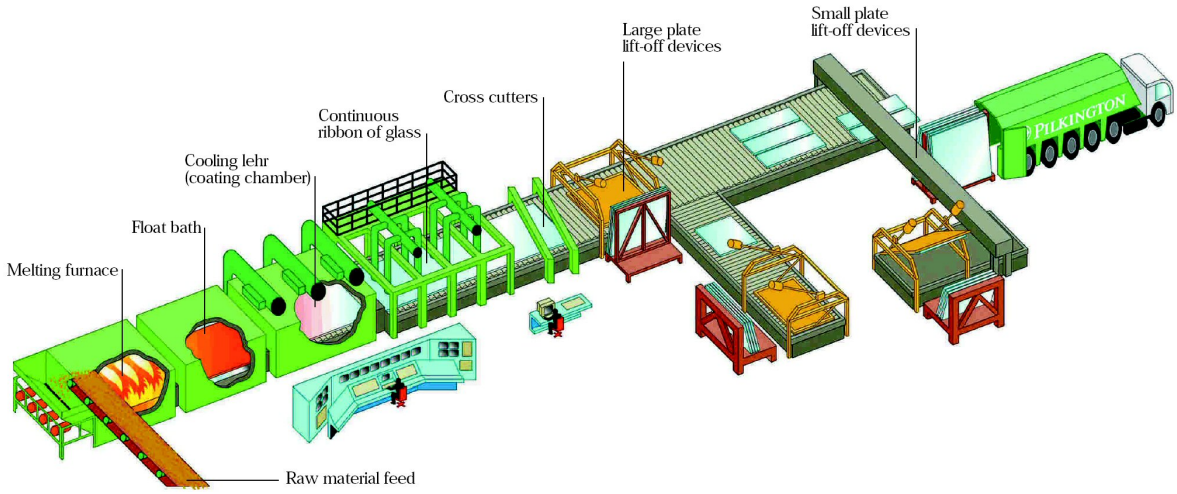

Figure 2.3: The Float process [8].

The process starts with heating the raw materials in a furnace up until a temperature around 1550 degrees Celsius, as described by glass manufacturer Saint-Gobain [9]. This heating process gets rid of any impurities and bubbles within the glass. The molten glass is afterwards poured on the surface of the molten tin bath. Subsequently the glass spreads evenly forming a ribbon of uniform thickness and viscosity. The use of tin instead of other materials as a liquid bath is based upon its low reactivity with the glass. The thickness of these glass ribbons without any mechanical adjustments is about 6.5mm. Any thicknesses deviating from this need external mechanical forcing to obtain the required thickness. Rollers above the bath are used to control this forcing and therefore the resulting in the required thickness and the width of the glass. The speed, angle and penetration of the rollers are the forced parameters that influence the size of the glass. In the meantime while floating continuously on top of the tin, the glass is cooled down to a temperature of around 600°C [9]. When cooled down and hardened enough, it can be taken out of the bath and placed onto rollers. It is crucial to be hardened enough before, to prevent the rollers leaving traces and markings on the surface of the glass. A uniform thickness and a smooth surface is achieved with this process, thus making this far more reliable and usable for glass applications like facade glazing.

Before entering the annealing lehr, a Pyrolitic coating can be applied to the glass to improve the quality and properties of the glass. By reaching the end of the floating process, the glass has cooled to a state where it acts rigid enough to be lifted. The glass will be lifted from the floating bath to the lehr by so called lift-out rollers. The lehr is the part in the production line where any residual stresses are released. The annealing is done inside a 190m sealed air-filled environment. The glass is in this part gradually cooled, which get rid of internal stresses and therefore increasing the durability of the glass [9].

After cooling down the glass can be cut into the desired dimensions. The standard dimensions that Saint-Gobain produces and delivers are 6000x3210mm and 3210x2250mm. Where the ”Overlength” glass panels can reach the size of 18000x3210mm [10].

(a) Overlength panels used in facades [10].

(b) Transportation of Overlength glass at Glasstec 2018 [11].

Figure 2.4: Oversized panels reaching lengths of 18 meters.

The transportation of oversized panels comes with its own challenges, but innovative designs of transportation trucks like figure 2.4b can overcome these challenges.

2.1.2. Detailing methods

Different detailing methods are used to ensure the material quality standards are met. The methods that are used most commonly are the detailing due to connections like hole drilling, and the cutting and polishing of the edges.

The detailing of connections plays a role in the production of the glass panels. Since holes for mechanical connections need to be drilled, these points reduce the strength performance locally. Three production methods for drilling are cylindrical drilling, conical drilling, and undercut holes [12]. All of these methods weakens the glass. Chamfering of the holes edges is used to increase the quality of a hole and therefore the overall strength performance.

Since float glass is continuously produced, to acquire the required length and dimensions of glass it needs to be cut during the production stage. This is most commonly done by mechanical cutting tables. Where water-jet cutting and laser cutting are used to cut glass as well. The cutting of glass comes with additional risks. The edge quality of the cut-side of the glass is usually sharp and vulnerable. Edge finishing is therefore needed to increase the strength performance of glass panels.

There are five common ways to finish the edges of a cut piece of glass [12]. The first option is to leave the edge finishing as it is cut. This leads to sharp edges of the glass panel. The second option is to have the edge finishing as arrissed, seamed or chamfered. This removes the sharp edges and will leave a chamfer of around 45°. The third type is to ground the glass edge. Grounding will lead to have either blank spots or no spots in the glass. Both types of finishing will leave the glass with a milky matte appearance. The last type of finishing is to polish the edges. With polishing the edges, the glass will have a clear appearance where the edges are chamfered at 45°. The difference with the chamfering option, is that the not only the corners of an edge are chamfered. The vertical end of the edge is polished as well. Different finishing details result in different edge strength properties.

2.2. Architectural and Structural Glass

Glass used as facade glazing has been around for centuries. Whereas the use of glass as structural elements is something that arose in the late 1980s [1]. This section describes the different types of strengthening glass, the implementation of robustness while designing and several engineering projects are shown.

2.2.1. Tempered glass

Glass is a material with no specific tensile strength. There is no reliable value to which the strength can be represented at all times. Bending tests results in scattered values of the strength with spreads up to 50% of the average strength in some of the cases [13].

To ensure the strength of glass and increase the mean strength, tempering methods are used. This process of heat treatment is used to create residual stresses which are desired in engineering. Since glass is weak in tensile-stresses occurring at surface flaws, the residual stresses can be used to compensate. By using heat treatment and rapid cooling, the surface cools down rapidly, where the core starts to cool down at a later stage. Therefore while the surface is cooled down, the shrinking of the core induces compressive stresses at the surface of the glass and the core stays in a tensile-stress state. Since the core does not contain any flaws, the chances of a crack initiating there are very slim. By having a surface already under compressive stress without external loading, this glass panel can withstand higher bending forces. Where the tensile stresses induced by the bending, first needs to outgrow the compressive residual stresses [14]. The principle of strengthening through tempering and its residual stresses is given in Figure 2.5.

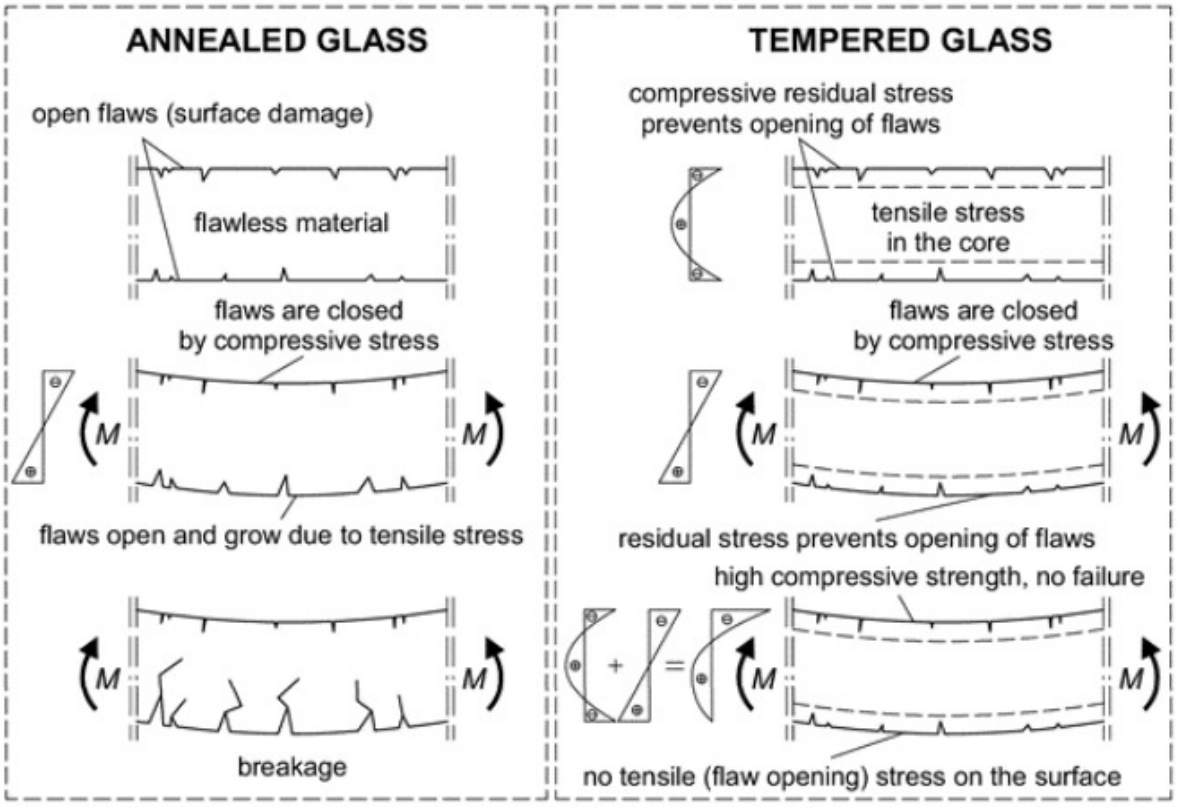

Figure 2.5: The residual stresses within tempered glass [14].

The glass is heated inside an oven to approximately 620-675°C and then cooled down rapidly by jets of cold air [14]. There are multiple stages of tempering used within the glass industry. The three terms being used in this document are described below, since this is the terminology accepted most widely.

Table 2.1: Terminology of different types of tempered glass [14].

Residual stresses at surface	Terminology used	Other frequently used terms
(zero to) none	Annealed Glass (ANG)	Float glass
Medium	Heat Strengthened Glass (HSG)	Partly toughened glass
High	Fully Tempered Glass (FTG)	Tempered Glass / (thermally) Toughened Glass

Fully tempered glass

Every type of heat tempered glass has its own properties. Fully tempered soda lime silica glass has residual compressive surface stresses varying between 80 MPa and 170 MPa [14]. A study performed by Veer, Louter and Bos in 2008 showed results of the strength being on average 157.4 MPa, alongside an average pre-stress of -100.6 MPa [15]. The NEN-2608-7-table-2 gives a characteristic bending strength of fully tempered glass of 120 MPa.

The fragmentation of the different types of tempered glass is noticeable as well. Due to the high internal stress, the fragments of glass after failure are smaller than that of HS glass or annealed glass, as can be seen in Figure 2.6. Therefore the fracture pattern is way more dense than the others. As an advantage, the smaller fragments cause less harm. On the other hand its post-failure performance is poor due to the tiny fragments [14].

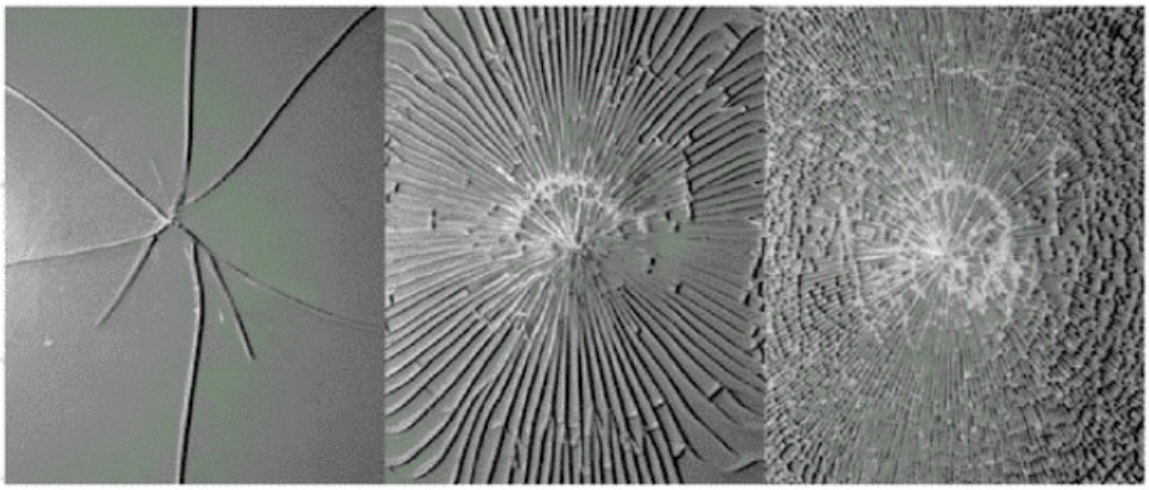

Figure 2.6: The different fracture patterns of annealed glass (left), heat strengthened glass (middle) and fully tempered glass (right) [14].

Heat strengthened glass

Heat strengthened glass uses the same cooling techniques as fully tempered glass, except that a lower cooling rate is used. Therefore, the residual stress and the tensile strength are lower in comparison. The residual compressive stress at the surface is varying between 40 and 80MPa [14]. The study performed by Veer, Louter and Bos showed an average failure stress of 104 MPa, alongside an average pre-stress of -64.3 MPa [15]. The NEN-2608-7-table-2 gives a characteristic bending strength of heat strengthened glass of 70 MPa.

The fragments of the fracture pattern of heat strengthened glass are bigger than those of fully tempered glass and smaller than those of annealed glass, as can be seen in Figure 2.6. Therefore, it has benefits with less harmful fragments than annealed glass, and a better post-failure performance than fully tempered glass.

Annealed glass

Annealed glass is glass as it is produced on the float line. No additional tempering is used, making it the weakest out of the three types of glass being described. The study of Veer, Louter and Bos showed results of an average failure stress of 42.0 MPa, alongside an average pre-stress of -4.5 MPa [15]. The NEN-2608-7-table-2 gives a characteristic bending strength of annealed glass of 45 MPa.

Annealed glass fails in large fragments, as can be seen in Figure 2.6. This makes annealed glass more harmful after failure than heat strengthened and fully tempered glass. Annealed glass can show similar fragmentation to heat strengthened glass, the cause is elastic energy stored internally due to the deformation of the glass.

Nickel-sulfide inclusion

For fully tempered glass there is another failure mode possible, besides failing due to high tensile stresses. This failure mode is called Nickel-Sulfide (NiS) inclusion. This spontaneous breakage can occur and because it is unpredictable it should not be neglected. During the production of fully tempered glass these Nickel-Sulfide inclusions can not be avoided completely. Due to the temperature change, the NiS particles can increase by about 4% in size due to a phase change [14]. A combination of high tensile stresses inside the core of the glass as well as these increase in volume of the NiS patricles can cause these sudden failures. A distinct butterfly-pattern can be seen at the initiation of the failure, as showed in Figure 2.7.

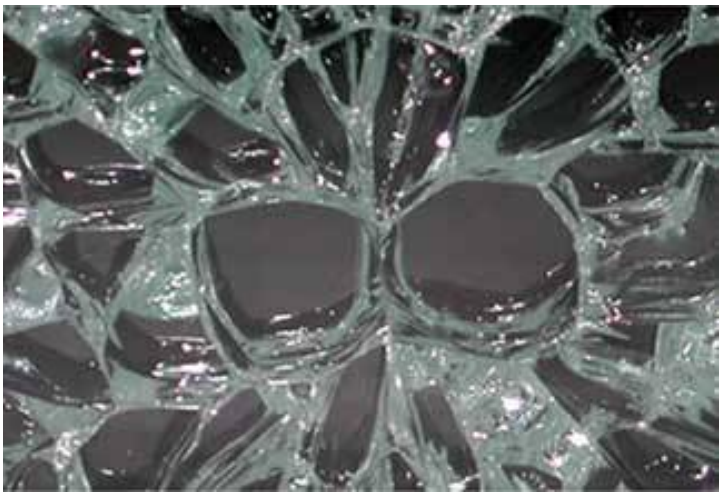

Figure 2.7: Distinct butterfly fracture pattern [16].

The Nickel-Sulfide Inclusions do start with a butterfly pattern, but not every butterfly pattern is caused by this inclusion. Fractography should identify the source of the butterfly fracture and can identify NiS with certainty. The risk of the spontaneous failures due to NiS can be reduced significantly by a so called heat-soak test. The process is described as the test consisting of slowly heating up the glass and maintaining a certain temperature for several hours [14]. This accelerates the phase change, therefore any glass that contains dangerous inclusions will fail in the process. At the end of the test the relatively good glass will remain as a whole piece without any failure.

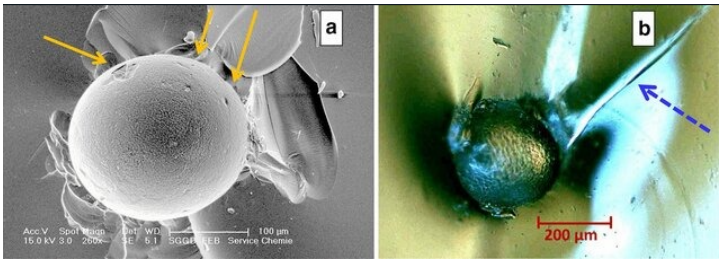

Figure 2.8: a) Nickel Sulfide inclusion into glass. b) Nickel Sulfide inclusion with intact surface [17].

2.2.2. Laminated glass

The sudden failure of glass loaded under tensile-stresses is a problem for engineering purposes. Since there is no warning right before failure, this can lead to significant consequences if the glass fails while serving as a structural element. Robustness is therefore necessary to ensure post-failure strength and a secondary load path which needs to transfer and withstand the remaining loads after failure of a glass pane.

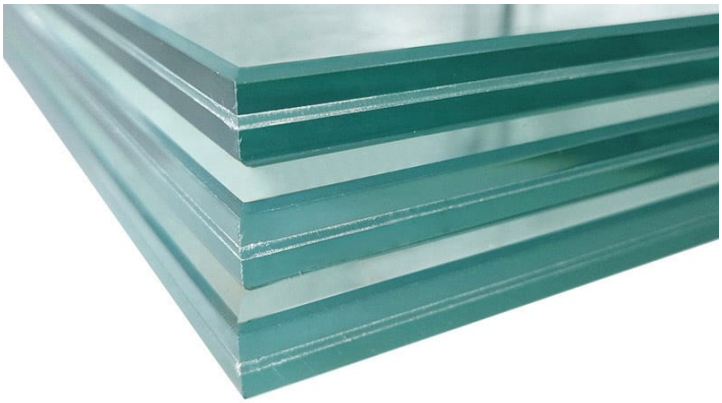

Figure 2.9: PVB-laminated glass [18].

A relatively simple yet necessary technique to ensure this robustness is laminating the glass. This means that the glass consists of a set of two or more panes with a separate transparent interlayer. The thickness and tempering of the glass panes may differ per element, since each pane may be used for different (environmental) surroundings.

The laminating process starts with rinsing the glass, subsequently applying the interlayer, adding the next glass pane on top and ending in an autoclave. This autoclave heats the laminated glass at appromixately 140°C. Heating the glass and interlayer and the pressure of 12-14 bar inside the autoclave ensure that no air is present between the glass and the interlayers [12].

When one of the laminated glass panes fails, the interlayer ensures that the fragments of the glass are retained. In addition it offers residual strength and reduces the risk of falling fragments causing injuries. There are different types of interlayers available. The most typical ones are mentioned in Table 2.2.

Table 2.2: Comparison of different interlayers [19].

Interlayer	Properties	Benefits	Considerations	Applications
Polyvinyl-Butyral (PVB)	Most common, optical clarity, flexibility and ability to adhere.	99% filtering of UV rays, several thicknesses, acoustic performance, cost-effective.	Not to be used where exposed to moisture or water.	Doors and windows, Internal balustrades, overhead glazing.
Sentry Glass Plus (SGP)	Better rigidity and tear resistance when compared to PVB.	Can be used in external exposed applications, superior edge stability, highest level of structural performance.	More expensive to other laminates.	Internal and external glazing, Security glass, floors, stairs, facades, aquariums.
Ethylene-Vinyl-Acetate	Alternative interlayer for safety glass, high moisture resistance.	Can be used in external exposed edge applications, customisable.	Less performing structural properties compared to SGP, cost-effective.	Switch Glass, Solar Panels.

Another benefit of laminated glass is that an engineer may reach required thickness which are unobtainable in the glass market for a single panel . A reduction in total thickness needs to be accounted for as described in chapter 2.2.4. The post-failure behaviour is a secondary effect related to the adhesion of the interlayers to the glass. After breakage, the glass fragments adhere to the interlayer, which introduces some remaining structural capacity. Annealed laminated glass has a better post-failure behaviour than heat strengthened and fully tempered glass. Heat strengthened glass does show a better post-failure behaviour than fully tempered glass. This is based on the capacity of the fragments, where larger fragments perform better than smaller fragments [14]. In conclusion the structural performance before failure increases with tempering, but the residual structural performance after breakage performs better with less tempering.

2.2.3. Curved and Bent glass

The application of innovative designs in glass is rising. Curved glass is an option to improve the design of building facades. Manufacturing glass in curved shapes comes with its challenges and these challenges and applications of curved glass are described in this subsection. Several methods can be used to obtain different solutions for different applications. Cold-bending and hot-bending of glass are commonly used in practise, whereas laser-based bending is currently under research, in which this thesis is also contributing. Laminating and prestressing bent glass comes with challenges, but is to a certain extent possible.

Cold bent glass

Cold bending of glass can be distinguished in the bending of glass by assembling and bending by lamination. Bending by assembling is in essence bending the glass plates and mounting the glass to a frame structure to keep the curved shape. The curvature is therefore limited to the bending strength of the glass [20].

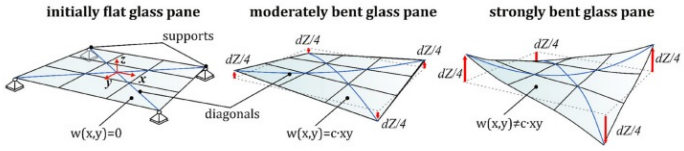

Figure 2.10: Cold bent glass pane [21].

The other bending technique is bending by lamination. The bending process is combined with the laminating process. The glass pane is fixed in a designated mould. An interlayer is then applied at a temperature of approximately 120°C and a pressure of 1 up to 12 bar is used [20]. Neugebauer describes the process where the interlayer will become soft and the glass layers will be connected. At the end of the laminating process the interlayer cools down and becomes stiff enough to hold the bent shape. This is possible because the shear forces are activated between the glass layers [20].

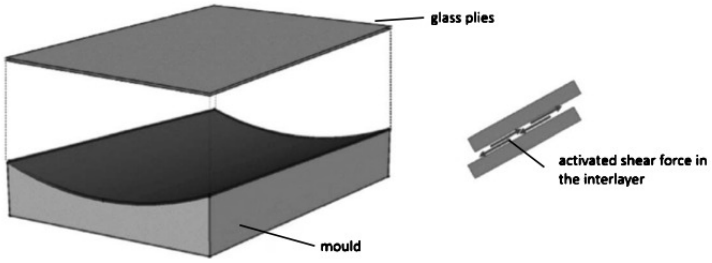

Figure 2.11: Cold bending by lamination [20].

Hot bent glass

Hot bending of glass is the most commonly used technique. This technique bends the glass at a temperature higher than 550°C. Moulds are used to let the softer and more viscous glass deform in the required shape. Gravity is the main component in this process, allowing the glass to sag in its demanded geometry [20].

The process starts with a flat sheet of annealed glass. The glass is then placed into an oven where depending on the glass composition the temperatures can reach 1200°C [22]. The bent glass is slowly cooled to allow the residual stresses to dissipate. Hot bent glass has some of the following characteristics [22]:

- Curvature: The hot bending process is used to manufactures glass shapes with a wide range of curves.
- Optical quality: Due to controlled heating and cooling, the optical quality of hot bent glass maintains a high level with minimal distortion or visible waves.
- Thickness: Hot bending can be used to introduce curvatures to various thicknesses.
- Edge quality: The edges of hot bent glass are usually smooth and uniform, as the higher temperatures allow for softening of the glass during the shaping process.

A second method is bent tempered glass. Both the hot bent glass and the bent tempered glass use similar processes, but each have its own applications and properties [22]. Migoglass describes the production of bent tempered glass as follows. The production of bent tempered glass contains two main steps consisting of the bending and the tempering. First a flat panel of annealed glass is heated to around 650°C. The heated glass is formed in a mould to obtain the required curvature and shape. After the bending process is finished, the curved glass is rapidly cooled to temper the glass and increase its strength.

Bent tempered glass has the following characteristics [22]:

- Increased strength: The tempering process increases the strength of the glass.
- Safety: The fragments of the broken glass are relatively small and less harmful compared to annealed glass.
- Thermal resistance: Bent tempered glass has increased resistance to thermal stresses.
- Dimensional stability: Bent tempered glass can maintain the shape of the glass, preventing warping or distortion over time.

Laser-based bent glass

Laser-based glass bending is a relatively new innovation regarding the bending of glass. In may 2017 Fraunhofer IWM published an article on laser-based bending of glass [23] and in October 2019, Fraunhofer IWM posted an article on their website about laser-based glass bending [24].

The first papers published based on this method, where significant progress was made, were published early 2024. Two articles were published that describe the use of lasers as a tool to bend soda lime silica glass. Liao et al. published an article of bending comparatively thin glass in different bending angles [25]. Where Bolakhrif et al. describes the laser-bending of low-E coated flat glass [26]. The study of Bolakhrif focuses on the optical performance of laser-bent glass, where the study of Liao describes the characterisation and process of bending thin (500 and 1000 μm) glass.

The three main steps to bend glass with a CO_2 laser as described by GLAPE GmbH are illustrated in Figure 2.12. A more extensive description of the laser-oven and the functionalities of its individual components are described in Section 2.3.3.

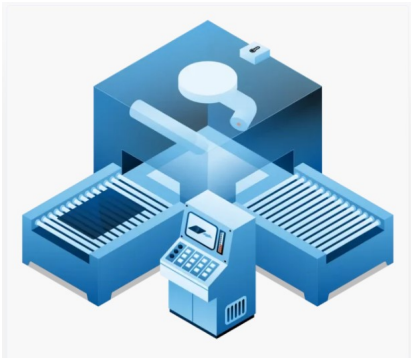

(a) Step 1: Preheating the oven and preparing the glass sample outside the setup.

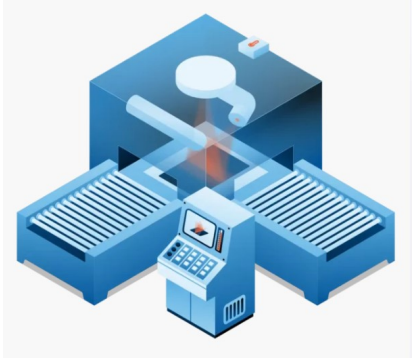

(b) Step 2: Placing the sample in the oven and applying localised heat with the laser.

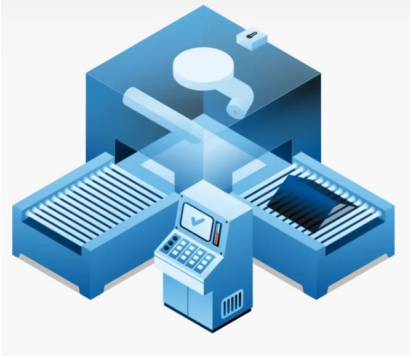

(c) Step 3: Gradually cooling down of the sample after laser-heating is applied.

Figure 2.12: The three main steps of the laser bending technology of glass [27]

The first main step in the laser-forming technology is the preheating of the oven. The sample is then placed within the oven to gradually increase in temperature as well. The maximum temperature of the glass requires to be below the point where the glass starts to become viscous. This ensures that the complete glass sample remains as a solid before the laser is applied. The next point in the processing is to apply the CO_2 laser to increase the temperature of the glass locally. This specific step results in the glass reaching a viscous state at the specified point or path of the laser.

Two distinctions are made, the bending and the forming of the glass. With laser-bending the glass bends around a corner, while with laser-forming the glass is sacked into a specific shape out of plane.

For the laser-bending process, when supported on one side and heated along a singular line, the flat glass sample will bend, creating a corner with a low bending radius, as visualised in Figure 2.13. Stopping the heating at the right time will lead to hardening of the softened point, and results in the sample being completely solid as at the start of the procedure.

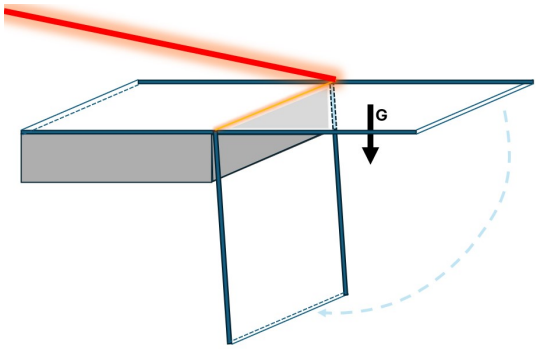

Figure 2.13: Bending glass around a corner by laser-induced heating.

The second method, laser-forming, is based on applying the laser in a certain shape/form. When heated, the shape pattern sags out of plane, resulting in an elevated part in the cross section. The shape of the pattern can be a rectangle, circle, triangle or any other 2D-shape. CAD-software is used to guide the laser, making it highly effective to use for any shape. Secondly, no mould is needed to obtain the desired depth. Figure 2.14 illustrates what happens in the oven for the laser-forming process.

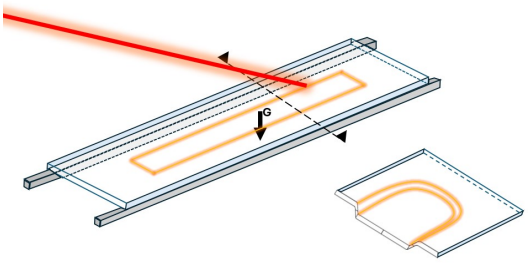

Figure 2.14: Forming glass with a sagged form, by laser-induced heating.

In both the studies of Liao and Bolakhrif, a CO_2-continuous wave laser is used. Since the method of Bolakhrif was able to bent glass with larger thicknesses, this method is taken as the source of information. This method is also used in manufacturing the samples used in this thesis. The process is based on a couple of steps. At the start flat glass panels are cleaned and put in an oven. The temperature at which the oven operates is around 570°C. During the laser-heating process an integrated CO_2 laser (10.6μm) was used to apply a linear pattern[26]. This induced localized heating and triggered the bending of the glass. The localized heating introduces the glass to become viscous. Due to clamping of the sample where no bend or shape is required, the sample starts to deform due to the presence of gravity. The laser heated parts begin to deform and the rest of the sample remains in a solid state. Bends with low bending radii lower than 10mm are possible. The laser-forming method is based on using the laser to create elevated shapes in flat glass, as can be seen in Figure 2.15b.

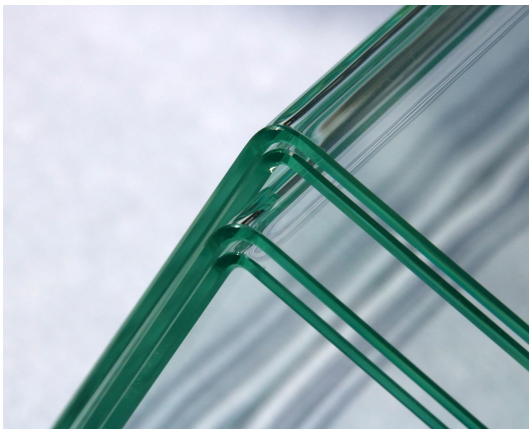

(a) Tight corner radii, by laser-based bending [24].

(b) Glass deformed by laser-forming [2].

Figure 2.15: Different applications of laser-based glass bending.

The development and research of this bending technique is in its early stages. This thesis therefore provides more insight in the predictability and the performance of laser-formed glass.

2.2.4. Designing with glass

Designing structures is generally governed by the Eurocode. Where for most building materials there is a separate Eurocode available, that of glass is still in development. There is on the other hand a norm used in the Netherlands to design glass structures. The code used for glass is the NEN 2608:2014-NL. In this code the required material properties, the basis of the design, calculation-strategies and the checks for the serviceability limit state (SLS) and the ultimate limit state (ULS) are described.

Mechanical Properties of glass

Glass is a material with unique mechanical properties. It is a homogeneous isotropic material and has an almost perfect linear-elastic behaviour with respect to its tensile strength capacity [28]. Glass can resist very high compressive forces and when absolutely no flaws or cracks are present, the tensile strength is also relatively very high. What makes glass perform less promising is the presence of surface flaws. These surface flaws create (microscopic) cracks in the glass, making small openings in the surface. When subjected to tensile stresses, these ”openings” are the weakest spots in the glass, making it around 1000 times less strong compared to a perfect glass surface without flaws.

The chemical composition of glass consists of multiple molecules. The main component of glass is Silicon Dioxide, also known as silica sand. Where Lime (CaO) and Soda(Na_2O) are the two other main components. Table 2.3 shows indicatory values of mass percentages of Soda Lime Silica Glass.

Table 2.3: Chemical composition of Soda Lime Silica Glass. [14]

	Soda Lime Silica
Silicon dioxide (SiO_2)	69%-74%
Clacium oxide (CaO)	5%-14%
Sodium oxide (Na_2O)	10%-16%
Boron-trioxide (B_2O_3)	-
Magnesium oxide (MgO)	0%-6%
Aluminium oxide (Al_2O_3)	0%-3%
Others	0%-5%

Table 2.3 shows the chemical composition of Soda Lime Silica Glass. Where Table 2.4 shows the mechanical properties.

Table 2.4: Mechanical properties of Soda Lime Silica Glass.

	Symbol	**Soda Lime Silica**	
Density	ρ	2500	kg/m^3
Young's Modulus	E	70.000	MPa
Poisson's ratio	ν	0.23	-
Hardness (Knoop)	$HK_{0.1/20}$	6	GPa
Coefficient of thermal expansion	α_T	9	$10^{-6}K^{-1}$
Specific heat capacity	c_p	720	$J/kg^{-1}K^{-1}$
Thermal conductivity	λ	1	$Wm^{-1}K^{-1}$

The strength of glass, Ultimate Limit State (ULS)

Glass does not yield making it a brittle material. The exact strength of glass is not a more or less exact number like that of common building materials like steel and concrete. A study described in O'Regan his book "Structural Use of Glass in Buildings" shows results of 740 tests being done on 6mm thick annealed glass [5]. The results of these test show that the failure stress at which glass fails scatters immensely. The distribution of the failure stresses does not relate to any probability function, making it highly unpredictable. A study performed by Veer, Louter and Bos confirms the scatter of failure stresses. This study on the other hand found conclusions regarding the distribution of the stresses. A Weibull distribution may describe the probability of failure, but is only valid in certain cases [15]. This study shows an average failure stress for lying annealed glass panels at 42 MPa, for lying heat strengthened glass at 104 MPa and for fully tempered glass at 157.4 MPa. Noticeable in this study is that a higher failure stress resulted in more fragmentation of the glass.

The NEN 2608:2014-8 states the following characteristic bending strength values of tempered glass. A design value for annealed glass needs to be designed by equation 2.1. Tempered glass needs to be calculated by equation 2.2 [29]. Both equations show a similar part and an extra strength relation is added for tempered glass, resulting in higher design strength values.

The design value of the bending strength ($f_{mt;u;d}$) of annealed glass is equal to:

$$f_{mt;u;d} = \frac{k_a \times k_e \times k_{mod} \times k_{sp} \times f_{g;k}}{\gamma_{m;A}} \tag{2.1}$$

Where [29]:

$f_{mt;u;d}$	Is the bending strength of annealed glass in N/mm^2.
k_a	Is the factor for the surface-effect regarding equation 2.3
k_e	Is the factor for the edge quality of the glass panel. Stresses regarding Table 2.7 need to be accounted for. For other situations k_e = 1 need to be applied.
k_{mod}	Is the modification factor depending on the load duration and the reference period regarding 8.3.3 (6).
k_{sp}	Is the factor for the surface structure of the glass regarding Table 2.6.
$f_{g;k}$	Is the characteristic value of the bending strength of the glass, in N/mm^2, where $f_{g;k}$ = 45 N/mm^2.
$\gamma_{m;A}$	Is the material factor of glass, where: $\gamma_{m;A}$ = 1.6 for situations where wind or isochoric pressure is the governing variable load case. $\gamma_{m;A}$ = 1.8 for any other situation.

The design value of the bending strength ($f_{mt;u;d}$) of tempered glass is equal to:

$$f_{mt;u;d} = \frac{k_a \times k_e \times k_{mod} \times k_{sp} \times f_{g;k}}{\gamma_{m;A}} + \frac{k_e \times k_z \times (f_{b;k} - k_{sp} \times f_{g;k})}{\gamma_{m;V}} \tag{2.2}$$

Where [29]:

$f_{mt;u;d}$	Is the bending strength of annealed glass in N/mm^2.
k_e	Is the factor for the edge quality of the glass panel. Stresses regarding section 2.7 need to be accounted for. For other situations k_e = 1 need to be applied.
k_a	Is the factor for the surface-effect regarding equation 2.3.
k_{mod}	Is the modification factor depending on the load duration and the reference period regarding 8.3.3 (6).
k_{sp}	Is the factor for the surface structure of the glass regarding 8.3.3 (1).
$f_{g;k}$	Is the characteristic value of the bending strength of the glass, in N/mm^2, where $f_{g;k}$ = 45 N/mm^2.
$\gamma_{m;A}$	Is the material factor of glass, where: $\gamma_{m;A}$ = 1.6 for situations where wind or isochoric pressure is the governing variable load case. $\gamma_{m;A}$ = 1.8 for any other situation.
k_z	Is the factor for the zone of the panel regarding 8.3.3 (7).
$f_{b;k}$	Is the characteristic value regarding Table 2.5 in N/mm^2.
$\gamma_{m;V}$	Is the materialfactor of tempered glass, where $\gamma_{m;V}$ = 1.2.

Table 2.5: Characteristic values of the bending strength of tempered glass [29].

Material	$\mathbf{k}_{sp} \times \mathbf{f}_{g;k}$	$\mathbf{f}_{b;k}$	$\mathbf{f}_{b;k}$ **-** $\mathbf{k}_{sp} \times \mathbf{f}_{g;k}$
	N/mm^2	N/mm^2	N/mm^2
Float glass - Heat strengthened	45	70	25
Float glass- Fully tempered	45	120	75

Equations 2.1 and 2.2 show several different safety factors. k_{sp} refers to the surface structure of the panel. This factor is dependent on the manufacturing process and has to be determined by Table 2.6.

Table 2.6: Factor for surface structure, k_{sp} [29].

Material	$\mathbf{k}_{sp}$
Floatglass	1.0
Figure glass	0.8
Enamelled glass at enamelled side	0.78
For non enamelled side, see floatglass	

The factor for the edge quality of the panel k_e needs to be determined by Table 2.7.

Table 2.7: Factor for edge quality, k_e [29].

Material	$\mathbf{k}_e$**, Loaded out-of plane**	$\mathbf{k}_e$**, Loaded in plane**^{a}
Annealed glass	0.8	0.8
Heat strengthened glass	1	0.8
Fully tempered glass	1	1
^{a} At polished edges		

When the glass panel is loaded by a distributed load and when a non-linear calculation is needed for calculating the bending stresses, the factor for the area-effect, k_a, need to be determined by equation 2.3.

$$k_a = 1.644 \times A^{-(\frac{1}{25})} \tag{2.3}$$

Where A is equal to the area of the load in mm^2. When the panel is loaded by a concentrated load with load-area $H_1 \times B_1$, the factor of the area-effect, k_a, can be determined by equation 2.3 with A being the area of the pointload $H_1 \times B_1$ in mm^2. In every other situation k_a = 1 may be assumed.

The modification factor for the load-duration of annealed glass needs to be determined by equation 2.4.

$$k_{mod} = (\frac{5}{t})^{\frac{1}{C}} \tag{2.4}$$

Where [29]:

k_{mod}	Is the modification factor depending on the load duration and the reference period regarding 8.3.3 (6).
c	Is the corrosion constant based on the temperature and humidity by Table 2.8
t	Is the load duration

Table 2.8: Corrosion constant, c [29].

Glass surface	Edge zone	Middle zone
Surface neighbouring a cavity of insulated glass. The cavity consists of air with a relative humidity of maximum 10%	16	27
Glass surface of laminated glass neighbours the interlayer	16	18
Other situations	16	16

The zone factor, k_z should be determined by Table:

Table 2.9: The zone factor, k_z [29].

Tempering type	Zone 1	Zone 2	Zone 3	Zone 4
Heat strengthened glass	1	1	Calculate	1
Fully tempered glass	1	0.9	as annealed	0.9

The zones as stated in Table 2.9 are defined by the following definitions [29]:

- Zone 1: The middle zone as visualised in Figure 2.16
- Zone 2: The edge zone of the panel. The width of the edge zone is 1.5 times as large as the glass thickness for heat strengthened glass. For fully tempered glass the width can be multiplied by 1 times the glass thickness
- Zone 3: The corner zone of the panel, following surface ABCD in Figure 2.16. When the edge is rounded with a minimum radius of r + x, zone 3 is not accounted for, instead the zone 2 is used. With x being the width of the edge zone and r is the radius of the inner circle calculated by equations 2.5 and 2.6.
- Zone 4: The zone surrounding drilled holes. The width of this zone 4 is 1.5 times the glass thickness for heat strengthened glass. For fully tempered glass this width is equal to the glass thickness.

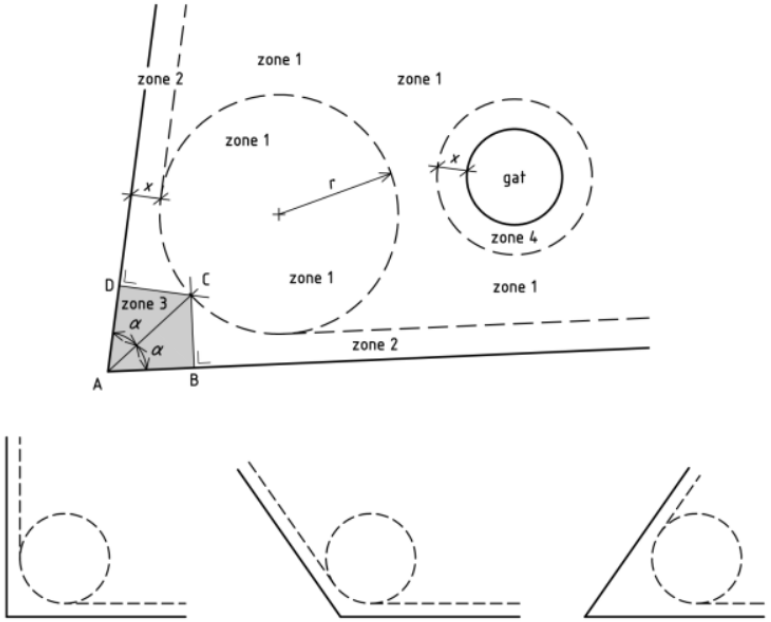

Figure 2.16: Zones of tempered glass [29].

Two equations are used when calculating the radius.

For n = 1:

$$r = (2 + \sqrt{2}) \times t_{pl} \tag{2.5}$$

For n > 1:

$$r = (2 + \sqrt{2}) \times t_{pl;i} \tag{2.6}$$

With [29]:

- n Is the amount of panels
- r Is the radius of the inner circle, in mm.
- t_{pl} Is the glass thickness of one glass panel, in mm
- t_{pl} Is the glass thickness of a laminated glass unit, in mm

Serviceability Limit State (SLS)

Three distinctions are made when checking the Serviceability Limit State (SLS). The first two account for deformations at the edges of glass units, where the third distinction is made by checking the deformation in the middle of a glass unit.

The first check is distinct for insulated glass units. The equation that needs to be checked is given in equation 2.7.

$$u_{max} \leq \frac{l_z}{200} \tag{2.7}$$

With [29]:

- u_{max} Is the maximum deformation at the edge of a insulated glass unit
- l_z Is the length of the edge of the insulated glass unit

The second check is distinct for single glass panels or laminated glass units. The equation that needs to be checked is given in equation 2.8

$$u_{max} \leq \frac{l_z}{100} \tag{2.8}$$

With [29]:

u_{max}	Is the maximum deformation at the edge of a insulated glass unit
l_z	Is the length of the edge of the insulated glass unit

The third check account for the deformations in the middle of a glass unit. The equation that needs to be checked is given in equation 2.9

$$u_{dia;max} \leq \frac{l_{dia}}{65} \leq 50 \tag{2.9}$$

With [29]:

$u_{dia;max}$	Is the maximum deformation in the middle of a insulated glass unit, in mm
l_{dia}	Is the largest diagonal of a glass unit

2.2.5. Strength and stiffness research projects

Significant research projects have been performed around the strength and stiffness parameters of Soda Lime Silica glass. In 2009 the journal of Fatigue and Facture of Engineering Materials and Structures published a paper by Veer et al. The article is called ”The strength of annealed, heat-strengthened and fully tempered float glass”[15]. This paper discusses the strength of glass and the way that there is no agreement on the validity of the characteristic values of glass. This research project tested sufficient glass samples on strength capacity.

The discussion stated that the ideal result would be a simple formula to calculate the strength of glass. The observations that led to the results of this research show that no simple solution exists. There is no unique solution as a result of the tests, as a large scatter of strength is observed. Normal statistics cannot describe the spread. The Weibull approach is valid, however, only in certain cases. The conclusions of the result state that it is doubtful whether a certain guaranteed minimum strength can be defined. Several factors influence the strength of glass, such as edge quality, the aspect ratio and pre-stress level [15].

The inhomogeneous statistics of bending test results makes determining the strength of glass complex. As stated, the edge quality is assumed to be of major influence to the strength capacity. The so-called ”hidden damage” of edges is assumed to be the explanation of the scatter. Veer and Rodichev researched the influence of tensile stressing on the bur-side of an edge against the broken side of an edge [13]. The cutting process of float glass leaves micro-cracks at the edge surfaces, and differences are observed in strength between the scored side and the broken side of the glass. The research project of Veer and Rodichev examined 190 glass panels and four distinct bending tests were performed. The samples were tested in a lying position with the bur-side upwards, where it is oriented in the compression zone and with the bur side downwards, where it is oriented in the tension zone. The other two tests were performed were the samples were standing with the bur either on the left or the right side. The tests show the average strength with the bur side in the tension side is some 20% less compared with the tests where the bur is on the compression side [13]. A noteworthy observation is that the failure stress on the bur side was much more consistent than that of the broken side.

The characteristic bending strength of annealed, heat strengthened and tempered glass is thoroughly researched. Weibull distribution seems to fit the scatter of results best, while it comes with extra considerations. This thesis provides strength capacity values of laser-formed glass, however, the sample size is minimal which leads to the need of caution when observing these results. The obtained results are related to the specific design and application, where other applications and designs might perform differently.

2.3. Laser bending of materials

The use of CO_2-lasers have varying purposes. Laser-cutting, surface treating and laser-heating are multiple applications where these lasers play a significant role. This section describes general information on CO_2-lasers and its use within the laser-bending process of glass.

2.3.1. Principles of CO_2-lasers

The first discoveries of a laser-beam dates from 1960. Theodore Maiman discovered a technique for monochromatic radiation in the infra-red spectrum and described it in an article published in August 1960 [30]. This discovery is seen as the invention of the very first laser as seen nowadays.

The word laser originally was an acronym for ”Light Amplification by Stimulated Emission of Radiation” [31]. The singular term ”laser” itself is used generally and is widely accepted to describe light amplifiers or generators. A laser is a source of light, similar to a common light bulb. Specific differences makes a laser unique as a light source. The light emitted by a laser is monochromatic, meaning that only one wavelength is emitted. A regular light bulb/source emits light in various wavelengths. A regular light source emits light in all directions, where lasers direct the light in one specific orientation or direction.

Common lasers consists of three things; a medium, a power source or so called ”pump” and a resonator. The medium for a CO_2-laser is the gas mixture consisting of carbon dioxide (CO_2), helium (He), nitrogen (N_2) and in some cases this mixture includes hydrogen (H_2), oxygen (O_2), water vapour and/or Xenon (Xe) [32]. The power source is an electrical discharge and the resonator consists of two mirrors. These mirrors amplify the radiation and a single certain wavelength is able to exit the resonator.

2.3.2. Laser bending of metals

The use of a laser beam to bend materials is called thermo-mechanical forming. The bending of sheet metal is done by introducing thermal stresses without the use of any external loading. The thermal expansion is blocked by surrounding material, resulting in thermal stresses in the heated areas. The bending of materials is based on three different mechanisms. A study performed by Kant et al. describes these three laser-bending mechanisms [33]. Temperature gradient mechanism (TGM), the buckling mechanism (BM) and the upsetting mechanism (UM) are described.

The temperature gradient mechanism (TGM) is used to bend the material in the direction of the laser source. The beam diameter is equivalent to the thickness of the material and a steep temperature gradient is required along the thickness. This steep gradient is obtained by high scanning speeds. A non-uniform expansion is introduced along the thickness of the sheet, because the temperature at the top is higher than the temperature at the bottom of the sample. The thermal expansion introduces compressive stresses within the material, while the material is unable to expand locally. The magnitude of these stresses are larger at the top, due to the temperature gradient. Contraction of the top part of the sheet is a result of these internal compressive stresses when the material cools down. This contraction and the difference in plastic deformation of the top and bottom part introduces the bending of the material in the direction of the laser source. Bending angles of 0.1 to 3° are possible when sheets are subjected to TGM [33].

In the buckling mechanism (BM), the difference in the temperature gradient is negligible [33]. BM is generally used for thin materials. The buckling stiffness is relatively low for thin materials, resulting in the buckling phenomenon when subjected to thermal expansion. Along a laser-line the material buckles and dependent on the direction of the buckle, the thin sheet bends towards or away from the laser source. Bending angles of 1 to 15° are possible when thin sheets are subjected to the BM [33].

The upsetting mechanism (UM) is used for thicker sheets of material. Isotherms occur when the laser heating is applied, resulting in a uniform increase of the temperature. This increase in temperature introduces thermal expansion along the full thickness of the material. Due to the restriction of expansion by the presence of the rest of the material, compressive stresses occur. When cooled down, these stresses introduce local shortening of the material resulting in bending of the sheet material.

2.3.3. Laser bending of glass

The bending of glass is different compared to that of metals, where the bending of glass changes the local viscosity of the material during the process. Fraunhofer IWM developed a customised system with several components to be able to bend glass by laser-induced heating, as visualised in Figure 2.17.

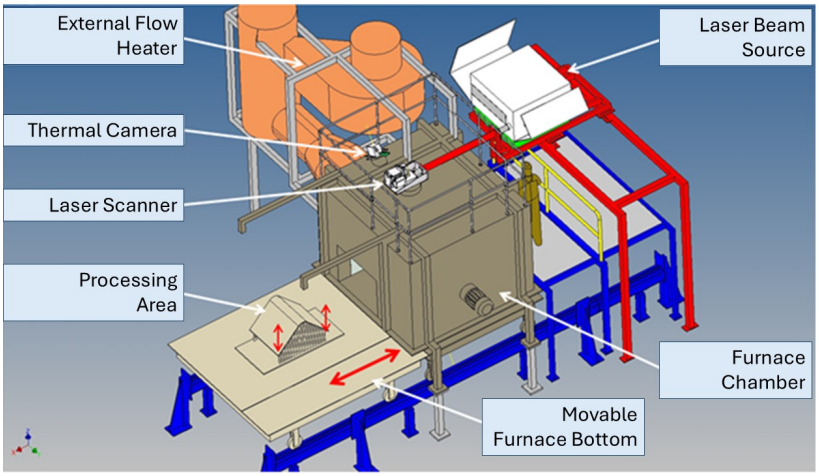

Figure 2.17: The glass bending furnace configuration with the different components highlighted [34].

The bending-oven was developed in 2012 as a Research and Development (R&D) project. It is used for several applications involving the heating and processing with a laser in addition to a regular furnace. The Master thesis of Sylvia Schlöglmann describes the oven that has been used for this thesis as well. Schlöglmann researched the effect of different parameters that influence the presence of white haze on glass samples to obtain her Masters degree in Chemistry at the University of Regensburg.

The information given in this section about the details of the different components is based on the descriptions given in the study by Schlöglmann, since the same oven is used [35].

The oven consists of multiple components, and three main components are elaborated on more extensively. The main components consists of the furnace, the CO_2 laser, and the laser scanner. A photo of the oven used by Fraunhofer IWM is shown in Figure 2.18.

Figure 2.18: The glass bending furnace used by Fraunhofer IWM. [34].

The furnace is a custom-made product of TS Elino GmbH, a company specialised in ovens and furnaces. This furnace is capable of reaching temperatures of 750°C. Alongside the furnace, a CO_2-laser is used in this configuration. The laser is a TruFlow 2700 model, where it uses a wavelength of 10.6μm. The CO_2-laser is positioned at the top of the furnace chamber, where the laser-beam is guided to the glass samples by adjusting the laser scanner. This laser scanner consists of movable mirrors and is a powerSCAN 50 by SCANLAB GmbH. The laser scanner is capable of guiding the laser-beam along a defined path. Predefined paths can be sketched by CAD-software beforehand, and free-drawing the paths on side is possible as well. This makes the use of a laser-scanner highly interesting in obtaining "unlimited" geometries and shapes for the laser-forming process. The possibility of processing and bending glass without the use of a mould, and within a matter of minutes, makes this development promising for further research.

2.3.4. Laser-bent glass research projects

The research of glass as a structural element has been steadily growing in the last 30 years. This development led to more structural glass projects and applications. In 2014 Jürgen Neugebauer wrote an article on the applications of curved glass in buildings [20]. Hot bending of glass is mentioned, cold bending of glass is mentioned, while laser-bending/-forming is not mentioned. This is because the first article of laser-based glass bending is published in 2017, as mentioned in Section 2.2.3. The current state of research and development of laser-formed glass and glass in general is described in this chapter to obtain the research gap that this research contributes to solve.

The development of laser-formed glass has not been thoroughly investigated. The thoughts of different applications of laser-bent glass products are stated by a spin-off of Fraunhofer IWM named GLAPE GmbH. GLAPE GmbH was founded in 2023 and provides ideas for the architectural and automotive industry [36]. Before the start of this thesis, Fraunhofer IWM was contacted about the development and possible collaboration options. No structural properties of laser-formed glass panels were researched up until the start of this thesis. Fraunhofer IWM did tests if there was an increase in stiffness, however, no validation or predicting models were performed and made.

Liao et al. published a paper in July 2024 called "Innovative laser-assisted glass bending approaches using a near-infrared continuous wave laser" [25]. This research showed the laser-bending method applied on thin glass samples. These samples had a thickness between 150μm and 1000μm. They achieved bending angles of 30°, 60° and 90° on soda-lime silica glass measuring thicknesses of 550μm, see Figure 2.19.

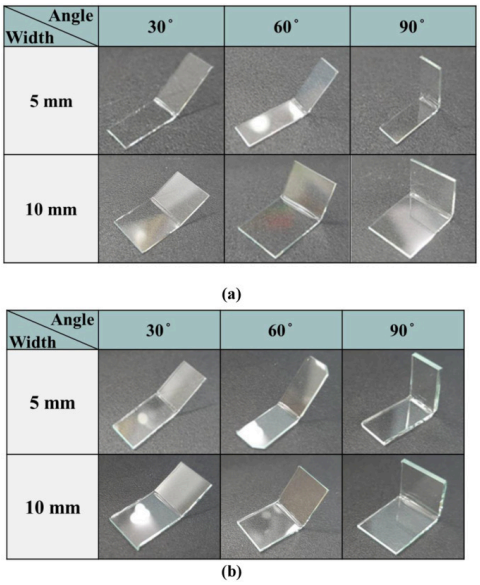

Figure 2.19: Bending angles reached with laser-bending techniques. a) Soda lime silica glass b) Borosilicate glass [25].

The paper by Liao et al. and a paper by Bolakhrif et al. [26], published at the same time in July 2024

are the only published articles found that describe the behaviour of laser-bent/formed glass. Bolakhrif's research shows glass bending technology as fit for purpose of coated bent glass [26]. Their research focusses on the optical performance of coated and uncoated bent glass. Furthermore, their research investigates the chemical composition before and after heat treatment.

As described in section 2.3.3, Sylvia Schlöglmann performed a Master Thesis in 2024 on the presence of haze in glass samples and the influence of the parameters and settings of the laser-oven [35]. This shows that the topic is at the very early stages of development, and an abundance of ideas are yet to be discovered and researched about the laser-bending technique of glass in general. This Thesis aimed to provide conclusions about the stiffness of laser-formed glass, filling a small part of the total research gap in laser-based bending of glass.

3

Parameter study

The first stage of this thesis consists of studying how different parameters influence the stiffness of laser-formed glass. Geometry changes in the cross section have substantial impact on the second moment of area (Inertia in short), which relates to the stiffness of the glass. The impact of changing parameters and the magnitude of influence is studied. Design considerations of utilising the geometry changes are stated and described at the end of this chapter.

3.1. Cross-sectional parameters

By designing glass panels it is good to understand the difference in behaviour of how a panel is supported. A two sided supported panel behaves as statically determined beam with bending primarily in one direction. Where four sides supported panels acts like a plate, where bending in both directions will occur. For this reason a statically determinate beam model is used to analytically get results from assumptions and parameter adjustments.

When designing a statically determined structure, the stiffness of this structure is directly related to the cross-sections geometry. Euler-Bernoulli beam equations show the relations between Inertia (I) and deformation (w) of a statically determined beam.

$$\rho A \frac{\partial^2 w}{\partial t^2} + EI \frac{\partial^4 w}{\partial x^4} = q \tag{3.1}$$

By rewriting the fourth space derivative into a relation of phi "φ" and kappa "κ", the following equations are obtained:

$$\varphi = -\frac{\partial w}{\partial x} \tag{3.2}$$

$$\kappa = \frac{\partial \varphi}{\partial x} \tag{3.3}$$

$$M = EI * \kappa = -EI * \frac{\partial^2 w}{\partial x^2} \tag{3.4}$$

Equilibrium will lead to the following constitutive relation related to the shear force and the moment present in the structural element, where q is the load acting on the element:

$$\rho A \frac{\partial^2 w}{\partial t^2} = \frac{\partial V}{\partial x} + q \tag{3.5}$$

$$\rho A \frac{\partial^2 w}{\partial t^2} = \frac{\partial^2 M}{\partial x^2} + q \tag{3.6}$$

$$\rho A \frac{\partial^2 w}{\partial t^2} + EI * \frac{\partial^4 w}{\partial x^4} = q \tag{3.7}$$

This constitutive relation, stated in equation 3.7, shows that the deformation ”w” of a system, that is loaded out of plane by load ”q”, is directly related to the second moment of area or otherwise called inertia ”I”. The time-related part of this equation does not play a role in the static calculations of a beam. The deformations are therefore inversely related to the stiffness of a structure. This inertia term relates to the cross section of a structure. In this case the cross section of a laser-formed glass panel.

Transforming a flat glass cross-section in a laser-formed one, has a major influence on the inertia of a cross section. Where the increase of height influences inertia by a power of three for rectangular cross-sections. There are multiple ways of increasing the height of a cross-section. At first, the thickness of flat glass panels can be increased to introduce more height in the cross-section. The downside of this is that more material is used, which is contradictory to the objective of this thesis: To be able to increase stiffness while reducing or retaining the material use. Therefore, another solution is needed to increase this relative height.

Corrugation or introducing a so called elevation, is a way to increase height while maintaining the same material thickness. This can, for example, already be seen in corrugated steel sheets for roofing solutions, see Figure 3.1.

Figure 3.1: Metal roofing sheet [37].

The concept of an elevation is visualised in Figure 3.2. Here an elevation is introduced and an increase in inertia is obtained. This concept is manufactured and used in the lab experiments, as described in chapter 4.

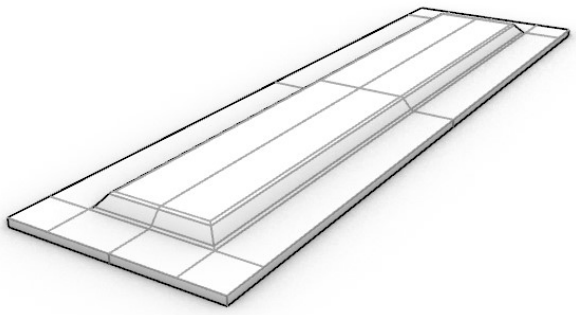

Figure 3.2: Main geometry concept.

Considering the stiffness increases by introducing these corrugations or elevations, it can be assumed this influences the stiffness of glass panels as well. By designing the new cross-sections for flat glass panels, the inspiration came from the metal roofing sheets. An elevation with a certain depth is introduced with the laser-forming technique and therefore the cross-section is adjusted. There are several parameters that can be adjusted within this bending process and influence the stiffness. These parameters are introduced to adjust a base-model, considering a cross-section at midspan as can be seen in figure 3.3.

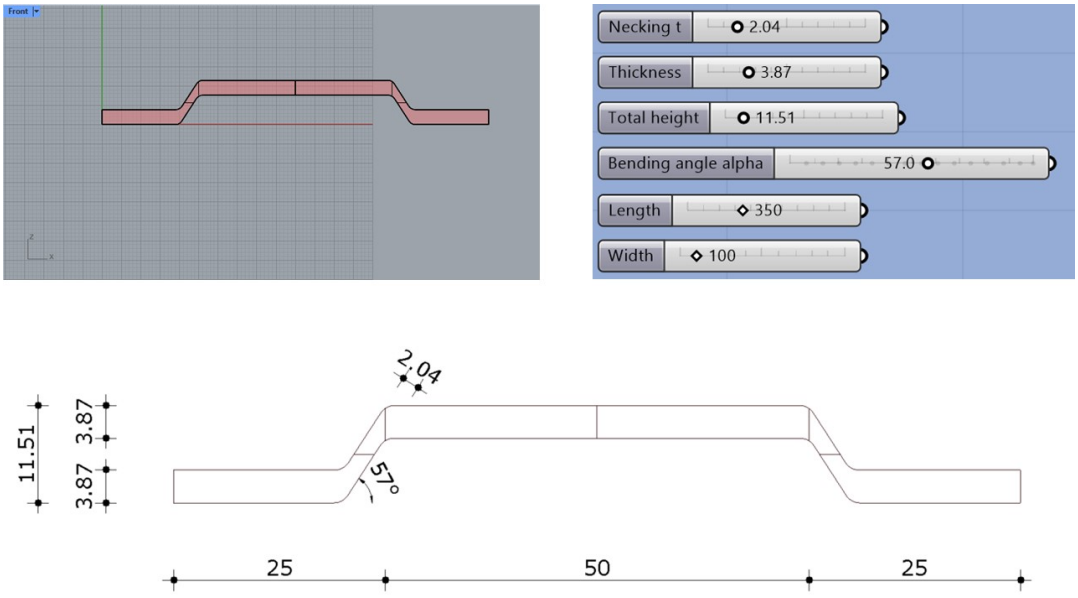

Figure 3.3: Cross section of sample Deep-10 as used in the lab-experiments.

3.1.1. Adjustable parameters

To be able to calculate and model different configurations of a design, a parametric model supports the efficiency in getting results and values related to the cross section. By adjusting the parameters, different values can be obtained immediately. The value of the inertia is obtained through built-in code blocks in Rhino/Grasshopper.

The parameters that are adjusted in this parametric model are:

- The Glass thickness.
- The Total height.
- The Bending angle.
- The Web thickness and the presence of necking.

In the following subsections, the different parameters will be addressed and elaborated.

Glass thickness

The glass thickness is the first parameter that can be adjusted. Four different thicknesses have been examined, this being 4mm, 8mm, 10mm and 15mm thick glass.

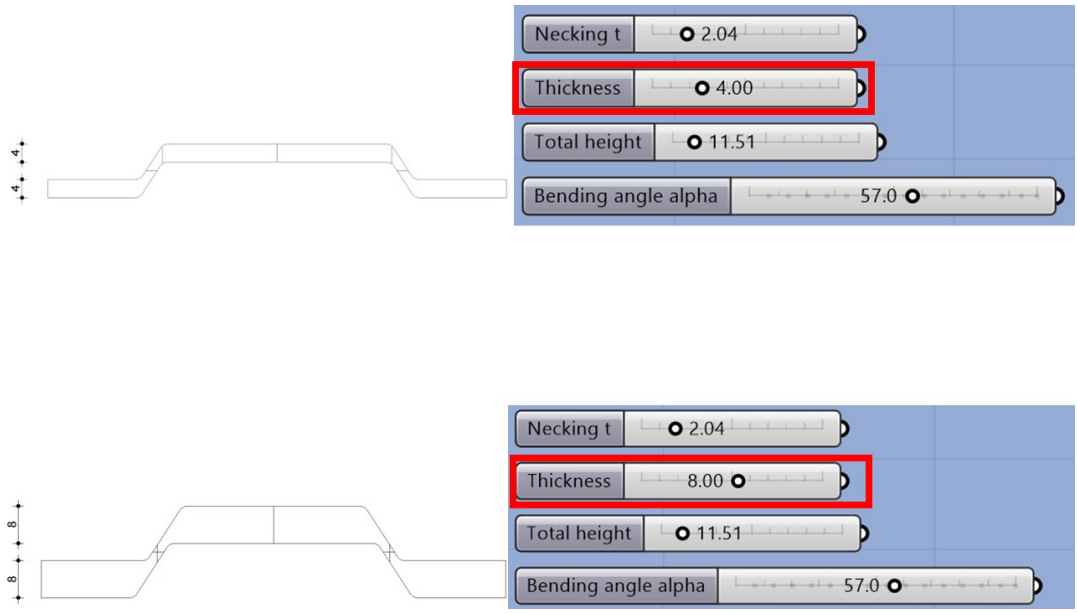

Figure 3.4: Adjustable thickness.

Total height

The total height has a major influence on the inertia. What should be considered is that the depth of the elevation is limited, since the necking will play a role in the production process. A more thick glass panel can have a deeper elevation than a thin glass panel. In the subsection of necking this will be further elaborated. Different elevation depths have been examined, based on the different glass thicknesses.

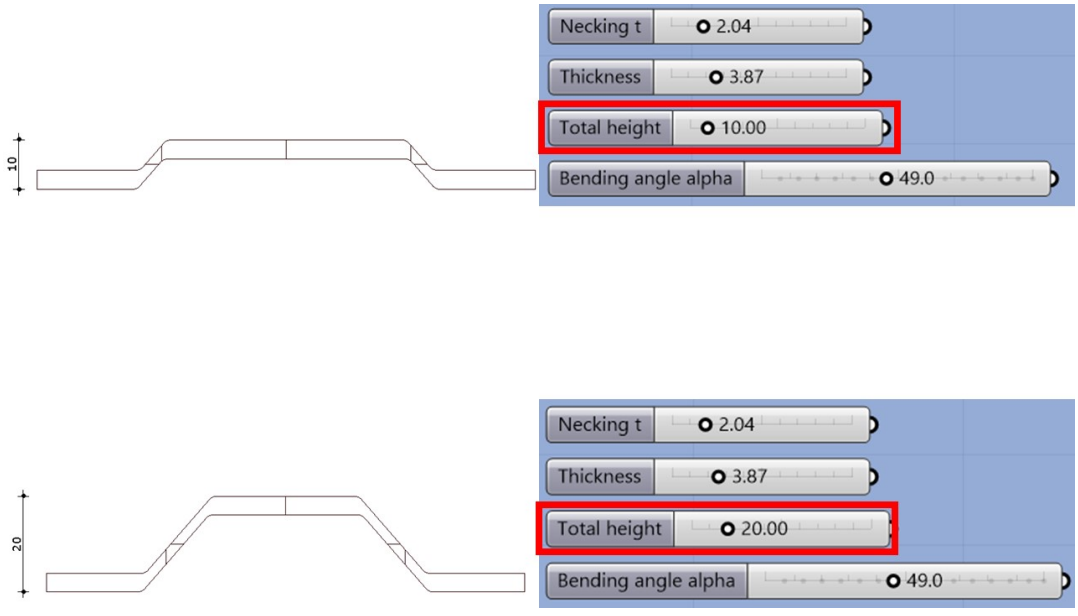

Figure 3.5: Adjustable total height.

Bending Angle

The bending angle needs to be an adjustable parameter, due to the constraint that the laser width is equal to 5mm. By adjusting the total height, the bending angle needs to change in relation to keep the width of 5mm. The different angles that have been examined range from 20-85 degrees in increments of 5 degrees.

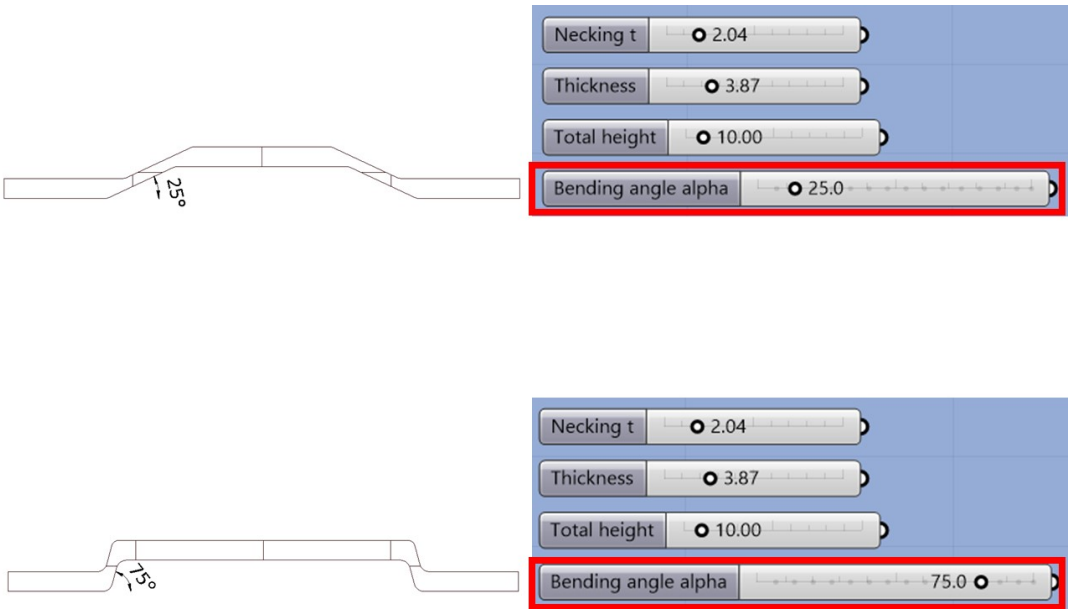

Figure 3.6: Adjustable angle.

Necking

To further introduce the presence of necking as an adjustable parameter, the necking itself will first be elaborated. Necking occurs when a material gets stretched. In this case, the glass becomes viscous after it is heated by the laser. This viscous part becomes thinner and sags deeper out of plane. This is due to the preservation of mass/cross-sectional area. In other words, no material is added or removed, so to maintain its mass, the deeper the glass is sagged, the thinner the web of the glass becomes.

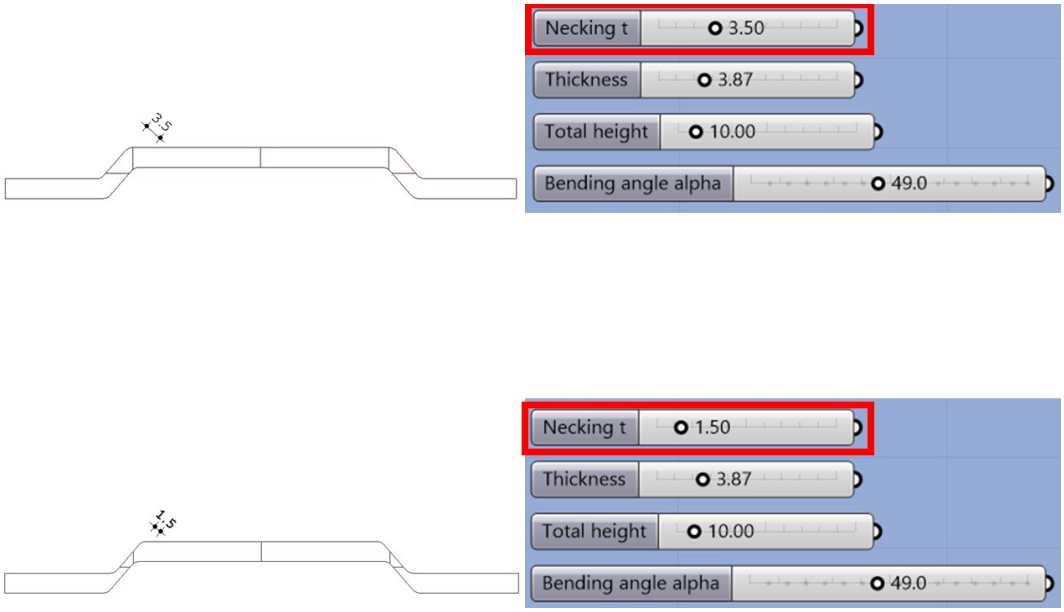

Figure 3.7: Adjustable web thickness (necking).

For every configuration, the web thickness is derived. In essence, the cross-sectional area needs to be the same as a flat panel of glass. In this model, the necking is present throughout the full ”web” of the laser-formed panel. The ”web” is seen as the part between the horizontally oriented parts in the cross section. The web can be almost vertical when a bending angle of 89 degrees has been reached, or it will be more diagonally when lower bending angles are realised. By comparing the presence of necking with the configurations where necking is not considered present, it is visualised to see if necking does play a major role in the stiffness of a laser-formed panel in Figure 3.8.

3.1.2. Sensitivity analysis

The parameters that influences the inertia are investigated. Visualisation of the adjustments having an impact or not is the next step in researching the different cross-section configurations. The goal is to visualise the inertia, depending on the bending angle and the thickness or elevation depth. With these results, different conclusions will be given in Chapter 8.

Inertia correlation

Four glass thicknesses are numerically studied. The thicknesses being 4mm, 8mm, 10mm, and 15mm, based on regular available, feasible thicknesses used for common glass projects. One goal of this analysis is to see whether there is a trend visible between the different thicknesses.

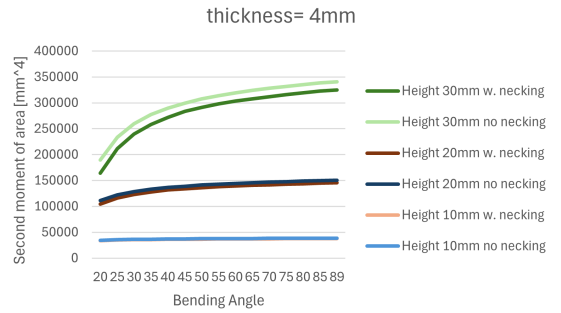

(a) Inertia related to bending angle and 4mm thick glass.

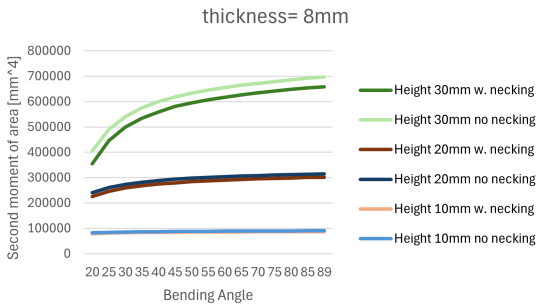

(b) Inertia related to bending angle and 8mm thick glass.

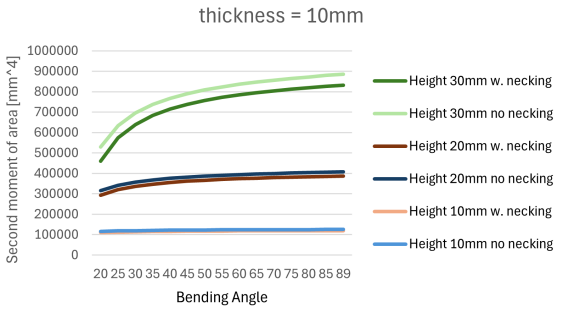

(c) Inertia related to bending angle and 10mm thick glass.

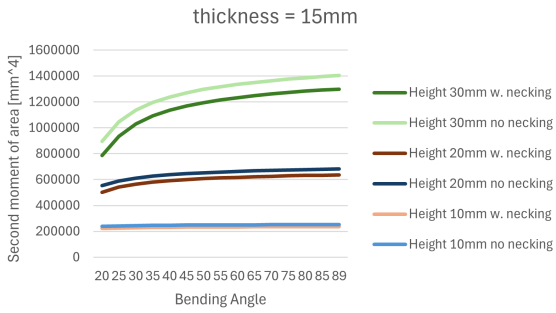

(d) Inertia related to bending angle and 15mm thick glass.

Figure 3.8: The second moment of area (Inertia) for every configuration.

In figure 3.8 the inertias of the configurations are displayed. The thickness of the sample does not significantly affect the trend of the inertia. In other words, all thicknesses show the same pattern. For lower elevation depths, the bending angle does not influence the inertia that much. For the 30mm elevation depth, the bending angle does influence the inertia in the angles smaller than 45 degrees. This can be explained by the fact that height influences inertia the most. Bending angles in the range up to 45 degrees gain more inertia when the angle grows. With bending angles larger than 45 degrees, the inertia is not affected as much, since the height of the web is not varying as much.

Manufacturing a 4mm thick panel, with a 30mm deep elevation is at this point in time not possible. The graphs in Figure 3.8 give insight into the evolution of inertia for multiple thicknesses.

A second observation with these graphs is the influence of necking on the inertia. The lower the elevation, the smaller the influence of necking. This phenomenon is as expected, since necking in general would be less with smaller elevations. The relation between inertia with necking and without the presence of necking is made visible in figure 3.9. The graphs show the relation of the inertia without necking divided by the inertia with necking. The graphs visualise that necking does give results leading into lower inertias.

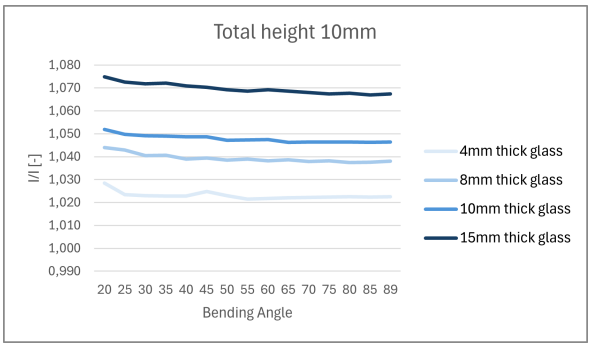

(a) Influence necking 10mm elevation.

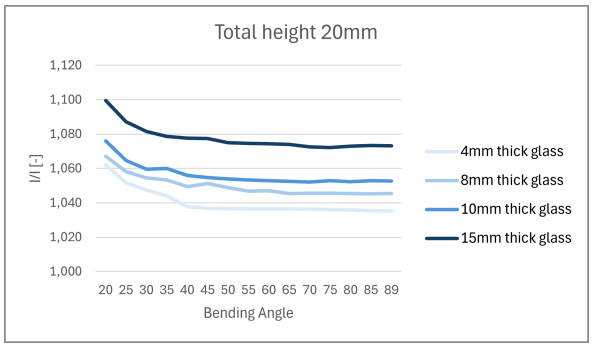

(b) Influence necking 20mm elevation.

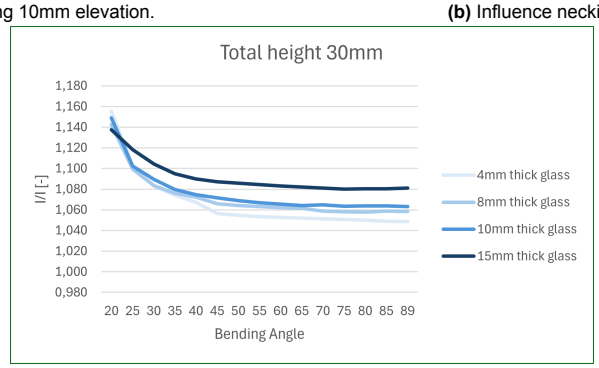

(c) Influence necking 30mm elevation.

Figure 3.9: The inertia without necking divided by the inertia with necking.

It is observed that with bending angles lower than 45 degrees, the necking plays a larger influence than with larger bending angles. Therefore, necking influences the height of the web by lower bending angles. With bending angles larger than 45 degrees, necking plays a role in the width of the web rather than the height. It can therefore be explained that the influence of necking remains relatively the same by larger bending angles. The graphs, on the other hand, show that the influence of necking remains between 2%-10% for the larger angles, depending on the elevation depth. The influence with lower bending angles shows a steeper trend, with a maximum influence of 15% for elevation depths of 30mm and a bending angle of 20 degrees.

3.2. Designs of laser-formed glass panels

The design of the two-sided supported sample is one of multiple design considerations made at the start of this thesis. To utilise the geometry of the glass to its full potential, different designs have been developed. Internal stresses relate to the applied force and the cross-sectional parameters. When designing, the applied force usually stays the same, so an effective way of choosing the right geometry is able to reduce the internal stresses of the glass.

3.2.1. Geometry 1

In the case of a four-point bending test, the bending-moment follows a simple line, as given in Figure 3.10a. The optimal geometry for a setup like this, results in an inverted height propagation following the same pattern of the moment line, as displayed in Figure 3.10b.

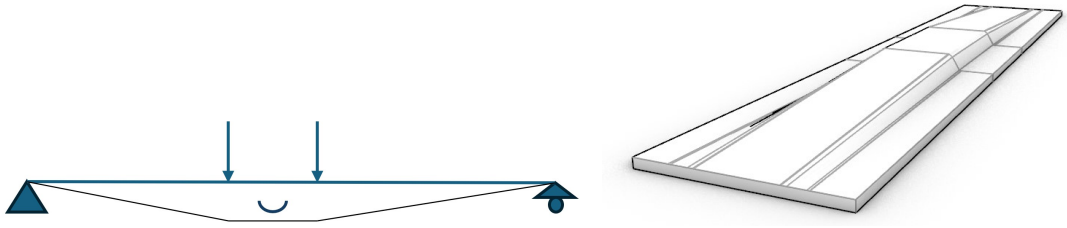

(a) Moment distribution line of a four-point bending test. **(b)** Render of design geometry.

Figure 3.10: The utilisation of geometry when following moment distribution lines of a four-point bending test.

Using this geometry in a four-point bending test will result in a more evenly distributed stress pattern. The cross-sectional inertia is highest where the bending moment is highest. Lowering the overall height in the sample linearly will follow the moment line, and therefore, the stress state decreases as well.

3.2.2. Geometry 2

The second geometry is based on the moment distribution line when subjected to a surface load such as wind pressure. A fully parabolic geometry suffices best for an evenly distributed load, as seen in Figure 3.11a. However, the laser-bending process at this point in time is not capable of creating fully parabolic bends or forming patterns. Therefore, creating a stepwise way to reach parabolic height values could be a way to replicate parabolic behaviour. The more steps, the closer it resembles a parabolic shape. The visualisation of two-step increments is shown in Figure 3.11b.

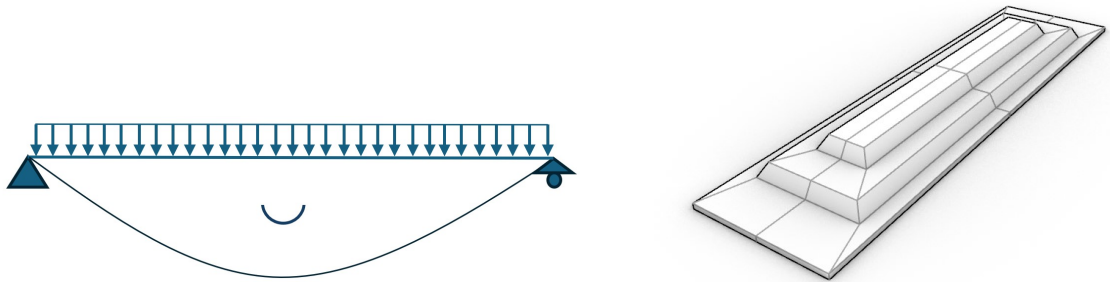

(a) Moment distribution line of a evenly distributed force. **(b)** Render of a double elevation.

Figure 3.11: The utilisation of geometry when following moment distribution lines of an evenly distributed load acting on a statically determined sample.

The alternative geometries 1 and 2 were insufficient for manufacturing during this thesis. Therefore, in the recommendations, it is suggested to further investigate these concepts when the possibilities within manufacturing are sufficient.

3.2.3. Geometry 3

The third geometry only has a single elevation, as visualised in Figure 3.12. This is the geometry used in the lab-experiments. Manufacturing capabilities were able to produce these type of panels. It shows no specific geometry relation to the applied load, however, the geometry should act more stiff. The inertia in the cross-section of midspan is increased by the laser-forming process, where Chapter 4 show how stiff the manufactured samples exactly performed.

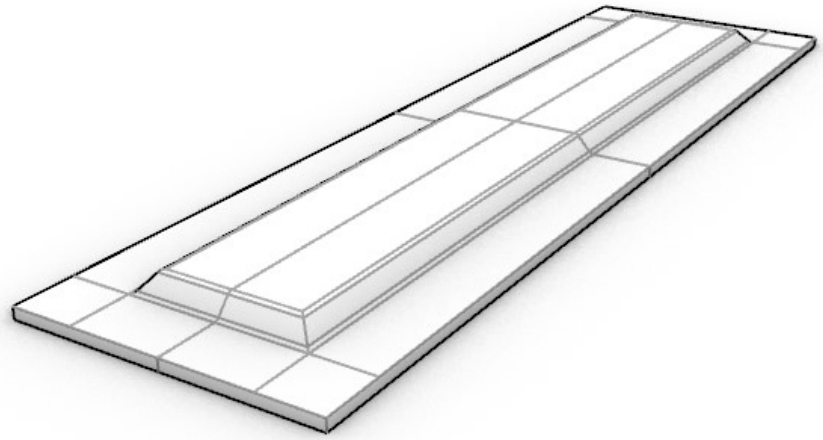

Figure 3.12: Main geometry concept.

4

Experimental lab tests

This chapter describes the experimental lab tests that have been performed during this thesis. The tests consists of 24 glass panels that are tested in a four-point bending test. This chapter starts with a description of the test setup and machine settings. Subsequently, it gives an overview of the test samples that has been examined. The results are described and discussed at the end of this chapter. The goal of these tests were to observe the stiffness increase or decrease of laser-formed glass panels. Four flat glass panels have been tested to obtain a reference value. 20 laser-formed glass samples have been tested, where the deformations and loads are measured. Three out of the twenty laser-formed samples contained strain-gauges to obtain a form of the stress distribution. This will be used to validate the FEM-models that have been made to predict the behaviour of laser-formed glass panels.

4.1. Test setup

The test that has been performed is the four-point-bending test. The EN 1288-3:2016 describes the procedures of testing glass samples with a four-point-bending test. For application purposes the sample dimensions differ from the specified specimen dimensions described in EN 1288-3:2016-6.2. The code describes a length L of 1100mm $\pm$ 5mm and a specimen width of 360mm $\pm$ 5mm. The samples tested in this thesis had a fixed length of 400mm and a width of 100mm.

The test machine used is an Instron 8872 servohydraulic press, as presented in Figure 4.1. The press was stationed in the Micro-lab of the CiTG-faculty of the TU Delft.

Figure 4.1: The Instron 8872 press used for the four-point-bending test.

Appendix C shows the specifications of the Instron 8872 and shows a maximum dynamic load capacity of 25kN. Early calculations showed a required load of around 100-200 Newton to obtain expected failure stresses of around 45 MPa. This press has a force accuracy of 1/1000 N, making it therefore useful for this test and its desired applied forcing.

To divide the single press into a four-point-bending test, the force distribution is managed by adding three additional layers of components. The components are a steel ball, a steel block and two steel cylinders. Figure 4.2 shows all components. The ball is used to compensate for any geometry deviations. If the top of the samples is not completely flat, the ball can compensate a little bit for any non-flatness. The steel block transfers the force of the press to the two cylinders. These cylinders rest on the top of the glass samples.

Figure 4.2: The three additional layers of components.

The extra weight of these additional components should be taken into account when defining the total force. The Instron measures the applied force, this measured force is excluding the additional weight. The total weight of the three components: the ball, the block and the cylinders combined was equal to 1474.2 grammes, see 4.3. The force that requires to be added to obtain the total applied force is then equal to 1474.2 * 9.81 = 14.46 [N]. The FEM-models are calculated with a force equal to the maximum measured force of the press and the additional 14.46 Newtons to obtain the numerically derived stresses at failure.

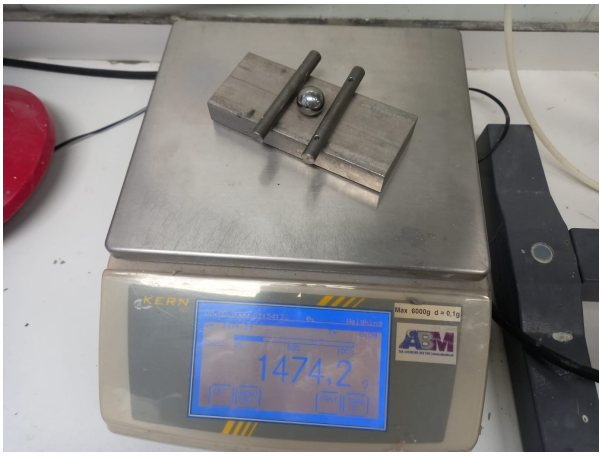

Figure 4.3: Weight of the additional components.

Every test used the same dimensions between the loads and the supports, displayed in Figure 4.4.

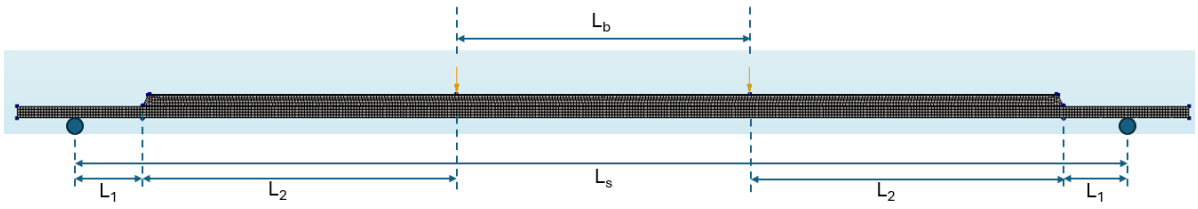

Figure 4.4: Testsetup dimensions.

L_1	The distance between the placement of the support and the edge of the elevation.	20 mm
L_2	The distance between the placement of the loads and the edge of the elevation.	105 mm
L_b	The distance between the bending rollers applying the load.	100 mm
L_s	The distance between the supporting rollers.	350 mm

The elevated part of the sample is in every test orientated to the top to guide the stresses through the necked webs to the supports. To ensure that the fragmentation of the sample remains together, an adhesive foil is applied to the top of the sample. The bottom part is not foiled, since this will influence the tensile-strength, making the tests unreliable.

Linear Variable Differential Transformers (LVDTs) are attached on the bottom side of 21 of the 24 tests to obtain a sense of strains occurring during the tests. The obtained strains were found to be invaluable since the LVDT's measured the strain over a length of 6cm. This is able to tell a mean strain over this length, but conclusions about stress-states in these areas are therefore invaluable. The strains obtained in three of the 24 tests are more valuable, since these were obtained with strain gauges. The strain gauges measure the strain over a length of 2mm and at a specific place in the sample. These strain gauges are therefore more reliable to give conclusions about the stress-states in the samples, during the four-point-bending tests.

4.2. Test samples

4.2.1. Dimensions

The laser-forming techniques are developed to form the glass, but the manufacturing process is not able yet to provide exact repetitive copies of a sample. This resulted in small deviations in the dimensions of each sample. Three categories have been made to distinguish most deviations, however each sample had its own unique dimensions. These deviations resulted into scattering performances in stiffness. The influence of these deviations require to be measured in order to make conclusions about the stiffness of each sample. Subsequently to be able to correctly predict the behaviour, all FEM-models were modelled with each unique dimensions.

Every sample had a total width of 100mm and a total length of 400mm. The area that is laser-formed was the same in every sample as well. The width of the laser, and therefore the width of the "bending-line" is equal to 5mm. The formed rectangle had dimensions of 60 by 310mm at the outside of the laser-line, and 50 by 300mm at the inside of the laser-line.

The thicknesses of the glass were measured with a digital caliper. This caliper measured with an accuracy of 0.01mm. The thickness of the sample and the thickness of the web (related to the necking) were measured with a precision of 0.01mm. The total height is measured but seemed more sensitive to small angle changes in the caliper, since the surfaces were not completely flat and parallel to each other. Deviations in results while comparing the FEM and the lab-tests could be a result of these accuracy insecurities. Figure 4.5 shows the location of the measured dimensions by the digital caliper. Note that the bending angle is not measured, but derived from the relation between the laser-width of 5mm and the total height.

Thickness (a)
Total height (b)
Bending angle (c)
Web thickness (d)

Figure 4.5: Location of dimensions.

Other observations regarding the uniqueness of the samples are obtained in addition to the dimensions. These observations are the bur side of the samples (top or bottom), and the location of failure initiation. All the dimensions and observations are described in Table 4.1.

Table 4.1: Dimensions of the samples.

Sample nr.	Thickness [mm]	Total height [mm]	Thickness web (Necking) [mm]	Bur side zone
Flat 1	3.89	3.89		Tension
Flat 2	3.89	3.89		Tension
Flat 3	3.89	3.89		Tension
Flat 4	3.89	3.89		Tension
Shallow 1	3.89	5.72	3.51	Tension
Shallow 2	3.88	5.76	3.55	Tension
Shallow 3	3.88	5.87	3.47	Tension
Shallow 4	3.87	5.57	3.57	Tension
Shallow 5	3.87	5.88	3.58	Tension
Shallow 6	3.87	8.73	2.83	Compression
Shallow 7	3.87	7.65	2.99	Compression
Shallow 8	3.87	6.29	3.43	Compression
Shallow 9	3.88	5.72	3.59	Compression
Shallow 10	3.87	5.81	3.66	Tension
Deep 1	3.89	9.80	2.20	Tension
Deep 2	3.88	9.70	2.13	Tension
Deep 3	3.90	8.75	2.29	Tension
Deep 4	3.90	9.19	2.79	Compression
Deep 5	3.89	10.04	2.06	Tension
Deep 6	3.89	9.59	2.28	Tension
Deep 7	3.89	10.12	1.88	Tension
Deep 8	3.87	10.36	1.80	Tension
Deep 9	3.86	12.11	1.25	Tension
Deep 10	3.87	11.51	2.04	Tension

4.2.2. Necking of the sample

One observation affects the geometry of each sample. This observation saw that the necking in the samples is not uniform across the whole laser-line. This means that the necking at one place in the sample deviates from the necking at another place. The necking is measured at a fragmented part of the glass after failure, a fragmented part is shown in Figure 4.6. Although some samples fragmented significantly (due to higher internal stresses) other samples did not fragment in relatively many pieces. This led that for some samples the necking could be observed in an abundance of different places, while with other samples only two or three locations could be observed. This deviation and non-uniformity is taken into account in concluding the stiffness of a sample.

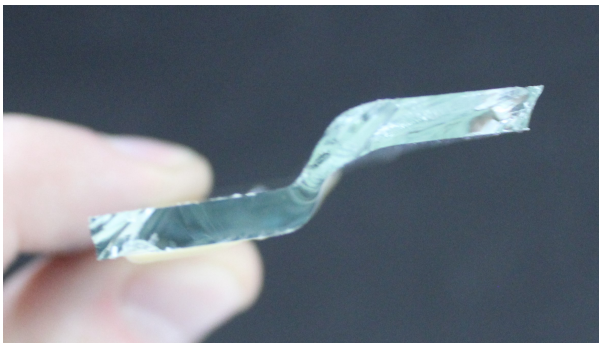

Figure 4.6: Necking clearly visible in a fragmented part of one of the failed samples.

4.2.3. Bur side of the edge

For every sample, it is checked whether the bur is located at the bottom or the top of the glass panel. The literature states that the bur side located at the tension-zone of the sample leads to lower edge strength, when unpolished. When observing the glass, the bur can be noticed by a rough cutting pattern at the edge of the glass. These micro-damages should reduce the strength of the glass by around 20%. The results found in Section 5.2.4 show, on the other hand, no such relation of a reduction in strength.

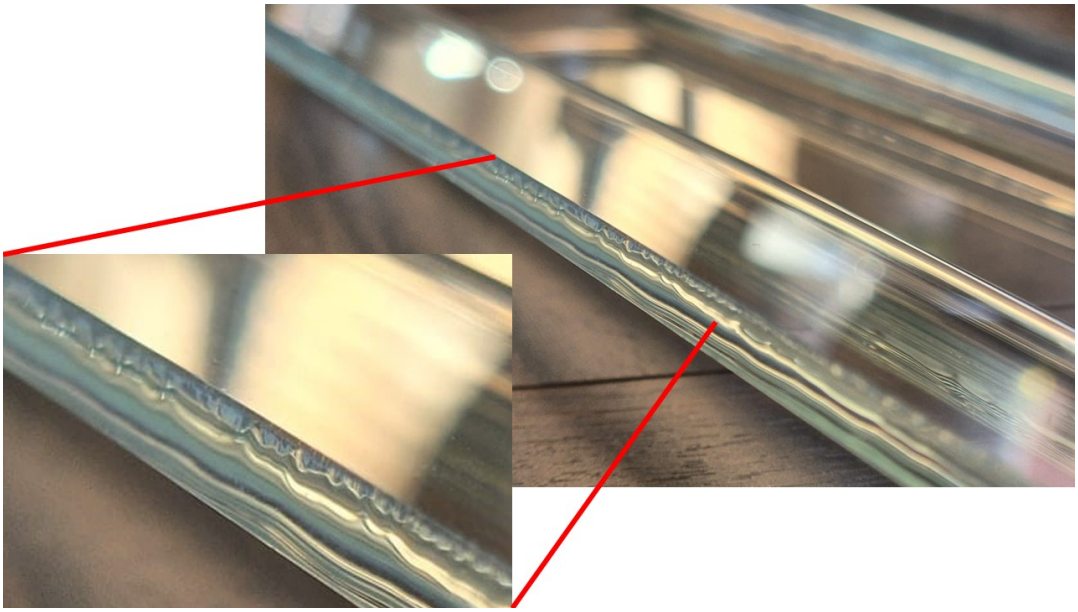

Figure 4.7: Locating the side of the bur as a consequence of cutting the glass from one side.

Figure 4.7 shows where the bur is located. The figure shows one of the samples with a clearly visible bur at the top of the edge. Since the sample is oriented upside-down, during the tests the bur acts in the tension-zone.

4.2.4. Residual stress observations

The laser-bending process is a process of heating glass in an oven and cooling it down (gradually). The cooling rate of the glass can influence the residual stress state of the glass. By rapidly cooling the glass, residual stresses, like within tempered glass, might be present. While annealing, slowly cooling the glass, allows the residual stresses to dissipate, as shown in Figure 2.5 in Section 2.2.1.

The presence of residual stresses in the glass samples require therefore to be checked. This is done with a test with polarised light and filters, so called photoelasticity. The principle is based on a combination of three things. A polarised light source is required, the glass object is required, and a polarised filter is required to look through to be able to visualise the residual stresses. The process of visualising residual stresses within the glass is shown in Figure 4.8.

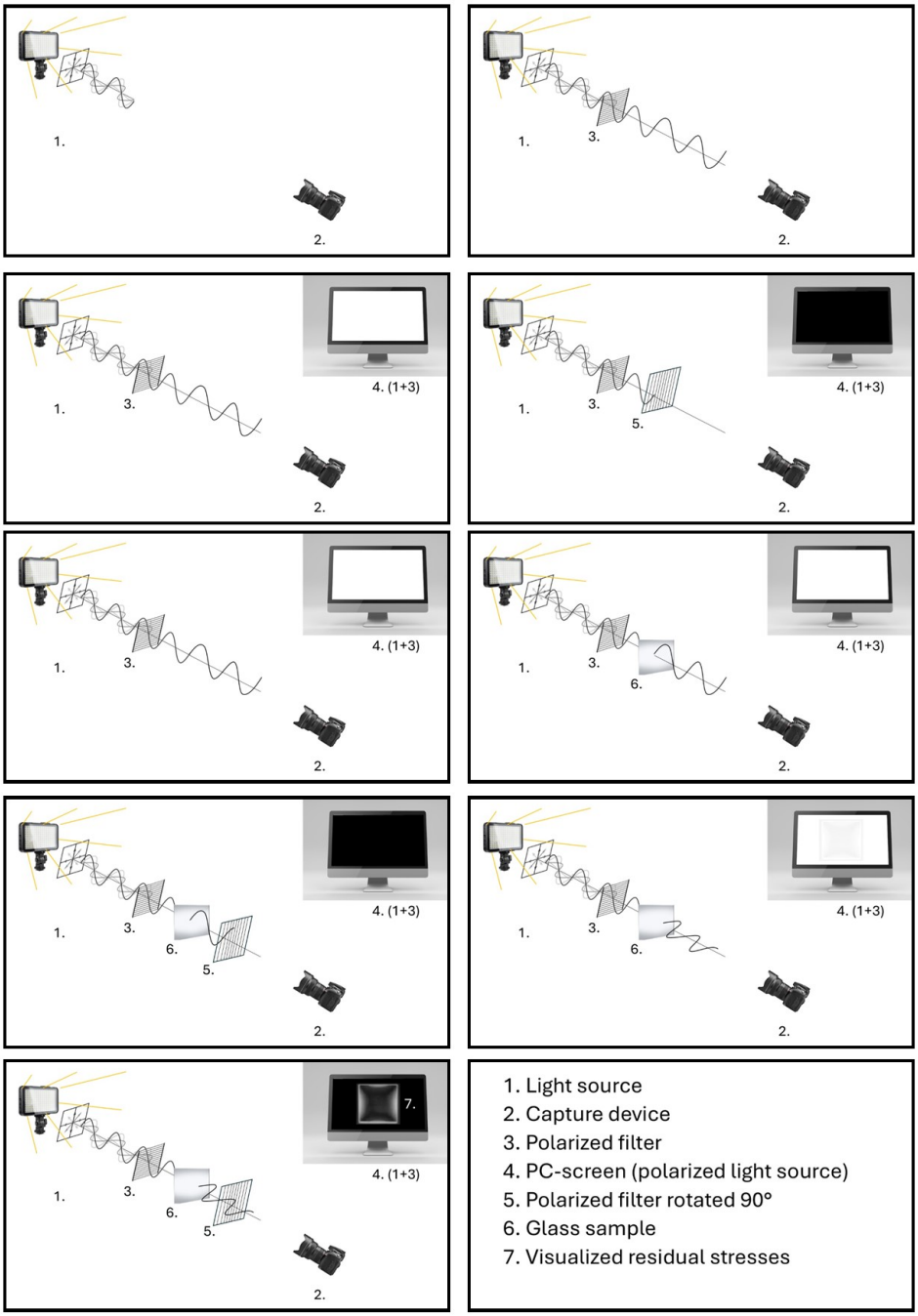

Figure 4.8: Visualising residual stresses within glass.

Every sample is observed with the method given in Figure 4.8 to check for the presence of residual stresses. A TV-screen is used as a polarised light source. Photos of the glass samples are taken in front of this screen. A polarised filter is attached to the camera to be able to capture any residual stresses. The background is therefore dark and any white light areas that are visible represents any residual stress within the glass. The residual stresses do appear because the polarised light is bent due to these stresses. Therefore they are not blocked by the second polarised filter.

Multiple observations were made while capturing the photos. Residual stresses do appear with this method. Small regions of stress around the corners in the bend are captured, see Figure 4.9a and Figure 4.9c. The stresses do seem to be of a relatively small magnitude, since the white area appears in a light manner. The presence of white areas were captured in every sample, making it a reoccurring phenomenon.

A second observation is that when the sample is positioned under an angle, new areas do appear on the captured photo, see Figure 4.9b. It is assumed that this relates to the orientation of the principle stress direction of the residual stresses. Within the second observation white regions around the elevation do stand out, it is assumed that these regions do relate to the areas on which the samples were supported within the oven.

(a) Captured residual stress in bend corners.

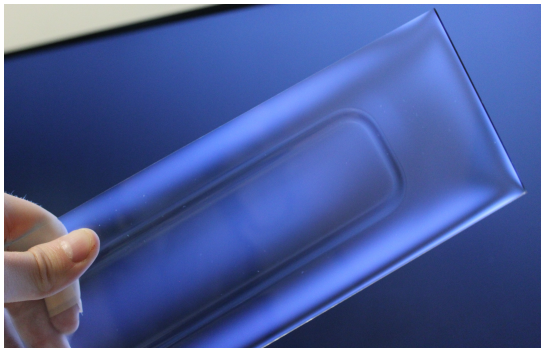

(b) Captured residual stress while positioned under an angle.

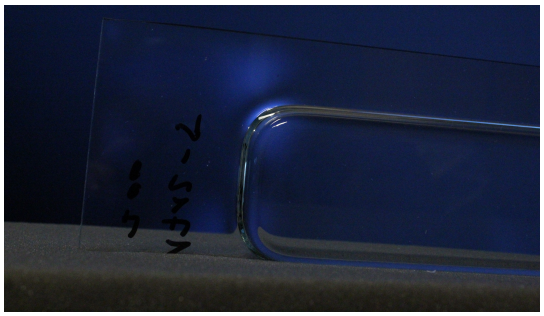

(c) Close look at residual stress in the corners.

Figure 4.9: Obtained residual stresses through photoelasticity.

The presence of residual stresses is relevant when cracks do initiate from within the glass, in contrary to the outer edges. When cracks initiate from the edges it correlates that the influence of the residual stress is minimal. No residual stress could be present at the edges and the quality of the edge is therefore governing for the strength of the glass, when the samples do fail from the edges.

4.3. Test results

This section describes the results obtained from doing 24 four-point-bending tests. Four flat samples were tested to obtain reference results, 10 tests were performed on samples with a shallow elevation (total height <8.75mm) and 10 tests were performed on samples with a deeper elevation (total height $\geq$8.75mm).

4.3.1. Failure loads and deformations

This subsection displays the applied loads and the corresponding deformations obtained throughout the tests. The failure force represents the highest applied force just before the glass samples failed. The applied force is regulated by the press, and the speed of the forcing was deformation based. Therefore, the speed was regulated at 0.05mm/s, and the development of the force during the test corresponds to the required speed.

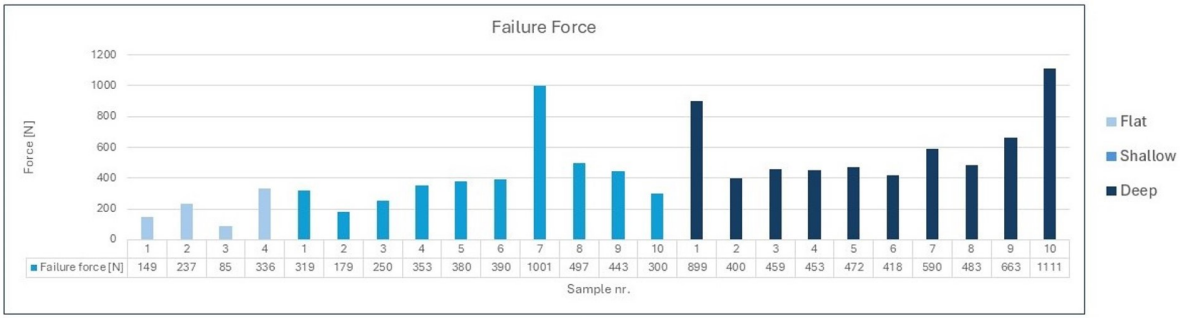

Figure 4.10: Barplot of the failure force obtained by the four-point-bending-tests.

Noticeable is the scatter of each obtained results. The boxplots, given in Figure 4.11, show that the performance of a deep sample is significantly better than the performance of flat pieces. Each sample had a higher failure load than the best performance of a flat sample. Six out of ten of the shallow samples performed better than the flat samples. Four tests came out to be less strong than the strongest flat sample. This is a cause of the scattering strength capacity of glass in general. The edge quality was poor, as the panels were not polished. Only one sample, sample ”deep-9”, did not fail from a crack initiated at the edge. Therefore it is assumed that the strength of the glass in this setup is based on the edge quality, subsection 4.3.4 states a more in depth explanation of this phenomenon.

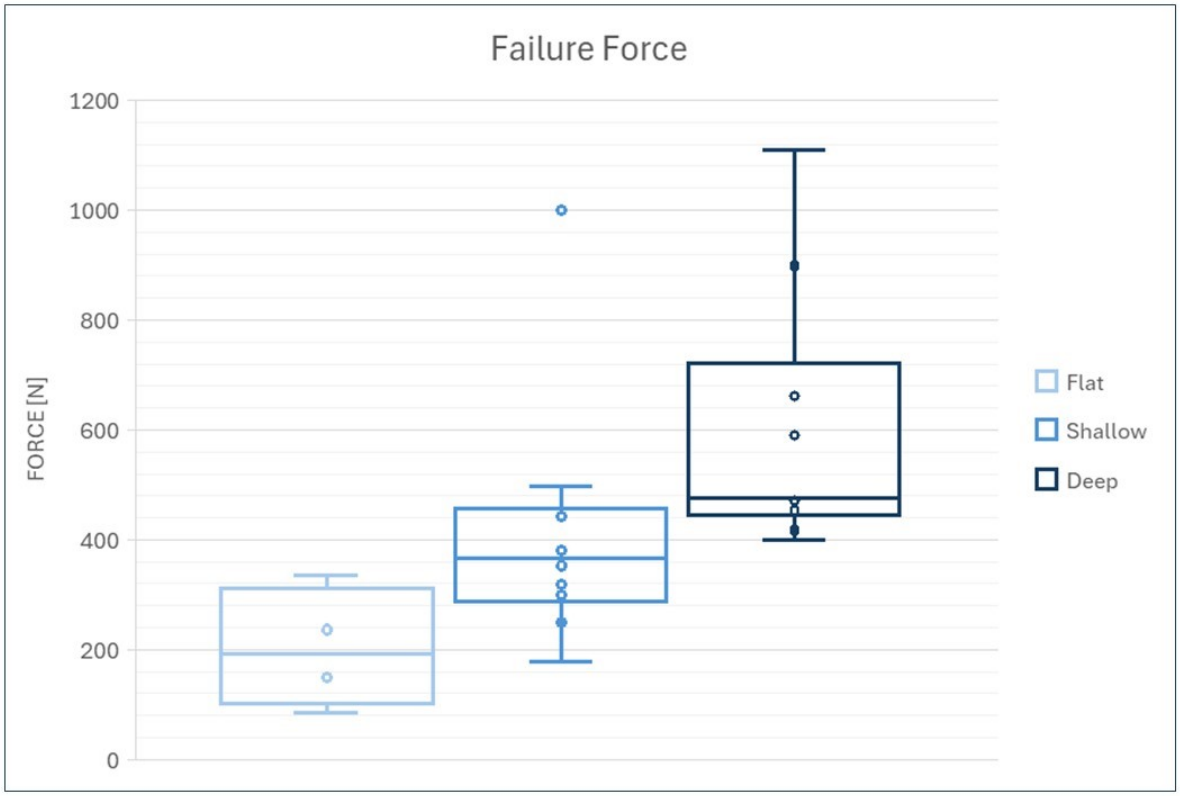

Figure 4.11: Boxplot of the failure force obtained by the four-point-bending-tests.

The deformations obtained in the tests are shown in Figure 4.12. These given numbers are the deformations of the press, therefore they should be compared to the deformations at the point of loading in the FEM-models.

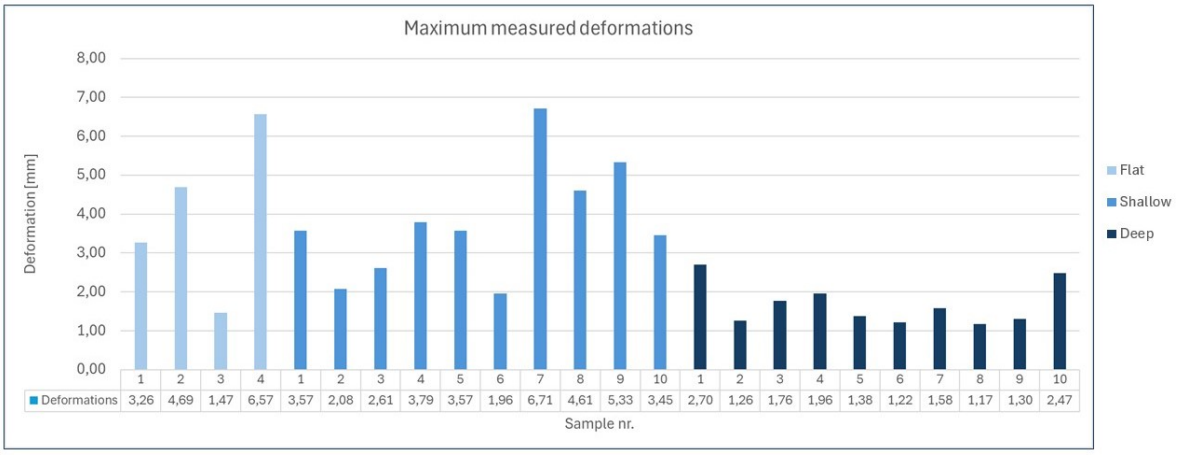

Figure 4.12: Maximum deformations of each test.

As expected, samples with a higher total height result in lower average deformations. The plot might give a false sense of stiffness, since the deformations do relate to the maximum applied force. This force scattered immensely, resulting in scattering deformations as well. A given result is that with similar geometries, a higher load results in higher deformations. This plot shows this relation.

Table 4.2: Failure loads and deformations

Sample nr.	Failure load [N]	Deformations [mm]	Failure location (y=...mm)
Flat 1	149.5	3.26	139
Flat 2	236.6	4.69	140
Flat 3	84.9	1.47	139
Flat 4	335.5	6.57	156
Shallow 1	319.5	3.57	131
Shallow 2	179.3	2.08	150
Shallow 3	250.0	2.61	134
Shallow 4	353.4	3.79	132
Shallow 5	380.1	3.57	119
Shallow 6	389.7	1.96	98
Shallow 7	1000.8	6.71	140
Shallow 8	497.0	4.61	77
Shallow 9	443.4	5.33	133
Shallow 10	300.0	3.45	120
Deep 1	899.0	2.70	175
Deep 2	399.9	1.26	144
Deep 3	459.4	1.76	135
Deep 4	453.3	1.96	164
Deep 5	471.6	1.38	115
Deep 6	417.8	1.22	112
Deep 7	590.4	1.58	159
Deep 8	482.5	1.17	137
Deep 9	662.5	1.30	20
Deep 10	1110.9	2.47	157

The summary of the failure forces are shown in Table 4.3. The obtained values show that the standard deviation of the deep samples is lower than the standard deviation of the other two. Meaning the behaviour of the samples is more in line with each other. This does not imply that the samples have a more regular strength. A cause is that the geometries of the deep samples are more similar.

Table 4.3: Statistical summary of the failure loads.

Sample	Min Failure load [N]	Max Failure load [N]	Mean Failure load [N]	STD [N]	STD/mean [%]
Flat Samples	85	336	202	94.2	47%
Shallow Samples	179	1001	411	214.8	52%
Deep Samples	400	1111	595	79.2	13%

4.3.2. Failure mechanisms

The scatter in the strength of glass makes predicting the failure behaviour and the corresponding failure mechanism an uncertain task. For every sample, the location of the initiating crack is measured after the tests, as can be seen in Table 4.2. The corresponding failure mechanism is observed in addition to the location.

It is observed that 19 out of the 20 laser-formed samples failed due to a crack initiated from the edge. Most of the initial ”first cracks” started at the edges in-between the applied loads. However, six of those 19 samples failed from the edge outside of the loads. This is a result of the scattering edge strength on microscopic level since the bur was untreated. Along the edge, larger flaws can be located outside of the location of the loads. Stating that the maximum stresses occurring at or in between the loads might not be governing as failure stress. Lower stresses further away from the loads might initiate failure as a result of this effect. Meaning the edge quality plays a significant role in the strength of the glass. The nineteen samples all showed the initial ”First cracks”, visualised in Figure 4.13. The initial crack is localised by observing where the waving fragmentation diverges from an original crack.

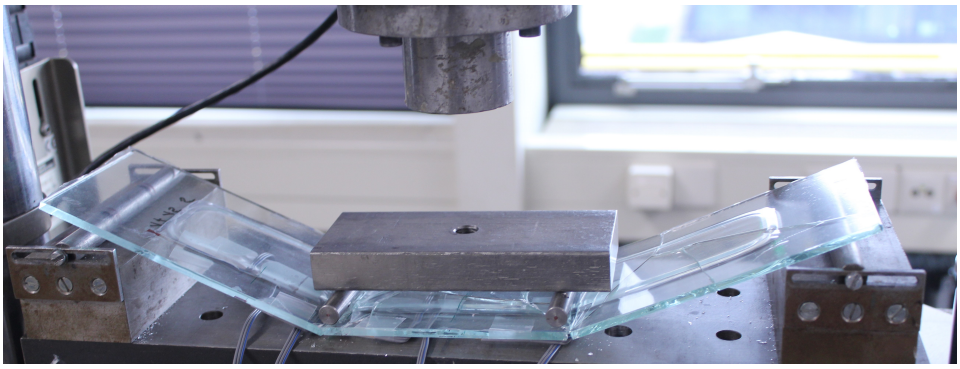

(a) Failed sample ”Shallow-10”.

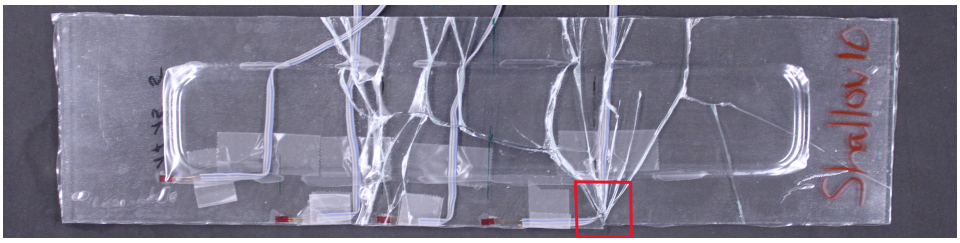

(b) ”First crack” of sample ”Shallow-10”.

Figure 4.13: The failure of sample ”Shallow-10”.

A single sample showed different behaviour. Sample ”Deep-9” failed from within the laser-bent area of the sample. This is the sample with the largest total height and the largest necking, resulting in the thinnest web of the laser-bent part of the glass. Section 5.2.7 will dive further into the analysis and predictability of the failure mechanism as the FEM-models are able to capture higher stresses at the bent location when necking appears to be governing. Figure 4.14 shows the different failure mechanism observed during the lab-tests. Note that the image is distorted by the adhesive foil that is attached to the top of the sample.

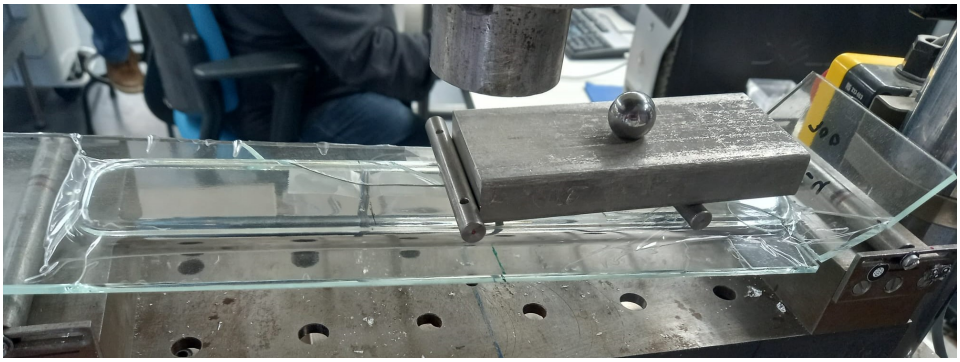

(a) Failed sample ”Deep-9”.

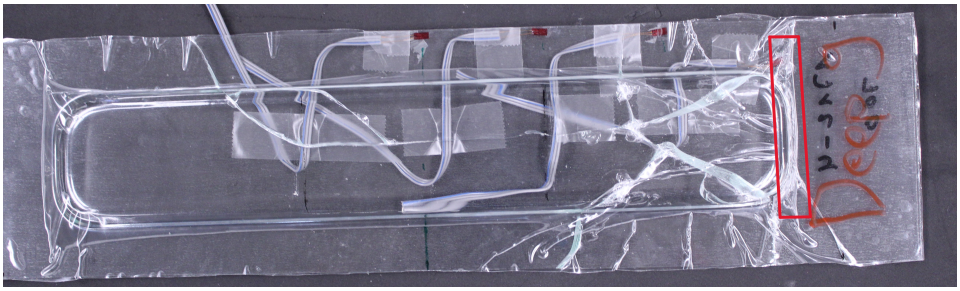

(b) ”First crack” of sample ”Deep-9”.

Figure 4.14: The failure of sample ”Deep-9”.

4.3.3. Stiffness

This subsection displays the differences in stiffness regarding the test results and the different geometries. The stiffness is the relation between force and deformation. Glass show linear stiffness behaviour with negligible plastic deformation. Immediate breakage when reaching the failure load is a result of this linear behaviour. The results of the tests do show this behaviour since the force-deformation curves do show linear behaviour before failure, while at failure there is no extra capacity left.

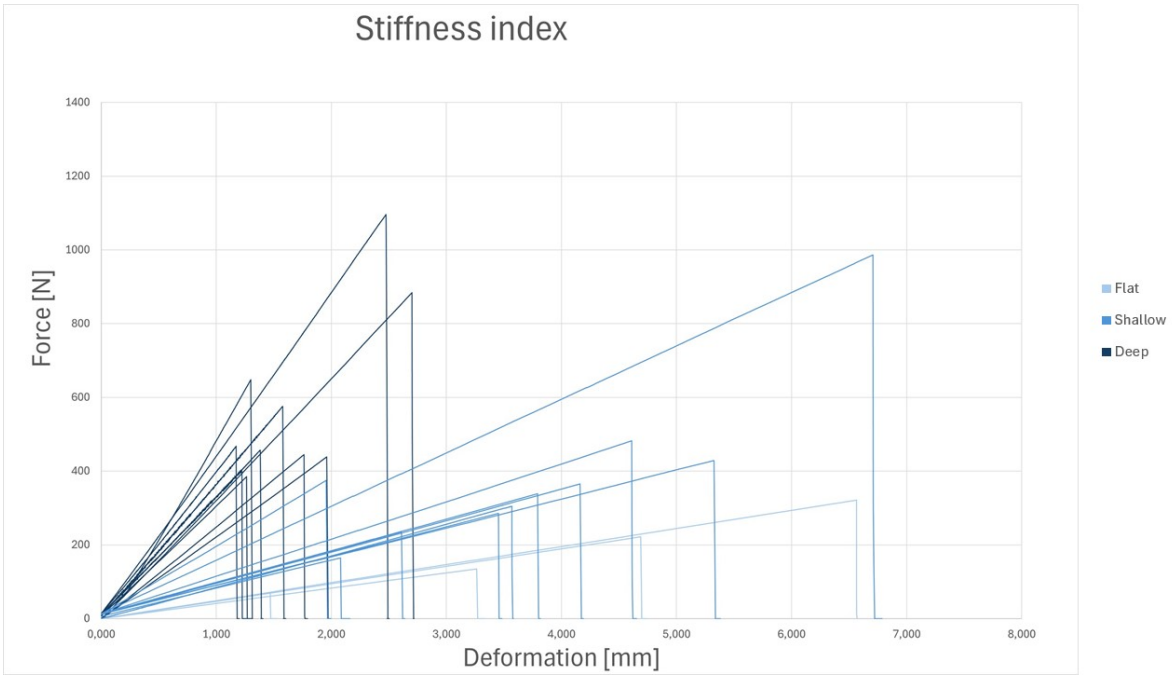

Figure 4.15: The force-deformation curves of every test.

When looking in Figure 4.15, the observation is that the deeper samples act more stiff than the shallow samples and the flat samples. The stiffness is defined by the slope of the curves: The steeper the curve, the stiffer the element. The shallow samples act more stiff than the flat samples as well. These are expected observations since the stiffness is related to the moment of inertia (or inertia in short) of a sample. The inertia grows the deeper the sample is, which explains the stiffer behaviour. A second observation is that every laser-formed sample (the shallow and deep ones) has a unique stiffness, contrary to the flat samples showing similar stiffness. This means that each sample has a unique geometry, which is confirmed by the dimensions observed in Figure 4.1.

Figure 4.16a shows the relative stiffness in relation to the flat samples. An observation is that the total height does influence the stiffness increase as expected. With inertia increasing cubically with increased height (for rectangles I = 1/12 * b * h^3), a significant increase in stiffness is expected. The plot shows a relative stiffness increase reaching values between 1.6 - 9.9 times as high as a flat sample. A trend comparison is made between the relative total height and the relative stiffness, as displayed in Figure 4.16b. This plot displays that the expected behaviour of increased height, does relate to higher stiffness. The relation is on the contrary not cubical. An exponential relation appears to match the stiffness increase more. This quadratic relation might be a consequence of the parallel-axis theorem. This theorem relates the increase in inertia to the increase in distance to the squared centroidal axis. Conclusions based on this assumption are left out of the scope of this thesis. On the other hand, the observation is worth mentioning and can be researched more thoroughly.

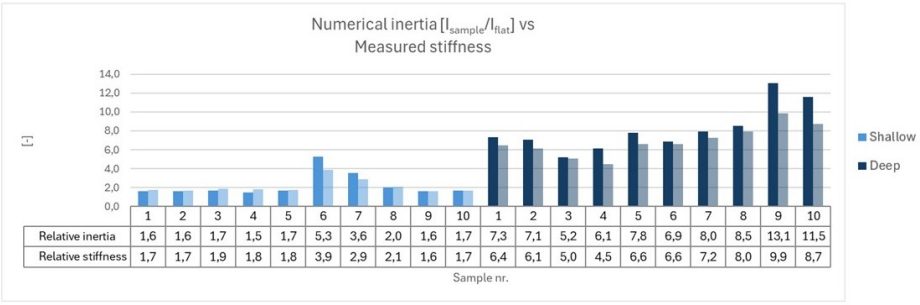

	1	2	3	4	5	6	7	8	9	10	1	2	3	4	5	6	7	8	9	10
Relative inertia	1,6	1,6	1,7	1,5	1,7	5,3	3,6	2,0	1,6	1,7	7,3	7,1	5,2	6,1	7,8	6,9	8,0	8,5	13,1	11,5
Relative stiffness	1,7	1,7	1,9	1,8	1,8	3,9	2,9	2,1	1,6	1,7	6,4	6,1	5,0	4,5	6,6	6,6	7,2	8,0	9,9	8,7

(a) The numerical derived inertia compared to the measured stiffness increase.

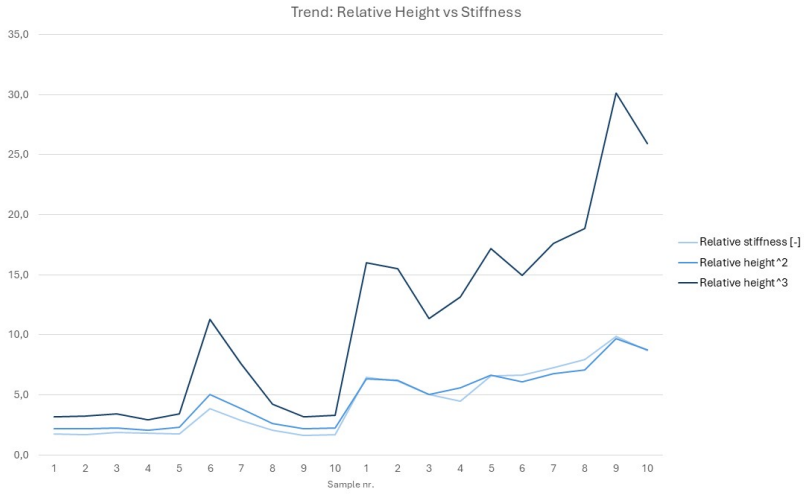

(b) Trend comparison total height vs relative stiffness.

Figure 4.16: Relative stiffness and the Trend related to the relative total height.

In order to check if the relative height relates to the inertia, the inertia of the cross-sections at midspan is computed. The inertia increase should, in theory, be similar to the stiffness increase if the glass panels act like an Euler-Bernoulli beam. The computation of the inertia is done in Grasshopper. In

Grasshopper each sample is modelled individually and a built-in code-block is used to retrieve the moment of inertia of the cross-sections at midspan. These moments of inertia are divided by the inertia of a flat sample, after which the relative inertia is computed.

A comparison is made with the stiffness, to visualise if there is a correlation between the two, as displayed in Figure 4.17. The computed moments of inertia do come with a precision error, since the samples were measured by hand. The necking is measured but not uniformly around the full laser-line, which means there could be a difference in the computed inertia and the real-life inertia.

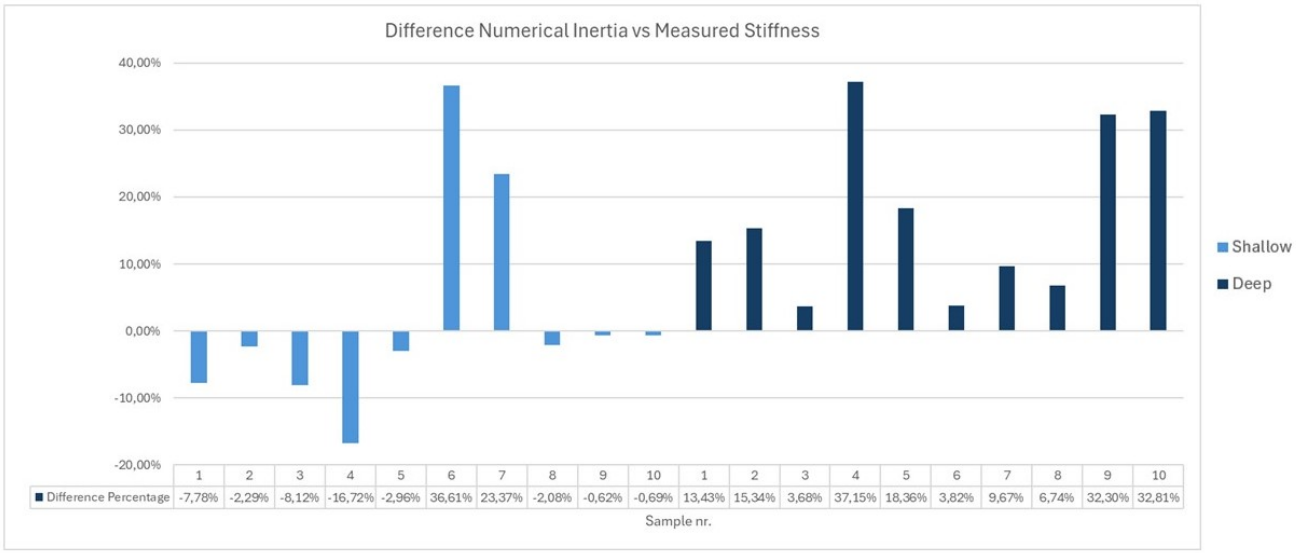

Figure 4.17: The numerical inertia difference towards the stiffness.

The plot shows that the increase in inertia overestimates the stiffness by a maximum of 37%. Especially the deep(er) samples show a larger deviation. Samples ”Shallow-6” and ”Shallow-7” have a higher total height and a larger inertia than the other eight shallow samples. This diversion is visible in the graph. For the eight other shallow samples, the increase in inertia almost matches the increase of stiffness, as a deviation of less than 15% is computed. The stiffness of the deep samples shows a similar trend towards the increase in inertia, as can be seen in Figure 4.16a. The deviations in the results can be explained by precision inaccuracies of measuring the samples. For engineers and designers it is advised to take the maximum overestimation of 37% into account by introducing a correction factor of 1.4 towards the inertia.

All the observations and computed relations are displayed in Table 4.4. This table shows the stiffness increase which relates to a flat sample being 100% stiff, and the values of the samples show how the samples relate to each other. The same holds for the increase in inertia and the total height. The table shows that the inertia increase relates to the increase in stiffness. However, the larger the total height, the more it deviate. The trend of the increase is similar for both the stiffness as the inertia properties.

Table 4.4: Stiffness parameters

Sample nr.	Thickness [mm]	Total height [mm]	Computed inertia [mm^4]	Stiffness index [N/mm]	Stiffness increase [-]	Inertia increase [-]	Total height increase [-]
Flat 1	3.89	3.89	491	47			
Flat 2	3.89	3.89	491	50			
Flat 3	3.89	3.89	491	58			
Flat 4	3.89	3.89	491	51			
Shallow 1	3.89	5.72	785	89.50	170%	160%	147%
Shallow 2	3.88	5.76	801	86.19	170%	160%	148%
Shallow 3	3.88	5.87	837	95.78	190%	170%	151%
Shallow 4	3.87	5.57	738	93.17	180%	150%	143%
Shallow 5	3.87	5.88	843	91.34	180%	170%	151%
Shallow 6	3.87	8.73	2590	199.33	390%	530%	224%
Shallow 7	3.87	7.65	1751	149.22	290%	360%	197%
Shallow 8	3.87	6.29	1004	107.80	210%	200%	162%
Shallow 9	3.88	5.72	787	83.26	160%	160%	147%
Shallow 10	3.87	5.81	821	86.92	170%	170%	149%
Deep 1	3.89	9.80	3591	332.85	640%	730%	252%
Deep 2	3.88	9.70	3473	316.59	610%	710%	249%
Deep 3	3.90	8.75	2570	260.61	500%	520%	225%
Deep 4	3.90	9.19	3017	231.28	450%	610%	236%
Deep 5	3.89	10.04	3840	341.09	660%	780%	258%
Deep 6	3.89	9.59	3377	341.99	660%	690%	247%
Deep 7	3.86	10.12	3904	374.26	720%	800%	260%
Deep 8	3.87	10.36	4171	410.83	800%	850%	266%
Deep 9	3.86	12.11	6414	509.71	990%	1310%	311%
Deep 10	3.87	11.51	5670	448.86	870%	1150%	296%

4.3.4. Stresses

This subsection will display the observed stresses obtained with the strain gauges and the fragmentation. Three samples contained strain gauges to measure the acting stresses during the four-point bending tests. Visualisation of the stress distribution allows for a check of the linear behaviour of the material. Secondly, the stress distribution and the ratio of the stress values between the different observation points allow for a verification check of the FEM-models.

Strain gauges

The strain gauges used in this research were TML strain gauges of the type FLA-2-11. The properties of the strain gauge are stated in Table 4.5.

Table 4.5: Properties of strain gauge TML FLA-2-11.

	Gauge length [mm]	Gauge width [mm]	Backing length [mm]	Backing width [mm]	Resistance [Ω]	Gauge factor
FLA-2-11-5LT	2	1.5	6.5	3	120	2.14

The resistance and gauge factor values need to be taken into account when tuning the measuring devices. The test setup consisted of a device that converts the resistance of the strain gauges to actual strains. The formula given in Equation 4.1 is used to calculate the strains.

$$GF = \frac{\Delta R/R_0}{\varepsilon} \tag{4.1}$$

GF is the gauge factor, ΔR is the change in resistance and R_0 is the original resistance value. The strains are then computed and obtained at every time step of the hydraulic press.

The location of the stresses is determined on a set of sample characteristics. The first applied strain gauge is located at the corner of the laser-bend to see if stress concentrations can be captured. The second applied strain gauge is located between the first and the third. The objective of this placement is to obtain the stress distribution between the first and third strain gauges. The third strain gauge is placed directly under the load. This is done because the FEM-models showed higher stresses occurring at the y-locations of the loads. The fourth location is at midspan, where it verifies the statement of the highest stresses occurring below the loads instead of midspan. The location of the strain gauges, and distance relative to the supports, is shown in Figure 4.18.

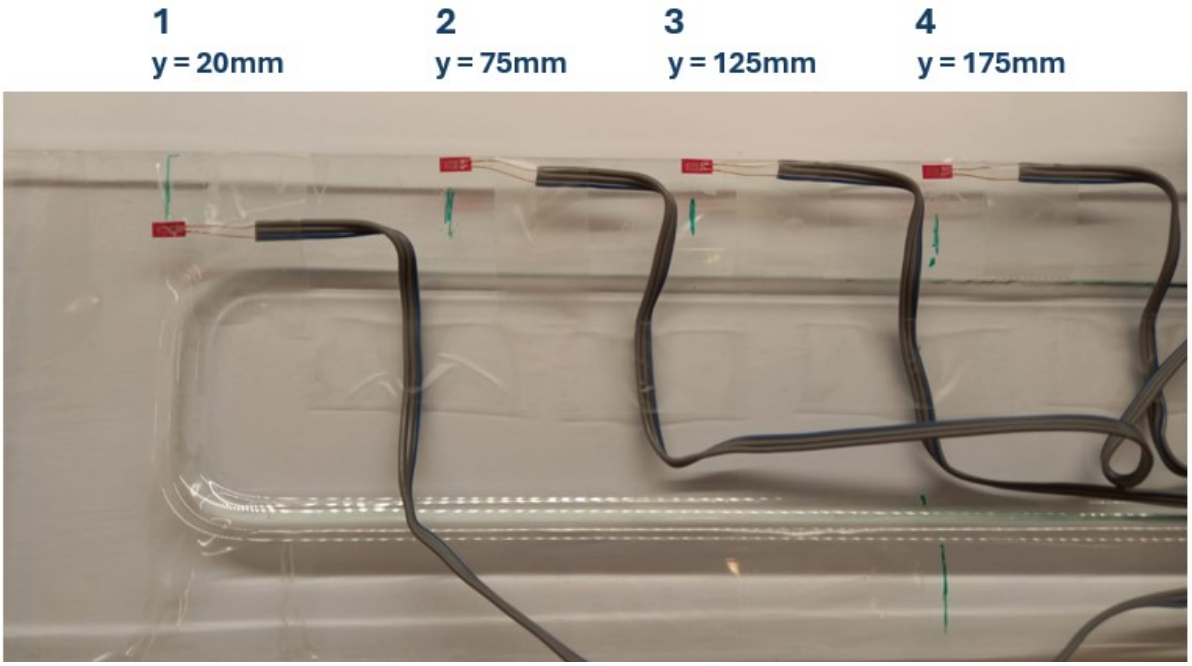

Figure 4.18: The location of the strain gauges.

Captured stress

The strains were captured during the full four-point bending tests. This strain is obtained as microns, the stresses are derived from this with the constitutive relation stated in equation 4.2.

$$\sigma = E * \frac{\varepsilon}{10^6} \tag{4.2}$$

To obtain stress, the strain is multiplied by the Young's modulus of glass. This Young's modulus is assumed to be constant and having the value of 70.000 N/mm^2. The focus of the stress evolution is on the linearity, magnitude, and ratio of the stresses compared to each individual location. The stress evolutions are plotted and visualised in Figure 4.19.

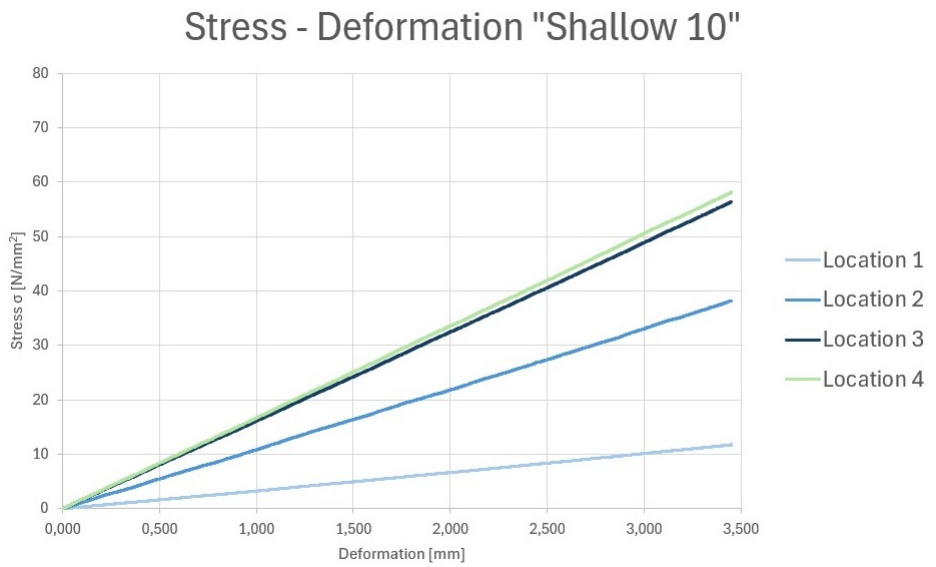

(a) The stress captured with the strain gauges in relation to the deformation of sample ”shallow-10”.

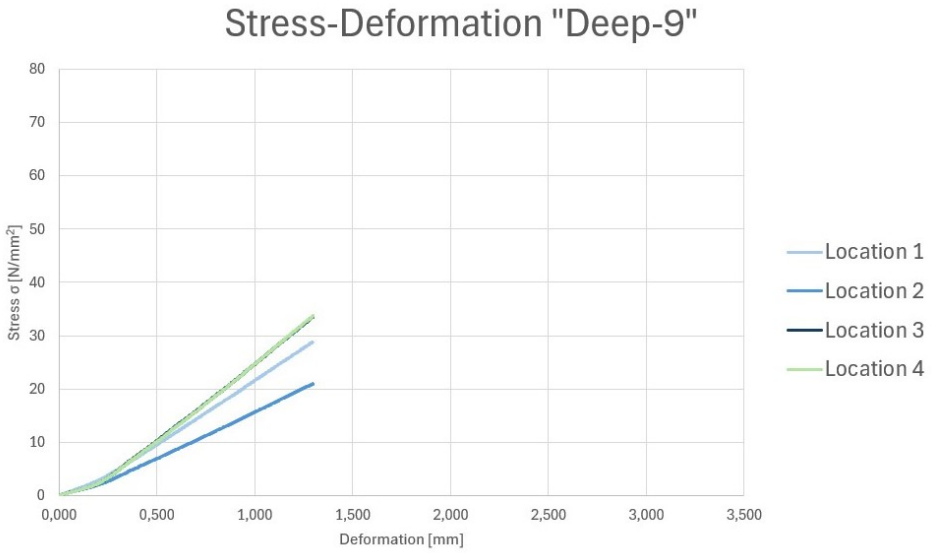

(b) The stress captured with the strain gauges in relation to the deformation of sample ”Deep-9”.

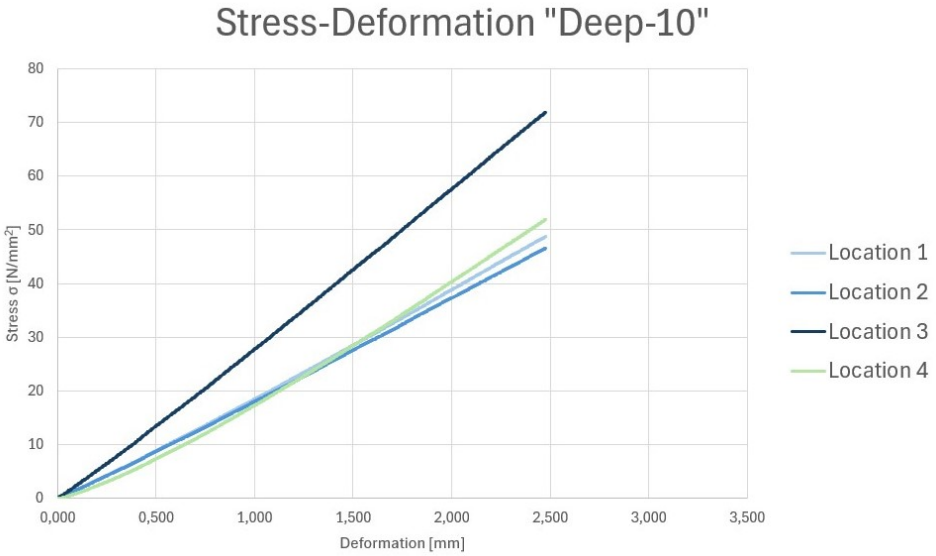

(c) The stress captured with the strain gauges in relation to the deformation of sample ”Deep-10”.

Figure 4.19: The stresses captured with the strain gauges.

Several observations can be made from the plots displayed in Figure 4.19. First, the test showed two distinct failure mechanisms. Samples ”Shallow-10” and ”Deep-10” failed due to a crack initiated from the edge, while sample ”Deep-9” failed due to a crack initiated from within the surface of the laser-bent part of the sample, as described in Subsection 4.3.2. The stress development of the first strain gauge at location 1 shows higher stresses than that of location 2. This phenomenon is not visible in the stress developments of ”location 1” in the plots of samples ”Shallow-10” and ”Deep-10”. Since location 1 seemed to endure higher stresses, it shows a good relation in why sample ”Deep-9” did fail at the bent-part. The stress distribution as described in Chapter 5, shows that the stresses at the edge of sample Deep-9 are significantly lower, which means that the surface strength is governing.

The second observation is that location 3 and 4 show similar stress results for samples ”Shallow-10” and ”Deep-9”. The FEM-models, which are described in Chapter 5, do show a similar behaviour, where the highest stresses do not need to be located specifically at midspan (location 4).

Furthermore, a third observation is the clear difference in the stresses present when the sample failed. This does not imply that this stress is equivalent to the failure stress. The point of failure differs from the observed points, so stating that the maximum observed stress is equal to the failure stress would be a false conclusion. The measurements confirm the minimum strength at the specific locations of the strain gauge. Table 4.6 shows the measured stresses at the time of failure of the sample.

Table 4.6: Stresses at the location of the strain gauges at time of failure.

	Stress location 1 [N/mm^2]	**Stress location 2 [N/mm^2]**	**Stress location 3 [N/mm^2]**	**Stress location 4 [N/mm^2]**
Sample ”Shallow-10”	12	38	56	58
Sample ”Deep-9”	29	21	34	34
Sample ”Deep-10”	49	47	72	52

The table shows different magnitudes of the values for each sample. Sample ”Shallow-10” shows stresses reaching 58 N/mm^2 at midspan, where the maximum observed stresses of ”Deep-9” reach 34 N/mm^2. Sample ”Deep-10” shows a maximum observed stress of 72 N/mm^2.

A visualisation of how these stresses relate to the numerically derived stresses is presented in Chapter 5.

4.3.5. Fragmentation

The four-point bending tests included the failure of each glass sample. The failure of the glass results in different fragmentation patterns of the samples. The fragmentation of every sample is captured with a camera, and the complete collection of images is given in Appendix D. The difference in fragmentation can be explained by the presence of internal stresses during the four-point bending tests. Fragmentation is related to the applied force. A higher force means that internal stresses increase, resulting in a larger fragmentation.

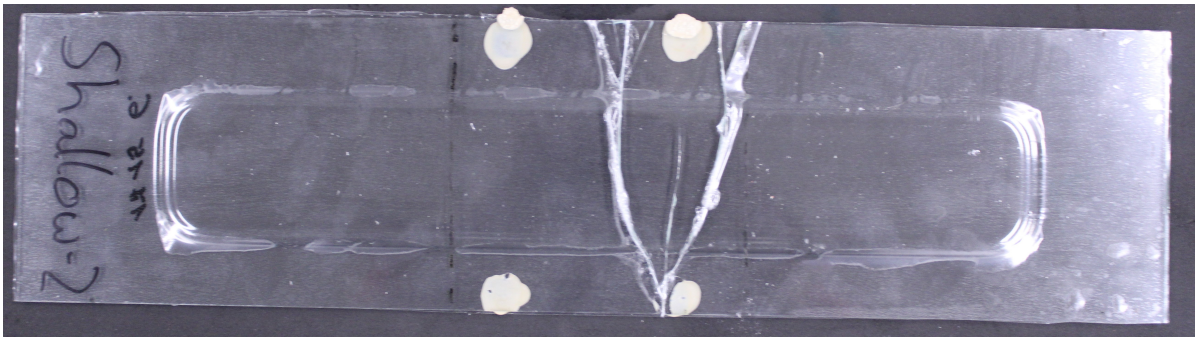

(a) Fragmentation of sample Shallow-2, which failed under a load of 180 N.

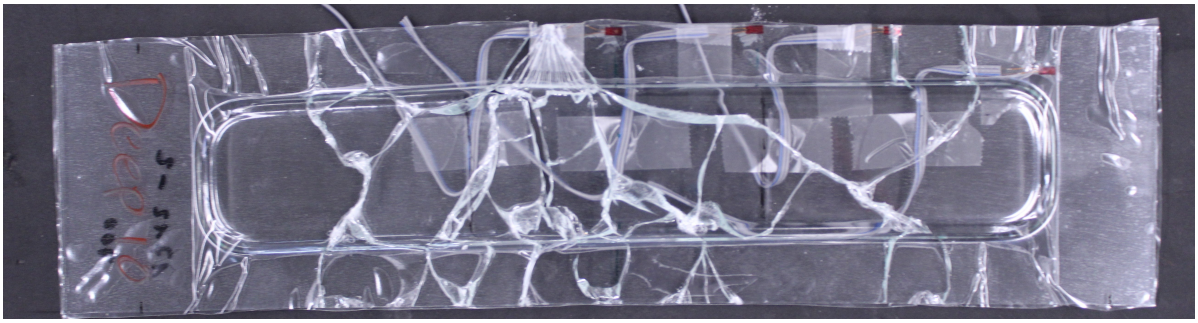

(b) Fragmentation of sample Deep-10, which failed under a load of 1111N.

Figure 4.20: Different fragmentation patterns and growth related to the applied force.

Figure 4.20 illustrates the difference in fragmentation of a sample that failed with a relatively low applied force and fragmentation of a sample that failed with the highest applied force. Sample ”Shallow-2” failed under a load of 179 N, resulting in very little fragmentation. From the initiating point of failure at the edge, the crack branches and splits into two main cracks.

Sample ”Deep-10” managed to withstand a load greater than 1 kN, reaching a failure force of 1111 N. The applied force of this magnitude resulted in large fragmentation. Many cracks propagated from the initial failure point. The branching of cracks is visible at the top of the sample. Therefore, the relation between internal stresses and the fragmentation pattern is visible in these tests.

5

FEM Modelling

This chapter describes the setup of the FEM-models. The precision and accuracy of the models are described, and the results of the deformation and stresses obtained through this numerical analysis are visualised.

5.1. Settings and setup in DIANA-FEA

This section describes the settings and set-up in DIANA FEA (DIANA in short) on how the glass elements were modelled in a FEM-programme.

5.1.1. Settings and modelling steps

In the course of CIEM1304 at the TU Delft, DIANA FEA proved to be sufficient to use as finite element modelling software for glass structures. Therefore, DIANA FEA is used as finite element modelling software during this thesis. The predictability of the samples relied on the methods used to model, the settings, and the setup of the model. The process was a mix of iterations consisting of assumption making and different modelling choices. This section describes the method used to model the glass samples numerically and retrieve reliable and comparable results.

A distinct difference is required in the description of this process. This chapter describes ”3D-models” and ”FEM-models”. These are each models with its own functions and applications:

The ”3D-models” are modelled in Rhino and Grasshopper. A Grasshopper script is made as described in Chapter 3. Rhino is the programme used to retrieve a solid 3D-model with the right geometry. No material properties are added yet. The model consists only of faces, edges, and vertices.

The ”FEM-models” are the models made in DIANA FEA. These models use the ”3D-models” as import-geometries in order to make the FEM-calculations, while pursuing other purposes in the process. The FEM-model is able to give material properties to the geometry and to apply loads. In addition to that, the FEM-model is able to generate a mesh to retrieve deformations, strains, and stresses.

The 3D-models are exported and imported as .stp (STEP-files). This ensures that the models act as one solid, without the use of any interface or other geometry conditions. This is visible in the ”type of shape” parameter in the FEM-model, as it is set as ”solid”.

The material class is set to ”Concrete and masonry”, since glass is not available as a material class in DIANA. The material model is set to ”Linear elastic isotropic” to model the isotropic behaviour of glass as well as its linear elastic properties. After the right class and material model are set, the properties of the material are defined. The material properties used in every model are given in Table 5.1.

Table 5.1: Material properties used in DIANA

Material property		
Young's modulus	70000	N/mm^2
Poisson's ratio	0.23	
Mass density	2.5e-09	T/mm^3

5.1.2. Loads

The loads are modelled as distributed forces on a target type called ”Edge”. A projection line is therefore required to be able to model a distributed force. Two lines at the top of the samples are modelled at y = 125mm and y = 225mm to divide the elevated part into 3 sections. These dimensions are the same as the locations of the force in the four-point bending tests. The modelled lines are projected at the shape to implement them into the solid shape. Figure 5.1 shows the two line loads that are modelled.

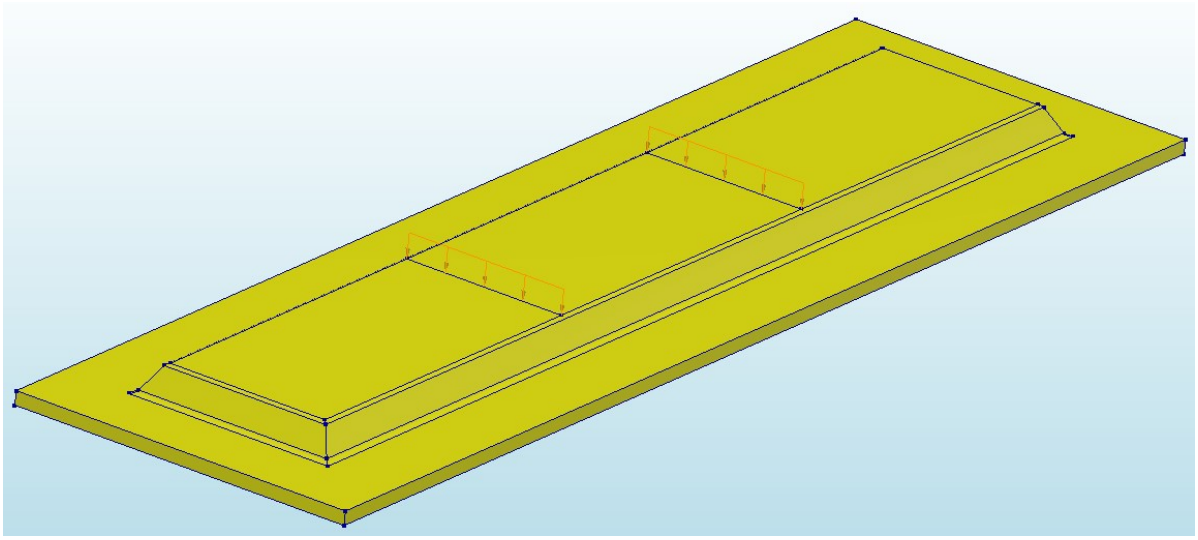

Figure 5.1: The loads modelled as line loads to represent the four-point bending tests.

5.1.3. Supports

To model the support behaviour, six degrees of freedom can be fixed or remain open. The six degrees of freedom are the translational behaviour in the X-, Y-, and Z-directions, and the rotational behaviour in the X-, Y-, and Z-directions. Modelling the support behaviour of a four-point bending test, is done by fixing the translation in Z-direction. To ensure that there are no singularity problems in the model, the sample needs to be fixed in the X- and Y-direction as well. Fixing one corner in both directions fixes the model in ”space”, meaning that the model cannot move randomly through an arbitrary space. A second corner needs to be fixed in only the X-direction. This allows for any elongation of the sample, while restricting rotations in unwanted spatial directions. The support conditions are visualised in 5.2.

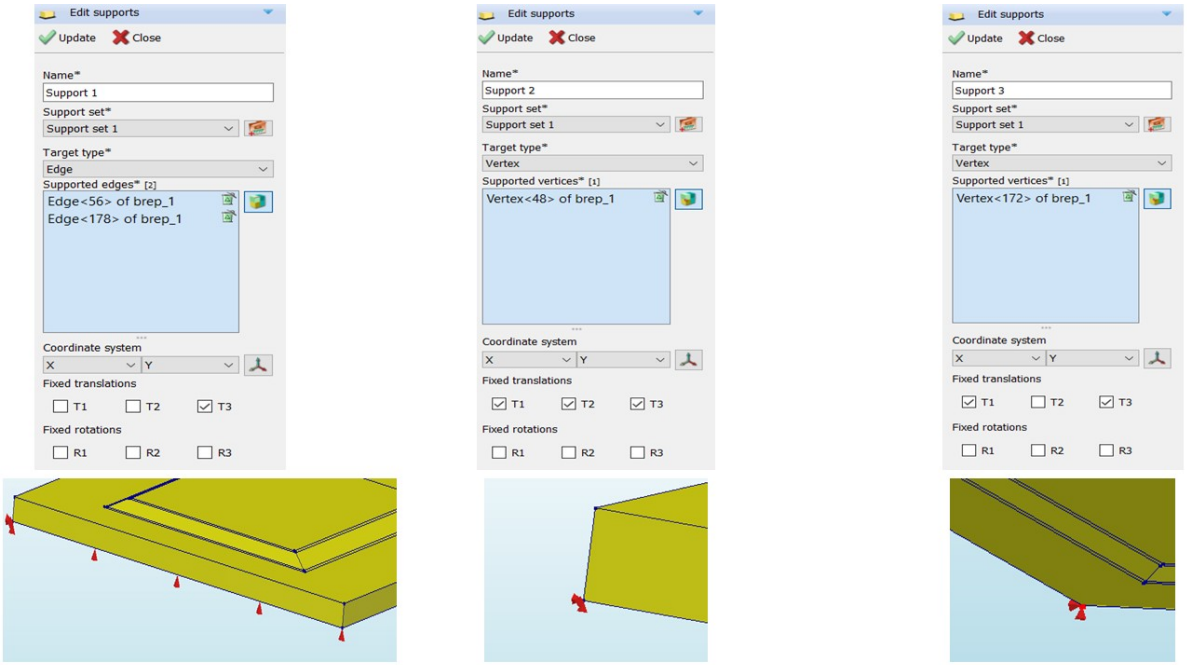

Figure 5.2: The support settings in the DIANA model, with the third condition viewed from below the sample.

5.2. Results

This section describes the results of the DIANA-models. A comparison is made with the experimental lab-tests to validate the models and to conclude if FEM can resemble the real-life behaviour.

Initially, three FEM-models were built. One FEM-model resembled the flat panels, one resembled the shallow samples, and the last one resembled the deep samples. The model of the flat samples sufficed, since no geometry differences were measured between the four flat samples. It quickly became apparent, that the two models resembling the shallow and the deep samples, did not manage to suffice directly. The deformations measured, when loaded by the same load as the corresponding lab-test, resulted either too high or too low. Individual models were made to resemble each sample, leading to results closer to the obtained data from the tests. Section 5.3 compares the results of the nominal models and the individual models based on the known changed geometries.

5.2.1. Sensitivity analysis

The mesh can be generated with different seeding methods. The element size can be determined by ”divisions” and ”element size”. The method used to generate the mesh used the element size seeding method. This allowed for a fixed size of the elements, resulting in mesh-sizes that fit the purpose and accuracy. A mesh-sensitivity analysis is performed to obtain insight into the relations between representable results and the corresponding computational time, as visualised in Figures 5.3, 5.4 and 5.5.

Finer meshes result in longer computational time. A balance between efficiency and reliable results determine whether smaller meshes are feasible.

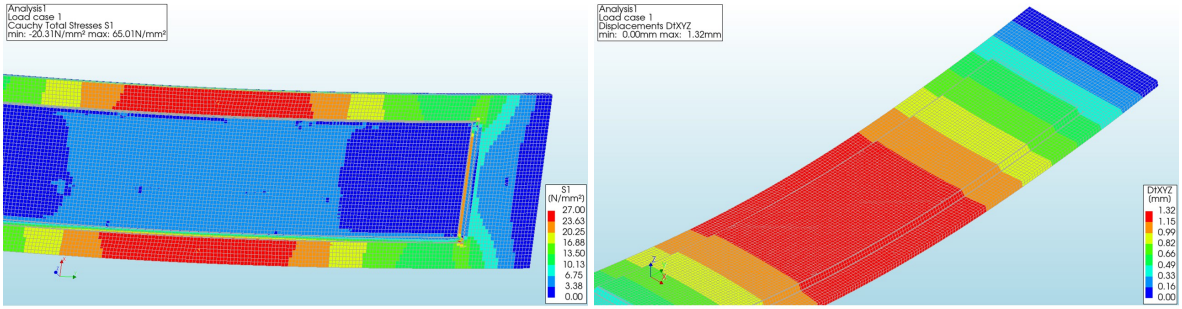

(a) Sensitivity of the mesh size regarding the stresses, when a 2mm element size is used.

(b) Sensitivity of the mesh size regarding the deformations, when a 2mm element size is used.

Figure 5.3: The sensitivity of adjusting the element size of the 2mm mesh.

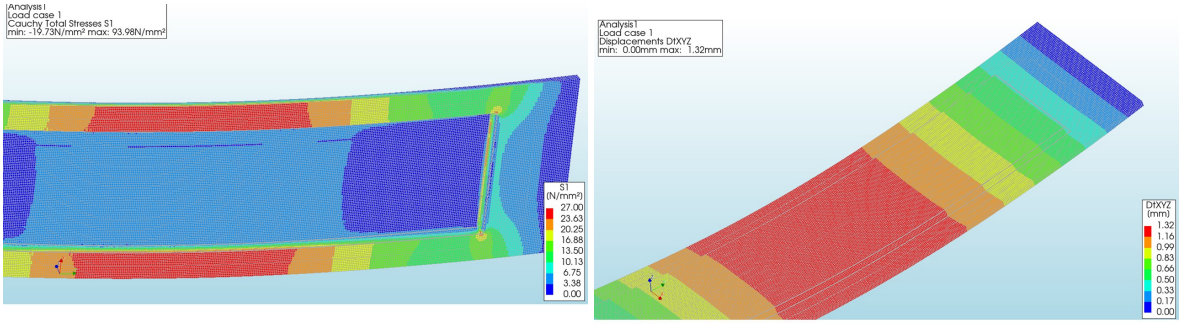

(a) Sensitivity of the mesh size regarding the stresses, when a 1mm element size is used.

(b) Sensitivity of the mesh size regarding the deformations, when a 1mm element size is used.

Figure 5.4: The sensitivity of adjusting the element size of the 1mm mesh.

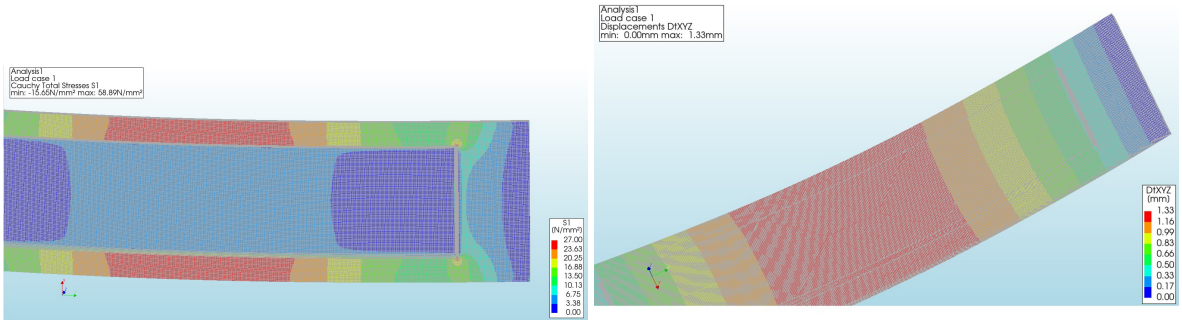

(a) Sensitivity of the mesh size regarding the stresses, when a 0.5mm element size is used.

(b) Sensitivity of the mesh size regarding the deformations, when a 0.5mm element size is used.

Figure 5.5: The sensitivity of adjusting the element size of the 0.5mm mesh.

The models displayed show the visual results of the different meshes. A finer mesh relates to more computational calculations that it requires to do. This is visible in the model becoming more grey due to the amount of integration points increasing. It allows for a more detailed visualisation when zoomed in, while in order to visualise it completely (the whole model visible in one shot), the amount of nodes results in less vibrant colours. The numerically derived results are, on the other hand, more precise. These models do contain fictitious values; only the sensitivity is tested in this sense.

The numerical results of the sensitivity-analysis are shown in Table 5.2.

Table 5.2: Results of the mesh sensitivity analysis.

Element size	Maximum stress at edge [N/mm^2]	Max deformations [mm]	Computational time
2mm (coarse mesh)	27.7	1.32	15 seconds
1mm (regular mesh)	27.6	1.32	2 minutes
0.5mm (fine mesh)	27.6	1.33	40 minutes

The numerical derived results for the maximum edge stresses and maximum deformations do not appear to be influenced by the size of the elements in the mesh. An observation is that there are differences in the maximum stresses occurring in the complete sample. Different mesh-sizes result in different peak-stresses and stress concentrations. However, the numerically derived peak stresses do not relate to the bending stresses that introduced failure from the edges, as observed in the lab tests. The peak-stresses appear to be acting on an element almost infinitely small.

Because of the stresses acting on a very small area, the chances of failure from within that exact spot are slim. Glass fails at the weakest point, depending on flaws and scratches on the surface. It means that in order to fail from the peak-stresses, the sample needed to be weak at that exact almost infinitely small spot. It may affect the performance of the glass, if the peak-stresses are immediately visible in areas of 1mm^2 (one full area consisting of 4 nodes). No samples were observed to fail due to peak-stresses; therefore, the FEM-models were mainly checked on the bending stresses occurring at the edges of the samples. On the other hand, the FEM-geometry does have inaccuracies, meaning the peak-stresses occurring in the FEM-model might not be present in real life.

A finer mesh is, furthermore, more sensitive to small inaccuracies in the modelled geometry. For example, sharp corners without filleting (rounding of the edges) tend to be a source of stress concentrations. Modelling the geometry in 3D with full details is time consuming. The trade-off between an accurate model and low modelling and calculation time led to the conclusion that a regular mesh with an element size of 1mm suffices.

5.2.2. Deformations

The first results that are compared to the data obtained in the tests are the deformations. A structural linear analysis is performed within the FEM-model. This analysis resulted in values obtained for the deformations of each node. The measured data during the lab-tests is the displacement of the press, so the value that corresponds needs to be obtained from the location of the loads. The deformations obtained in the FEM-model do come with inaccuracies. The measured data should filter out the stiffness deformations within the press, while the compression of the three additional components, as described in Chapter 4.1 and Figure 4.2, is not taken care of. Compression and therefore lowering of the supports is not taken into account, meaning the results of the FEM-model deviates from the real-life behaviour. The model aims to represent the real-life behaviour, without the need to investigate the stiffness properties of the supports and the loading elements. A visualisation is shown in Figure 5.6.

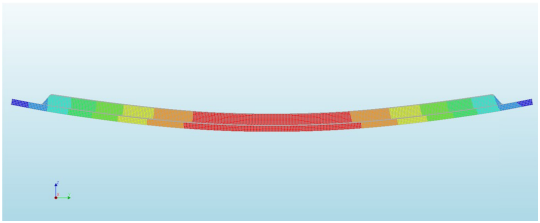

Figure 5.6: Visualisation of a deformed sample in DIANA FEA.

Results of the flat samples

The deformations of the flat samples are relatively large due to the low stiffness of the panels. A scatter in the results is visible in Figure 5.7. This scatter is in correspondence with the scattering failure forces.

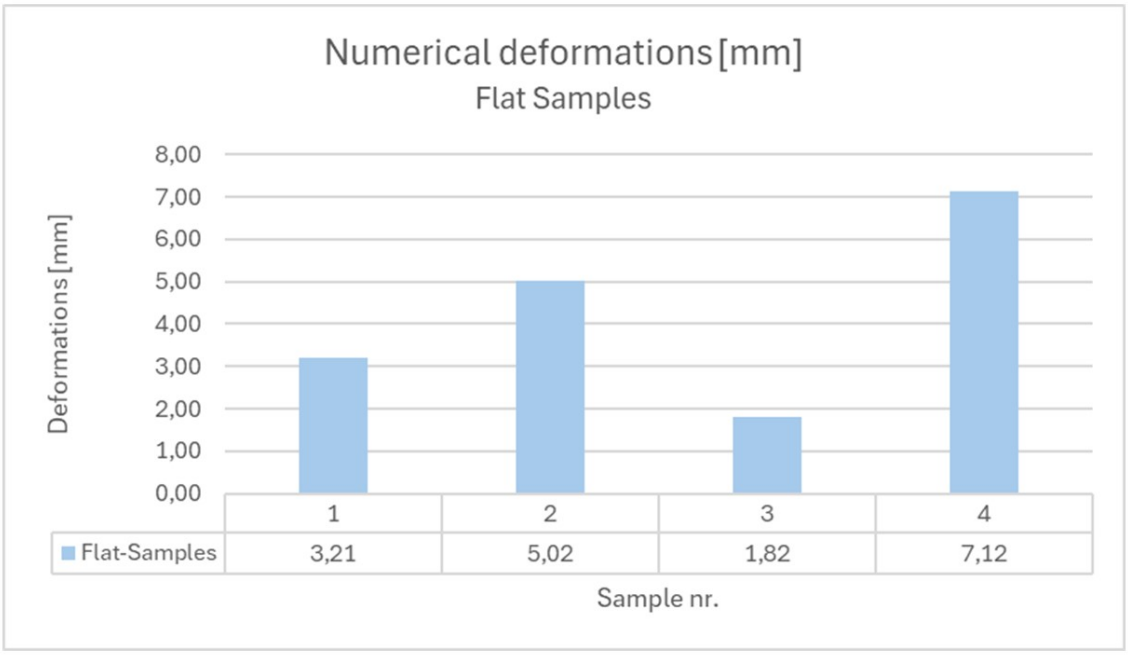

Figure 5.7: The numerically derived deformations of the flat samples.

Results of the shallow samples

The deformations of the shallow samples are presented in Figure 5.8. The scatter is immediately visible, corresponding to the different geometries and different loading conditions.

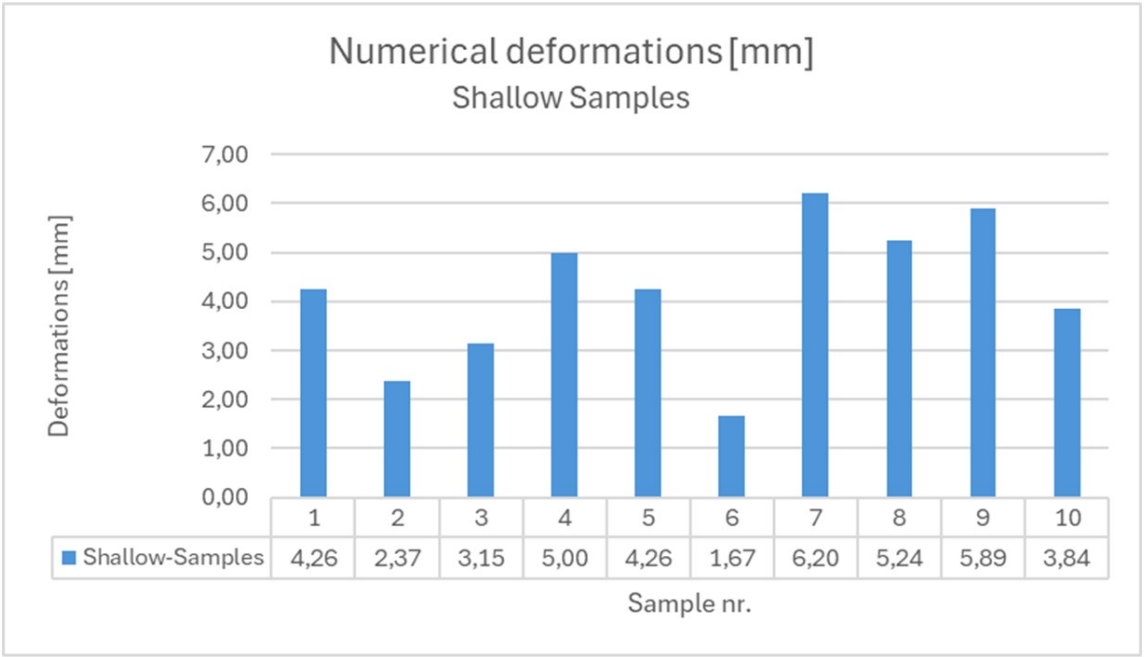

Figure 5.8: The numerically derived deformations of the shallow samples.

Results of the deep samples

The deformations of the deep samples are presented in Figure 5.9. The deep samples show a scatter, although less than the shallow samples because the geometries are more similar to each other.

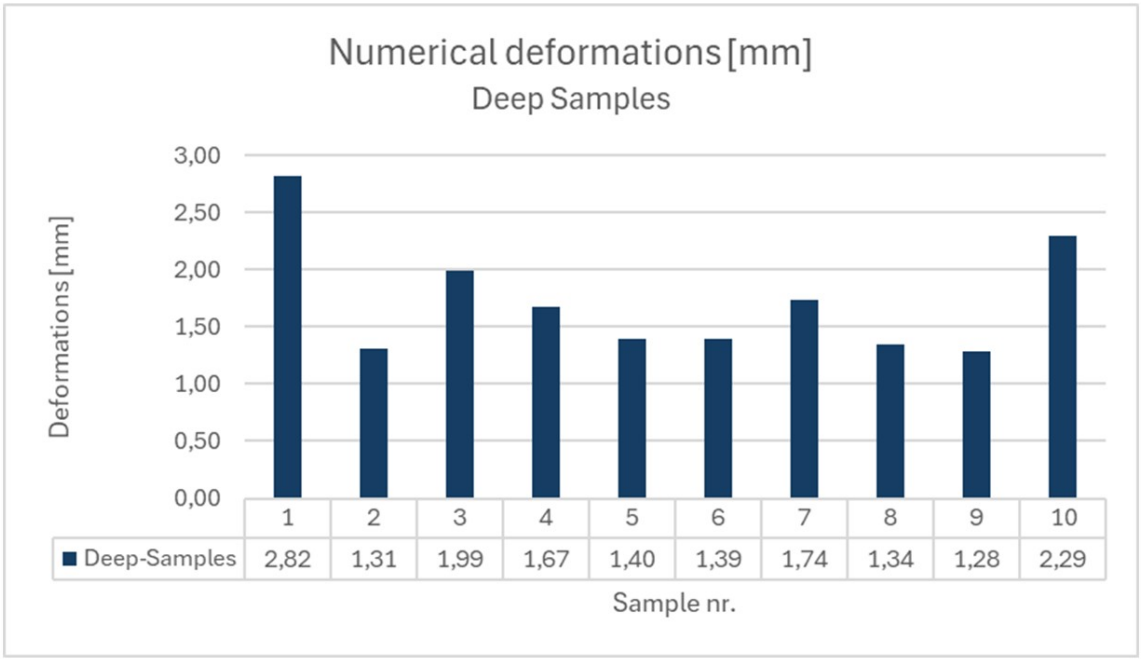

Figure 5.9: The numerically derived deformations of the deep samples.

Comparison to measurements

The results are valuable when they do align with the data obtained from the lab-tests. Figure 5.10 shows both obtained deformations of each sample. This graph shows that the FEM-model is able to predict the deformations well, but full precision and resemblance is difficult to obtain.

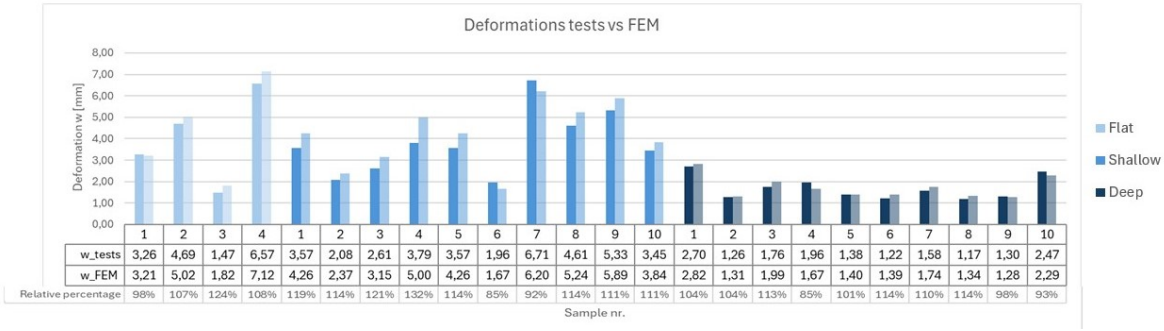

	1	2	3	4	1	2	3	4	5	6	7	8	9	10	1	2	3	4	5	6	7	8	9	10
w_tests	3,26	4,69	1,47	6,57	3,57	2,08	2,61	3,79	3,57	1,96	6,71	4,61	5,33	3,45	2,70	1,26	1,76	1,96	1,38	1,22	1,58	1,17	1,30	2,47
w_FEM	3,21	5,02	1,82	7,12	4,26	2,37	3,15	5,00	4,26	1,67	6,20	5,24	5,89	3,84	2,82	1,31	1,99	1,67	1,40	1,39	1,74	1,34	1,28	2,29
Relative percentage	98%	107%	124%	108%	119%	114%	121%	132%	114%	85%	92%	114%	111%	111%	104%	104%	113%	85%	101%	114%	110%	114%	98%	93%

Figure 5.10: The measured deformations and the numerically derived deformations.

The difference between the obtained values is visualised in Figure 5.11. This shows that 18 out of the 24 samples act stiffer in real-life than they do in the FEM-models. The deviations are for 20 out of the 24 samples lower than 15%. Both Figures 5.10 and 5.11 tell that the FEM-models are able to obtain the deformations, with a margin of error. These deviations do occur due to several factors that influence the accuracy.

First, the geometries are measured by hand, with a digital caliper, which comes with precision errors. A consequence is that the FEM-geometry might differ from the real-life geometry. Secondly, the stiffness of the supports and additional components in the test was set to be infinite, resulting in a difference in the boundary conditions compared to the real-life setup. Lastly, material properties such as the Young's

modulus and the Poisson's ratio were assumed and set fixed. It is not investigated whether these material properties are influenced by the laser-forming process, and whether the properties remain the set values.

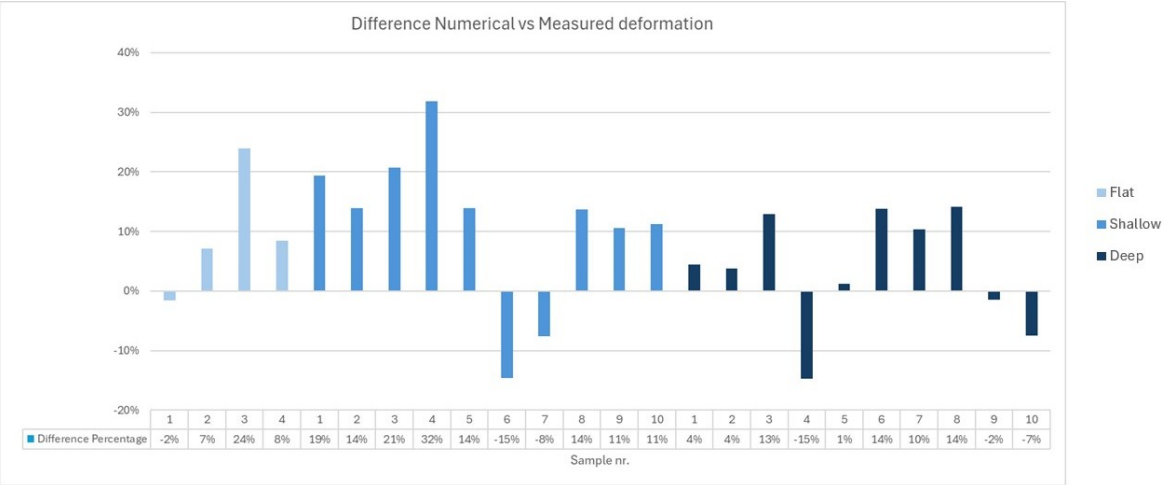

Figure 5.11: The difference between the measured deformations and the numerically derived deformations.

The summary of the found deformations is shown in Table 5.3. The deformations do show high standard deviations, meaning that the samples do not behave similarly to each other. One cause is the differences in geometry, while the strength of glass scatters as well.

Table 5.3: Statistical summary of the deformations.

Sample	Min Deformation [mm]	Max deformation [mm]	Mean deformation [mm]	STD [mm]	STD/mean [%]
Flat Samples (tests)	1.47	6.57	4.00	1.87	47%
Shallow Samples (tests)	1.96	6.71	3.77	1.39	37%
Deep Samples (tests)	1.17	3.45	1.84	0.71	38%
Flat Samples (FEM)	1.82	7.12	4.29	1.99	46%
Shallow Samples (FEM)	1.67	6.20	4.19	1.40	33%
Deep Samples (FEM)	1.28	2.82	1.72	0.48	28%

5.2.3. Stiffness

After retrieving the deformations of the samples, the stiffness can be derived. Dividing the applied load by the numerically derived deformations results in a stiffness index. The values are visible in the graph shown in Figure 5.12. A pattern is visible that shows that the stiffness increases relative to the total height.

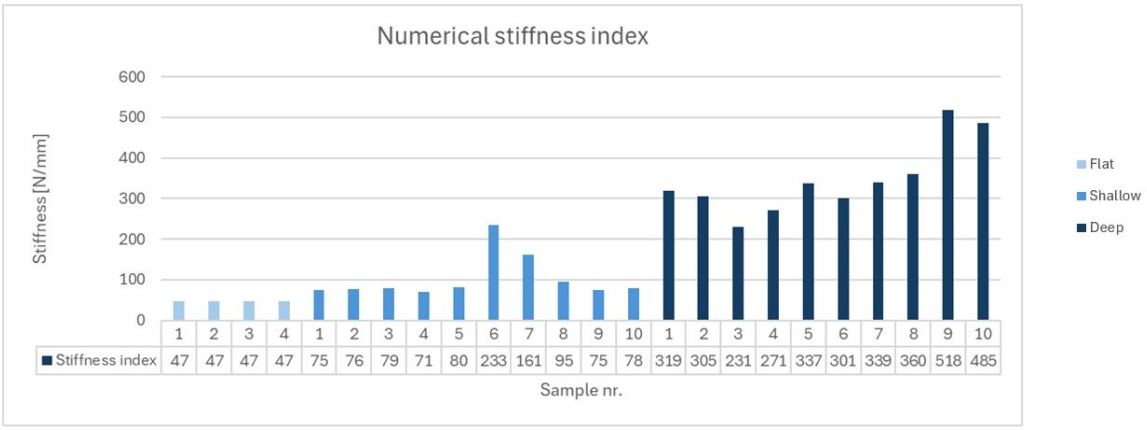

Figure 5.12: The numerically derived stiffness values.

The comparison of the numerically derived stiffness to the measured stiffness is made. The graph in Figure 5.13 tells the applicability of the FEM-models. The models are able to predict the stiffness behaviour of the real-life samples, with the pattern aligning with small deviations.

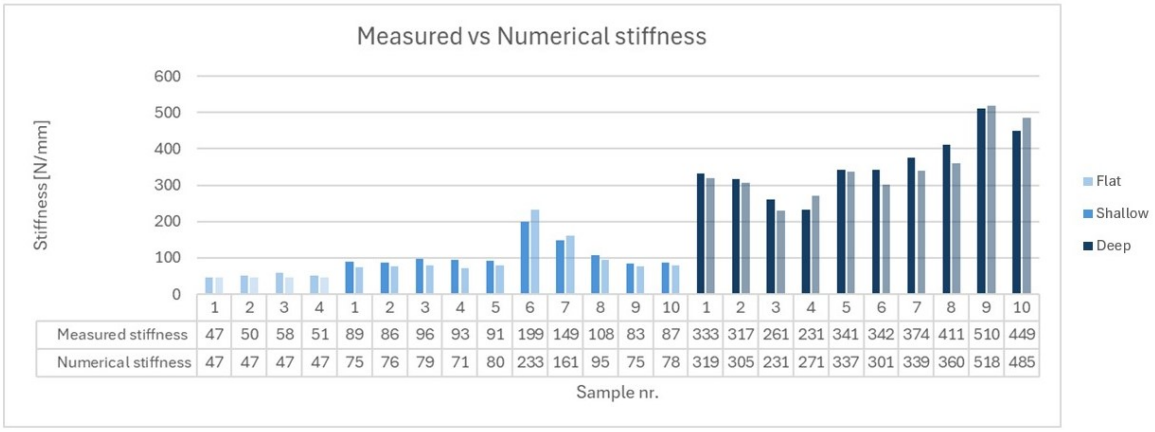

Figure 5.13: The measured and the numerically derived stiffness values.

The numerical deformations of the samples were higher, meaning that the numerical stiffness is lower than the actual stiffness of the samples. Figure 5.14 shows the inverse behaviour. The overestimation of the stiffness can be compensated by using a correction factor of 1.2 when designing towards the FEM-deformations, since the largest overestimation is 17%.

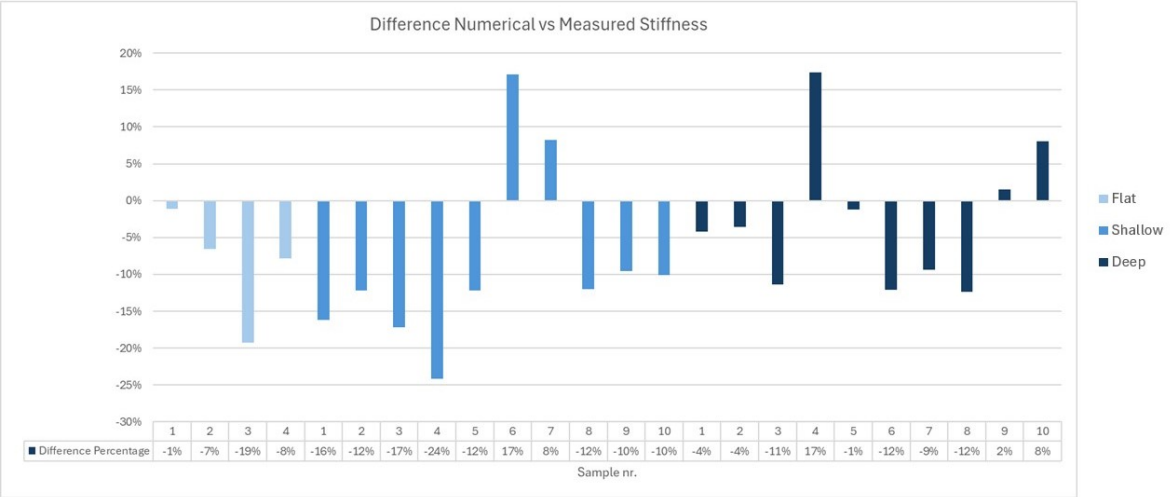

Figure 5.14: The difference between the measured and the numerically derived stiffness values.

The summary of the stiffnesses is shown in Table 5.4. Due to irregular geometries the laser-formed samples do show scattering stiffnesses. The deep samples show a better fit than the shallow samples. The low value of the standard deviation of the flat samples is because there is no geometry difference between the samples.

Table 5.4: Statistical summary of the stiffness.

Sample		Min stiffness [N/mm]	Max stiffness [N/mm]	Mean stiffness [N/mm]	STD [N/mm]	STD/mean [%]
Flat (tests)	**Samples**	47.10	57.82	51.62	3.89	8%
Shallow (tests)	**Samples**	83.26	199.33	108.25	35.44	33%
Deep (tests)	**Samples**	231.28	509.71	356.81	79.21	22%
Flat (FEM)	**Samples**	46.56	47.13	46.87	0.26	1%
Shallow (FEM)	**Samples**	70.68	233.37	102.39	50.51	49%
Deep (FEM)	**Samples**	230.86	517.58	346.58	85.08	25%

The FEM-models predict the samples as less stiff. This results in the calculations being conservative, since the actual samples perform better.

5.2.4. Stresses

To be able to get insight into the strength of the laser-formed glass samples, first the applied strain gauges do give values of 3 out of the 20 samples. To gain more insight, the stresses appearing in the FEM-models are analysed. The obtained stresses represent the stresses at the point of failure of the samples. This does not conclude that these are the actual stresses that occurred during the lab-tests. A visualisation of the location of crack initiations is shown in Figure 5.15.

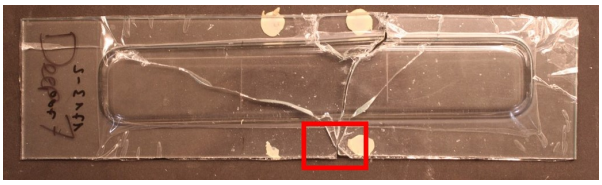

Figure 5.15: Crack initiation location

Results of the flat samples

The flat samples all failed from a crack initiated at the edge. The stresses shown in Figure 5.16, were retrieved from the FEM-model at the location of this initiating crack. This leads to a value based on numerical derivation, which does not imply that these were the actual failure stresses due to modelling inaccuracies.

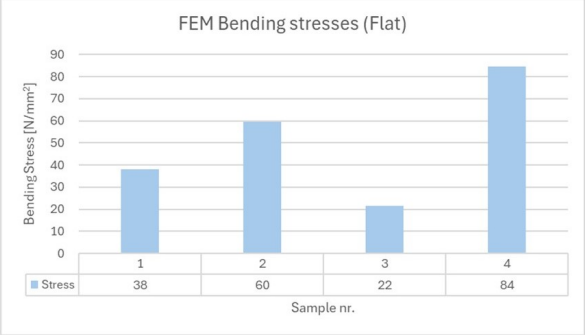

Figure 5.16: The derived failure stresses of the flat samples.

The size of the dataset is minimal, therefore caution is needed when stating conclusions of the strength of the glass. The visible scatter is expected as a result of the strength properties of glass in general.

Results of the shallow samples

The shallow samples failed from cracks initiating in the edge as well. Figure 5.17 shows high values of the derived bending stresses. Where a range of 40-60 MPa is expected, 7 out of the 10 samples do show higher values. Conclusions based on this dataset are hard to state because of these values.

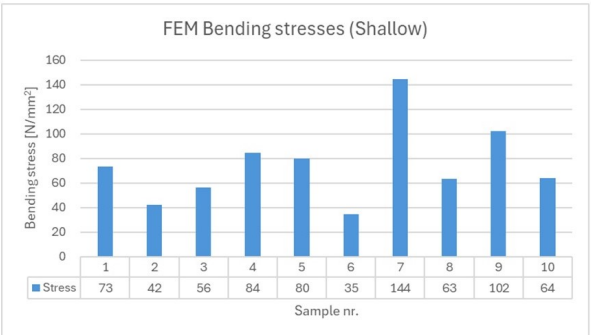

Figure 5.17: The derived failure stresses of the shallow samples.

Results of the deep samples

The results of the deep samples show less scatter, and only two out of the ten derived stresses are outside the expected values. Figure 5.18 shows that the stresses of ”Deep-1” and ”Deep-10” are high, while the rest of the dataset show expected and similar results. Sample ”Deep-9” failed from the web of the bent. The value obtained for the stress is the maximum value at the edge, since the exact location of the initiation isn't found. The maximum value of the web shows at least the minimum strength of the web, resulting in a conservative value found for the failure stress of the sample.

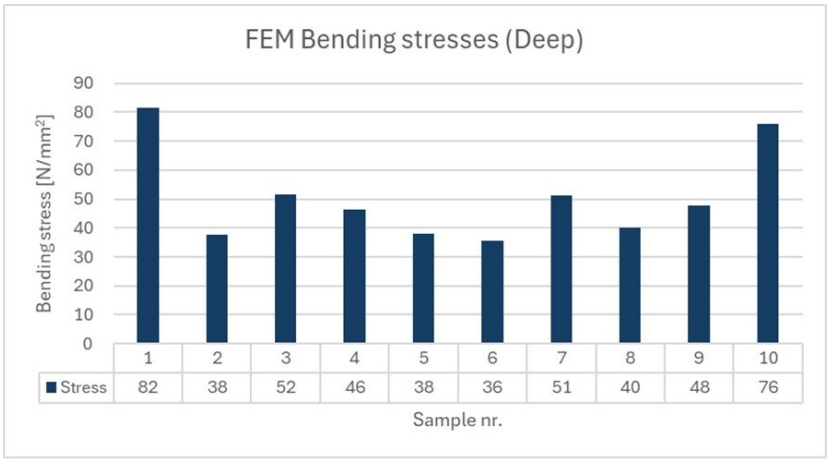

Figure 5.18: The derived failure stresses of the deep samples.

5.2.5. Summary of the stresses

The summary of the numerically derived failure stresses is shown in Table 5.5.

Table 5.5: Statistical summary of the stresses.

Sample	Min stress [N/mm^2]	Max stress [N/mm^2]	Mean stress [N/mm^2]	STD [N/mm^2]	STD/mean [%]
Flat Samples (FEM)	21.5	84.4	50.9	23.6	46%
Shallow Samples (FEM)	34.7	144.4	74.5	29.9	40%
Deep Samples (FEM)	35.6	81.6	50.6	15.2	30%

Although the size of the datasets is small, statistics are performed. Weibull distributions with least squared regression-plots are made to obtain insight into the numerically derived 5%-fractile and the 95% confidence interval values.

Statistics of the flat samples

The statistical analysis of the flat samples is performed and concluded insufficient. The dataset consists of only 4 values, resulting in an insufficient dataset. The results are obtained and observed in Table 5.5. The values found are used to visually provide insight into the derived stresses. Plotting distribution functions of data consisting of 4 points, may lead to false conclusions. Therefore, no statistical analysis is performed.

Statistics of the shallow samples

Secondly, the statistical analysis of the shallow samples is performed. The dataset consists of 10 values. Still the size of the dataset is small, meaning again that the statistics should be concluded with caution. The probability estimator used for the Weibull plots is the mean rank probability estimator. This estimator is equal to: i/(n+1).

Shallow-Samples (n=10)

Fractile [%]	Stress [MPa]	95% CI lower [MPa]	95% CI upper [MPa]
0.8%	11.15	11.05	11.25
5%	24.33	24.2	24.46
50%	72.82	72.69	72.96
Selected 5.0%	24.33	24.2	24.46

Shallow-Samples (n=10)

Min Stress [MPa]	Max Stress [MPa]	Mean Stress [MPa]	Coeff. of variation [%]	Goodness of fit, p_{AD}
34.7	144.4	74.47	42.39	51.89

Figure 5.19: The derived statistical values of the FEM-stresses of the shallow samples.

The Weibull probability density function and the Weibull cumulative density function (CDF) are plotted in Figure 5.20. The distribution shows that 95% of all the values are greater than 24.33N/mm^2.

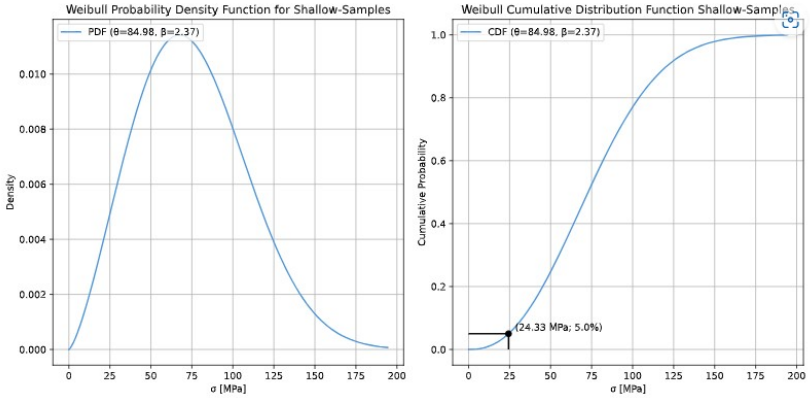

Figure 5.20: The PDF and CDF of the FEM-stresses of the shallow samples.

Statistics of the deep samples

Lastly, the statistical analysis of the deep samples is performed. The dataset consists of 10 samples as well, meaning again that the statistics should be concluded with caution.

Deep-Samples (n=10)

Fractile [%]	Stress [MPa]	95% CI lower [MPa]	95% CI upper [MPa]
0.8%	12.23	12.03	12.42
5%	22.08	21.88	22.29
50%	50.66	50.5	50.81
Selected 5.0%	22.08	21.88	22.29

Deep-Samples (n=10)

Min Stress [MPa]	Max Stress [MPa]	Mean Stress [MPa]	Coeff. of variation [%]	Goodness of fit, p_{AD}
35.6	81.6	50.58	31.64	4.06

Figure 5.21: The derived statistical values of the FEM-stresses of the deep samples.

The Weibull probability density function and the Weibull cumulative density function are plotted in Figure 5.22. The distribution shows that 95% of all the values are greater than 22.08N/mm^2.

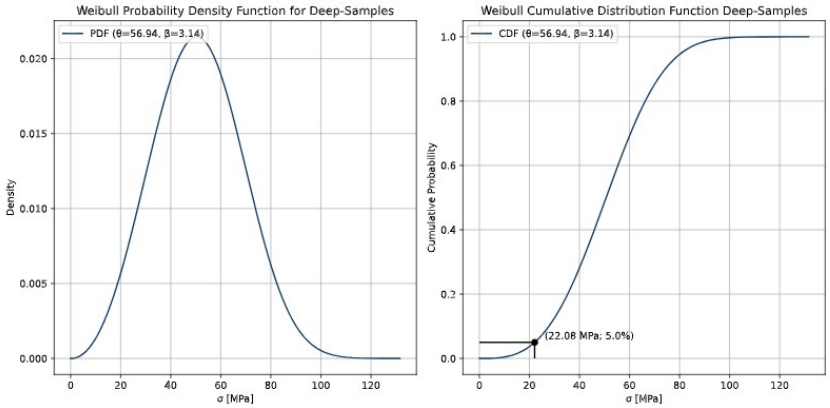

Figure 5.22: The PDF and CDF of the FEM-stresses of the deep samples.

The obtained numerical derived failure stresses of the 5%-fractile appear to be on the lower end. The flat samples perform way less than expected. Therefore it is hard to conclude these values represent the actual failure stresses that occurred during the lab-tests. The shallow- and the deep samples performed better numerically, based on the derived statistics. The values show similar results compared to strength values found in literature.

The total logarithmic CDF Weibull Plot is visualised in Figure 5.23. This plot confirms that the deep and shallow samples perform better in FEM. However, the CDF of the flat samples are based on only four samples, resulting in a CDF which might be misleading.

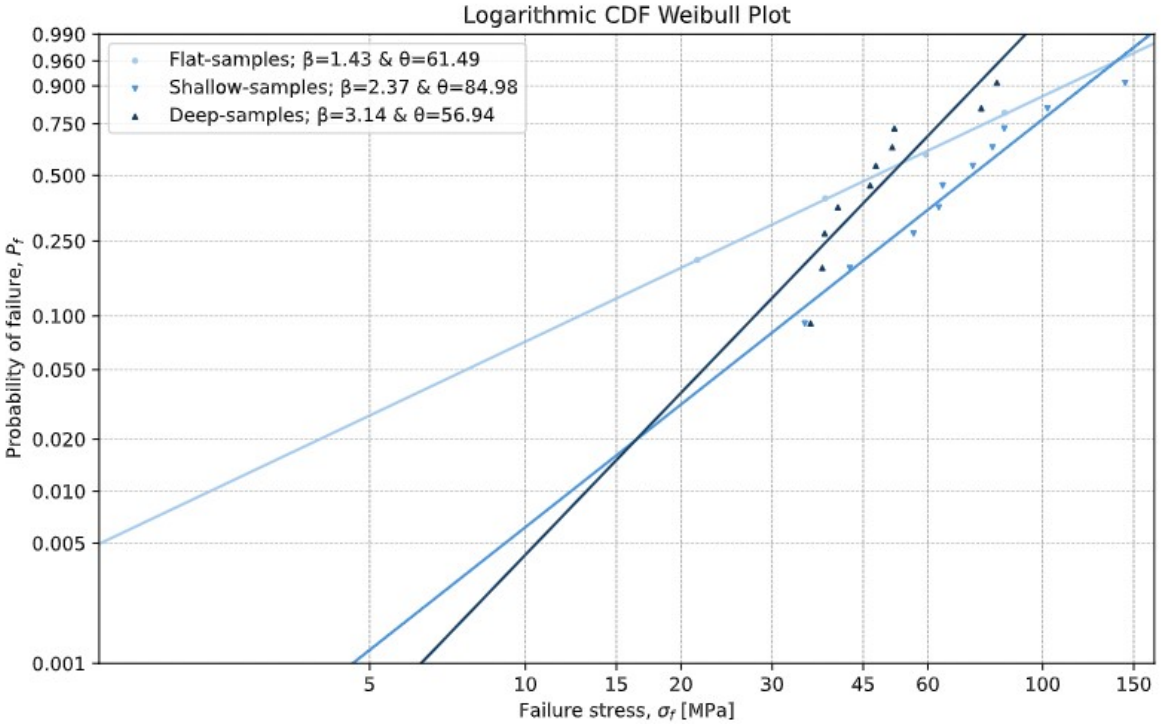

Figure 5.23: The logarithmic CDF Weibull Plot of all three datasets.

5.2.6. FEM-stresses compared to lab-test data

Three samples had strain gauges attached to the bottom of the sample. A check is performed on how the stresses obtained from the strain gauges compare to the numerical derived stresses obtained from the FEM-models. Table 5.6 shows the numerically derived stresses at the locations of the strain gauges.

Table 5.6: The numerically obtained stresses from the FEM-models.

Sample	Stress location 1 [N/mm^2]	Stress location 2 [N/mm^2]	Stress location 3 [N/mm^2]	Stress location 4 [N/mm^2]
Shallow-10	15	42	66	70
Deep-9	57	25	42	42
Deep-10	56	45	74	76

Figures 5.24, 5.25, and 5.26 show the comparisons between the measured stresses and the numerical derived stresses.

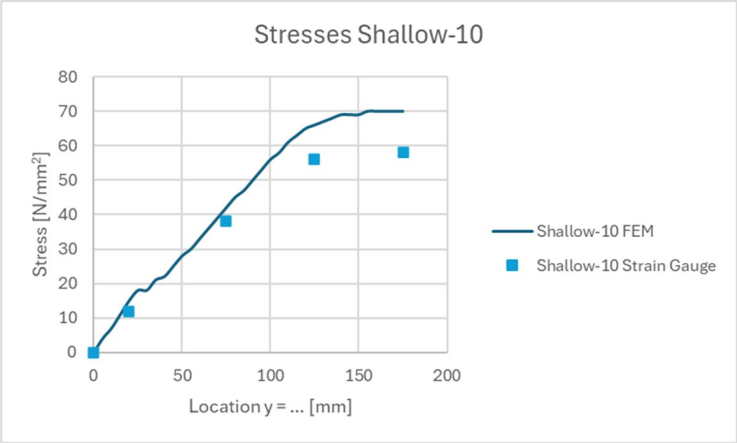

Figure 5.24: The measured stress compared to the FEM-derived stresses of sample ”Shallow-10”.

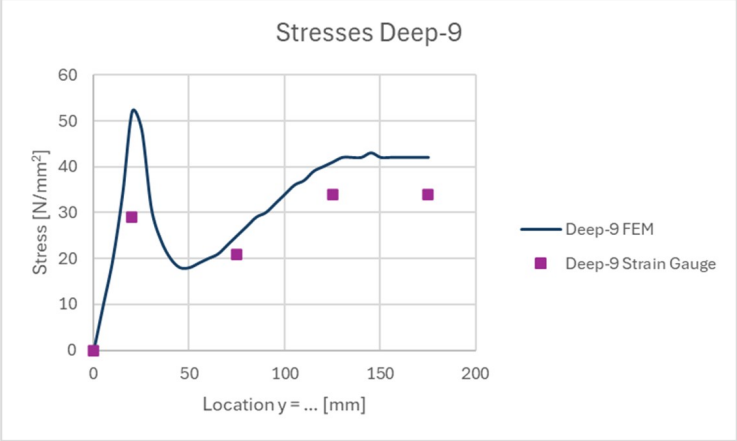

Figure 5.25: The measured stress compared to the FEM-derived stresses of sample ”Deep-9”.

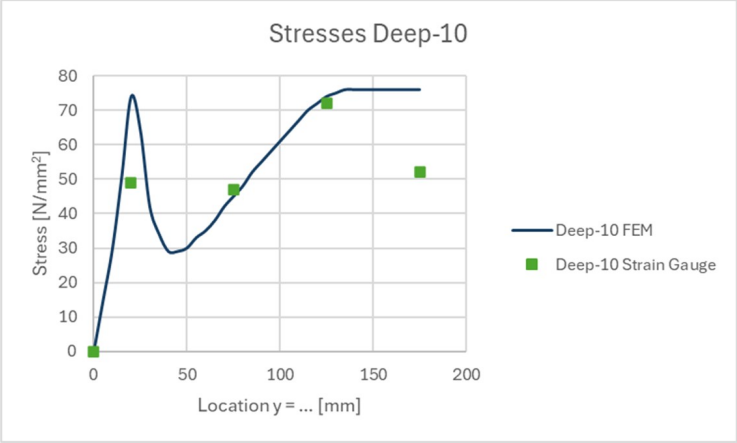

Figure 5.26: The measured stress compared to the FEM-derived stresses of sample ”Deep-10”.

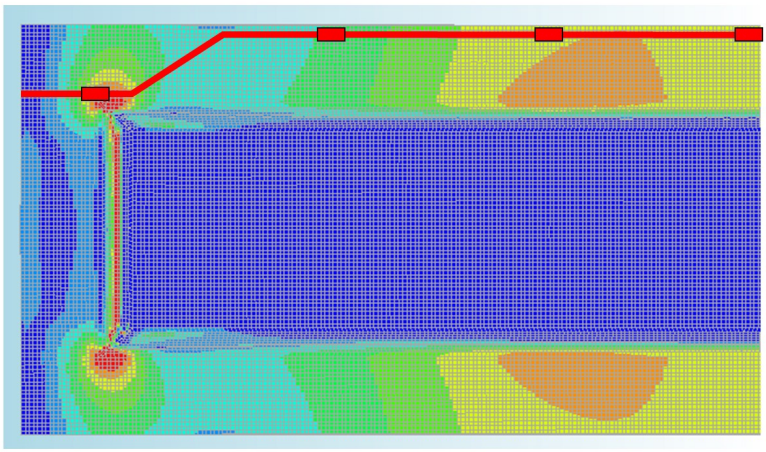

Figure 5.27: The line indicates the location of the measured FEM results as well as the location of the strain gauges.

The stresses show some similarity. The results require to be observed with caution, as there are only 12 locations measured and compared. The trend of the shallow sample is visible in the FEM-derived stresses as well. The stiffness of the FEM-model showed to be 10% less, which also has an impact on the stresses. The derived stresses are all higher than the measured stress, which is related to the decrease in stiffness, as a lower stiffness corresponds to higher bending stresses. This results in conservative calculations, because the present stresses are lower than the computed ones.

Sample ”Deep-9” showed large stress concentrations at location 1 in the FEM-model. To be able to capture stress concentrations with a strain gauge, it needs to be placed on the exact position, which would be based on luck. The other locations show a similar pattern for the FEM-stress compared to the measured stress. The FEM-derived stresses are again higher than measured. However, the stiffness of the FEM-model was predicted almost correctly with the FEM-model behaving 2% less stiff than the sample in the lab-tests. Due to this observation, the bending stresses are harder to predict correctly with FEM.

Sample ”Deep-10” showed different behaviour, with two of the four FEM-derived stresses being almost identical to the measured stresses. This FEM-model acted 7% less stiff than the sample in the lab-tests. This confirms that the stresses are hard to predict correctly. Many factors influence the numerically derived stresses, and therefore obtaining the stresses from FEM needs to be taken with caution. However, the results of the FEM are conservative in relation to the actual present stresses during the tests.

5.2.7. Necking influence in FEM

The presence of necking within laser-formed glass is significant. Larger necking results in smaller web-thicknesses. The effect of the thickness of the web was observed in the failure mechanism of sample ”Deep-9”. This sample failed in the web, instead of the edge of the glass, which was the case for all of the other samples. The relation between the thickness of the web and the initial thickness of the sample is investigated.

This subsection shows the influence of necking and how FEM is able to capture higher stress values along the web, when necking plays a role.

Two distinct failure mechanisms are described in Chapter 4.3.2. The FEM-models are checked whether these differences are visible. First, sample ”Deep-1” is used as a comparison. Figures 5.28 and 5.29 show the differences that the FEM-models were able to capture. Deep-1 shows high stress areas along the edge (red/orange), while simultaneously the stresses in the web are lower (green). The sample shows peak stresses occurring in the corners of the bend, but these are on a small area, decreasing the probability of failure initiating from those points. Sample Deep-9 on the other hand shows much more larger high stress (red) areas in the web. The larger these areas become, the higher the chance of a failure initiating from those areas.

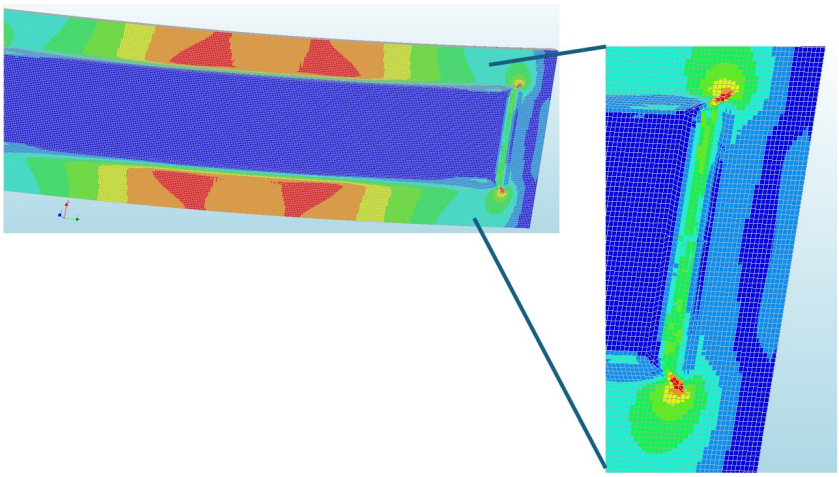

Figure 5.28: The stress state of sample Deep-1, showing high stresses (red) at the edge and low stresses in the web.

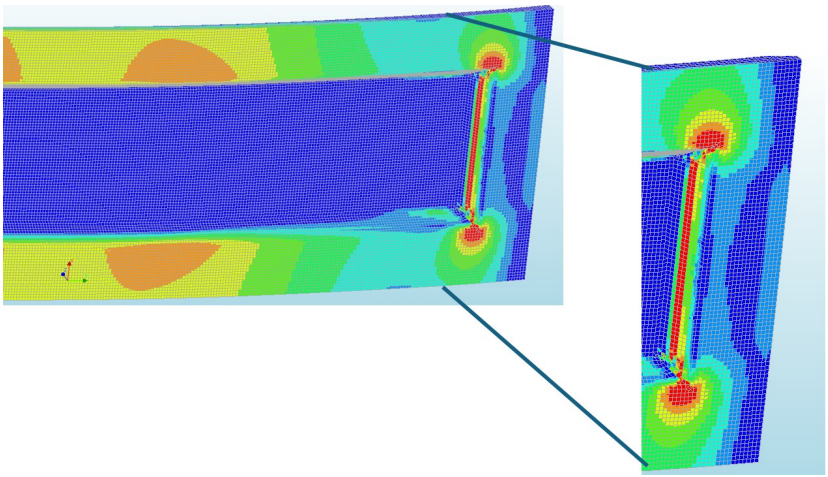

Figure 5.29: The stress state of sample Deep-9, showing lower stresses at the edge and higher stresses (red) in the web.

For a 4mm thick (3.89mm) glass panel, the total laser-forming depth at which this failure mechanism was visible is 12mm, corresponding to a web thickness of 1.25mm.

5.3. Nominal models

This section describes the use of a nominal model instead of individual models to represent every individual sample. The use of a nominal model can be of great benefit when proven to lead to the same results with less time and work needed in the preparation.

Two nominal models are built to represent the shallow samples and the deep samples. The geometries used for these models are described in Table 5.7.

Table 5.7: The geometry of the nominal models

Model	Total height [mm]	Bending angle [mm]	Web thickness [mm]	Sample thickness [mm]	Inertia [mm^4]	Area [mm^2]
Shallow Samples Nominal	6.00	23	3.50	3.89	887	388
Deep Samples Nominal	10	51	2.00	3.89	3791	382

The change in inertia between the nominal models and the individual models is calculated, as well as the deformation difference. Since these two are related, the deformations difference need to result in the inverse of the inertia difference.

The parameters that have been obtained are visualised in Table 5.8. This check is done to see if the Nominal models result in the same deformations obtained in the individual models, when looking only to the inertia difference.

Table 5.8: The differences in geometry of the individual (ind.) and the nominal (nom.) models.

Sample nr.	Individual Inertia [mm^4]	Nominal Inertia [mm^4]	Relative Inertia (I/I)	Individual deformation [mm]	Nominal deformation [mm]	Relative deformation $(w/w)^{-1}$
Shallow-1	785	887	0.89	4.26	3.80	0.89
Shallow-2	801	887	0.90	2.37	2.15	0.91
Shallow-3	837	887	0.94	3.15	2.98	0.95
Shallow-4	738	887	0.83	5.00	4.20	0.84
Shallow-5	843	887	0.95	4.74	4.51	0.95
Shallow-6	2590	887	2.92	1.67	4.63	2.77
Shallow-7	1751	887	1.97	6.2	11.84	1.91
Shallow-8	1004	887	1.13	5.24	5.89	1.12
Shallow-9	787	887	0.89	5.89	5.29	0.90
Shallow-10	821	887	0.93	3.84	3.57	0.93
Deep-1	3591	3791	0.95	2.82	2.7	0.96
Deep-2	3473	3791	0.92	1.31	1.2	0.92
Deep-3	2570	3791	0.68	1.99	1.38	0.69
Deep-4	3071	3791	0.80	1.67	1.37	0.82
Deep-5	3840	3791	1.01	1.40	1.42	1.01
Deep-6	3377	3791	0.89	1.39	1.23	0.91
Deep-7	3904	3791	1.03	1.74	1.78	1.02
Deep-8	4171	3791	1.10	1.34	1.54	1.15
Deep-9	6414	3791	1.69	1.28	1.99	1.55
Deep-10	5670	3791	1.51	2.29	3.33	1.45

The values of the differences in the fourth and seventh column of Table 5.8 need to align to allow the nominal models to be usable. Figures 5.30 and 5.31 show that the difference in inertia of the nominal models against the individual models appears to be of the same magnitude as the inverse difference in deformation. Meaning that, if the inertia of the sample is 2.3 times higher than the inertia of the nominal model, it can be assumed that the deformations of the individual model are 2.3 times less than the nominal model.

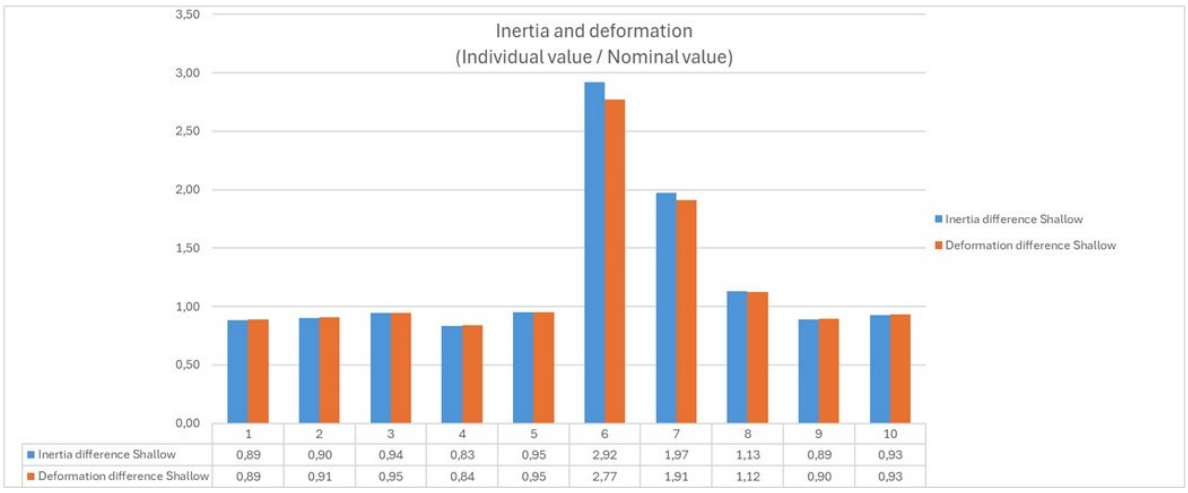

Figure 5.30: The differences in Inertia, next to the inverse difference in deformation of the shallow samples.

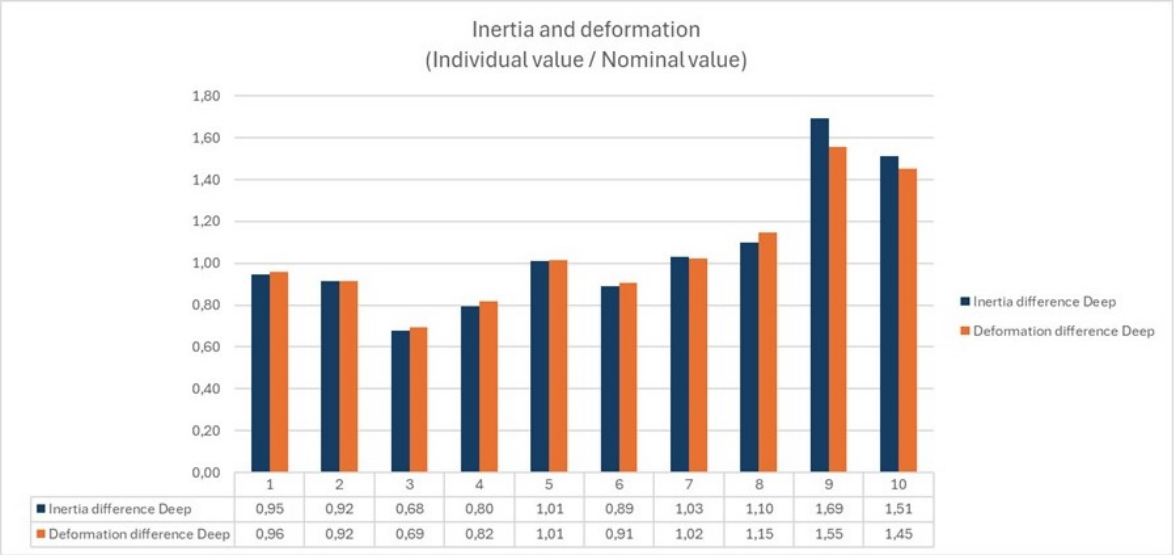

	1	2	3	4	5	6	7	8	9	10
Inertia difference Deep	0,95	0,92	0,68	0,80	1,01	0,89	1,03	1,10	1,69	1,51
Deformation difference Deep	0,96	0,92	0,69	0,82	1,01	0,91	1,02	1,15	1,55	1,45

Figure 5.31: The differences in Inertia, next to the inverse difference in deformation of the deep samples.

It can be concluded that a nominal model can be used to predict the deformations of individual geometries. The procedure starts by computing the inertia of the individual geometry. Secondly the difference compared to the inertia of the nominal model need to be computed. For example, the inertia of the individual geometry is 1.22 times higher than the inertia of the nominal model. The loads need to be applied to the nominal model, the deformations corresponding to these loads are obtained. It can now be said that the deformations of the individual geometry are then 1.22 times less than the obtained deformations of the nominal model.

Sample Deep-9 showed the largest difference of 1.55/1.69 = 0.92. Therefore, the deformations need to take into account an accuracy error of maximum 10% in order to calculate conservatively.

For stresses, individual models are required to be able to predict the failure mechanism and the effect of necking. Individual models are able to show larger stresses in the web because of larger necking. Every geometry need to be modelled with their own necking values, so it can be visualised if the necking is too large and the stresses in the web do occur to be higher than at the edges. A nominal model only shows results where the stresses are lower in the web than at the edge.

6

Case study comparison

This chapter aims to show how the findings of this thesis can be implemented in real sized applications. The increased sizes are hypothetical, since the manufacturing capabilities limit the workable size by $1m^2$. First a comparison is made on the lab tests itself. The configuration used and the sizes used within the tests are compared to a flat panel of glass to visualise the gain in stiffness. Secondly a fictitious case study is used to see how real sized panels should behave, according to the results of the thesis.

6.1. Test setup comparison

A comparison of the laser-formed glass panels to flat glass panels shows the actual performance increase. First, the test-results are used to compare which flat glass thickness results in the same stiffness properties as laser-formed glass. Sample ”Deep-10” is used as a comparison to show to what extent the laser-forming process acts stiffer. Figure 6.1 shows the location of the bends in the cross section at midspan.

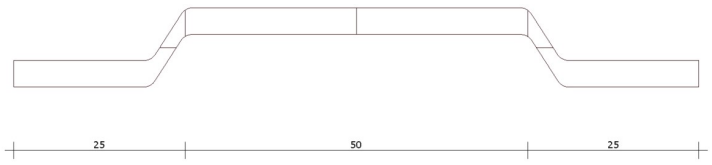

Figure 6.1: Cross section of 3D-laser-formed panel, with the location of the bends.

The test-results of ”Deep-10” showed that a laser-formed sample, subjected to the failure load of 1111N deformed 2.48mm. Multiple FEM-models have been built to check which flat glass thickness results in the same stiffness properties. The flat glass panels were loaded in the same manner and with the same magnitude and the corresponding deformation was checked. The results of these FEM-models compared to ”Deep-10” are stated in Table 6.1.

Table 6.1: Deformations of sample ”Deep-10” compared to various flat glass thicknesses.

Sample (Thickness)	Deformation at point of loading [mm]
Sample ”Deep-10”	2.48
Flat 4mm	23.40
Flat 5mm	11.04
Flat 6mm	6.39
Flat 8mm	2.70
Flat 8.2mm	2.52
Flat 8.3mm	2.43
Flat 10mm	1.39

The table shows that the sample ”Deep-10” had better stiffness properties than a flat 8mm thick panel. The ”Deep-10” panel had an initial thickness of 3.87mm, and the FEM-models used the stated thicknesses of rounded numbers. More thicknesses are checked, and an 8.2mm and 8.3mm thick panel showed corresponding deformations of 2.52mm and 2.43mm.

This concludes that a laser-formed glass panel of 3.87mm performs as stiff as a flat 8.3mm panel, in the setup used during the lab tests. This comparison results in a material reduction of 53%.

6.2. Case study comparison

Using the strategies and findings obtained through this research a fictitious case study has been checked for the applicability of laser-formed glass. The case study is based on larger dimensions and wind-loading acting on the glass surface. The stiffness of flat glass is compared to the stiffness of laser-formed glass to reduce the material use. The dimensions like total height, the web thickness and bending angle are extrapolated from the dimensions used in the lab-tests.

Figure 6.2, shows the visualisation of an upscaled laser-formed glass panel.

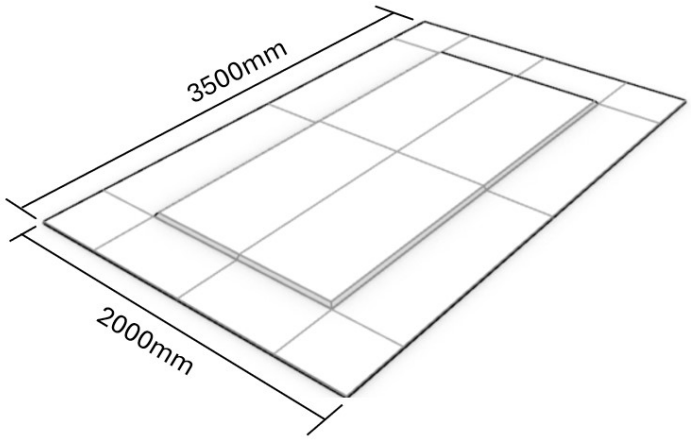

Figure 6.2: 3D-laser-formed panel.

Table 6.2 shows the constraints and loads to which the glass is subjected. For calculation purposes, the panel is simply supported on the top and bottom, and the loading conditions are equal to a building height of 15m in an urban setting in area II of the Netherlands, resulting in a value of 0.80 kN/m^2.

Table 6.2: Constraints of fictitious case study.

Constraint		unit
Height panel	3.50	[m]
Width panel	2	[m]
Wind pressure	0.80	[kN/m^2]

A quick and concise calculation is made to verify that laser-formed glass is actually capable of reducing the material use, while looking at the deformations of a panel. The check is done based on a singular equation corresponding to a distributed load on a simply supported beam:

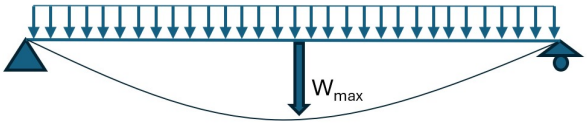

Figure 6.3: A distributed force on a simply supported beam.

$$w_{max} = \frac{5}{384}\frac{ql^4}{EI} \tag{6.1}$$

The total load on the full surface is equal to:

$$q_{total} = 0.8 * 3.50 * 2.00 = 5.6kN \tag{6.2}$$

The load acting in the simply supported beam setup is equal to:

$$q_{total} = 0.8 * 2.00 = 1.6kN/m \tag{6.3}$$

6.2.1. Stiffness (SLS)

The code describes that the maximum allowed deformation, in the middle of the glass panel, is equal to 1/65 * l_{dia} for single glass panels or laminated glass units, as described in equation 2.9 stated in Chapter 2. The maximum allowed deformation is therefore equal to 4031/65 $\leq$ 50 = 50mm.

Setting equation 6.1 equal to 50mm, results in a minimum second moment of area equal to 8.93e5mm^4. This is corresponding to an equivalent thickness of 17.5mm. Since 17.5mm thick glass is not commonly available, the desired thickness can be reached by 19mm thick glass with a design thickness of 18mm.

Laser-forming is able to obtain relatively high inertias with low initial panel thicknesses. Subsection 4.3.3 shows a correction factor of 1.4 is advised for computing Inertias. This means a higher inertia is needed for laser-formed panels, resulting that an inertia of 1.2502e6mm^4 is required.

Table 6.4 shows the geometry used to obtain the required inertia.

Table 6.3: Geometry of fictitious case study.

Constraint		unit
Original thickness	9.7	[mm]
Total height	25.1	[mm]
Thickness web	5.00	[mm]
Bending angle	49	[○]
Width panel	2000	[mm]
Obtained inertia: I	1.2502e6	[mm^4]

Concluding from this small calculation, it confirms the statement that laser-formed glass panels are able to reduce the material use of single panel glass. In this small case-study a flat glass panel of 18mm thick was required to satisfy equation 6.1 and equation 2.9. The thickness that is required when laser-forming is applied is equal to 9.7mm. A material reduction of 46%.

6.2.2. Stresses (ULS)

When comparing the stresses, a simplified calculation is made by checking its Section Modulus (W) and the acting moment based on the applied load. The maximum moment acting on the simply supported panel is equal to:

$$\frac{1}{8} * q * l^2 = \frac{1}{8} * (1.5 * 1.6) * 3.5^2 = 3.68kNm \tag{6.4}$$

Deriving the maximum tensile stress is done with equation 6.5.

$$\sigma_{max} = \frac{M * z}{I} = \frac{M}{W} \tag{6.5}$$

The section modulus of a flat panel is equal to $\frac{1}{6}$*b*h^2.

The glass strength is based on the following considerations:

- Float glass: k_{sp} = 1.0
- Linear calculation: k_a = 1.644 * (3500*2000)$^{1/25}$ = 0.88
- Strength: Annealed: k_e = 0.8
- Load duration 50 years: k_{mod} = 1
- Annealed glass: $f_{g;k}$ = 45 N/mm^2
- Wind is governing load case: $\gamma_{m;A}$ = 1.6

The design value of the bending strength ($f_{mt;u;d}$) of annealed glass is equal to:

$$f_{mt;u;d} = \frac{k_a \times k_e \times k_{mod} \times k_{sp} \times f_{g;k}}{\gamma_{m;A}} = \frac{0.88 * 0.8 * 1 * 1.0 * 45}{1.6} = 19.8N/mm^2 \tag{6.6}$$

Combining equations 6.4, 6.5 and 6.6 results in a required section modulus of: W = 185859 mm^3.

For a flat sample, this section modulus is equal to $\frac{1}{6}$*2000*h^2 where h should have an equivalent thickness equal to: 23.6mm.

The modified laser-formed requires a section modulus equal to 185859 mm. With the following geometry, based on scaling sample ”Deep-10”, the requirements are set. Figure 6.4 shows the cross section and the locations of the bends.

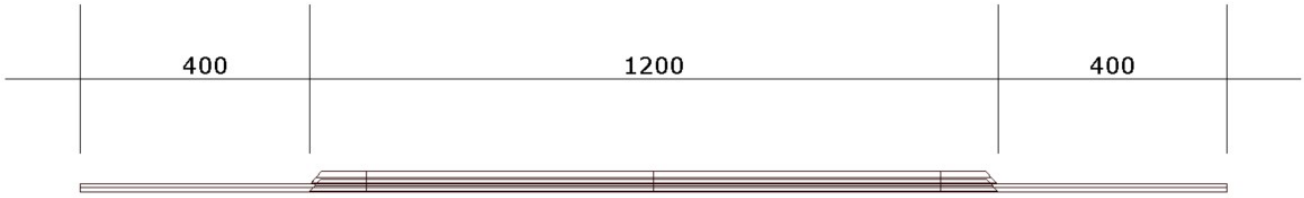

Figure 6.4: Cross section of 3D-laser-formed panel.

Table 6.4: Geometry of fictitious case study.

Constraint		**unit**
Original thickness	14.5	[mm]
Total height	36.5	[mm]
Thickness web	7.64	[mm]
Bending angle	49	[○]
Width panel	2000	[mm]
Obtained Inertia: I	3850000	[mm^4]
Distance to centroidal axis: z	20.22	[mm]
Obtained Section modulus: W	190406	[mm^3]

The parameters are scaled by the original thickness, compared to sample ”Deep-10”. Therefore, the maximum reachable total height = 11.51/3.87 * 14.5 = max 43mm. The minimum web thickness = 2.04/3.87 * 14.5 = 7.64mm. Therefore, in theory, this is achievable with a thickness of 14.5mm thick glass.

The bending stresses would be 3.68 kNm / 190406 mm^3 = 19.3 N/mm^2. This concludes that a laser formed glass panel with an original thickness of 14.5mm, results in similar bending stresses as a flat 23.6mm thick panel. Resulting in a material reduction of 39%.

The lab-tests on the other hand showed hard predictability of the bending stresses. Therefore the beneficial results should be taken with caution. However, theoretically, the laser-formed samples in this comparison do show a benefit in material reduction.

6.2.3. Limitations

The use of laser-formed glass is subjected to multiple limitations. Design considerations like robustness and user safety are not considered in this design comparison. With the use of annealed glass, the fragments when the panel fails are big, and could potentially cause harm when the fragments do fall down. A suggestion for improving the robustness of annealed laser-formed glass with a single ply would be by implementing transparent adhesive foil to reduce the chance of the fragments from falling down. Tempering and laminating the laser-formed glass could solve these limitations, but the technology does not allow for these types of safety yet. Future research should conclude whether these types of safety measures can be implemented for laser-formed glass panels.

7

Discussion

This research shows that the stiffness of laser-formed glass panels is predictable and relates to the increase in inertia of the cross-section. However, the research outcomes show limitations and the results need to be interpreted with caution. This chapter describes the interpretation of the results, the implications, and the limitations of this research. The challenges, constraints and observations regarding the applicability of the results are discussed.

The research question of this thesis is the following: ”What is the structural performance of laser-formed glass panels, when loaded out-of-plane until failure?”. This research shows that the stiffness is directly related to the increase in inertia. Geometry parameters and phenomena, such as necking, have an influence on the predictability of the failure mechanism, whereas DIANA FEA is able to visualise this failure mechanism. Lastly, the findings are that the tested laser-formed panels, with an original thickness of 3.89mm, show similar stiffness properties as 8.3mm flat glass panels. Saving 53% in material use, when observing the stiffness properties.

7.1. Interpretation

This research aimed to contribute to the development and knowledge of laser-formed glass. The structural properties are discussed and conclusions about the stiffness and the strength are constructed. This section describes the interpretation of these findings and how this contributes to the development of the laser-forming process of glass and the applicability to building and structural engineering.

7.1.1. Sensitivity analysis

Flat cross-sections have a poor performance, in a structural sense. To increase its performance, two things can be increased. stiffness and strength. With a stiffer cross-section, smaller deformations can be reached. Meaning a structure, when subjected to a certain load, deforms. The amount of which it deforms relates to the stiffness of the structure. Increasing the stiffness can be achieved by changing the geometry of a cross-section. The second moment of area, or inertia in short, is the geometry parameter that is directly linked to the stiffness of a structure.

Understanding of the behaviour of the stiffness when adjusting the cross-sectional geometry is of importance. The laser-forming process is able to adjust the geometry by editing four parameters: The thickness of the glass, the total height of the elevation, the bending angle and the thickness of the web. By adjusting the geometry parameters, the inertia is changed. The sensitivity analysis gives an answer to the magnitude in which the adjustments do influence the change in inertia.

7.1.2. Lab tests results

Lab-tests are performed to check whether the changes in geometry are visible in real-life behaviour as well. The oven process of laser-forming might alter the structural behaviour of glass. Literature and research development have not yet been able to proof the preservation of stiffness when glass is subjected to the laser-forming process. Lab-tests were able to provide this proof.

The results show that the increase of inertia has a similar trend/pattern as the stiffness of the glass samples during the tests. It is worth discussing that there is still a slight difference in the compared results between the numerically derived inertia increase and the stiffness increase. The effect of extension or compression of other materials and products within the test-setup were not taken into account. In addition, the inertia is based on geometry measured by hand. It might even be a hypothesis that the Young's modulus, which was set at a constant value of 70.000 N/mm^2 changes during longer laser-forming procedures. These two sources of inaccuracy, or the hypothesis, could lead to differences in the comparison between the increase in inertia and stiffness. 3D-scanning of the full sample could eliminate a large part of the measurement inaccuracies to improve the derivation of the inertia terms of each sample.

One sample out of the 20 laser-formed samples showed a different failure mechanism. This sample failed in one of the bends, that was laser-formed, where the other 19 failed from the edges. This singular sample made a significant change in the approach of both the effect of necking and on how the FEM-models should be interpreted. Implying that the edge strength is governing for all samples in this test-setup is not valid due to this single observation.

7.1.3. FEM-results

The use of FEM in this thesis is a method to be able to predict the behaviour of laser-formed glass. The predictability shows its importance when used in engineering. Before manufacturing, the structural behaviour requires to be verified as safe. Predicting the behaviour by utilising FEM leads to checks for the serviceability towards deformations as well as to verify if the product is not subjected by stresses larger than the strength of the material.

The FEM-models showed predictability in two senses. The stiffness showed similar results with the lab-tests data, and the stress state showed insight into the failure mechanisms. The validity of the FEM-models can be discussed. The results show trends and similar behaviour compared to the obtained measurements from the lab-tests. However, for a FEM-model to completely resemble the real-life, the FEM-model itself needs to represent the sample completely. This was not the case, since the 3D-model was modelled based on modelling simplifications and measurements. The results of the FEM are therefore useable, but do not represent the real-life behaviour completely. For 15 out of the 20 laser-formed samples, the samples behaved stiffer dan predicted. The FEM-models do appear to give conservative results. The use of a correction factor of at least 1.2 is able to conservatively predict the stiffness behaviour, since all the less stiff samples were less than 20% of the FEM-models stiffness.

The stress comparison between the FEM-derived stresses and the measured stress obtained from the applied strain gauges, showed that the bending stresses are harder to predict. The FEM-derived values are able to visualise the stress distribution to the user, while the actual stress values should not be taken for the actual present stresses during the tests. The stress-values derived from FEM are higher than the actual present stresses, meaning the calculations are conservative.

The use of nominal models and individual models is checked. Nominal models are able to predict the stiffness of individual geometries, however a maximum difference of 9% is observed. Therefore a correction of 10% should be considered in order to calculate conservatively. However, nominal models are not capable of correctly visualising the failure mechanisms. Therefore the use of individual models is strongly advised, due to the presence of larger necking. Larger necking could lead to different failure mechanisms and individual models are capable of showing this, nominal models are not.

7.1.4. Case study

The case study is set up to be able to upscale the idea of using laser-formed glass in facade panels. The comparison shows that 14.5mm thick laser-formed glass can be applied to a situation where normally an equivalent thickness of 23.6mm thick flat glass was needed. The author is fully aware that this is a major simplification of calculations, however due to time constraints, this is found a simple way to visualise the increase in the stiffness and strength performance by laser-formed glass panels.

7.2. Implications

The results of this thesis describe the implications of the development and understanding of the behaviour of laser-formed glass panels. The ability to predict the behaviour through FEM-analysis, in addition to the findings about the stiffness of laser-formed glass, serves as a basis for further research and development.

The practical implications are that the knowledge gained within this thesis helps the understanding of laser-formed glass. By considering necking as an important factor, designers and engineers are able to design based on a failure mechanism. This research highlights the importance of checking multiple failure mechanisms, like failure from the edges as well as failure within the web of the bend.

For further research perspective, this thesis highlights the performance of one particular design, a single elevation. Optimal designs, might lead to better performances. The geometry is already sufficient to reduce the material use by 53% when looking at the stiffness, while the design used in this thesis is not optimal. Further research and optimal designs might be able to improve the stiffness even better.

7.3. Limitations

This research comes with constraints, assumptions, and limitations. This section describes what has been the observations on the way, and how limitations may influence the gathered results and knowledge.

3D-modelling and measurements

The 3D-model is built to represent the actual samples. The modelling method is subjected to some limitations. Firstly, a challenge is to model completely closed models. This is necessary for DIANA to work with solid FEM-models. The solution of modelling double-curved faces in the modelling phase of this thesis were not found. The decision is made to simplify the model, by applying one curvature instead of two. The modelled curvature is the one that influences the stress-distribution most optimal by judgement of the author. When stressed vertically, the modelled curvature leads to a smoother transition from the top of the sample towards the supports. The non-rounded face has less of an impact in the transition zones.

The dimensions of the geometries are subjected to precision errors. The 3D-model is based on the input of four adjustable parameters: The thickness, the total height, the bending angle, and the web thickness. An observation that introduced inaccuracies in the 3D-model, is that the web thickness is not constant along the whole laser-formed pattern. The modelled geometry is based on the thinnest measured web thickness (to model conservatively towards the stiffness), but thicker web is measured at different positions along the laser-path. All the dimensions are measured with a digital caliper. The measuring is performed with caution, however measuring the total height appeared to be based on how parallel the bottom and the top face were clamped in the caliper. The measurement of the height could vary between a full millimetre, and the final measurement was based on the judgement of the observer.

7.3.1. Sensitivity analysis of geometry parameters

The sensitivity analysis that is performed at the start of the thesis supports statements about the increase of inertia. However, in practice, 4mm thick panels are not able to sag 30mm. In theory, this is possible by the laws of conservation of mass, but at this moment of time, under the current process conditions, this is not feasible. The sensitivity analysis is, on the other hand, useable and gives good insight in how the inertia is affected by which parameter.

7.3.2. Lab-tests

The obtained data from the lab tests, need to be observed with care. The force applied to the sample is assumed to be precise. However, the deformations obtained from the tests, represent the deformation of the press. This results in the fact that the obtained deformation is not exactly the same as the deformation of the sample. In the FEM-modelling the deformation is measured at the location of the load, except the compression of other test-setup elements is not taken into account. The full rigidity of the supports is assumed, where in reality this is resembled as a support with a certain spring stiffness.

The placement of the load-dividing cylinders is done by hand as well. The location of the cylinders was

marked on each sample, with a spacing of 10 centimetres. However, the precision of the placement of the cylinders is prone to inaccuracies.

7.3.3. Sample size

The sample size influences the reliability of the data. Statistical analyses have been performed on three datasets consisting of 4, 10, and 10 samples each. The amount of samples per dataset is slim. The goodness of fit, due to the sample size, of the performed Weibull analysis are questionable. However, the performed tests gave usable results which led to answers of the research questions. More samples were preferred, but due to costs, manufacturing capabilities and time, the author is already satisfied and grateful with the 20 laser-formed samples that have been manufactured and shipped to test.

7.3.4. FEM-modelling

The FEM-modelling is based on assumptions, modelling decisions, and modelling constraints. Creating a model representing real life 100% would be near impossible, although a model is created that is useful. The user of the FEM-models requires to be aware of its limitations and how the FEM-model differs form representing the samples. The first constraint that deviates from real behaviour is the use of supports that are infinitely stiff. The supports used in the lab-tests do have certain stiffness values, which now have been neglected. The second deviation of the real behaviour is the modelling of the loads. The load applying cylinders which rest on the top surface do have a certain contact area. This contact area is now modelled as a single line load. Major consequences of modelling the contact area as a single line have not been observed. The line loads do result in compressive stress concentrations at the exact location of the line, however, the effect on the stiffness is minimal.

Where the stiffness show similar results as the lab-tests, to obtain the correct stresses seemed more difficult. The stresses of the FEM-model resulted to be higher than the actual measured stresses. This is an inaccuracy, however in a conservative way.

The use of nominal models seemed unsuccessful. The models are not capable of visualising different failure mechanisms. There is as well a difference of a maximum of 9% in predicting the stiffness from a nominal model. Due to time constraints, it is not observed where this difference originates. This is a consequence of the nominal models not being useful in the first place.

8

Conclusion

This research aimed to provide knowledge about the structural behaviour of laser-formed glass panels. The main research question is constructed as:

”What is the structural performance of laser-formed glass panels, when loaded out-of-plane until failure?”

To support the main research question, four sub-research questions have been formulated. The conclusions of these sub-questions support the understanding and the final formulation of the conclusion of the main research-question.

Sub-question 1: ”What is the influence of the forming geometry on the inertia and the stress distribution?”

- Four commonly used glass thicknesses have been used as a basis for the sensitivity analysis regarding the geometry. The panels were 4mm, 8mm, 10mm, and 15mm thick. The starting point is a flat panel of glass, a laser-formed elevation is introduced with four different adjustable parameters. The first being the thickness, secondly, the total height after laser-forming, thirdly, the angle of the laser-bend, and lastly, the thickness of the web of the glass after laser-forming. For each configuration the second moment of area, or inertia in short, is numerically computed. The sensitivity analysis showed that for bending angles greater than 45 degrees, the inertia is not influenced as much as with lower bending angles. Reaching higher bending angles relates to thinner webs, making the use of tighter bending corners invaluable for the stiffness. The lab-tests showed that the increase in total height had a quadratic relation to the stiffness. The parallel-axis theorem might be the origin of this phenomenon, this is not further researched but recommended for future work.
- The effect of thinner webs is visible when looking at failure mechanisms. The results of 20 performed lab-tests showed two failure mechanisms. 19 out of the 20 laser-formed samples failed from the edge of the glass panel, relating to poor edge quality. One sample failed from the laser-formed bend. This sample, sample ”Deep-9”, had the thinnest web in the cross-sectional geometry. This showed that the influence of the web thickness is related to the failure mechanism of the glass. The web thickness of sample ”Deep-9” was equal to 1.25mm, a third of the original thickness.
- Because of the two failure modes observed in the tests, a designer or engineer should check laser-formed panels on a minimum of two failure-modes. Other failure mechanisms were not captured in these lab-test. This does not imply the observed failure mechanisms are the only ones to check. By performing more tests, with different geometry configurations, other failure modes might introduce themselves.

Sub-question 2: ”What is the stiffness and strength capacity of out-of-plane loaded glass panels?”

- Twenty laser-formed glass panels were tested and modelled in FEM. The four-point bending tests confirmed the hypothesis that laser-formed glass panels behave more stiff than flat glass panels. The tests showed that laser-formed samples are able to increase the stiffness of a 3.87mm thick flat panel, to stiffness properties similar to that of 8.3mm thick flat panels, an increase of 113%. This conclusion is based on the deformation found in relation to the highest load applied to the sample. Sample ”Deep-10” was subjected to a load of 1111N, resulting in final deformations of 2.48mm. A flat 8.2mm thick glass panel deforms 2.52mm and a flat 8.3mm panel deforms 2.43mm, meaning the Deeep-10 sample, with an original thickness of 3.87mm, had similar stiffness properties as an equivalent 8.3mm thick glass panel.
- Two methods are investigated regarding the predictability of the stiffness of laser-formed panels. The first method is based on the change in inertia, compared to the change in stiffness. The increase in inertia resulted in a similar increase in stiffness. The deeper elevations showed larger deviation, resulting in a maximum deviation of 37%. This deviation needs to be taken care of when designing laser-formed glass structures without the use of predicting FEM-models. A correction factor of 1.4 is advised when the stiffness of the laser-formed panels is derived from only utilising the inertia properties of the cross-section.
- The second method relies on the use of FEM-software to compute the deformations of laser-formed glass panels. FEM showed representable results and for 15 out of 20 samples FEM underestimated the stiffness. This relates to conservative calculations, meaning the samples acted stiffer in real-life compared to the FEM, resulting in lower deformations in real-life. The other five samples overestimated the stiffness, however, the difference is below 17%. A designer or engineer is therefore advised, based on the results of the tests, to use a correction factor of 1.2 toward the obtained FEM deformations. This results in representable but conservative calculated deformations.
- Regarding the derivation of the stresses acting in the laser-formed glass panels, the results of the measured and the FEM-derived stresses show a larger scatter. The results are that FEM is representable to obtain a sense of stress propagation and distribution. The observations were that the stresses obtained with applied strain gauges showed lower stress than the FEM-models, but the distribution showed similar results. Concluding that the FEM-models are able to predict representable stress distribution, and the values of the derived stresses are up to 30% higher than the measured stresses. This concludes that the derivation of the stresses in FEM is conservative.
- FEM-models were used to numerically derive the stress and strength at the location of the failure during the tests. Statistical analyses were performed to obtain a 95% confidence interval and obtain the 5%-fractile value of the shallow and deep sample sets. Weibull distribution plots were made to obtain the following 5%-fractile values of the two datasets. The shallow samples showed a 5%-fractile failure stress of 24N/mm^2. The deep samples showed a 5%-fractile failure stress of 22N/mm^2. These values are obtained from FEM-derived stresses, which does not imply that these were the actual stresses present during the lab-tests. To obtain more certain values of the strength of laser-formed panels, a larger sample size is needed.

Sub-question 3: ”How can the structural behaviour be modelled in DIANA FEA to resemble real life behaviour?”

- Individual DIANA FEA-models were built to represent each sample. The use of DIANA showed similar deformations compared to the lab tests, with a deviation of a maximum of 17%. The stress state obtained with FEM-showed similarity to the measured stresses with strain gauges. The values of the FEM-stresses appeared to be higher than the actual measured stress. This results for designing and engineering purposes, the FEM-derived stresses lead to conservative calculations.
- To check the need for individual models, the results are compared to the use of one nominal model for the shallow samples, as well as the use of one nominal model for the deep samples. Both results show that by utilising the inertia difference, the user is able to convert the obtained FEM-deformations. The obtained FEM-deformations of the nominal model need to be divided by the inverse of the change in inertia, to obtain the value of deformations of the individual model.

The nominal model, on the other hand, is not able to visualise different failure mechanisms. This concludes that there is a need for individual models in order to visualise different failure mechanisms.

- The FEM-models showed the importance of checking two types of failure mechanisms. Sample ”Deep-9” had a different failure mechanism than the 19 other samples. The individual FEM-models were able to capture the deviating stress behaviour of ”Deep-9”, showing higher stresses in the web of the bend, compared to higher stresses in the edges for the other samples. The necking value, and therefore the web thickness of the glass plays a major role in the prediction of this failure mechanism.

Sub-question 4: ”Is laser-forming beneficial for reducing the material use of glass panels?”

- Two case studies have been performed to check hypothetically if laser-forming glass panels result in higher stiffness. The first comparison was made for the situation used in the four-point bending setup during the tests. Sample ”Deep-10” showed the same stiffness properties as an 8.3mm thick flat glass panel. Resulting in the conclusion that when a sample requires to have a stiffness value of 8.3mm thick flat glass, the configuration of sample ”Deep-10” suffices and a material reduction of 53% is achieved.
- The other case study is based on larger scales. A panel of 3.5m x 2.00m that is subjected to windloads is calculated as a flat glass panel and a laser-formed glass panel. As for the stiffness properties, the laser-formed glass panels are able to reduce the material use by 46% in this case study. For strength properties, observing the bending stresses, the laser-formed glass panels are able to reduce the material use by 39%.

The main research question:

”What is the structural performance of laser-formed glass panels, when loaded out-of-plane until failure?”

The answers of the sub-questions are combined and used to answer the main research question. The stiffness of flat glass can be greatly improved by utilising laser-formed glass. The results of four-point bending tests on 20 laser-formed samples showed that the stiffness properties of 3.87mm thick flat glass are improved up to the stiffness properties of 8.3mm flat glass. The use of FEM-models has been proven to represent the actual stiffness behaviour in real-life, when a correction factor of 20% is included to maintain conservativeness in the calculations and not overestimate the stiffness of the real-life samples.

FEM-models are able to obtain stress distributions as well as stress values, although the use of strain gauges showed that these FEM-values were higher than the measured values. The strength obtained through Weibull-analyses is based on numerically derived FEM-stresses, which gave 5%-fractile strengths of 24N/mm^2 for the shallow dataset and 22N/mm^2 for the deep dataset.

This research showed the importance of modelling geometries individually to be able to observe the failure behaviour of laser-formed glass. The necking values and therefore the thickness of the web in the bend area need to be checked cautiously to see whether the stresses in the web outgrow the stresses in the edge of the glass sample.

This research concludes that the use of laser-formed glass significantly improves the stiffness of flat glass panels by a maximum of 215% with the data collected since 8.3mm thick flat glass shows the same stiffness as 3.87mm thick glass. Other optimal geometries might be able to increase this value more. The results are promising to further investigate and develop the knowledge and the use of laser-forming of glass.

9

Recommendations

This research is performed in a time span of 8 months. While being able to answer the main research question, other questions and recommendations arose in the duration of this thesis. Due to limited time and resources, some of these questions could not have been answered yet. This section describes the recommendations towards further research and focus points towards the manufacturing capabilities of laser-formed glass. First the recommendations that follow this specific thesis are stated, where in the other sections the dreams and visions of future applications are described.

Recommendations following up this research
The following recommendations are directly related to the results found in this thesis and can improve the reliability of the results. The stresses during the lab-tests were hard to capture and verify. To be able to tell more precise about the values of the stress and the failure mechanisms, two recommendations are able to improve the validity of the findings. First, Digital Imaging Correlation (DIC) could be implemented to obtain the full stress-state during the test. This technique is able to capture the actual stresses during the test of a whole sample, resulting in reliable results of the full stress-state. Secondly, it is recommended to capture the tests with high speed cameras to locate the exact crack initiation and propagation.

The next recommendation that improves the statements of the thesis is to evaluate the environmental impact of the whole laser-forming process. It is proven that for stiffness, material can be reduced. However, does the reduction in material compensate for the use of a laser-forming oven and the power used to double manufacture the glass?

The design configuration
The first dream/recommendation is based on the design of the samples that have been tested. During this thesis a single elevation is used, where this is not the optimal design. For a more evenly distributed stress-state, different design configurations can lead to even better performances than already found during this thesis. A design following the moment distribution line, based on the load conditions, should already be able to distribute the stresses more evenly. Chapter 3.2 showed two designs, geometry 1 and geometry 2, based on this principle. The relation between the increased height and the stiffness being quadratic, need to be investigated more thoroughly as well.

The influence of necking
The second recommendation is based on the influence of necking regarding the original thickness of the sample. Thicker samples could lead to higher elevations. For 4mm thick glass a total height limit is reached for about 12mm. The experience through manufacturing saw that higher elevations introduced failures during the laser-forming process. The thickness of the web seemed to be too low that the sample failed under its own weight during the process. Further research should give conclusions about the maximum total height that can be achieved for every sample thickness.

A second check that could be achieved in researching this web thickness is to observe at which exact web thickness the failure mechanism changes from failure from the edge to failure from the web. A web

thickness of 1.25mm resulted in a different failure mechanism during this thesis. It is recommended to investigate at what web thickness this phenomenon is the case for other sample thicknesses like 5mm, 6mm, 8mm, 10mm, and 15mm. A study resulting in an answer to the question: ”How far can we go?”.

Robustness and strength

The laser-forming process is at this stage only applicable for single glass panels. To be able to design with structural glass, robustness should be taken care of. Laminating glass is one way of introducing robustness. A major challenge lies ahead when laser-formed glass panels need to be laminated. First, the manufacturing process requires to reproduce the exact desired shape over and over again while minimising the tolerances. Any shape deviations might lead to high stress concentrations, which should be avoided. Research should conclude whether the effect of the geometry differences when laminating results in these high stress concentrations and/or what the effect is on the strength and stiffness.

A second recommendation is to investigate how the strength of laser-formed glass can be increased. Is it possible to heat-strengthen or even fully temper the laser-formed glass, and how do the residual stresses behave in the laser-formed areas?

Regarding the residual stresses, it is worth investigating what the actual residual stress is inside laser-formed glass. When the failure-mode is not at the edge of the glass, the residual stress influences the strength of the surface of the glass. Is it possible to combine tempering in the laser-forming process by adjusting the cooling rate and therefore simultaneously have tempering and laser-forming in one single process?

References

[1] Lenk P., Weber F., and Dodd G. *Structural Glass Walls Gravity and Stability elements*. 2019. URL: https://www.glassmachine.com/structural-glass-walls-gravity-and-stability-elements/ (visited on 05/22/2024).

[2] Glape. *Glape sample*. 2024. URL: https://glape.de/wp-content/uploads/2023/10/5_absenkungen_knick_expanded.jpg.

[3] Marcio Luis Ferreira Nascimento. “Brief history of the flat glass patent - Sixty years of the float process”. In: *World Patent Information* ().

[4] Brandon McNair. *12 Examples of Volcanic Glass Types You Should Know*. 2022. URL: https://geologybase.com/volcanic-glass/.

[5] O’Regan. *Structural Use of Glass in Buildings*. The Institution of Structural Engineers, 2015.

[6] Pilkington. *Crown Process*. 2025. URL: https://www.pilkington.com/en-gb/uk/about/heritage/crown-process.

[7] SCHOTT. *Hot forming out of the melt - Up-draw*. 2025. URL: https://www.schott.com/en-gb/expertise/glass-melting-and-hot-forming?tab=452d7626.

[8] Pilkington. *The float process*. 2025. URL: https://www.pilkington.com/en-gb/uk/architects/information-hub/glass-information/about-glass/the-float-process.

[9] Saint-Gobain. *Technical Information about Glass | Saint-Gobain-Glass*. 2025. URL: https://eg.saint-gobain-glass.com/technical-information-about-glass#batch-plant.

[10] Saint-Gobain. *Overlength | Saint-Gobain-Glass*. 2025. URL: https://www.saint-gobain-glass.com/OVERLENGTH#technical-information.

[11] Saint-Gobain. *Glass forever | Saint-Gobain-Glass*. 2017. URL: https://nl.saint-gobain-building-glass.com/nl/glass-forever.

[12] Belis et al. *Handbook of Glass*. Springer, 2019.

[13] Frederic Veer and Yurii Rodichev. “The strength of glass, hidden damage”. en. In: *Challenging Glass Conference Proceedings* 2 (2010), pp. 395–404. ISSN: 2589-8019. DOI: 10.7480/cgc.2.2428. URL: https://proceedings.challengingglass.com/index.php/cgc/article/view/78 (visited on 02/26/2025).

[14] Matthias Haldimann, Andreas Luible, and Mauro Overend. *Structural Use of Glass*. en. Google-Books-ID: zIjQw1ghHxAC. IABSE, 2008. ISBN: 978-3-85748-119-2.

[15] F. A. Veer, P. C. Louter, and F. P. Bos. “The strength of annealed, heat-strengthened and fully tempered float glass”. en. In: *Fatigue & Fracture of Engineering Materials & Structures* 32.1 (2009). _eprint: https://onlinelibrary.wiley.com/doi/pdf/10.1111/j.1460-2695.2008.01308.x, pp. 18–25. ISSN: 1460-2695. DOI: 10.1111/j.1460-2695.2008.01308.x. URL: https://onlinelibrary.wiley.com/doi/abs/10.1111/j.1460-2695.2008.01308.x (visited on 09/03/2024).

[16] glazingguru. *What is Nickel Sulphide Inclusion?* 2018. URL: https://www.glazingguru.org/uncategorized/nickel-sulphide-inclusion/.

[17] Andreas Kasper. “Spontaneous cracking of thermally toughened safety glass. Part one: Properties of nickel sulphide inclusions”. In: *Glass Structures & Engineering* 4 (Oct. 2019), pp. 1–35. DOI: 10.1007/s40940-018-0083-8.

[18] Moore. *PVB laminated Glass*. URL: https://pvb-film.cn/pvb-laminated-glass/.

[19] Toughglass. *PVB, SGP, EVA interlayers. What is the difference?* Aug. 14, 2019. URL: https://www.toughglass.com.au/pvb-sgp-eva-interlayers-what-is-the-difference/.

[20] Jürgen Neugebauer. “Applications for curved glass in buildings”. en. In: *Journal of Facade Design and Engineering* 2.1-2 (2014), pp. 67–83. ISSN: 2213302X. DOI: 10.3233/FDE-150016. URL: https://www.medra.org/servlet/aliasResolver?alias=iospress&doi=10.3233/FDE-150016 (visited on 05/02/2024).

[21] Maximilian Laurs and Markus Feldmann. “Contribution to the design of cold bent glass”. en. In: *Glass Structures & Engineering* 10.1 (Jan. 2025), p. 2. ISSN: 2363-5150. DOI: 10.1007/s40940-024-00289-6. URL: https://doi.org/10.1007/s40940-024-00289-6 (visited on 02/26/2025).

[22] Migoglass. *What’s the difference between Hot Bent Glass and Bent Tempered Glass?* July 23, 2024. URL: https://www.migoglass.com/info/what-s-the-difference-between-hot-bent-glass-a-97931770.html.

[23] Fraunhofer-Gesellschaft. *Bending sheet glass using lasers and gravity*. en. URL: https://phys.org/news/2017-05-sheet-glass-lasers-gravity.html (visited on 03/20/2025).

[24] Fraunhofer IWM. *How to bend flat glass perfectly around corners*. Oct. 1, 2019. URL: https://www.fraunhofer.de/en/press/research-news/2019/october/how-to-bend-plate-glass-perfectly-around-corners.html.

[25] Wei-Xiang Liao et al. “Innovative laser-assisted glass bending approaches using a near-infrared continuous wave laser”. In: *Optics and Lasers in Engineering* 178 (July 2024), p. 108162. ISSN: 0143-8166. DOI: 10.1016/j.optlaseng.2024.108162. URL: https://www.sciencedirect.com/science/article/pii/S0143816624001416 (visited on 04/30/2024).

[26] Najoua Bolakhrif et al. “Laser-based bending of low-E coated flat glass: a comparative experimental study”. en. In: *Glass Structures & Engineering* 9.2 (June 2024), pp. 201–208. ISSN: 2363-5150. DOI: 10.1007/s40940-024-00263-2. URL: https://doi.org/10.1007/s40940-024-00263-2 (visited on 08/21/2024).

[27] GLAPE GmbH. *Glass forming process with CO2 laser technology*. 2024. URL: https://glape.de/glass-forming-process/.

[28] NEN-EN 1288-1. *NEN-EN 1288-1*. 2016. URL: https://connect.nen.nl/Standard/PopUpHtml?RNR=216872&search=&Native=1&token=9a6cf858-ff02-4e0d-84df-0153e96c9495.

[29] NEN 2608:2014 NL. *NEN 2608:2014 NL*. 2014. URL: https://connect.nen.nl/Standard/PopUpHtml?RNR=199169&search=&Native=1&token=336962bf-c31a-4ede-85ad-bc0ddccebfe6.

[30] T. H. Maiman. “Stimulated Optical Radiation in Ruby”. en. In: *Nature* 187.4736 (Aug. 1960). Publisher: Nature Publishing Group, pp. 493–494. ISSN: 1476-4687. DOI: 10.1038/187493a0. URL: https://www.nature.com/articles/187493a0 (visited on 03/31/2025).

[31] Trotec. *How do lasers work, basics of laser technology laser*. 2016. URL: https://www.trotec laser.com/en/resources/faqs/how-does-a-laser-work.

[32] R. Paschotta. *CO₂ Lasers*. RP Photonics Encyclopedia. Available online at https://www.rp-photonics.com/co2_lasers.html. 2005. DOI: 10.61835/u9k"title="Thislinkwillreloadthecurrentpage.. URL: https://www.rp-photonics.com/co2_lasers.html (visited on 03/31/2025).

[33] Ravi Kant, Parag M. Bhuyan, and S. N. Joshi. “Experimental Studies on TGM and BM Dominated Curvilinear Laser Bending of Aluminum Alloy Sheets”. en. In: *Lasers Based Manufacturing: 5th International and 26th All India Manufacturing Technology, Design and Research Conference, AIMTDR 2014*. Ed. by Shrikrishna N. Joshi and Uday Shanker Dixit. New Delhi: Springer India, 2015, pp. 69–91. ISBN: 978-81-322-2352-8. DOI: 10.1007/978-81-322-2352-8_5. URL: https://doi.org/10.1007/978-81-322-2352-8_5 (visited on 03/31/2025).

[34] Fraunhofer IWM. $Panorama_{B}eschickungseite_{z}ugeschnittenandbersicht_{G}lasbiegeofen$. 2024.

[35] Sylvia Schloeglmann. “Process Optimisation of a Laser-based Glass Shaping Technology”. Master’s thesis. University of Regensburg, Sept. 2024.

[36] Najoua Bolakhrif. *Precision glass bending: craftsmanship meets technology*. en-US. 2024. URL: https://glape.de/ (visited on 03/20/2025).

[37] Freemantle. *Metal roofig sheet*. 2019. URL: https://roofrepairquote.com.au/types-of-roofing-sheets/.

A

Appendix A: Excel of inertia computations

This appendix shows data of all the computed inertias corresponding to different geometries.

Glass thickness	Groove Depth	Bending angle	N	web t [mm]	Inertia I [mm^4]	I without necking	I flat	I/I
4	30	20	0,6	2,8	164277	189814	533	1,155
4	30	25	0,7	2,6	211610	233226	533	1,102
4	30	30	0,8	2,4	239774	259709	533	1,083
4	30	35	0,9	2,2	258231	277385	533	1,074
4	30	40	1	2	271739	290015	533	1,067
4	30	45	1	2	283549	299571	533	1,057
4	30	50	1,1	1,8	291377	307281	533	1,055
4	30	55	1,2	1,6	297765	313683	533	1,053
4	30	60	1,3	1,4	303145	319098	533	1,053
4	30	65	1,4	1,2	307806	323791	533	1,052
4	30	70	1,5	1	311949	327947	533	1,051
4	30	75	1,6	0,8	315721	331700	533	1,051
4	30	80	1,7	0,6	319234	335148	533	1,050
4	30	85	1,8	0,4	322577	338368	533	1,049
4	30	89	1,9	0,2	325016	340821	533	1,049
4	20	20	0,6	2,8	104649	111127	533	1,062
4	20	25	0,7	2,6	115937	121929	533	1,052
4	20	30	0,8	2,4	122780	128596	533	1,047
4	20	35	0,9	2,2	127529	133137	533	1,044
4	20	40	0,9	2,2	131501	136450	533	1,038
4	20	45	1	2	134077	139017	533	1,037
4	20	50	1,1	1,8	136129	141115	533	1,037
4	20	55	1,2	1,6	137825	142859	533	1,037
4	20	60	1,3	1,4	139272	144350	533	1,036
4	20	65	1,4	1,2	140542	145656	533	1,036
4	20	70	1,5	1	141686	146825	533	1,036
4	20	75	1,6	0,8	142740	147892	533	1,036
4	20	80	1,7	0,6	143736	148881	533	1,036
4	20	85	1,8	0,4	144699	149816	533	1,035
4	20	89	1,9	0,2	145406	150535	533	1,035
4	10	20	0,6	2,8	33527	34481	533	1,028
4	10	25	0,6	2,8	34728	35541	533	1,023
4	10	30	0,7	2,6	35408	36220	533	1,023
4	10	35	0,8	2,4	35879	36697	533	1,023
4	10	40	0,9	2,2	36228	37053	533	1,023
4	10	45	1,1	1,8	36428	37334	533	1,025
4	10	50	1,1	1,8	36721	37567	533	1,023
4	10	55	1,1	1,8	36969	37764	533	1,022
4	10	60	1,2	1,6	37125	37935	533	1,022
4	10	65	1,3	1,4	37264	38087	533	1,022
4	10	70	1,4	1,2	37392	38224	533	1,022
4	10	75	1,5	1	37512	38351	533	1,022
4	10	80	1,6	0,8	37626	38471	533	1,022
4	10	85	1,7	0,6	37739	38585	533	1,022
4	10	89	1,8	0,4	37821	38673	533	1,023
8	30	20	1,1	5,8	355233	405812	4267	1,142
8	30	25	1,3	5,4	445843	490101	4267	1,099
8	30	30	1,5	5	499676	541290	4267	1,083
8	30	35	1,7	4,6	534945	575533	4267	1,076
8	30	40	1,9	4,2	559640	600112	4267	1,072
8	30	45	2	4	580468	618757	4267	1,066
8	30	50	2,2	3,6	595274	633505	4267	1,064
8	30	55	2,4	3,2	607301	645572	4267	1,063
8	30	60	2,6	2,8	617387	655730	4267	1,062
8	30	65	2,8	2,4	626090	664489	4267	1,061
8	30	70	2,9	2,2	634983	672204	4267	1,059
8	30	75	3,1	1,8	641910	679149	4267	1,058
8	30	80	3,3	1,4	648345	685659	4267	1,058
8	30	85	3,6	0,8	653452	691722	4267	1,059
8	30	89	3,8	0,4	657858	696331	4267	1,058
8	20	20	1,1	5,8	224882	239962	4267	1,067
8	20	25	1,3	5,4	246445	260770	4267	1,058
8	20	30	1,5	5	259472	273631	4267	1,055
8	20	35	1,7	4,6	268101	282399	4267	1,053
8	20	40	1,8	4,4	275179	288804	4267	1,050
8	20	45	2,1	3,8	279419	293733	4267	1,051
8	20	50	2,2	3,6	283832	297683	4267	1,049
8	20	55	2,3	3,4	287481	300956	4267	1,047
8	20	60	2,5	3	290123	303745	4267	1,047
8	20	65	2,6	2,8	292870	306179	4267	1,045
8	20	70	2,8	2,4	294918	308349	4267	1,046
8	20	75	3	2	296804	310322	4267	1,046

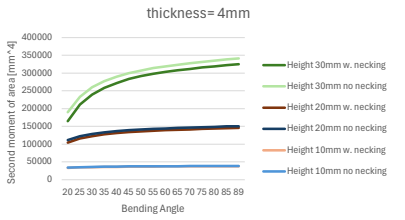

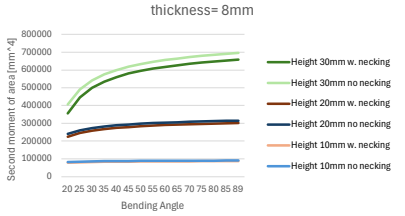

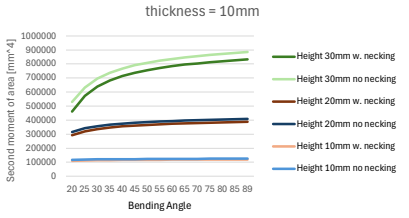

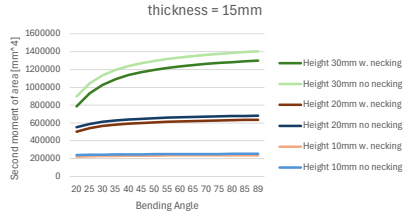

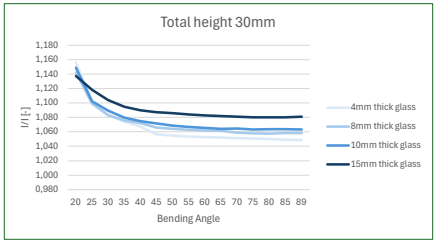

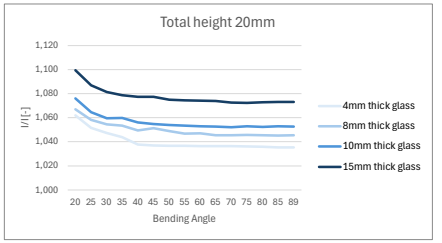

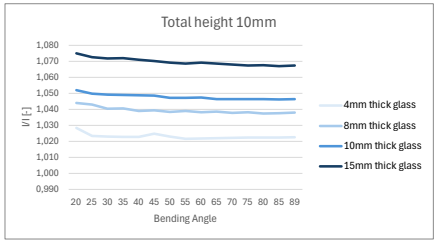

8	20	80	3,2	1,6	298581	312145	4267	1,045
8	20	85	3,4	1,2	300293	313857	4267	1,045
8	20	89	3,6	0,8	301512	315192	4267	1,045
8	10	20	1,1	5,8	79044	82521	4267	1,044
8	10	25	1,3	5,4	81063	84546	4267	1,043
8	10	30	1,4	5,2	82502	85843	4267	1,040
8	10	35	1,6	4,8	83370	86752	4267	1,041
8	10	40	1,7	4,6	84151	87433	4267	1,039
8	10	45	1,9	4,2	84627	87967	4267	1,039
8	10	50	2	4	85130	88403	4267	1,038
8	10	55	2,2	3,6	85442	88770	4267	1,039
8	10	60	2,3	3,4	85814	89089	4267	1,038
8	10	65	2,5	3	86049	89371	4267	1,039
8	10	70	2,6	2,8	86355	89626	4267	1,038
8	10	75	2,8	2,4	86555	89862	4267	1,038
8	10	80	2,9	2,2	86830	90082	4267	1,037
8	10	85	3,1	1,8	87021	90293	4267	1,038
8	10	89	3,3	1,4	87147	90457	4267	1,038
10	30	20	1,4	7,2	460186	528685	8333	1,149
10	30	25	1,6	6,8	573832	632471	8333	1,102
10	30	30	1,9	6,2	638343	695364	8333	1,089
10	30	35	2,1	5,8	682904	737403	8333	1,080
10	30	40	2,3	5,4	714170	767566	8333	1,075
10	30	45	2,5	5	737610	790429	8333	1,072
10	30	50	2,7	4,6	756416	808502	8333	1,069
10	30	55	2,9	4,2	771681	823285	8333	1,067
10	30	60	3,1	3,8	784471	835727	8333	1,065
10	30	65	3,3	3,4	795490	846459	8333	1,064
10	30	70	3,6	2,8	803948	855915	8333	1,065
10	30	75	3,8	2,4	812834	864406	8333	1,063
10	30	80	4,1	1,8	819906	872161	8333	1,064
10	30	85	4,4	1,2	826642	879355	8333	1,064
10	30	89	4,6	0,8	832322	884799	8333	1,063
10	20	20	1,4	7,2	293354	315643	8333	1,076
10	20	25	1,6	6,8	320475	341162	8333	1,065
10	20	30	1,8	6,4	336872	356916	8333	1,060
10	20	35	2,1	5,8	346859	367644	8333	1,060
10	20	40	2,2	5,6	355561	375472	8333	1,056
10	20	45	2,4	5,2	361683	381491	8333	1,055
10	20	50	2,6	4,8	366540	386311	8333	1,054
10	20	55	2,8	4,4	370535	390303	8333	1,053
10	20	60	3	4	373927	393704	8333	1,053
10	20	65	3,2	3,6	376890	396671	8333	1,052
10	20	70	3,4	3,2	379545	399317	8333	1,052
10	20	75	3,7	2,6	381538	401721	8333	1,053
10	20	80	3,9	2,2	383853	403945	8333	1,052
10	20	85	4,2	1,6	385673	406035	8333	1,053
10	20	89	4,4	1,2	387279	407636	8333	1,053
10	10	20	1,3	7,4	110048	115764	8333	1,052
10	10	25	1,5	7	112627	118233	8333	1,050
10	10	30	1,7	6,6	114197	119811	8333	1,049
10	10	35	1,9	6,2	115266	120917	8333	1,049
10	10	40	2,1	5,8	116086	121743	8333	1,049
10	10	45	2,3	5,4	116717	122391	8333	1,049
10	10	50	2,4	5,2	117386	122920	8333	1,047
10	10	55	2,6	4,8	117796	123365	8333	1,047
10	10	60	2,8	4,4	118152	123751	8333	1,047
10	10	65	2,9	4,2	118599	124092	8333	1,046
10	10	70	3,1	3,8	118883	124401	8333	1,046
10	10	75	3,3	3,4	119154	124686	8333	1,046
10	10	80	3,5	3	119417	124953	8333	1,046
10	10	85	3,7	2,6	119678	125208	8333	1,046
10	10	89	3,9	2,2	119852	125406	8333	1,046
15	30	20	1,8	11,4	787151	895464	28125	1,138
15	30	25	2,4	10,2	934764	1045300	28125	1,118
15	30	30	2,8	9,4	1028300	1135500	28125	1,104
15	30	35	3,1	8,8	1092000	1195700	28125	1,095
15	30	40	3,4	8,2	1136500	1238700	28125	1,090
15	30	45	3,7	7,6	1169200	1271200	28125	1,087
15	30	50	4	7	1194200	1296800	28125	1,086

15	30	55	4,3	6,4	1215300	1317700	28125	1,084
15	30	60	4,6	5,8	1233000	1335300	28125	1,083
15	30	65	4,9	5,2	1248200	1350400	28125	1,082
15	30	70	5,2	4,6	1261600	1363700	28125	1,081
15	30	75	5,5	4	1273600	1375600	28125	1,080
15	30	80	5,8	3,4	1283300	1386400	28125	1,080
15	30	85	6,3	2,4	1292600	1396500	28125	1,080
15	30	89	6,7	1,6	1298700	1404100	28125	1,081
15	20	20	2,1	10,8	502501	552522	28125	1,100
15	20	25	2,4	10,2	541780	588972	28125	1,087
15	20	30	2,7	9,6	565341	611373	28125	1,081
15	20	35	3	9	580858	626565	28125	1,079
15	20	40	3,3	8,4	591740	637611	28125	1,078
15	20	45	3,6	7,8	599715	646075	28125	1,077
15	20	50	3,8	7,4	607259	652835	28125	1,075
15	20	55	4,1	6,8	612706	658419	28125	1,075
15	20	60	4,4	6,2	617314	663164	28125	1,074
15	20	65	4,7	5,6	621332	667295	28125	1,074
15	20	70	4,9	5,2	625601	670970	28125	1,073
15	20	75	5,2	4,6	628879	674304	28125	1,072
15	20	80	5,6	3,8	631376	677380	28125	1,073
15	20	85	6	3	633830	680266	28125	1,073
15	20	89	6,3	2,4	635910	682474	28125	1,073
15	10	20	1,9	11,2	222391	239051	28125	1,075
15	10	25	2,2	10,6	226120	242517	28125	1,073
15	10	30	2,5	10	228321	244721	28125	1,072
15	10	35	2,8	9,4	229705	246259	28125	1,072
15	10	40	3	9	231023	247405	28125	1,071
15	10	45	3,2	8,6	232013	248302	28125	1,070
15	10	50	3,4	8,2	232896	249032	28125	1,069
15	10	55	3,6	7,8	233628	249646	28125	1,069
15	10	60	3,9	7,2	233983	250177	28125	1,069
15	10	65	4,1	6,8	234560	250646	28125	1,069
15	10	70	4,3	6,4	235089	251069	28125	1,068
15	10	75	4,5	6	235589	251459	28125	1,067
15	10	80	4,8	5,4	235863	251824	28125	1,068
15	10	85	5	5	236356	252172	28125	1,067
15	10	89	5,3	4,4	236490	252442	28125	1,067

B

Appendix B: Grasshopper script 3D-models

This appendix shows the grasshopper script that is made to model the 3D-geometries.

Appendix B: Final Grasshopper script used for FEM-modelling

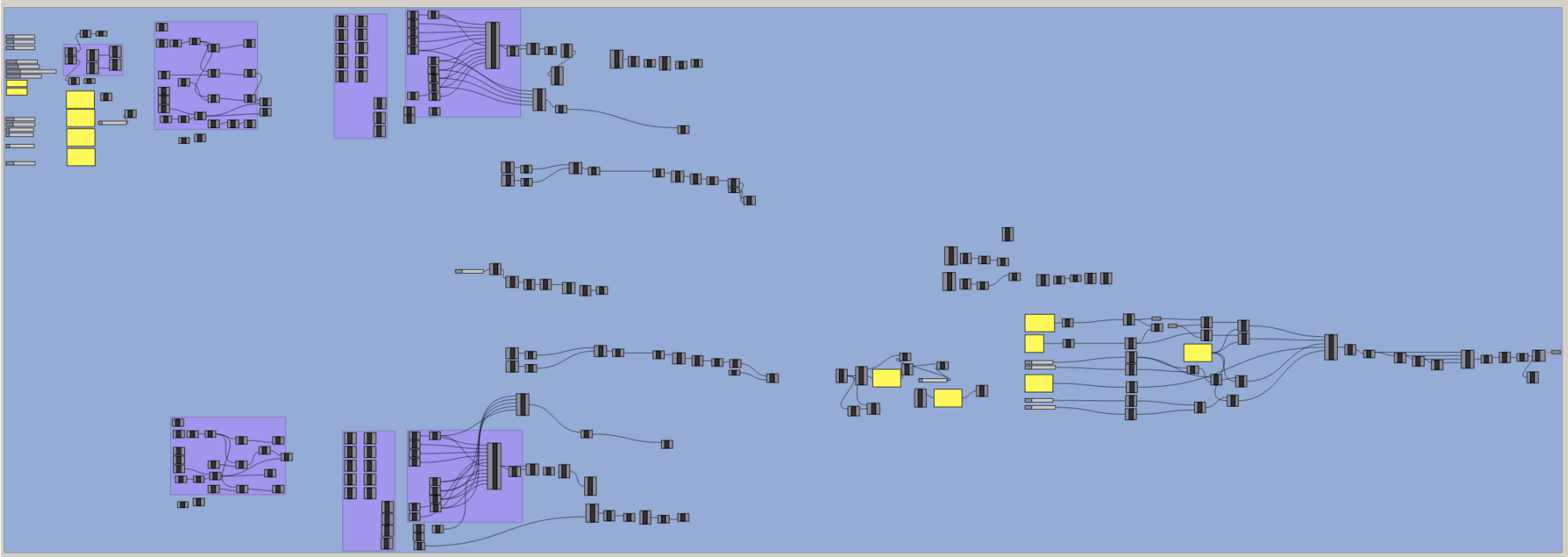

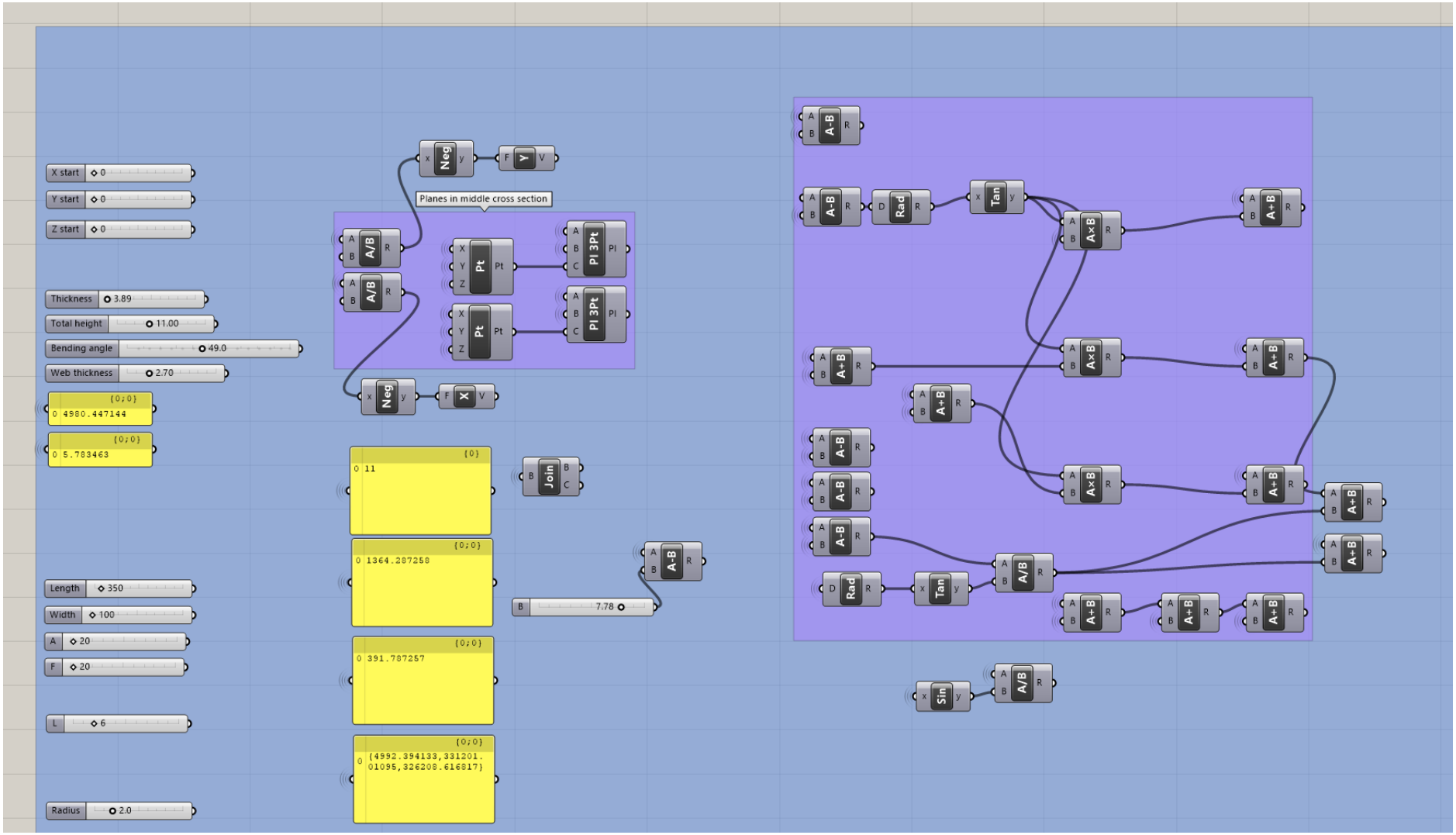
X start 0
Y start 0
Z start 0
Thickness 3.89
Total height 11.00
Bending angle 49.0
Web thickness 2.70
{0;0}
0 4980.447144
{0;0}
0 5.783463
Length 350
Width 100
A 20
F 20
L 6
Radius 2.0
Neg
Y
Planes in middle cross section
A/B
Pt
Pl 3Pt
Neg
X
{0}
0 11
Join
{0;0}
0 1364.287258
{0;0}
0 391.787257
{0;0}
0 {4992.394133,331201.01095,326208.616817}
A-B
7.78
Rad
Tan
A×B
A+B
Sin

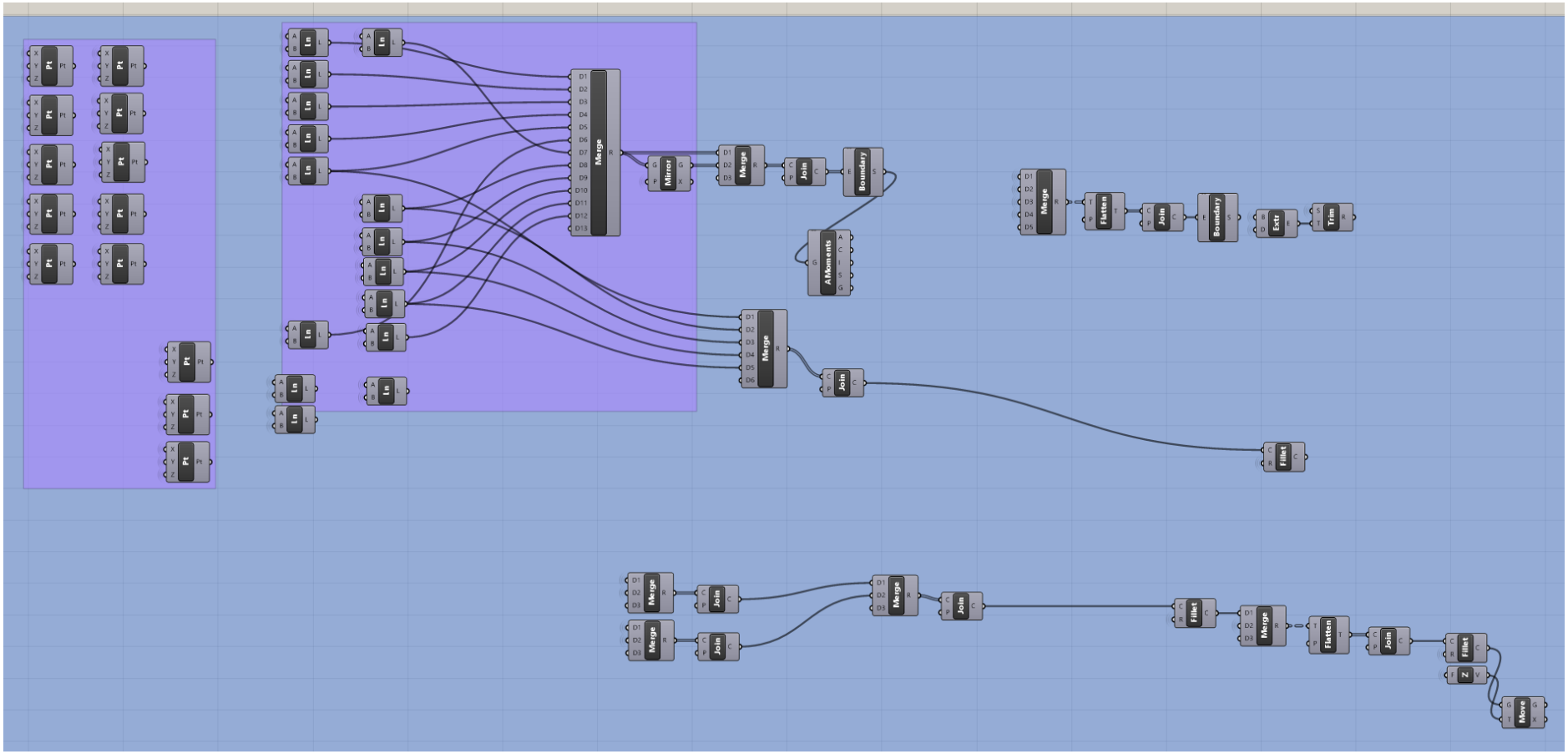
Pt
In
Merge
Mirror
Join
Boundary
AMoments
Flatten
Extr
Trim
Fillet
Move

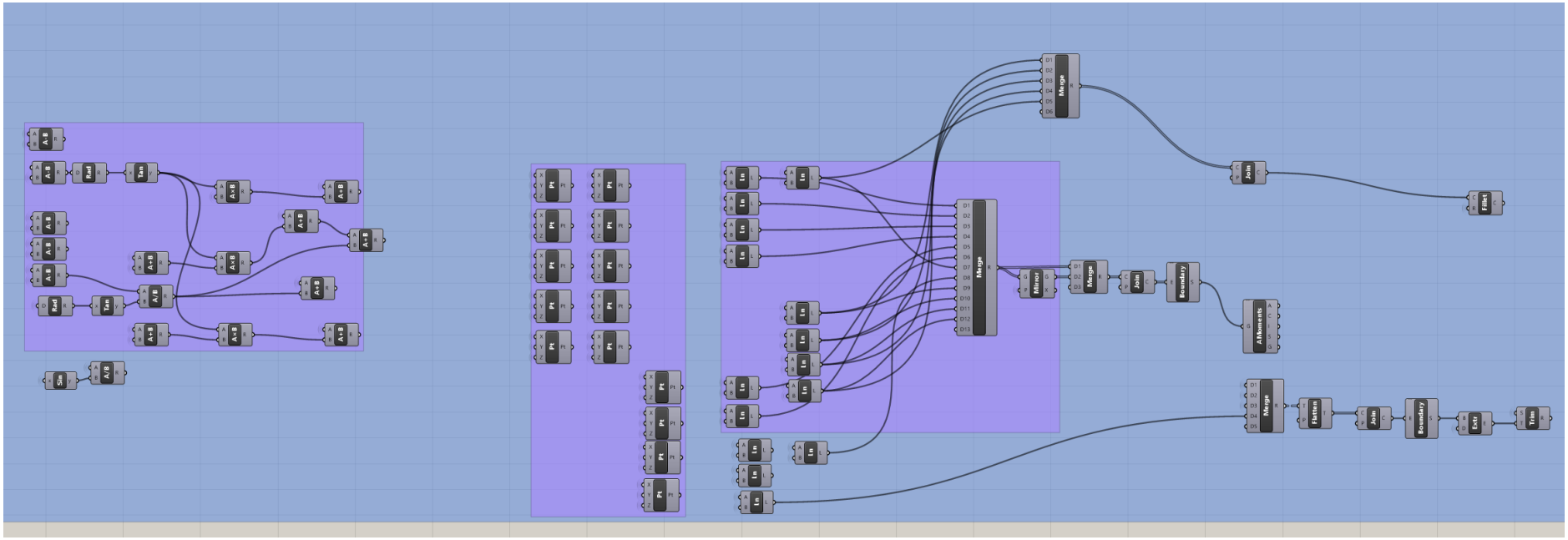
A+B
Rad
Tan
Sin
A/B
Pt
Ln
Merge
Mirror
Join
Boundary
AMoments
Fillet
Flatten
Explode
Trim

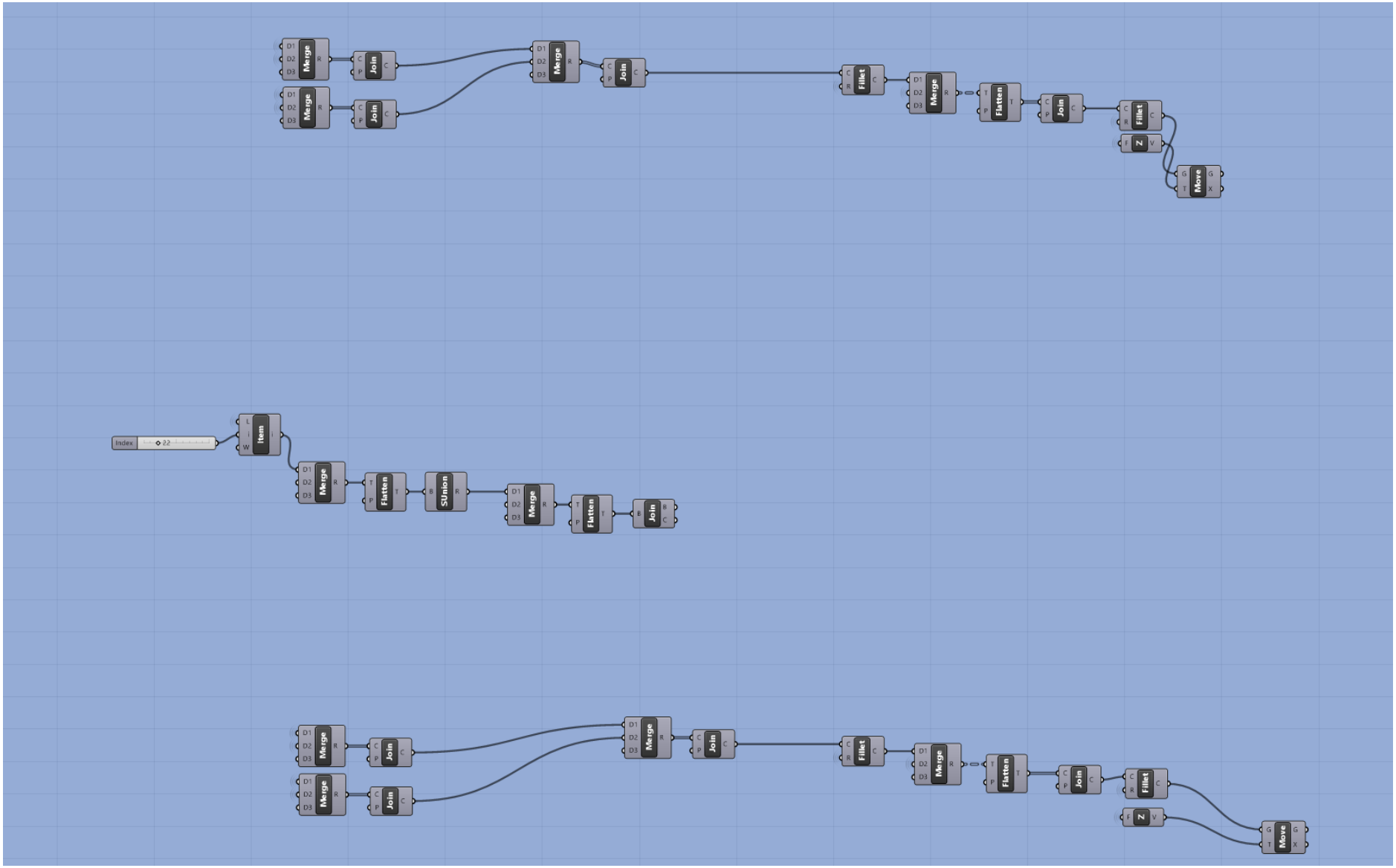
Merge
Join
Merge
Join
Merge
Join
Fillet
Merge
Flatten
Join
Fillet
Z
Move
Index
22
Item
Merge
Flatten
SUnion
Merge
Flatten
Join
Merge
Join
Merge
Join
Fillet
Merge
Flatten
Join
Fillet
Z
Move

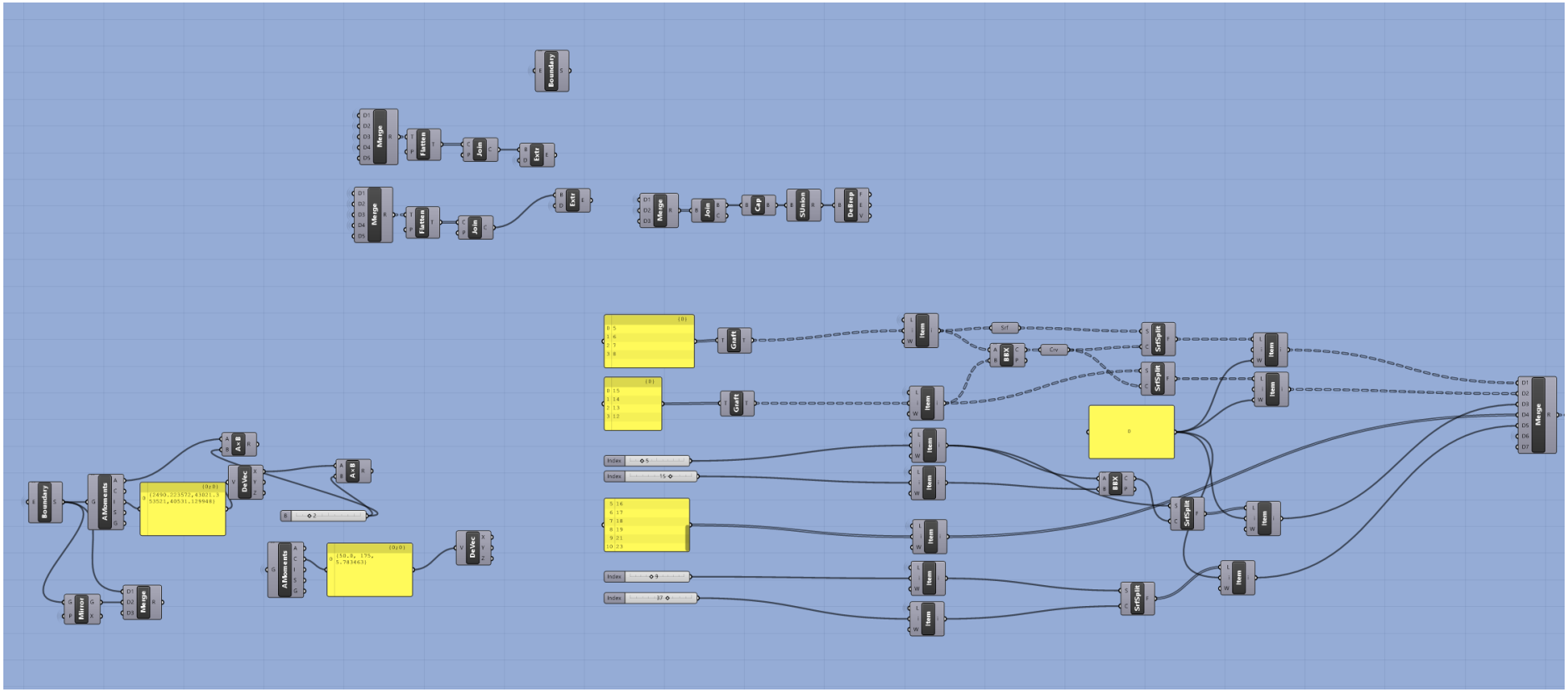
Boundary
Merge
Flatten
Join
Extr
Merge
Flatten
Join
Extr
Merge
Join
Crv
Slnsn
DsBrep
{0}
Graft
Item
Srf
BBX
Crv
SrfSplit
SrfSplit
Item
Item
{0}
Graft
Item
Item
Item
Index
Index
BBX
SrfSplit
Item
Item
{5;16;17;18;19;21;23}
Index
Index
Item
Item
SrfSplit
Item
Merge
A+B
A-B
DeVec
{0;0}
{2490.323572,43021.383521,40531.129948}
Boundary
AMoments
Mirror
Merge
AMoments
{0;0}
{50.0, 175, 5.7834463}
DeVec

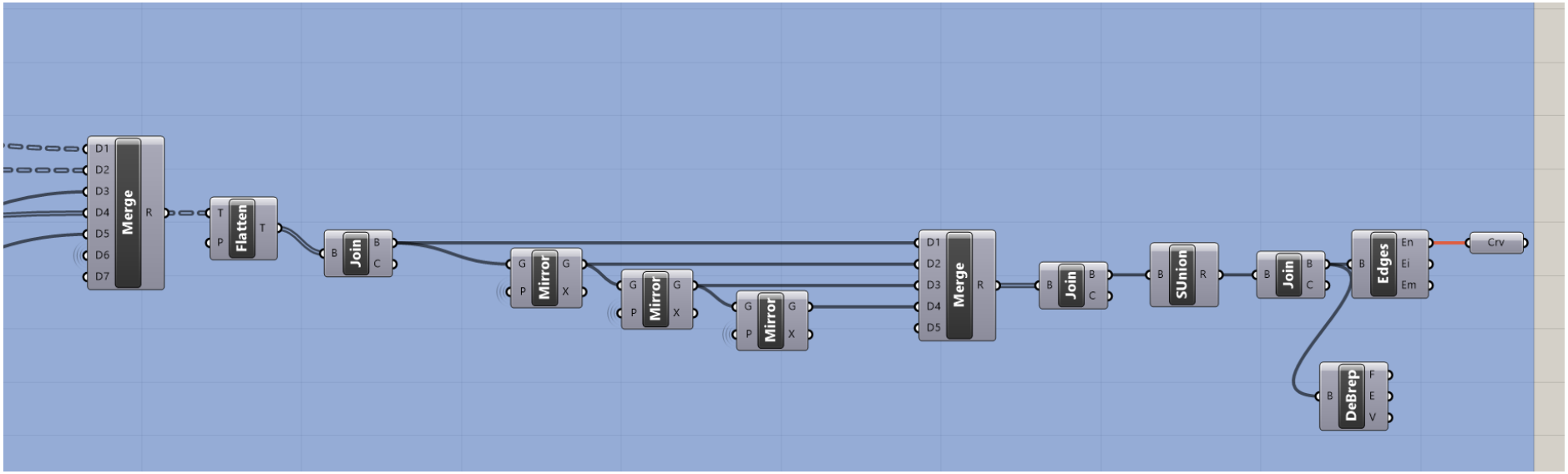
D1
D2
D3
D4
D5
D6
D7
Merge
R
T
P
Flatten
T
B
Join
B
C
G
P
Mirror
G
X
G
P
Mirror
G
X
G
P
Mirror
G
X
D1
D2
D3
D4
D5
Merge
R
B
Join
B
C
B
SUnion
R
B
Join
B
C
B
Edges
En
Ei
Em
Crv
B
DeBrep
F
E
V

C

Appendix C: Properties of Instron machine - Four-point bending test

INSTRON®

The difference is measurable®

8872 SERVOHYDRAULIC FATIGUE TESTING SYSTEM

25 kN

The Instron® 8872 is a compact tabletop servohydraulic testing system that meets the challenging demands of various static and dynamic testing requirements. With the actuator in the upper crosshead and a lower t-slot table, the 8872 makes an ideal platform for a variety of medical devices, biomaterials, advanced materials, and other component testing.

FEATURES

- Double-acting servohydraulic actuator with force capacity up to ±25 kN (±5620 lbf)
- High-stiffness, precision-aligned load frame with twin columns and actuator in upper crosshead
- 100 mm (4 in) of usable stroke
- Designed for both dynamic and static testing on a variety of materials and components
- Choice of hydraulic configuration and dynamic performance to suit application
- Adjustable upper crosshead with hydraulic lifts and manual locks fitted as standard for easy adjustment of daylight
- Patented$_1$ Dynacell™ load cell technology for faster testing and reduction of inertial errors
- Compact tabletop servohydraulic fatigue testing system – frame requires less than 0.4 m² (4.3 ft²) of space
- Hydrostatic bearing actuators for higher side-load resistance or material critical applications, such as low-cycle fatigue
- Designed to be used with the 3520 Series of Hydraulic Power Units
- Compatible with a large range of grips, fixtures, chambers, video extensometers, protective shields, and other accessories
- Patented stiffness based tuning algorithm that enables users to tune a variety of specimens in seconds

CONTROLLER AND SOFTWARE

The Instron 8872 is supplied with a digital 8800MT controller that provides full system control including features such as stiffness based tuning, amplitude control, specimen protect, 19-bit resolution across the full range of transducers,and adaptive control technology. It also allows access to WaveMatrix 2 Dynamic Testing Software, Bluehill® Software for static tests and other application specific software, such as the Fracture Mechanics suite.

FRAME SPECIFICATIONS

Daylight Opening (Maximum Between Load Cell and Actuator at Mid-stroke, with Largest Capacity Actuator)	mm	1017
	in	40
Dynamic Load Capacity	kN	±25
	lbf	±5620
Actuator Stroke (Total)	mm	100
	in	4
Actuator Force Rating	kN	25
Configuration		Twin-Column High-Stiffness Load Frame with Actuator in Upper Crosshead and T-Slot Base
Lift and Locks		Hydraulically-Powered Lifts and Locks
Load Cell		Patented[1] Dynacell™ Fatigue-RatedLoad Cell with Capacity to Suit Actuator
Load Weighing Accuracy		±0.002% of Load Cell Capacity or 0.5% of Indicated Load, Whichever is Greater - Down to 1/250th of Full Scale
Hydraulic Pressure Supply (Required)	bar	207
	psi	3000
Electrical Supply		Single-Phase Mains 90-132 or 180-264 V 45/65 Hz with Power Consumption 800 VA Max
Operating Environment		+10 to +38 °C (+50 to +100 °F) with 10 to 90% Humidity Non-Condensing
Frame Stiffness	kN/mm	260
Maximum Frame Weight (Dependant on Final Configuration)	kg	287
	lb	634

MECHANICAL INTERFACE

Load Cell	M20 × 1.5 Right Hand Central Thread
Actuator	M20 × 1.5 Right Hand Central Thread
Table and Crosshead	4 × M10 Holes on a 280 mm × 90 mm for Accessory Mounting 6 × M10 × 20 Deep on 100 mm PCD (Table) with 40 mm Location Diameter 4 × M10 T-Slots Running Front and Back, Spaced 80 and 100 mm From Center Line

ACCESSORIES

2742-301	±30 kN Fatigue-Rated Hydraulic Wedge Grips
2780-118	Fracture Mechanics Grips for 12.5 mm Wide Compact Tension Specimen
2810-181	3-Point Fatigue-Rated Bend Fixture
2810-184	4-Point Conversion Kit for 2810-181
2840-119	150mm (6 in) Diameter Compression Platens

1) US Patent Number 6508132

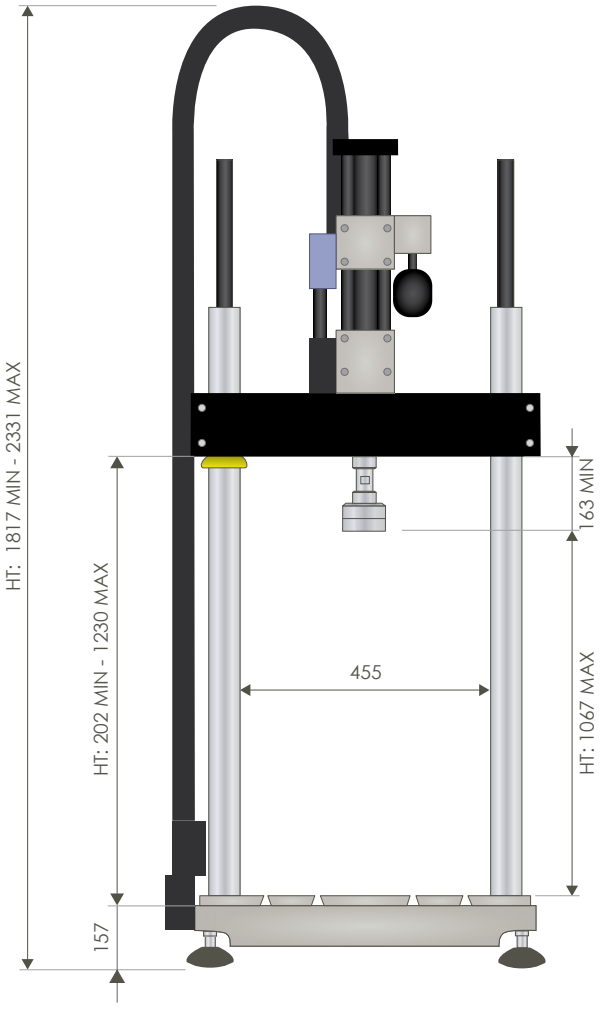

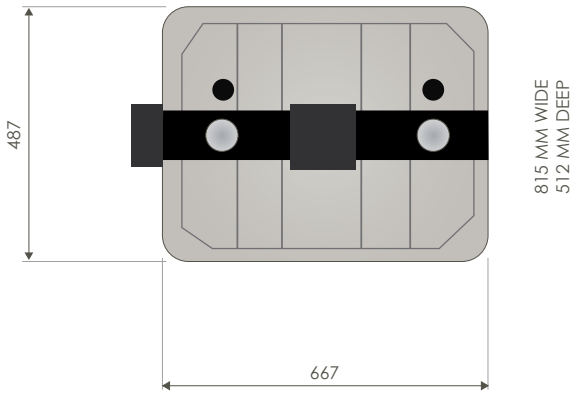

Instron® 8872 Dimensions (All Dimensions in mm)

www.instron.com

INSTRON®

Worldwide Headquarters
825 University Ave, Norwood, MA 02062-2643, USA
Tel: +1 800 564 8378 or +1 781 575 5000

European Headquarters
Coronation Road, High Wycombe, Bucks HP12 3SY, UK
Tel: +44 1494 464646

D

Appendix D: Images of failure fragmentation

This appendix shows all the fragmentation images of the samples that were tested.

Appendix D: Images of failure fragmentation

Sample Flat -1

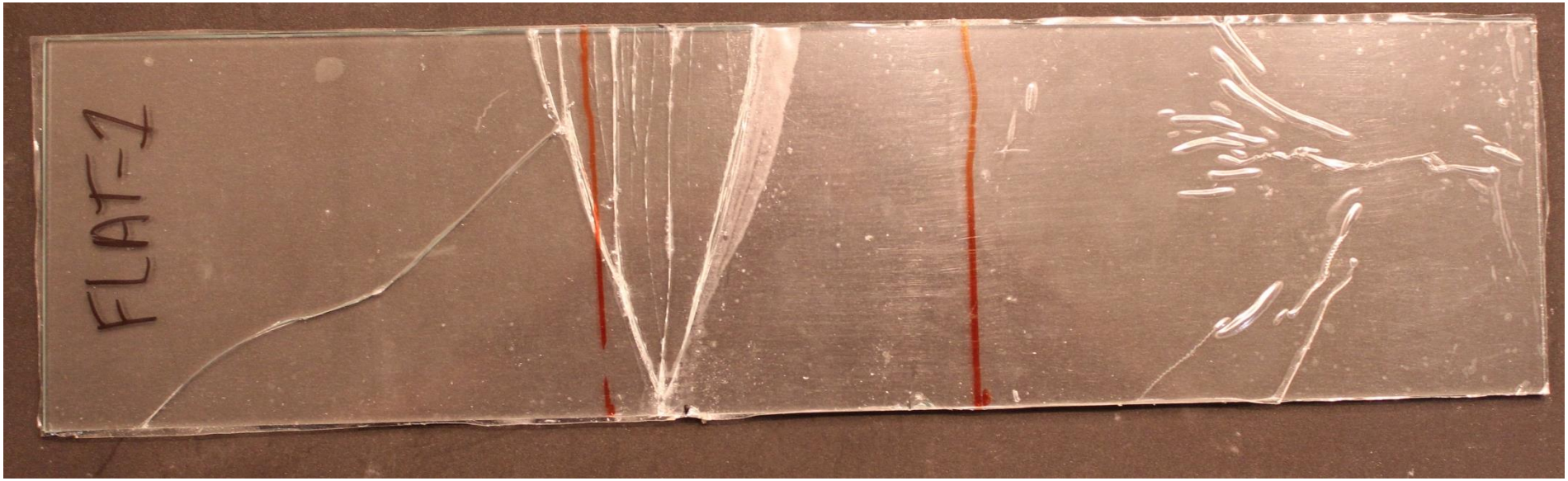

Sample Flat -2

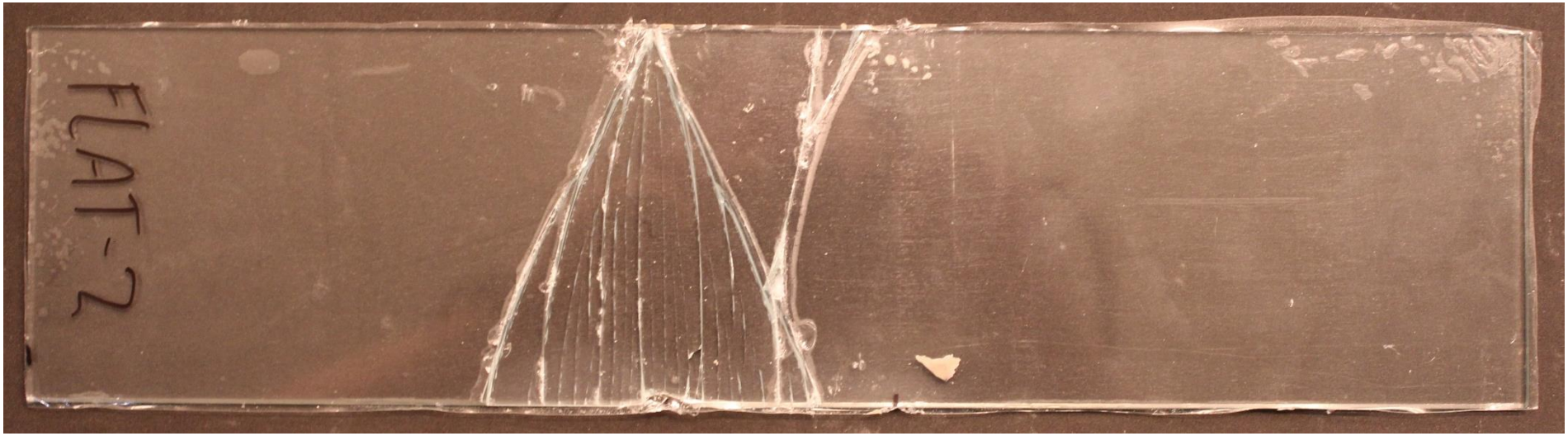

Sample Flat -3

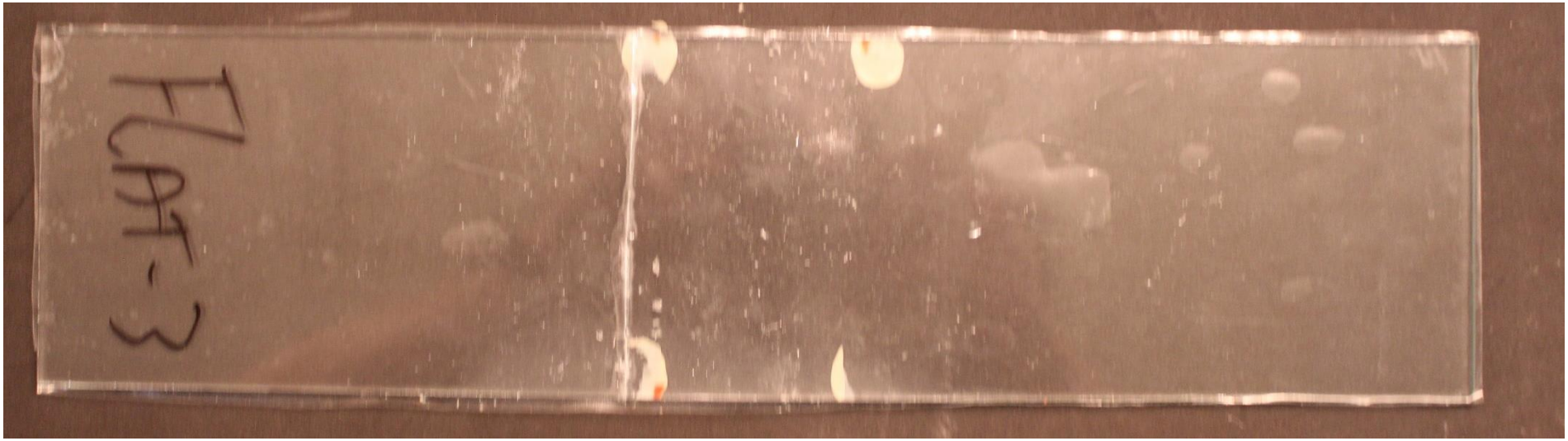

Sample Flat -4

Sample Shallow-1

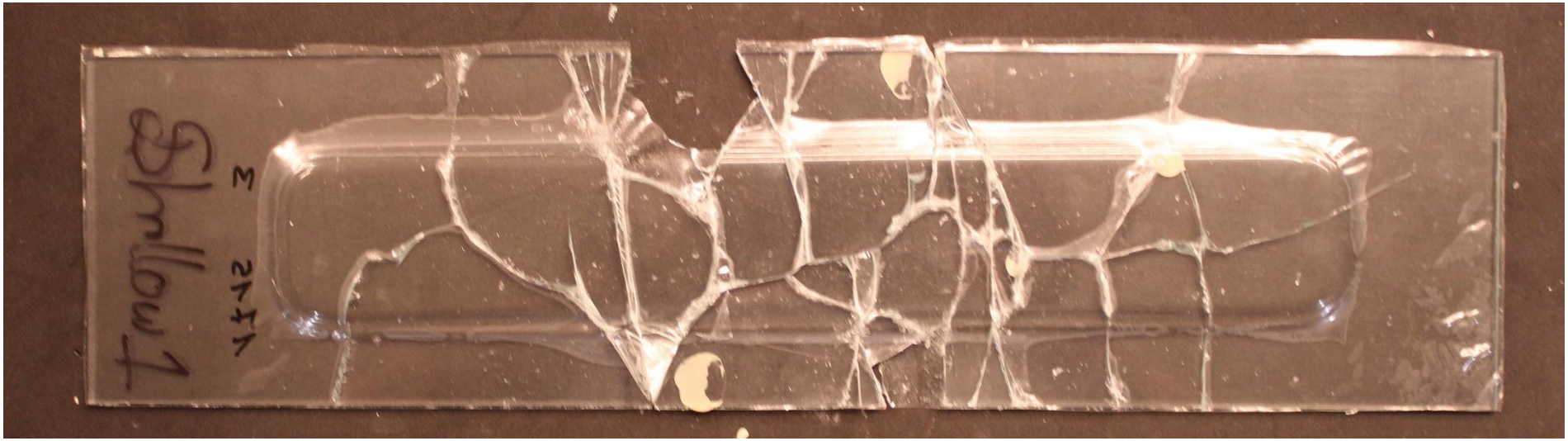

Sample Shallow-2

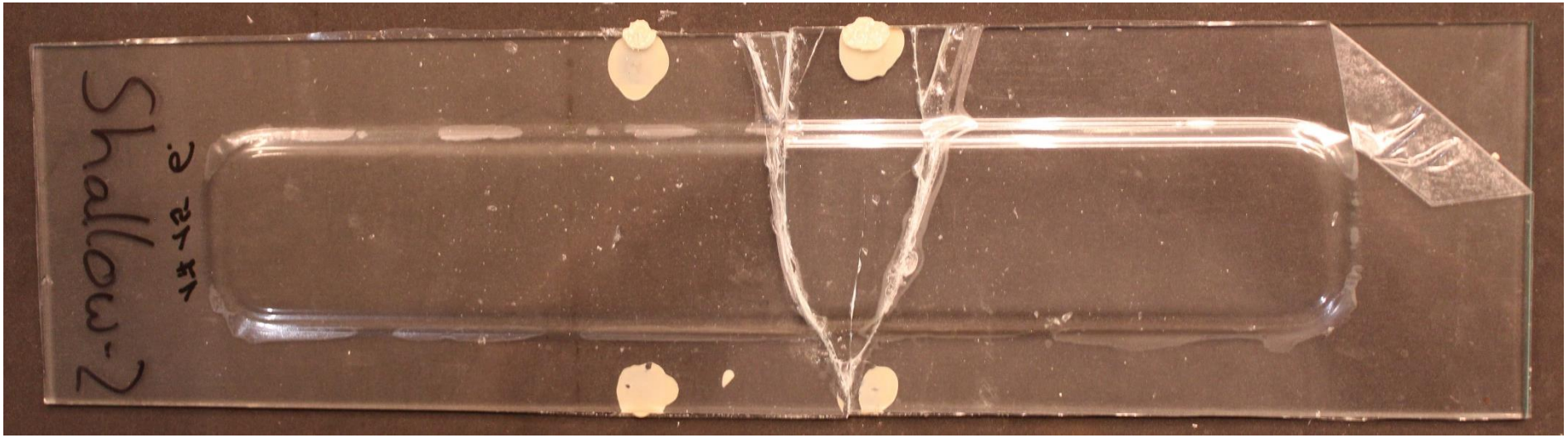

Sample Shallow-3

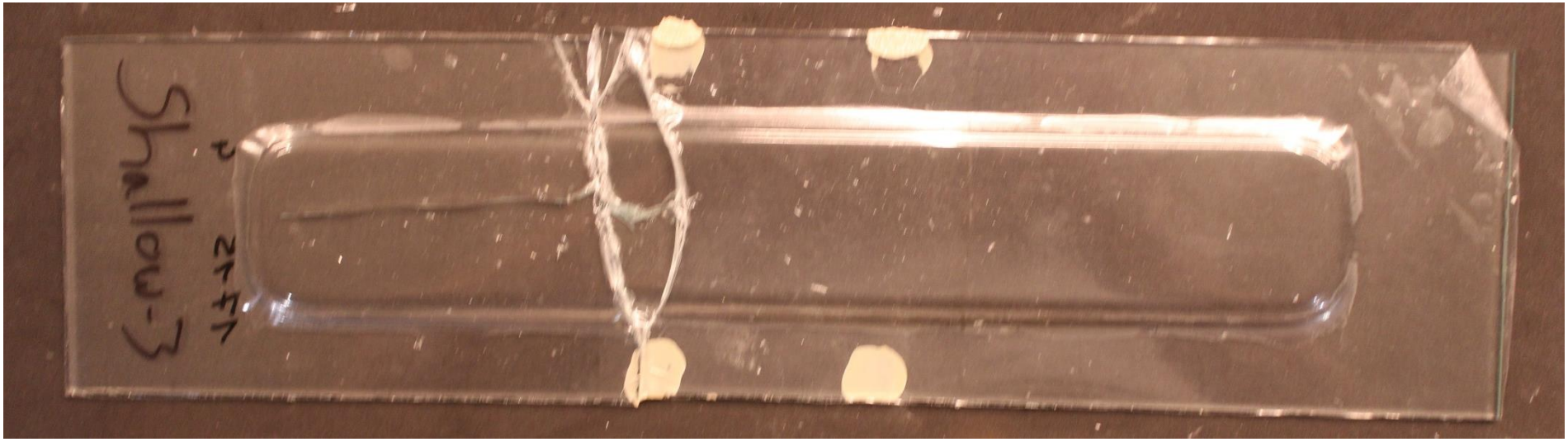

Sample Shallow-4

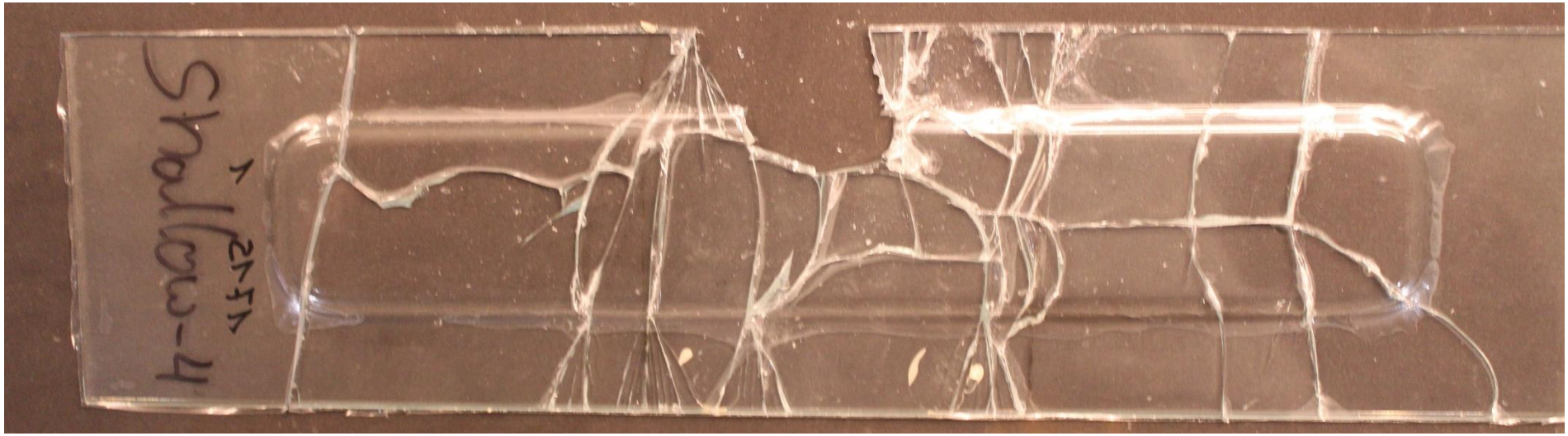

Sample Shallow-5

Sample Shallow-6

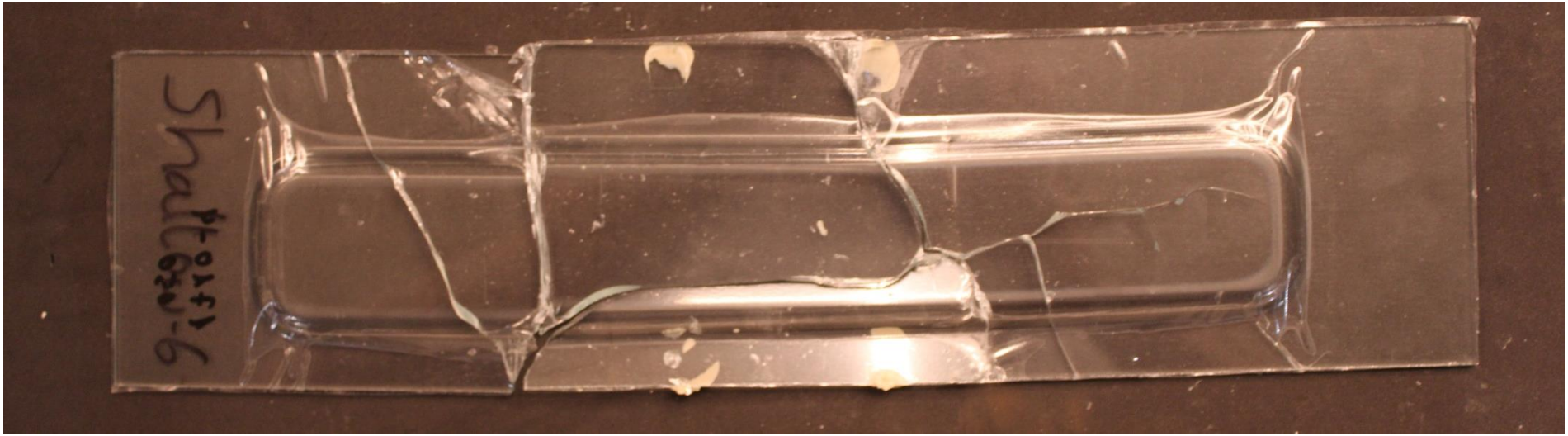

Sample Shallow-7

Sample Shallow-8

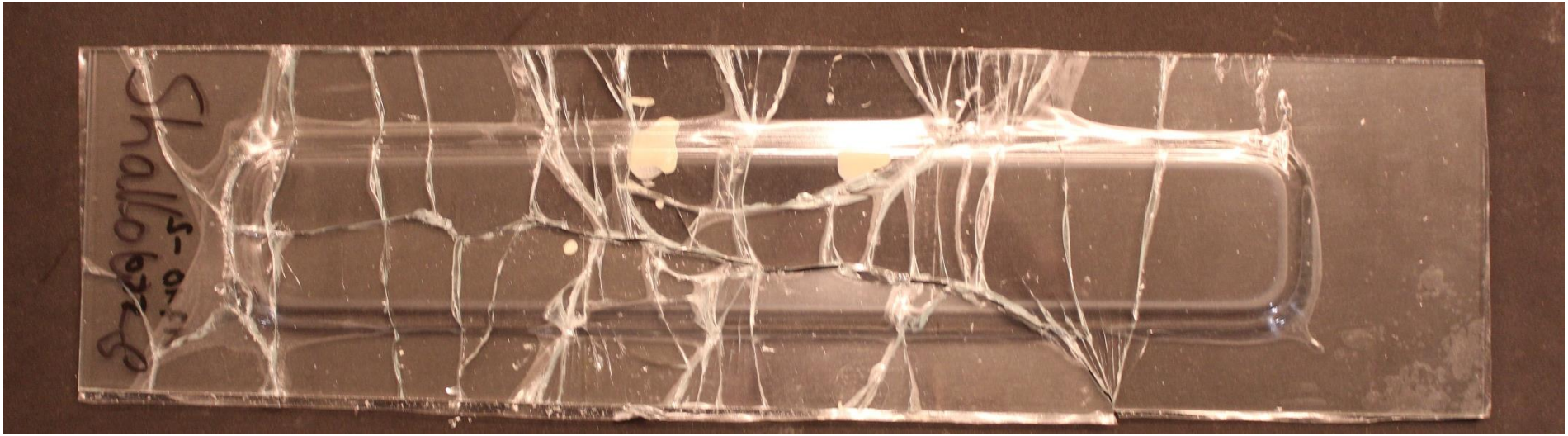

Sample Shallow-9

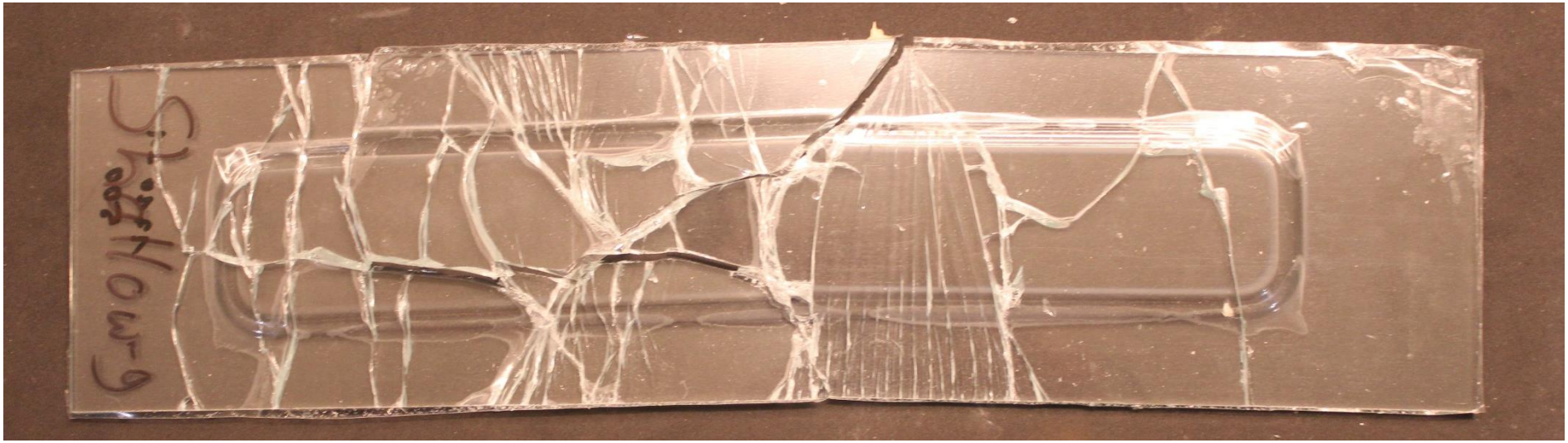

Sample Shallow-10

Sample Deep-1

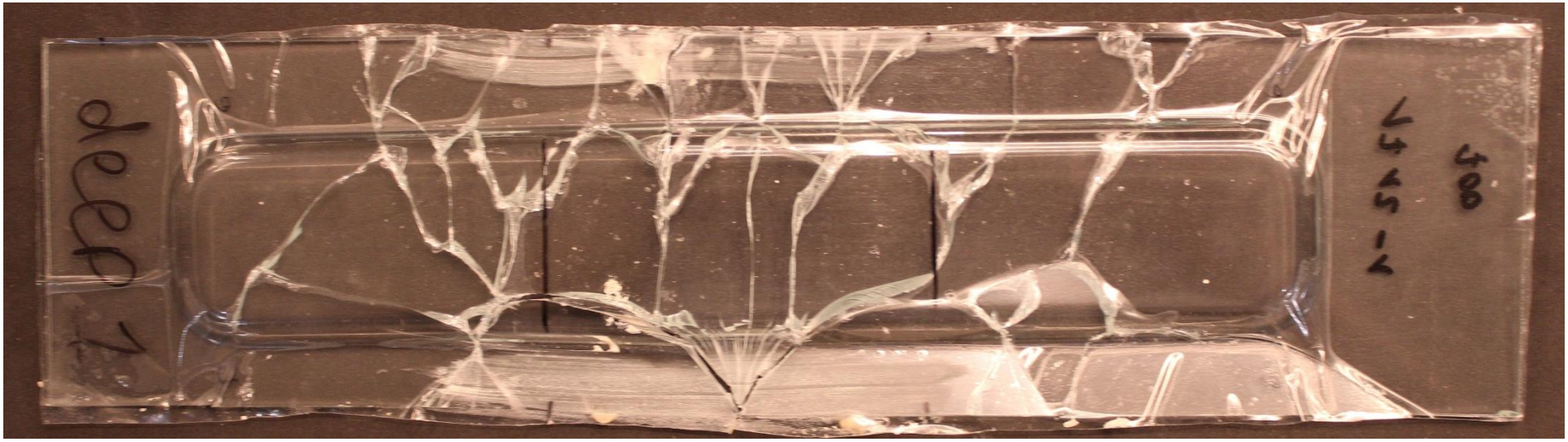

Sample Deep-2

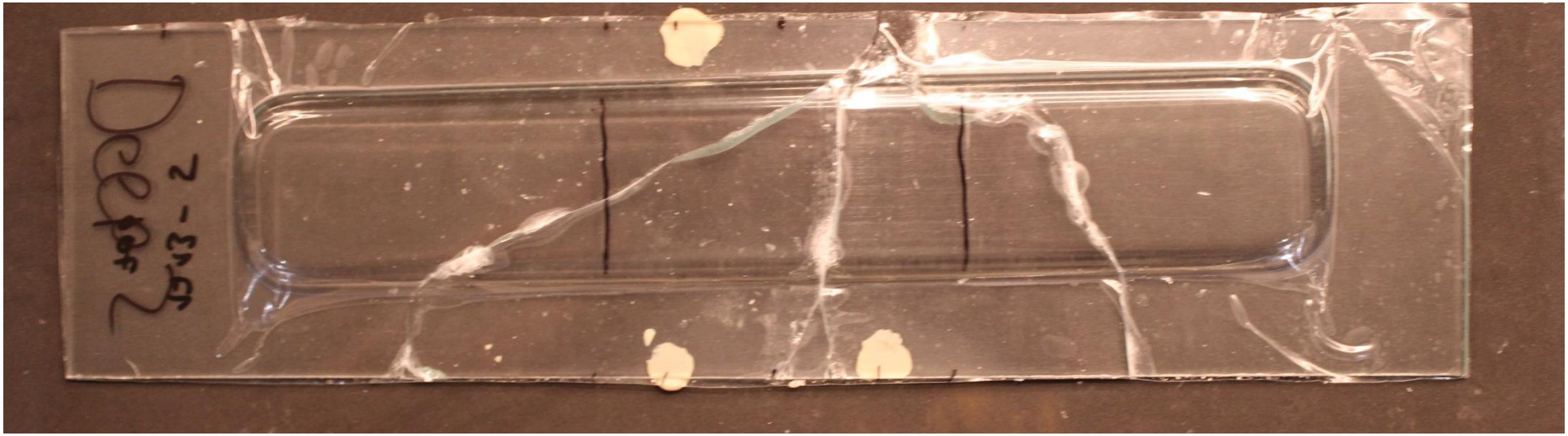

Sample Deep-3

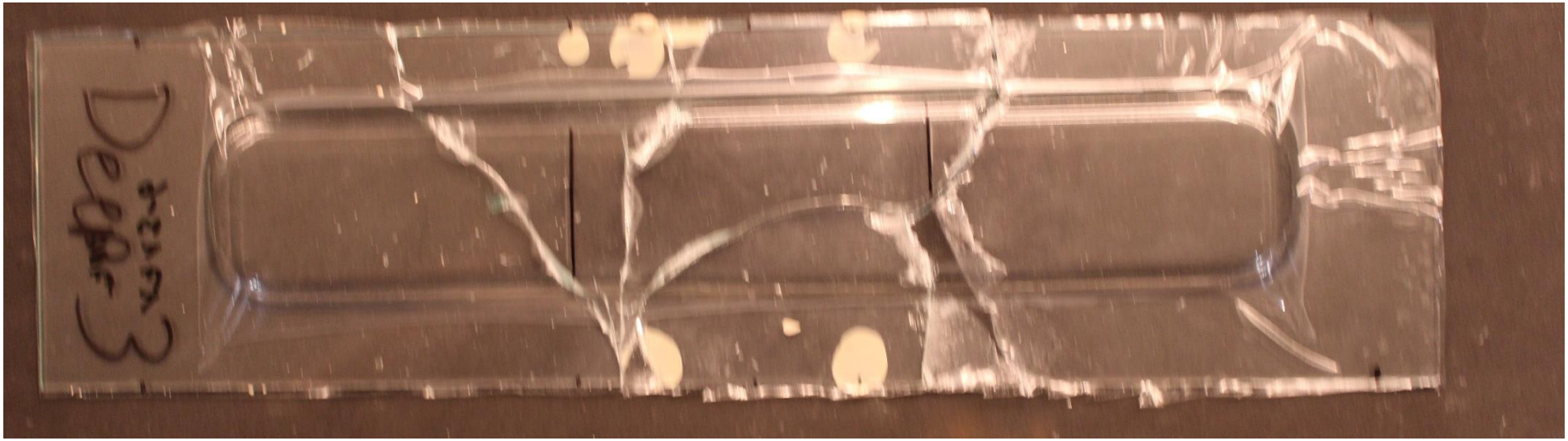

Sample Deep-4

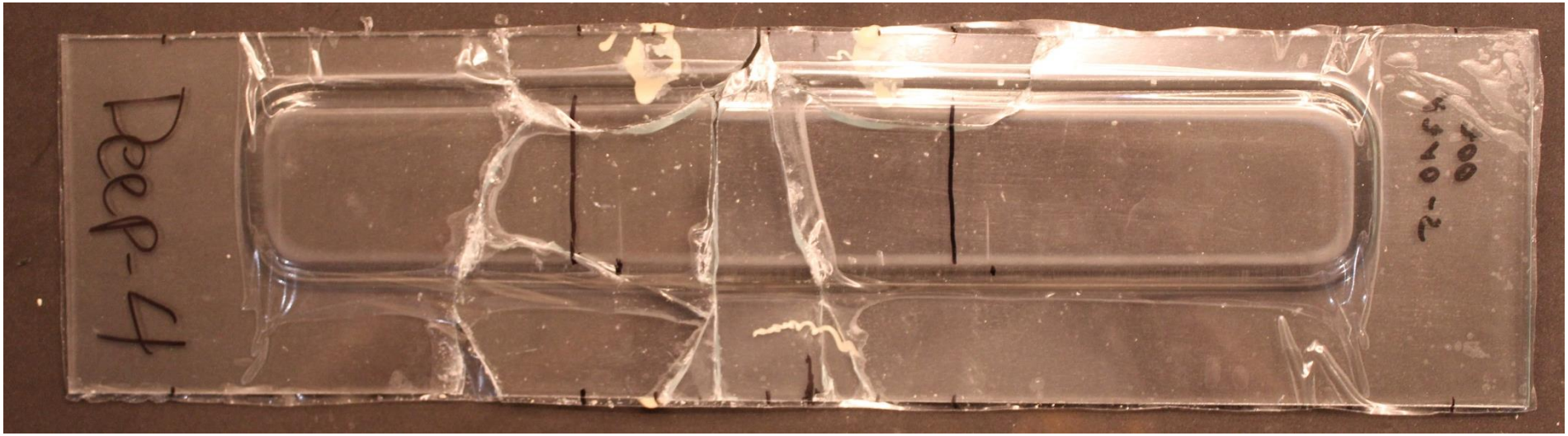

Sample Deep-5

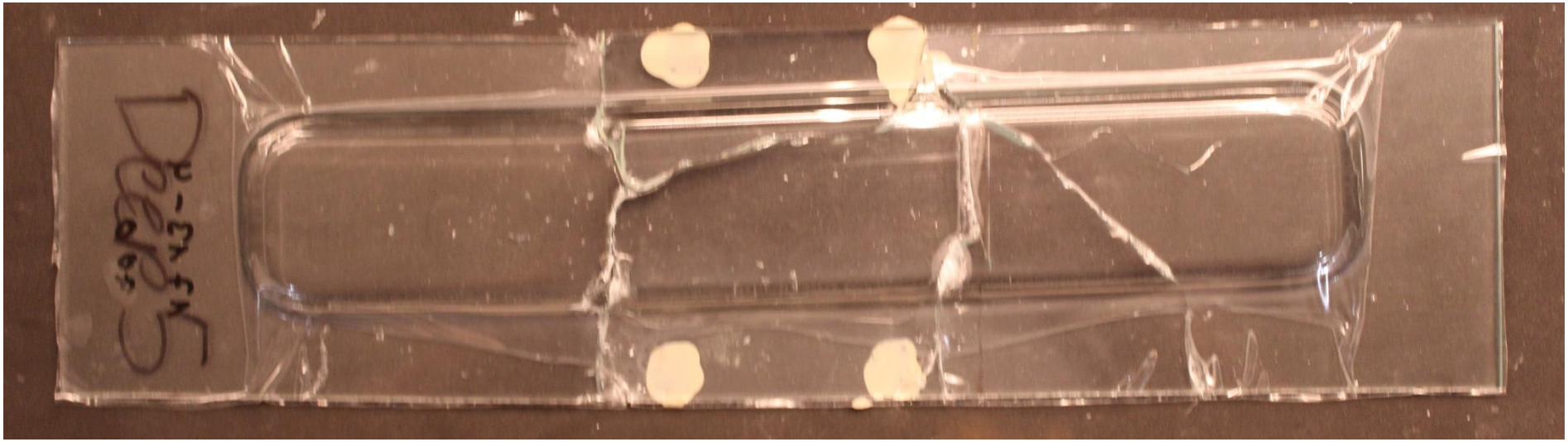

Sample Deep-6

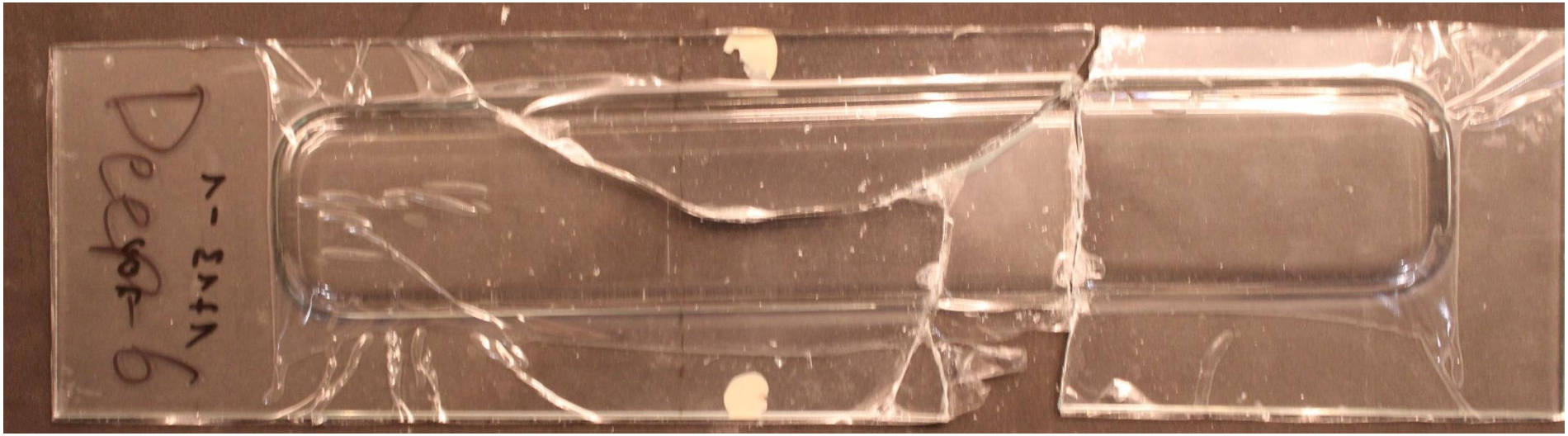

Sample Deep-7

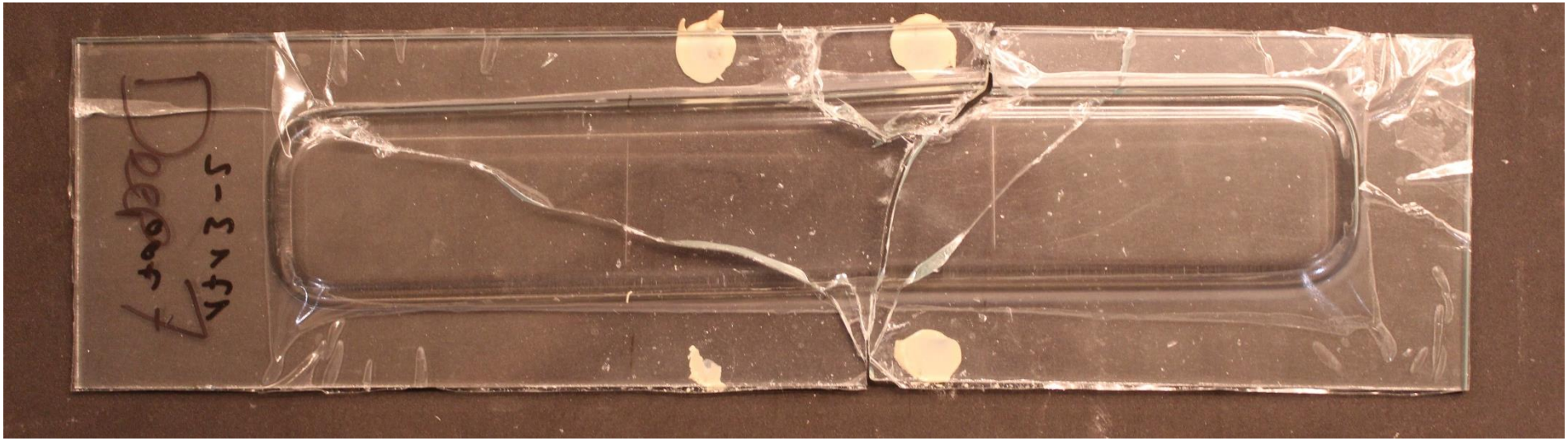

Sample Deep-8

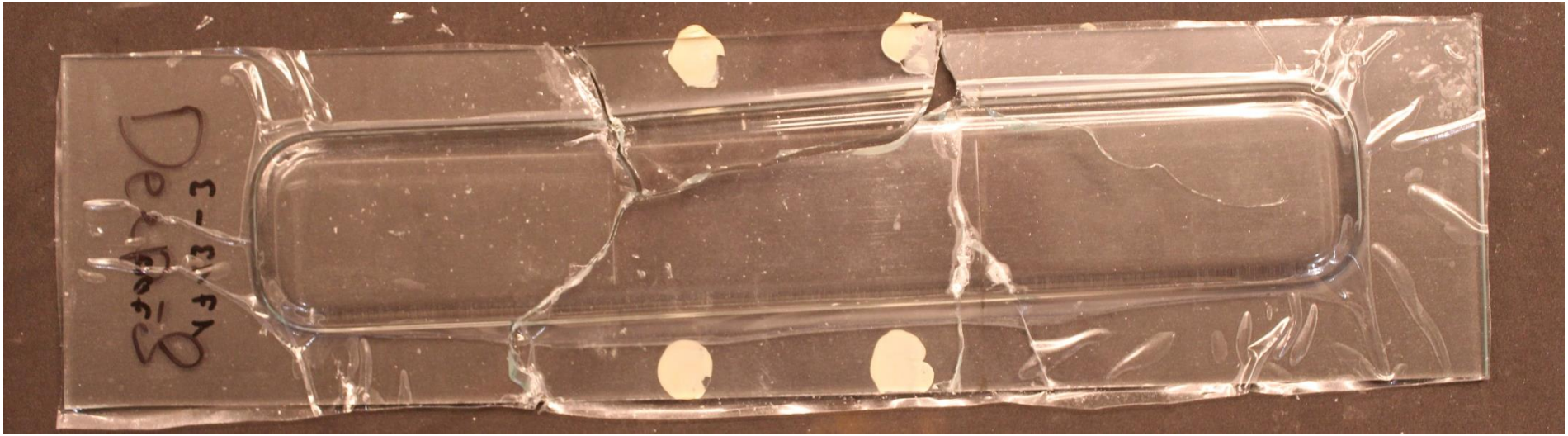

Sample Deep-9

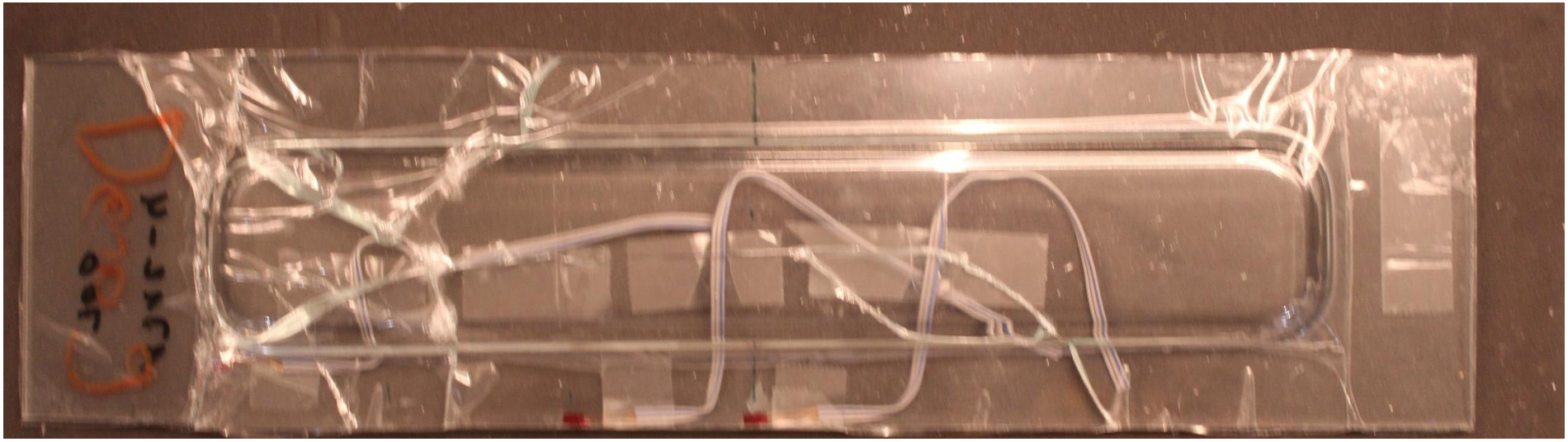

Sample Deep-10

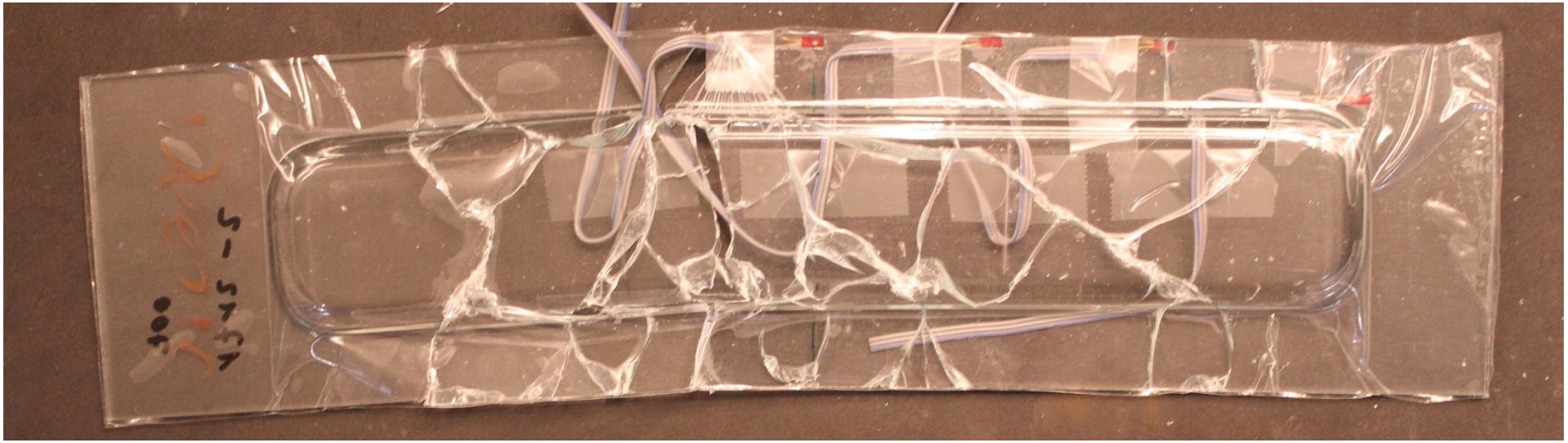

E

Appendix E: Force-Deformation plots

This appendix shows the different Force-deformation plots that show the obtained data of the four-point bending tests.

Appendix E: Force-Deformation plots

This appendix shows the force-deformation plots. These plots contain the data obtained by the four-point bending tests.

Flat - 1

Max force by hydraulic press: 135 N

Corresponding deformation by hydraulic press: 3.26 mm

Note: The stiffness is computed by the "second" slope of the plot.

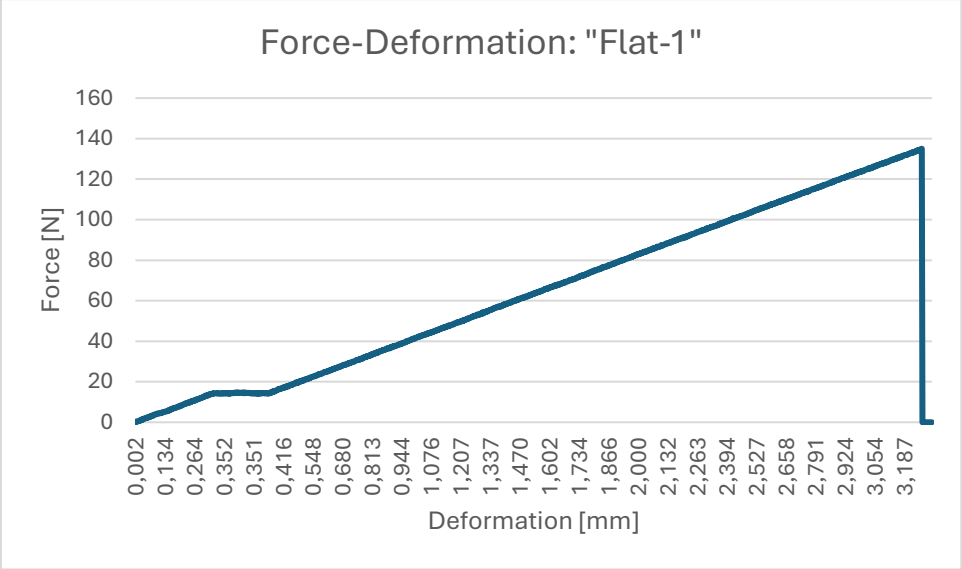

Flat - 2

Max force by hydraulic press: 222 N

Corresponding deformation by hydraulic press: 4.69 mm

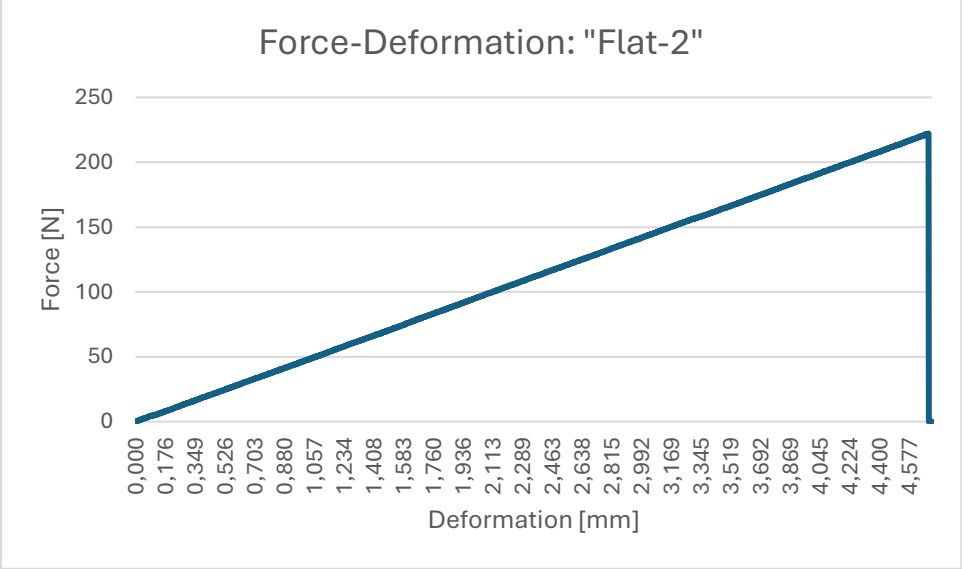

Flat - 3

Max force by hydraulic press: 70 N

Corresponding deformation by hydraulic press: 1.47 mm

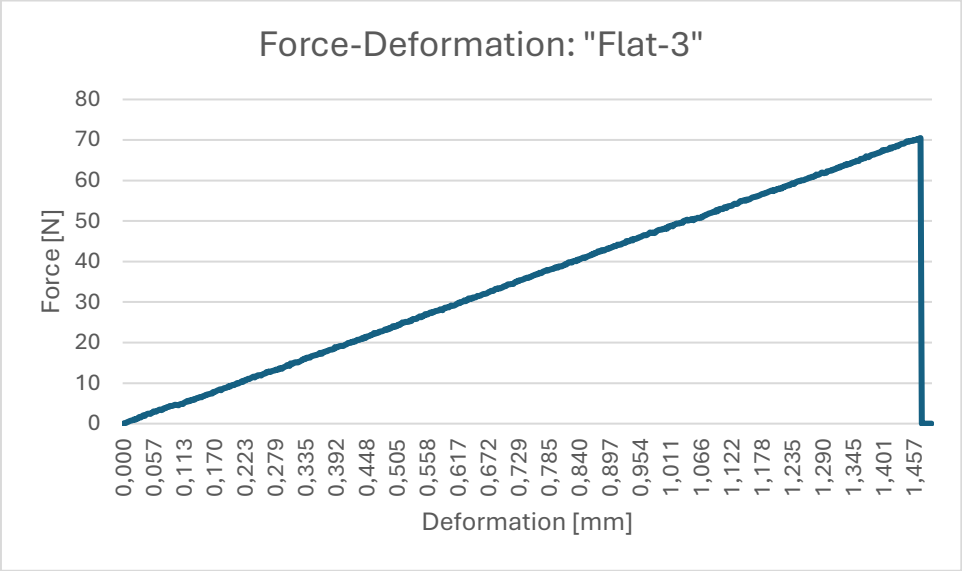

Flat - 4

Max force by hydraulic press: 321 N

Corresponding deformation by hydraulic press: 6.57 mm

Note: The plateau at the end of the tests is not taken into account when deriving the stiffness.

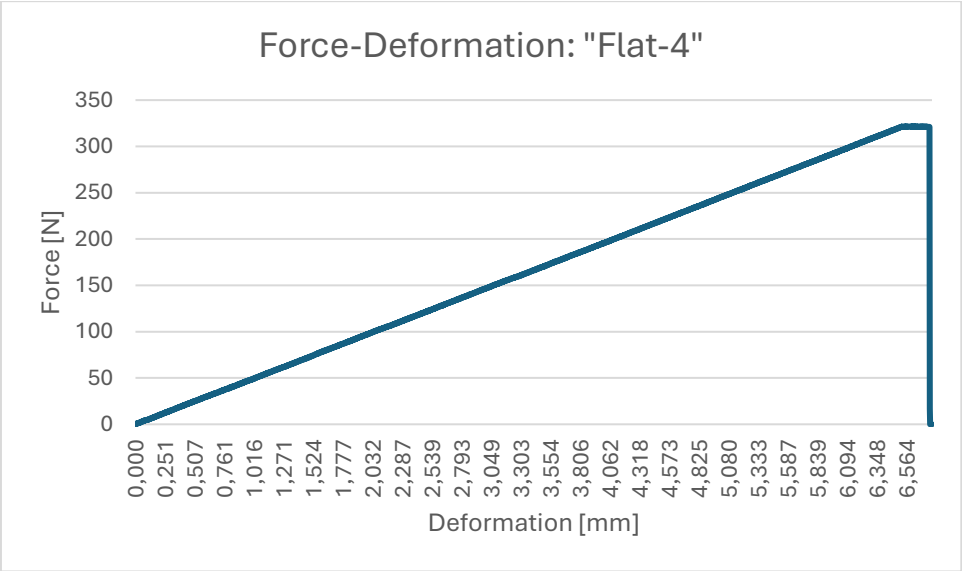

Shallow - 1

Max force by hydraulic press: 305 N

Corresponding deformation by hydraulic press: 3.57 mm

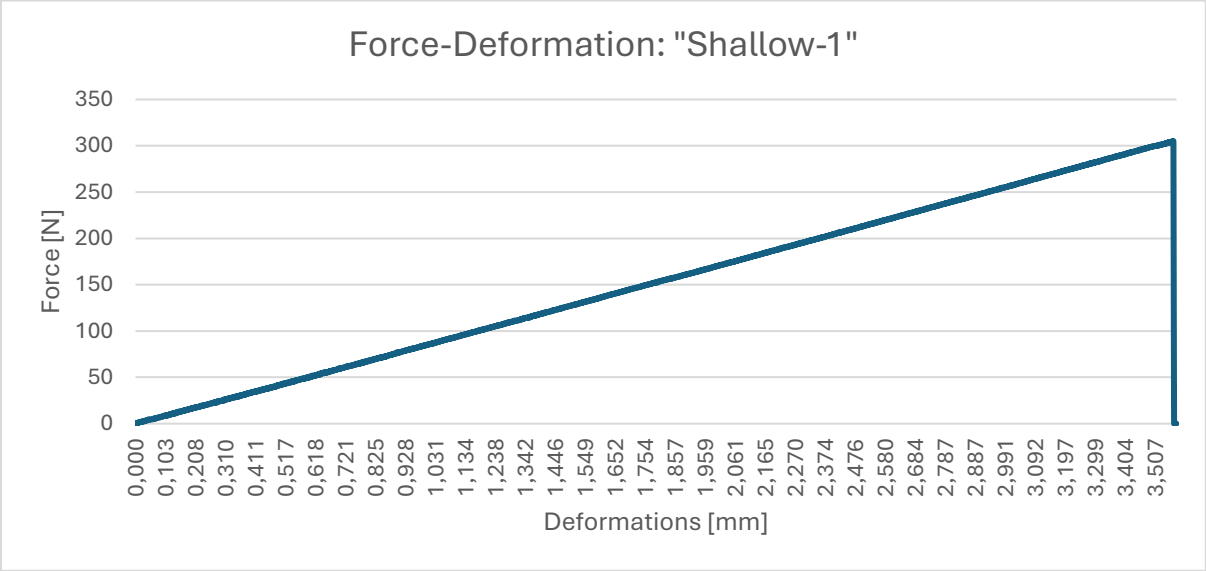

Shallow - 2

Max force by hydraulic press: 165 N

Corresponding deformation by hydraulic press: 2.08 mm

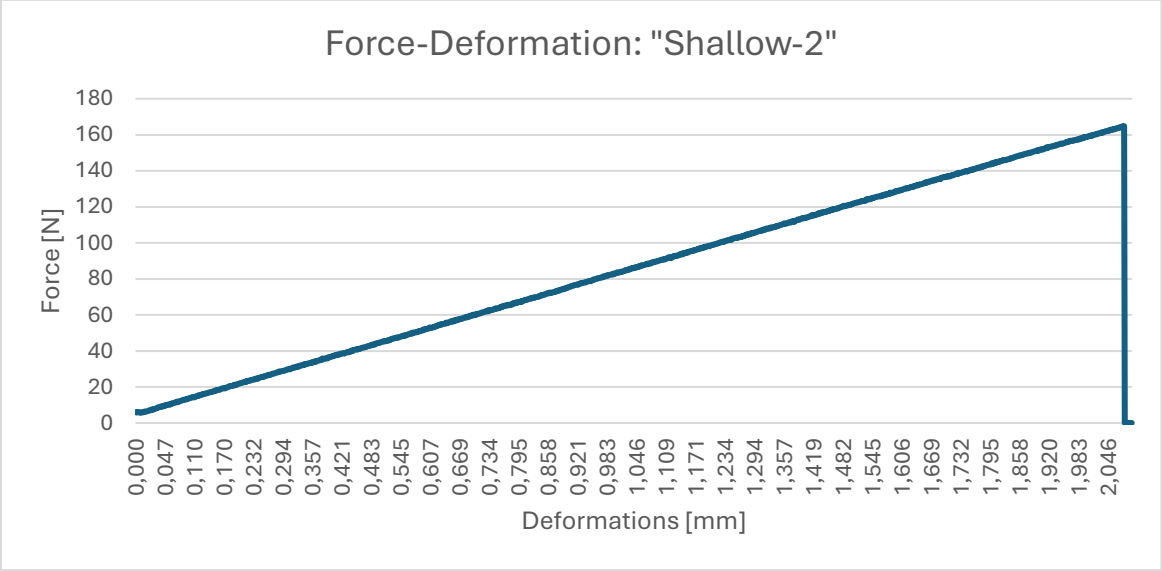

Shallow - 3

Max force by hydraulic press: 236 N

Corresponding deformation by hydraulic press: 2.61 mm

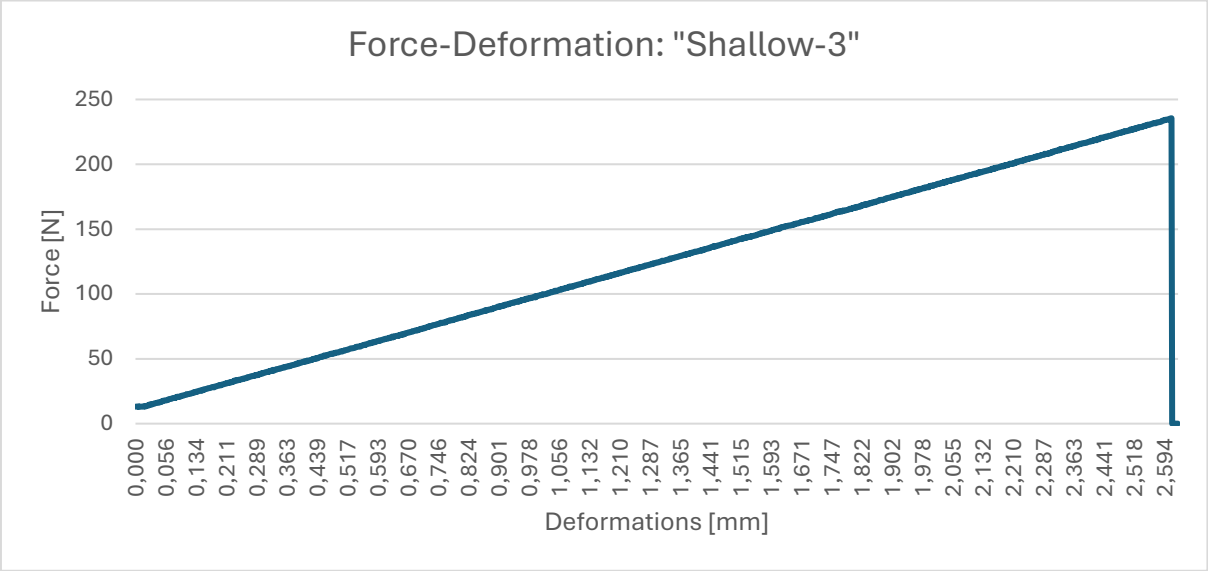

Shallow - 4

Max force by hydraulic press: 339 N

Corresponding deformation by hydraulic press: 3.79 mm

Note: The stiffness is computed by the "second" slope of the plot.

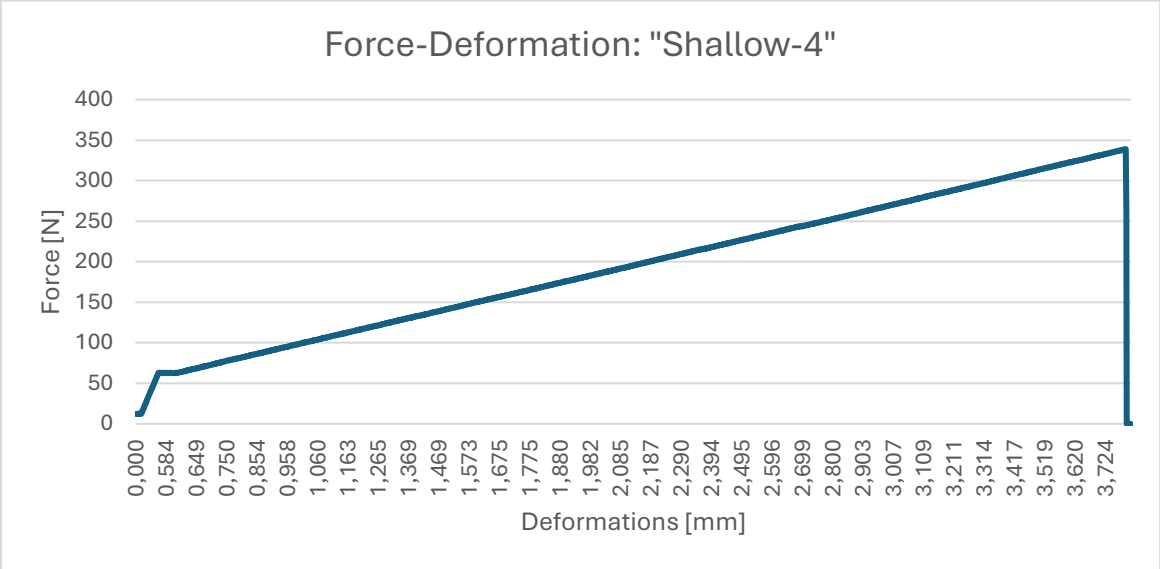

Shallow - 5

Max force by hydraulic press: 366 N

Corresponding deformation by hydraulic press: 4.16 mm

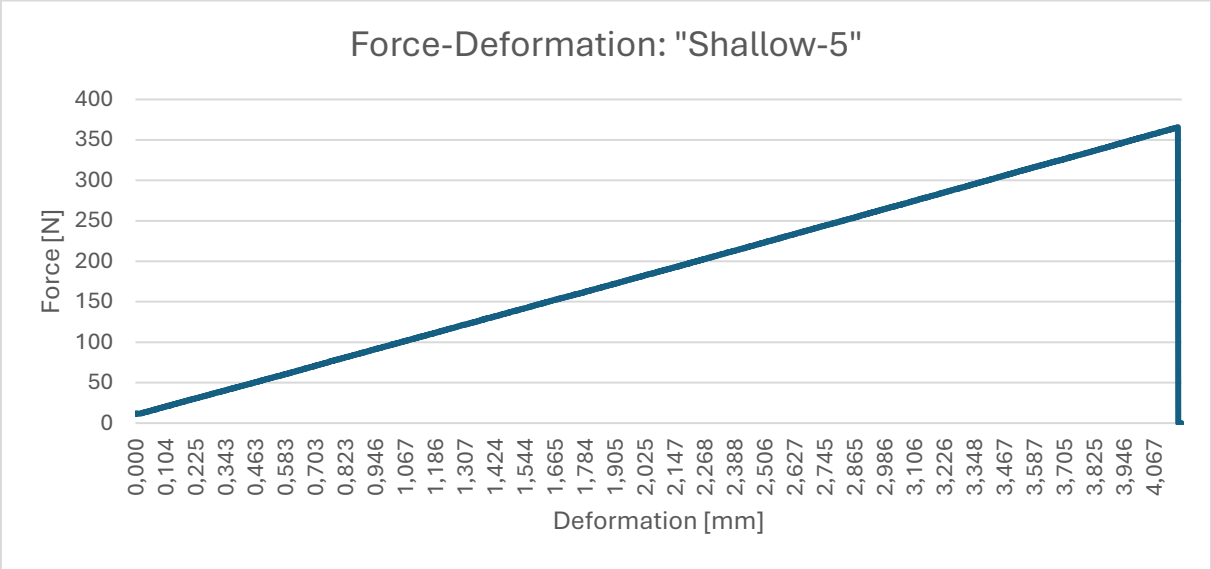

Shallow - 6

Max force by hydraulic press: 375 N

Corresponding deformation by hydraulic press: 1.96 mm

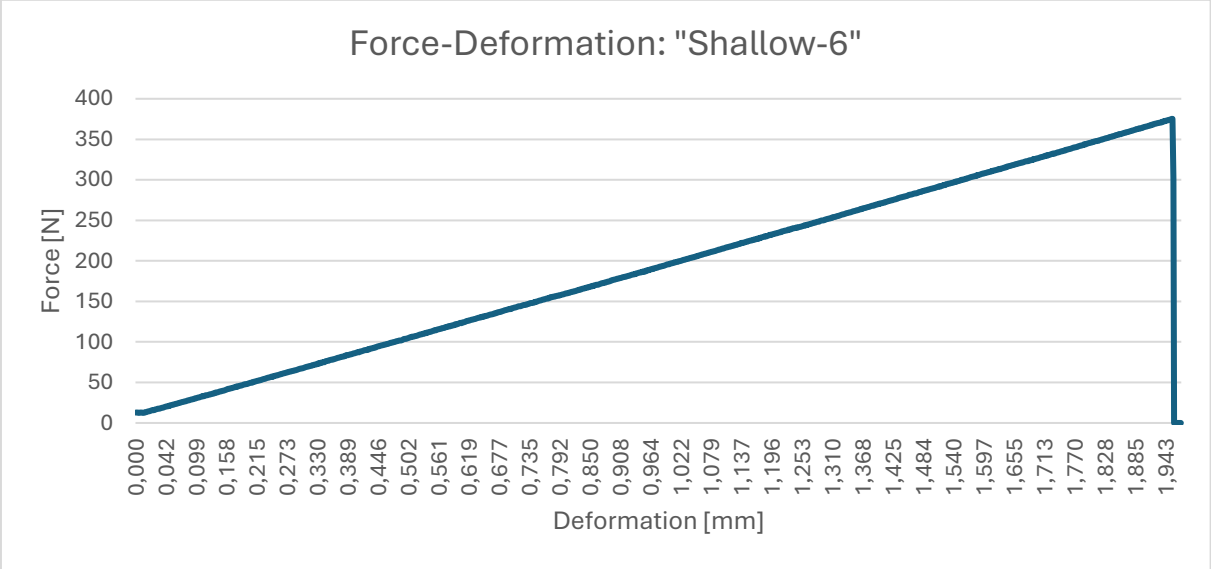

Shallow - 7

Max force by hydraulic press: 986 N

Corresponding deformation by hydraulic press: 6.71 mm

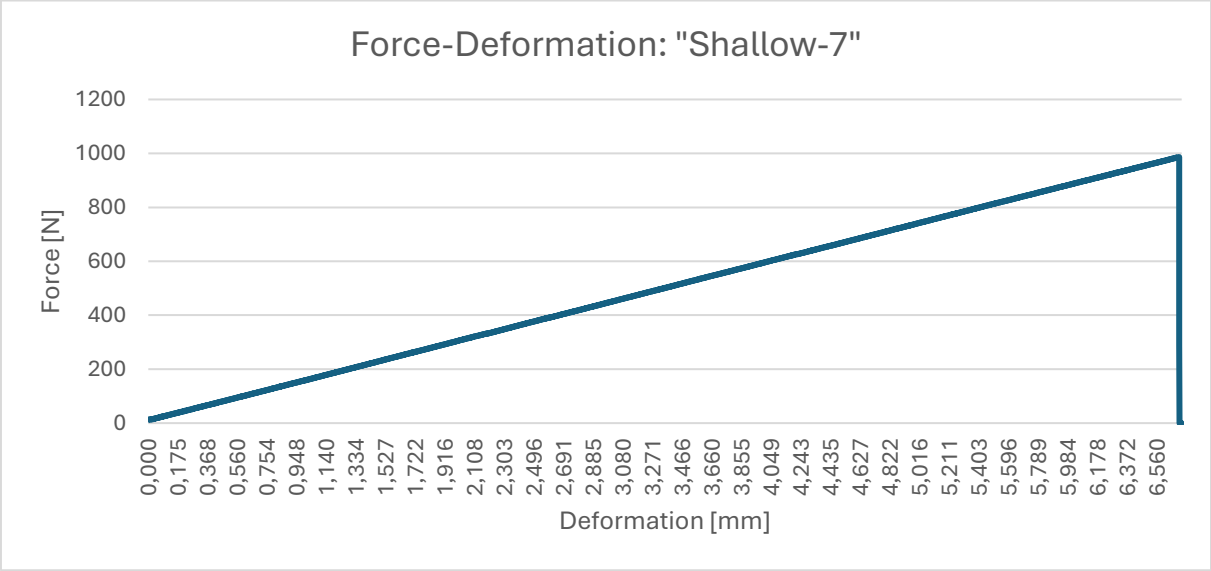

Shallow - 8

Max force by hydraulic press: 483 N

Corresponding deformation by hydraulic press: 4.61 mm

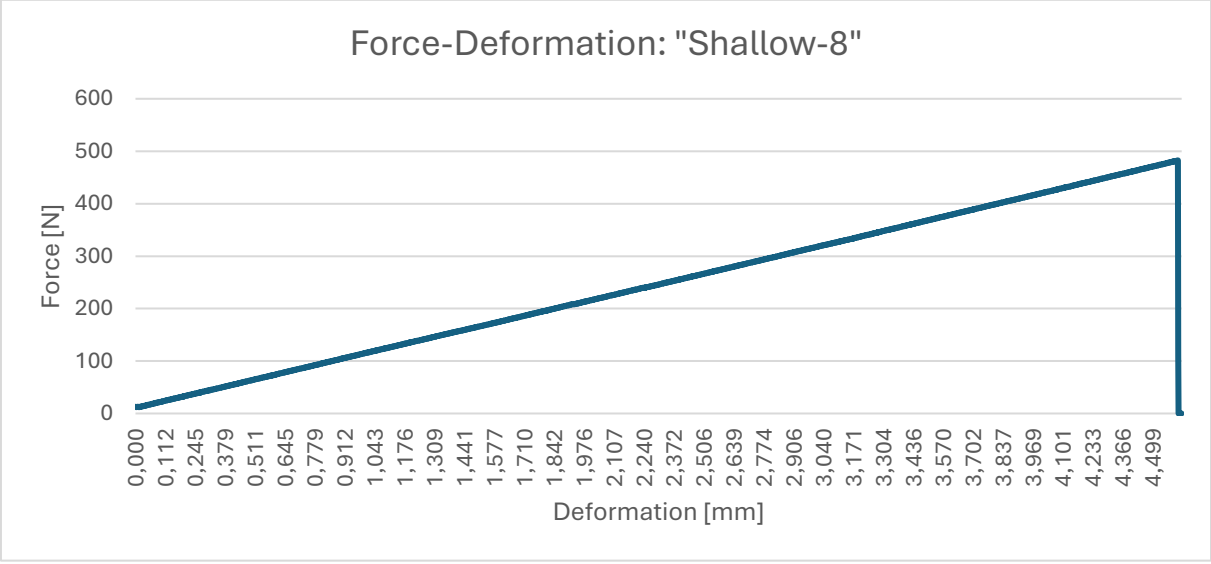

Shallow - 9

Max force by hydraulic press: 429 N

Corresponding deformation by hydraulic press: 5.33 mm

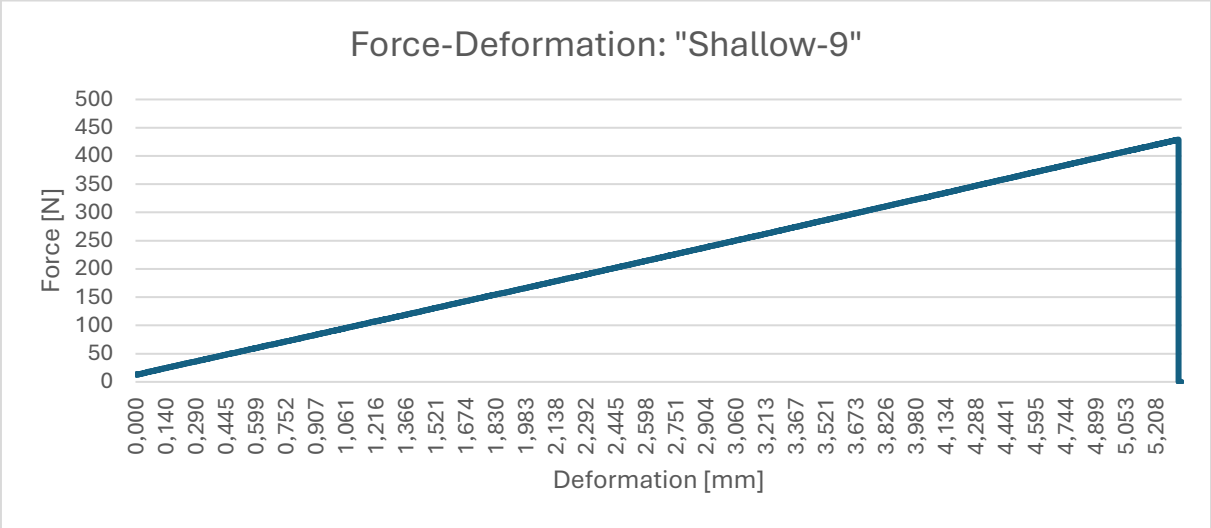

Shallow - 10

Max force by hydraulic press: 286 N

Corresponding deformation by hydraulic press: 3.45 mm

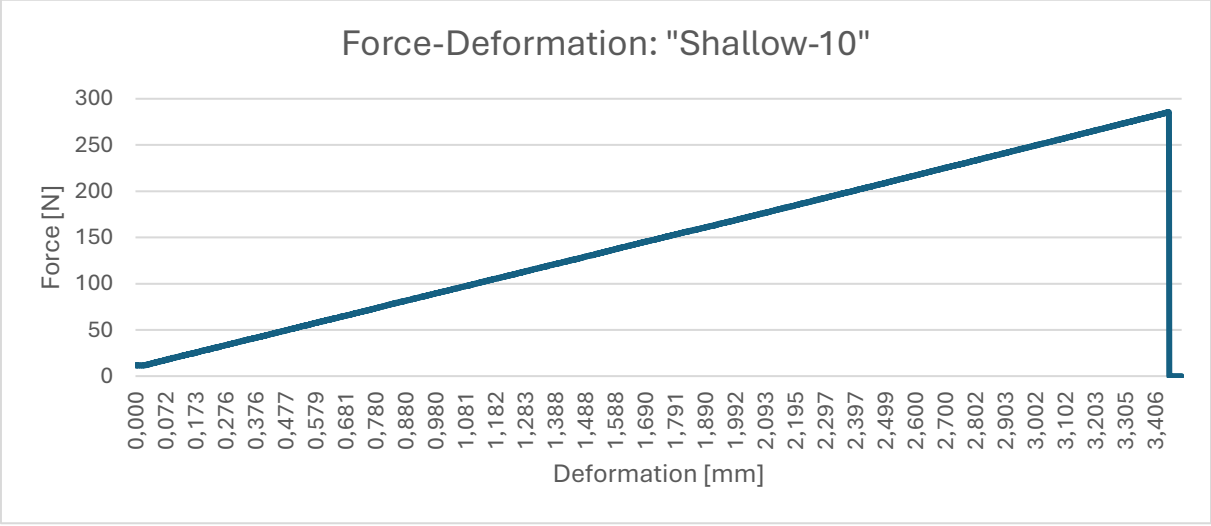

Deep - 1

Max force by hydraulic press: 885 N

Corresponding deformation by hydraulic press: 2.70 mm

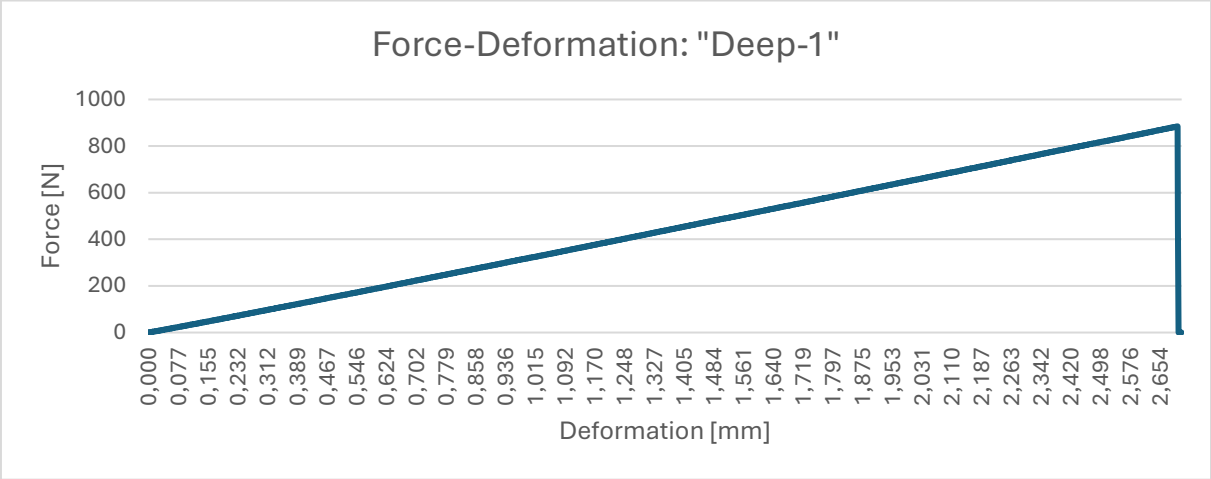

Deep - 2

Max force by hydraulic press: 385 N

Corresponding deformation by hydraulic press: 1.26 mm

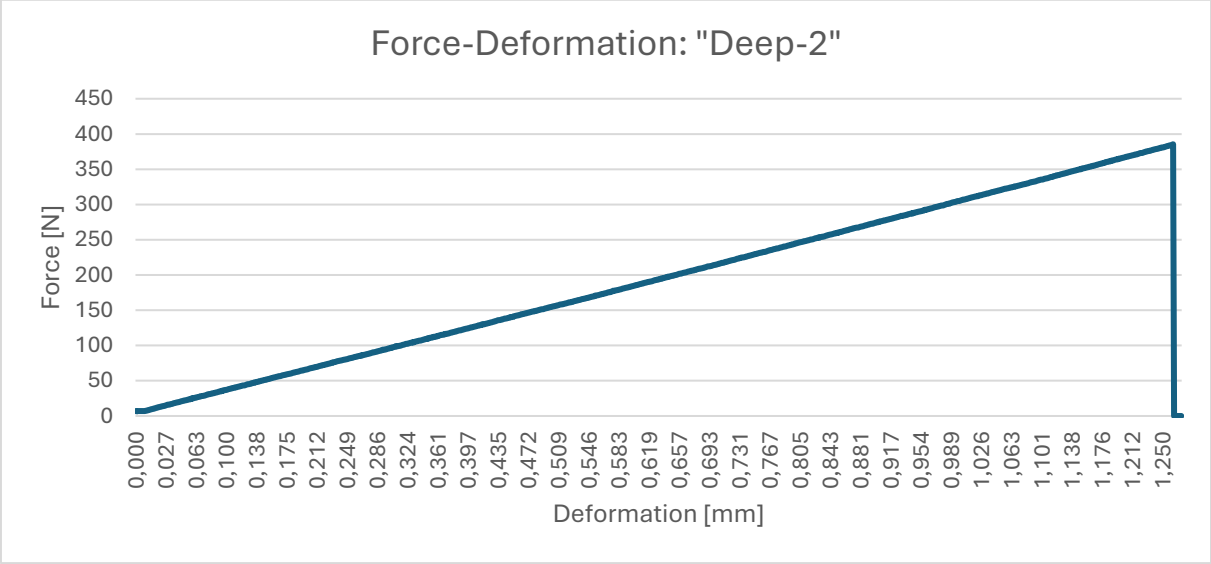

Deep - 3

Max force by hydraulic press: 445 N

Corresponding deformation by hydraulic press: 1.76 mm

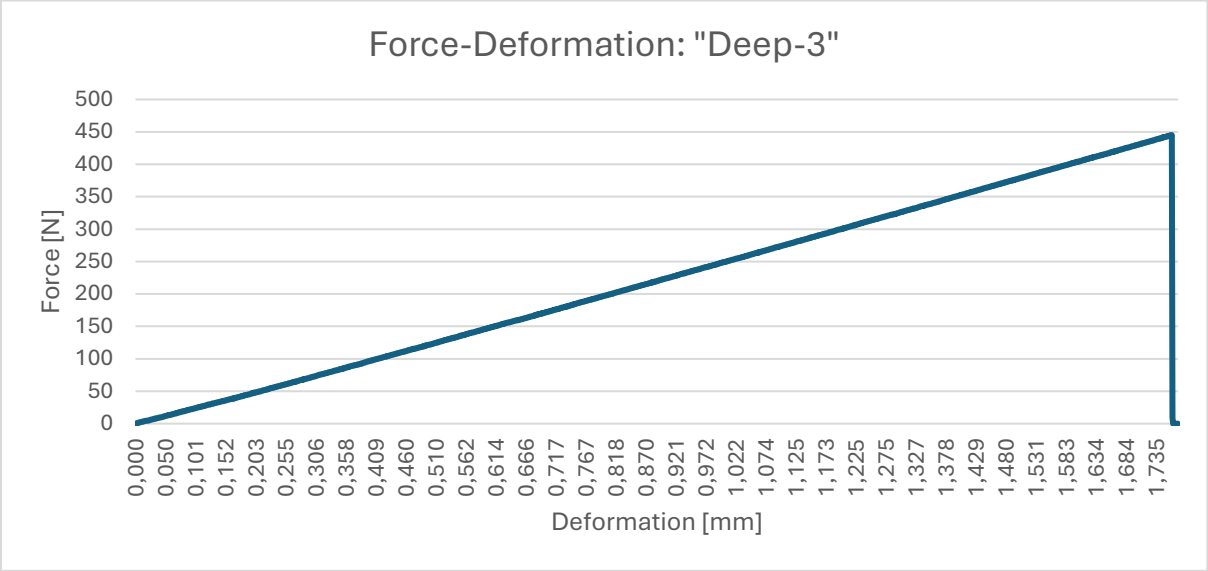

Deep - 4

Max force by hydraulic press: 439 N

Corresponding deformation by hydraulic press: 1.96 mm

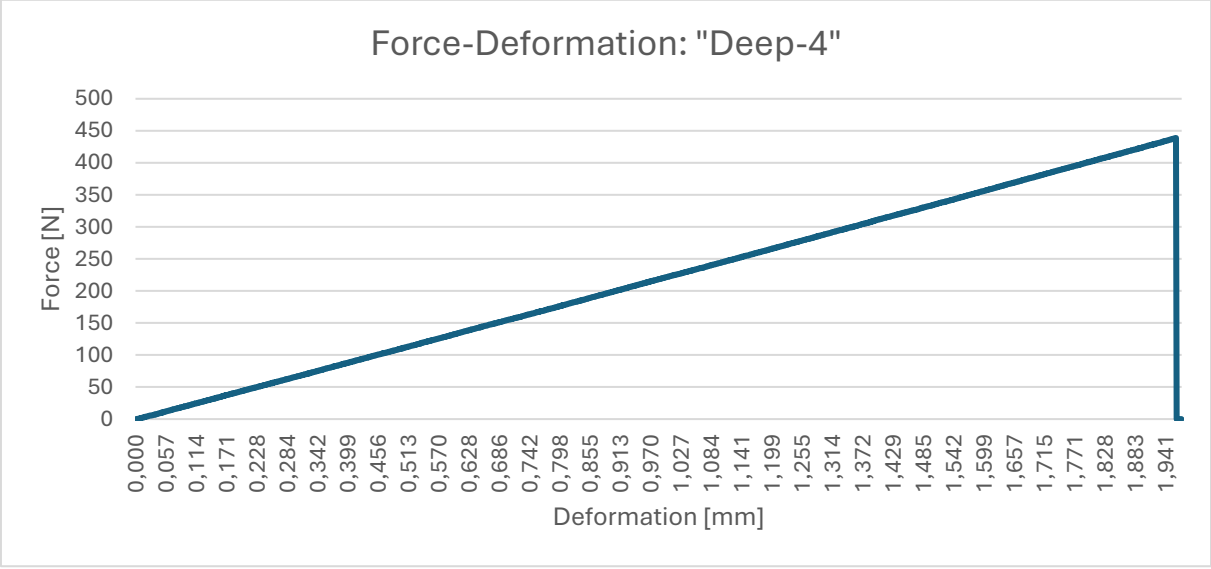

Deep - 5

Max force by hydraulic press: 457 N

Corresponding deformation by hydraulic press: 1.38 mm

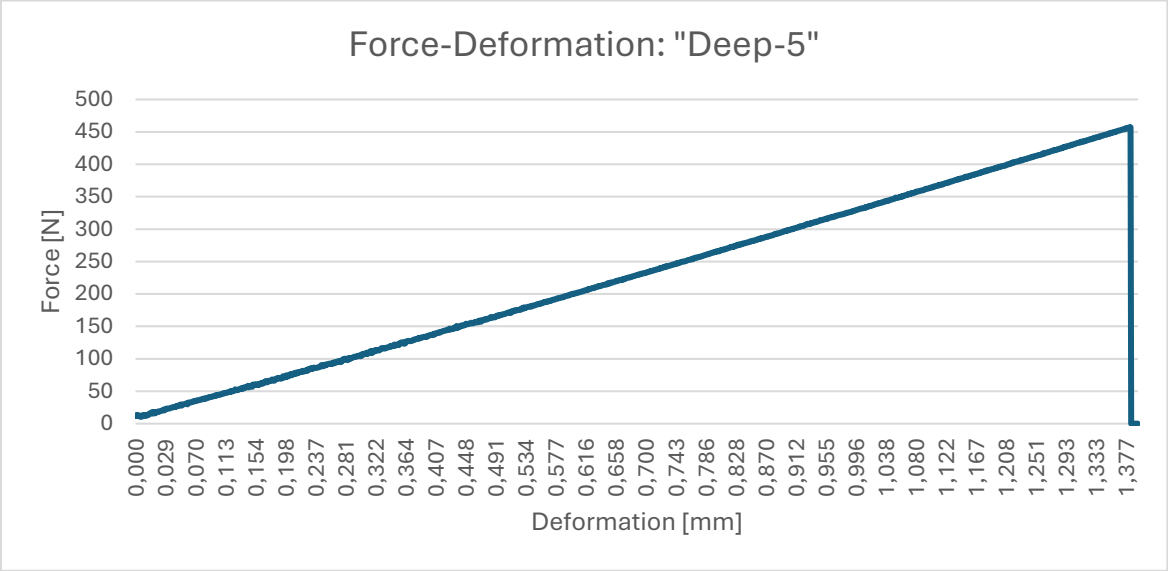

Deep - 6

Max force by hydraulic press: 403 N

Corresponding deformation by hydraulic press: 1.22 mm

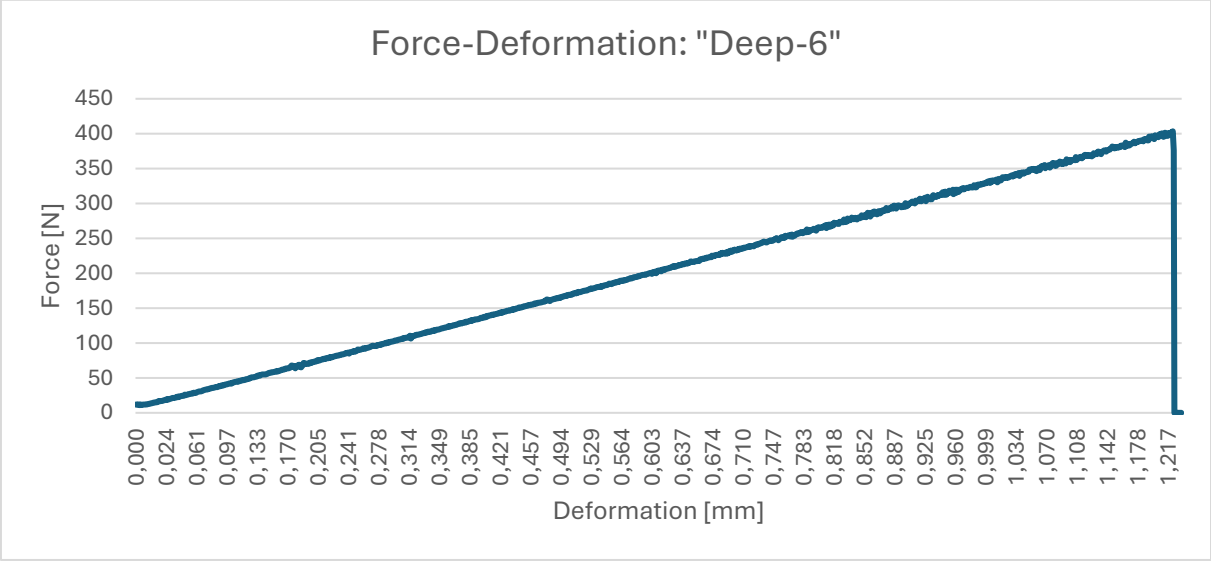

Deep - 7

Max force by hydraulic press: 576 N

Corresponding deformation by hydraulic press: 1.58 mm

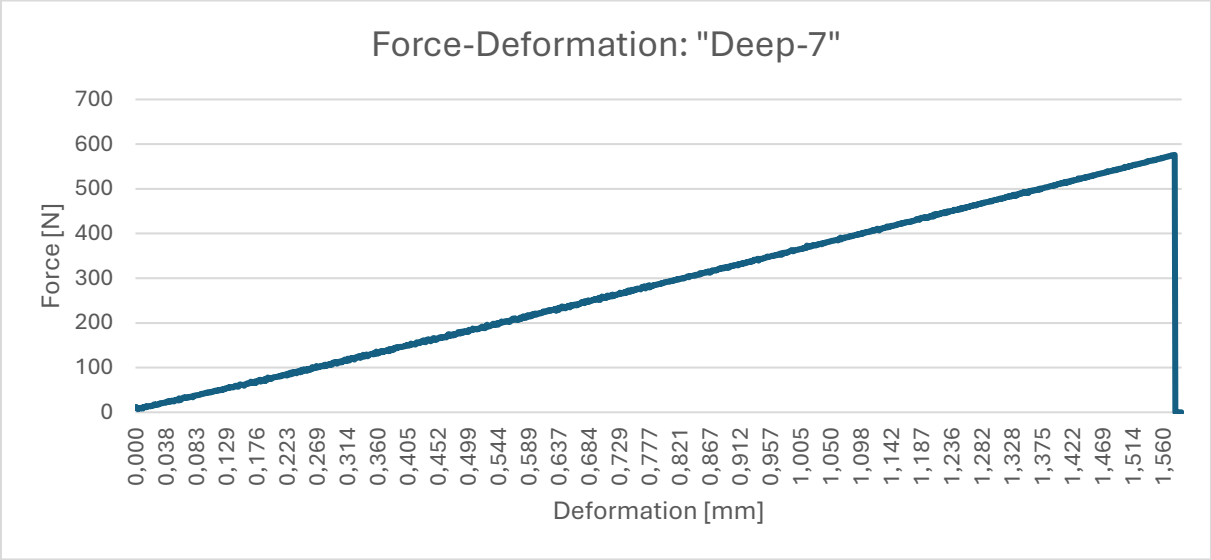

Deep - 8

Max force by hydraulic press: 468 N

Corresponding deformation by hydraulic press: 1.17 mm

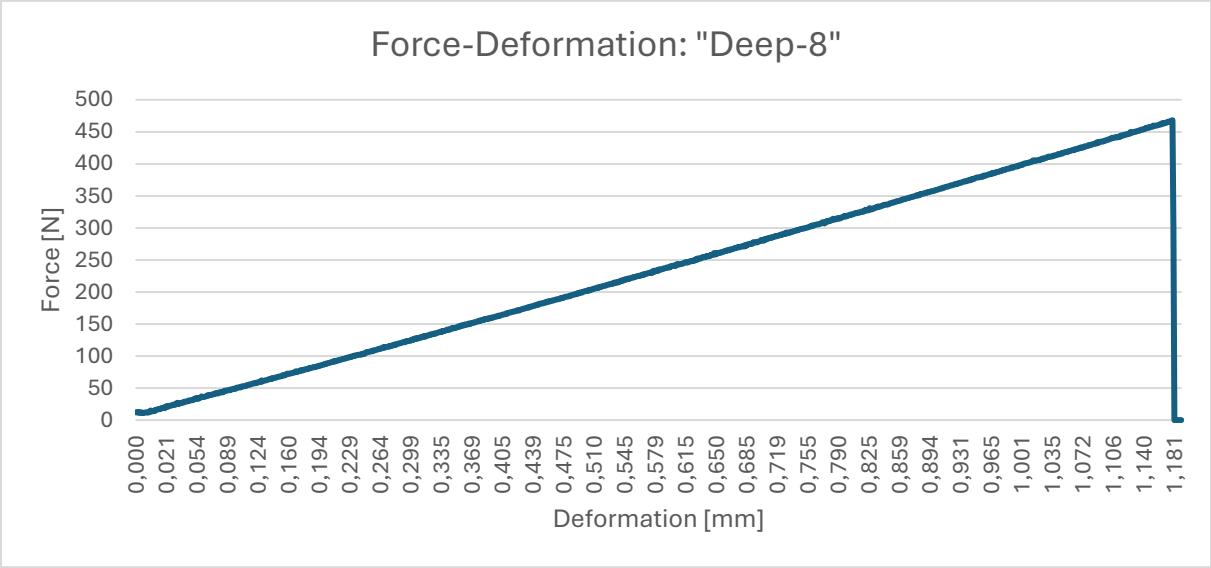

Deep - 9

Max force by hydraulic press: 648 N

Corresponding deformation by hydraulic press: 1.30 mm

Note: The stiffness is computed by the “second” slope of the plot.

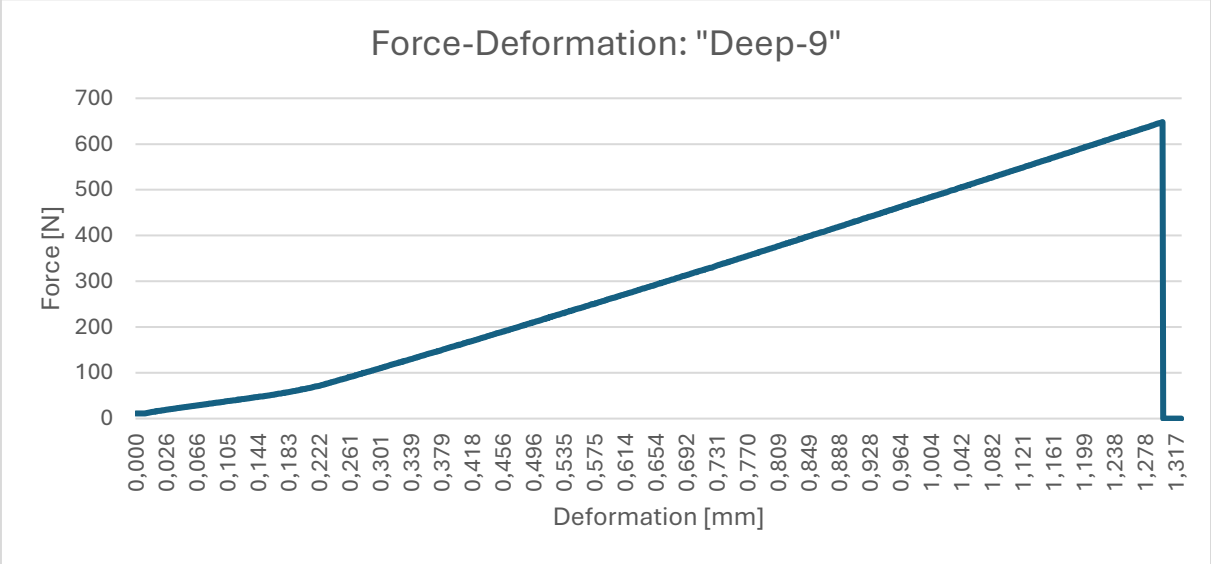

Deep - 10

Max force by hydraulic press: 1096 N

Corresponding deformation by hydraulic press: 2.48 mm

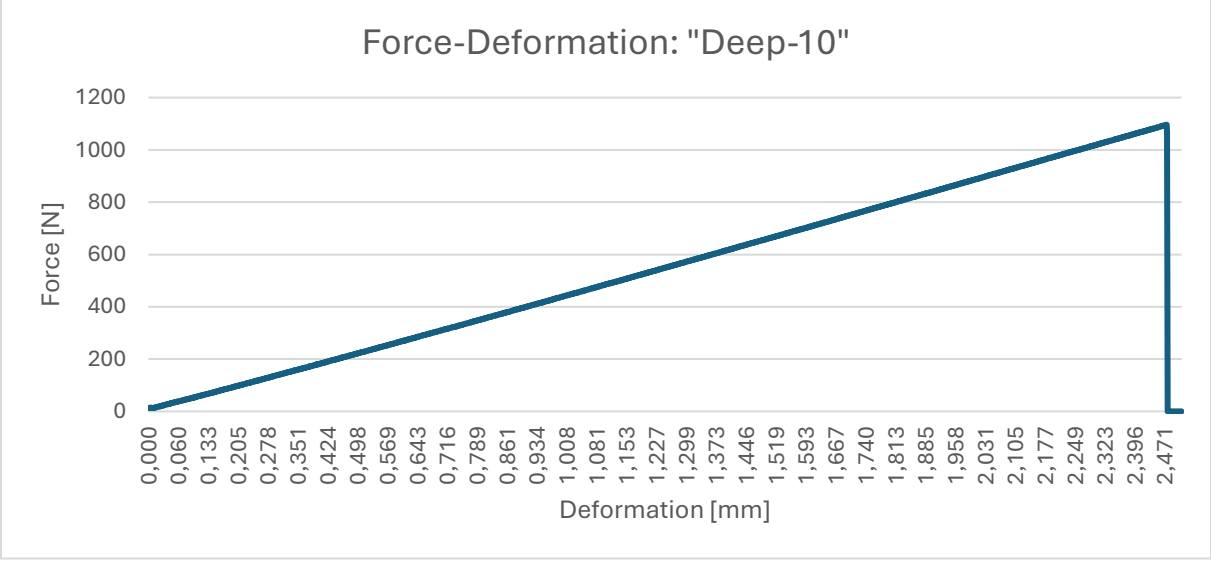

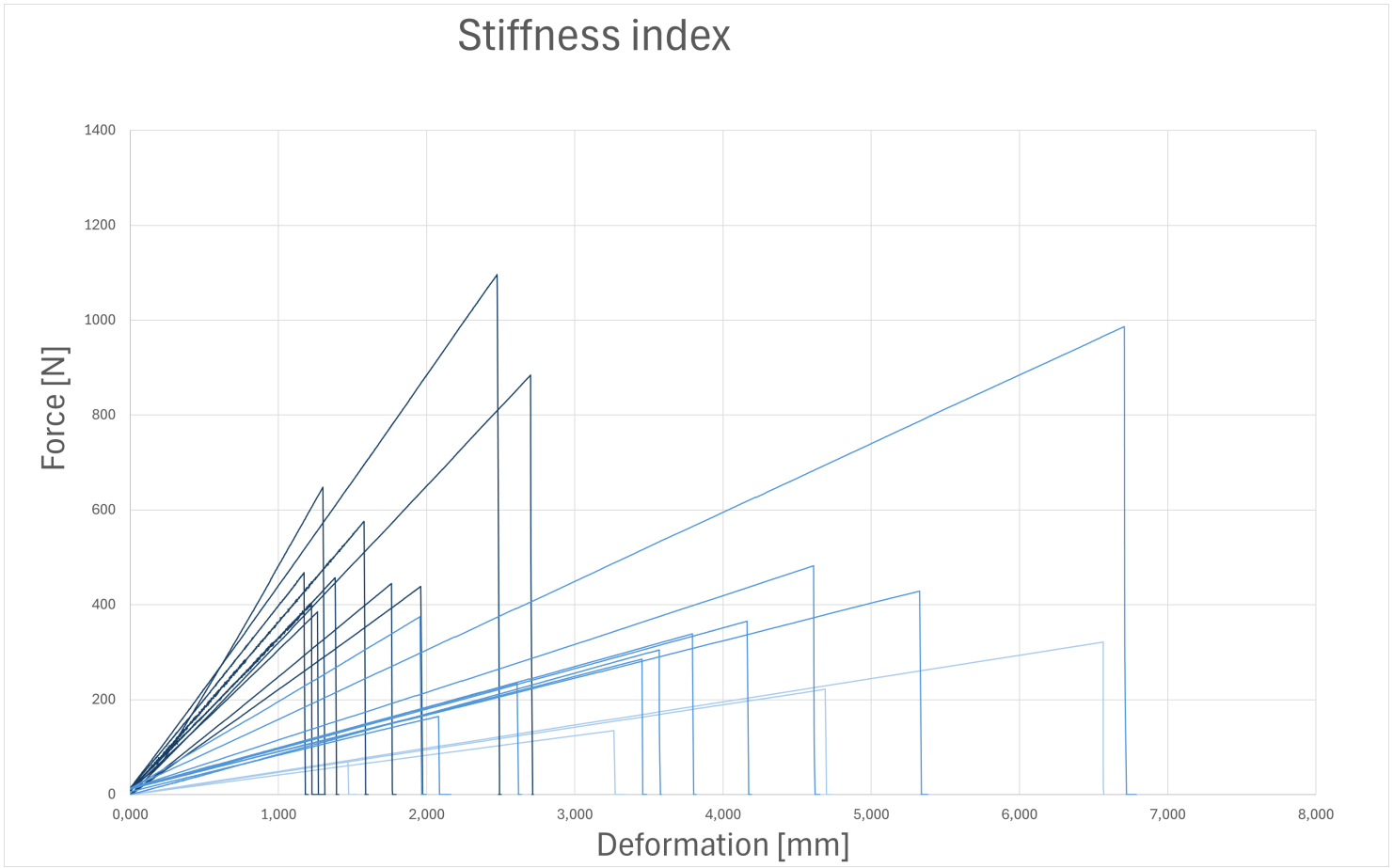
Stiffness index
Force [N]
1400
1200
1000
800
600
400
200
0
0,000
1,000
2,000
3,000
4,000
5,000
6,000
7,000
8,000
Deformation [mm]

Appendix F: FEM model output

This appendix shows the output of all the individual FEM-models.

Appendix F: Output FEM-Results tests

This appendix shows the FEM-Results obtained by modelling in DIANA FEA. Starting with 4 flat samples, 10 shallow samples and 10 deep samples.

The output contains the deformations and principal stresses obtained when applying the maximum loads obtained from four-point-bending tests.

Flat – 1

Loads: 149N + Global self-weight

Deformations (as seen from above):

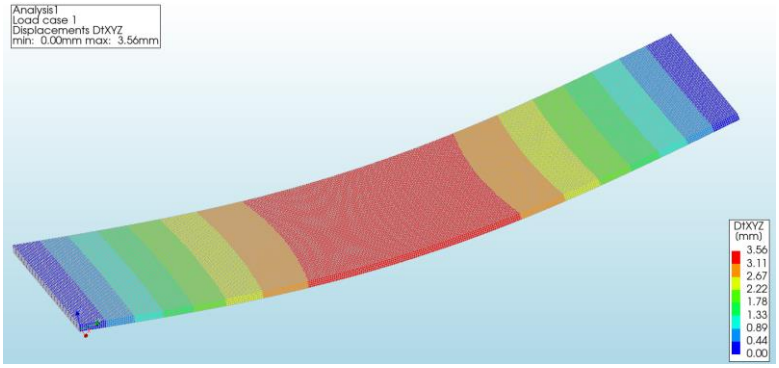

- Deformation at place of loading: 3.21mm

case	case id	case value	node	X [mm]	Y [mm]	Z [mm]	DtXYZ [mm]
Load cas...	1	0	1	0	225	3.89	3.20739
Load cas...	1	0	2	0	125	3.89	3.20843
Load cas...	1	0	3	100	225	3.89	3.20739
Load cas...	1	0	4	100	125	3.89	3.20843

Tensile principal stresses (as seen from below):

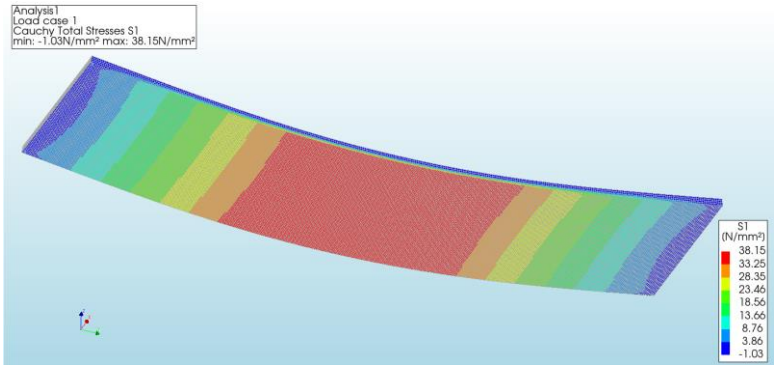

- Tensile principal stress at place of initiation of failure: 38 N/mm^2

case	case id	case value	element	node	layer	X [mm]	Y [mm]	Z [mm]	S1 [N/mm^2]
Load cas...	1	0	2996	550	1	100	139	4.44089e-16	38.042
Load cas...	1	0	3012	550	1	100	139	4.44089e-16	38.0391

Flat – 2

Loads: 237N + Global self-weight

Deformations (as seen from above):

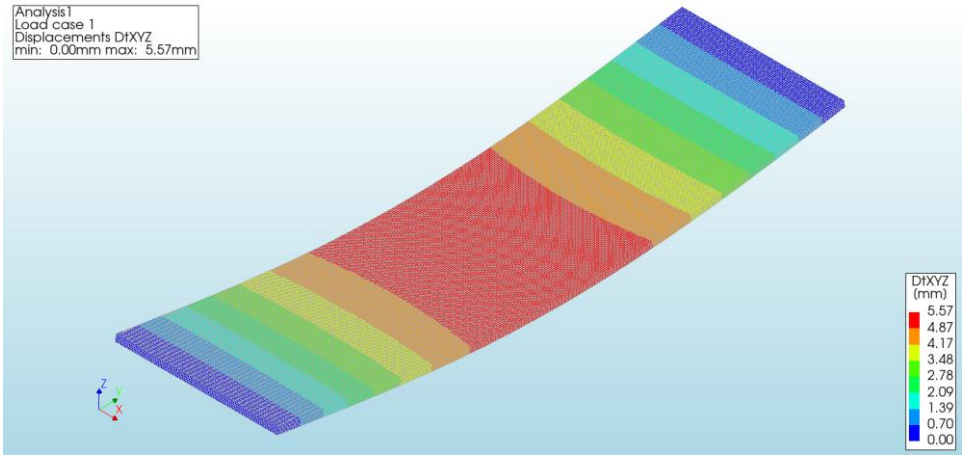

- Deformation at place of loading: 4.26mm

case	case id	case value	node	X [mm]	Y [mm]	Z [mm]	DtXYZ [mm]
Load cas...	1	0	1	74.1943	125	5.72	4.2618
Load cas...	1	0	2	25.8057	125	5.72	4.26178
Load cas...	1	0	3	74.1943	225	5.72	4.26037
Load cas...	1	0	4	25.8057	225	5.72	4.2605

Tensile principal stresses (as seen from below):

- Note: Without peak stresses acting

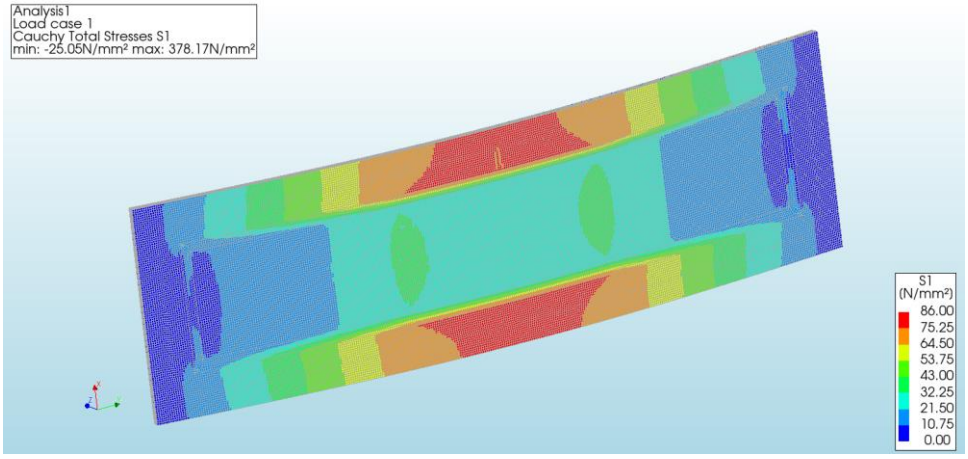

- Tensile principal stress at place of initiation of failure: 60 N/mm^2

case	case id	case value	element	node	layer	X [mm]	Y [mm]	Z [mm]	S1 [N/mm²]
Load cas...	1	0	3012	551	1	100	140	0	59.5277
Load cas...	1	0	3028	551	1	100	140	0	59.5224

Flat – 3

Loads: 85N + Global self-weight

Deformations (as seen from above):

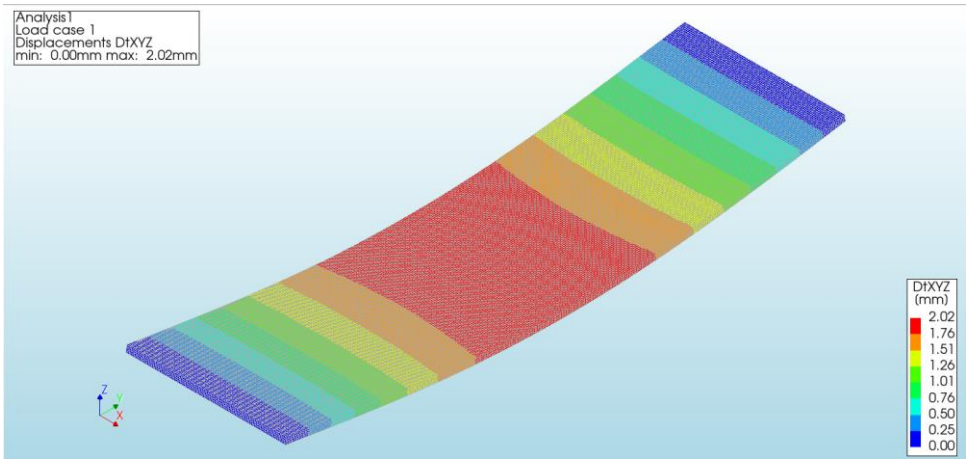

- Deformation at place of loading: 1.82mm

case	case id	case value	node	X [mm]	Y [mm]	Z [mm]	DtXYZ [mm]
Load cas...	1	0	1	0	225	3.89	1.81792
Load cas...	1	0	2	0	125	3.89	1.81851
Load cas...	1	0	3	100	225	3.89	1.81792
Load cas...	1	0	4	100	125	3.89	1.81851

Tensile principal stresses (as seen from below):

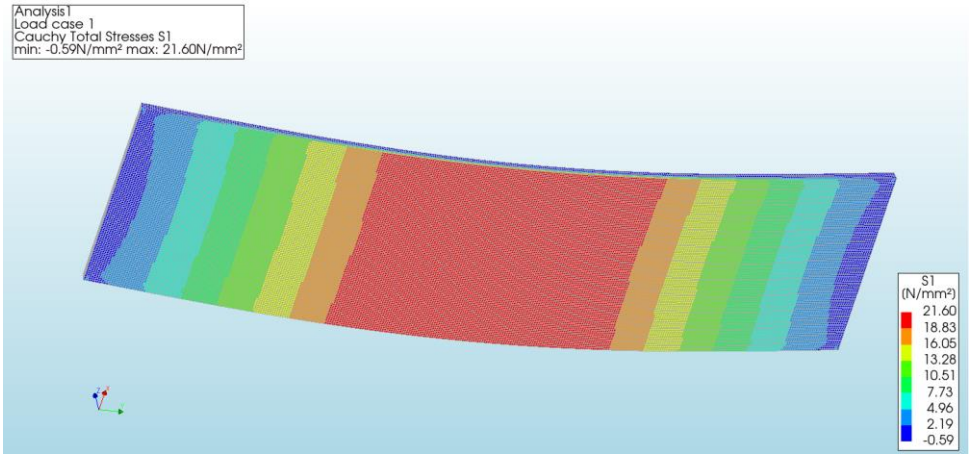

- Tensile principal stress at place of initiation of failure: 22 N/mm^2

case	case id	case value	element	node	layer	X [mm]	Y [mm]	Z [mm]	S1 [N/mm^2]
Load cas...	1	0	2996	550	1	100	139	4.44089e-16	21.549
Load cas...	1	0	3012	550	1	100	139	4.44089e-16	21.548

Flat – 4

Loads: 336N + Global self-weight

Deformations (as seen from above):

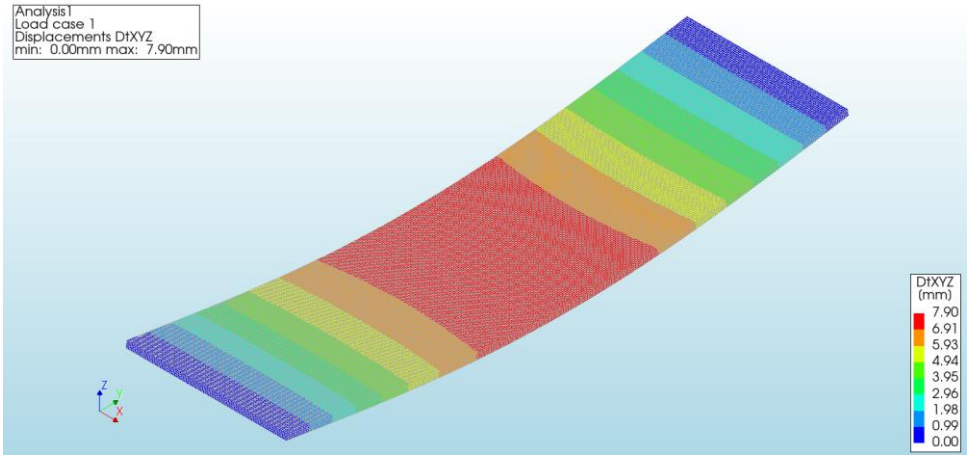

- Deformation at place of loading: 7.12mm

case	case id	case value	node	X [mm]	Y [mm]	Z [mm]	DtXYZ [mm]
Load cas...	1	0	1	0	225	3.89	7.12318
Load cas...	1	0	2	0	125	3.89	7.12548
Load cas...	1	0	3	100	225	3.89	7.12318
Load cas...	1	0	4	100	125	3.89	7.12548

Tensile principal stresses (as seen from below):

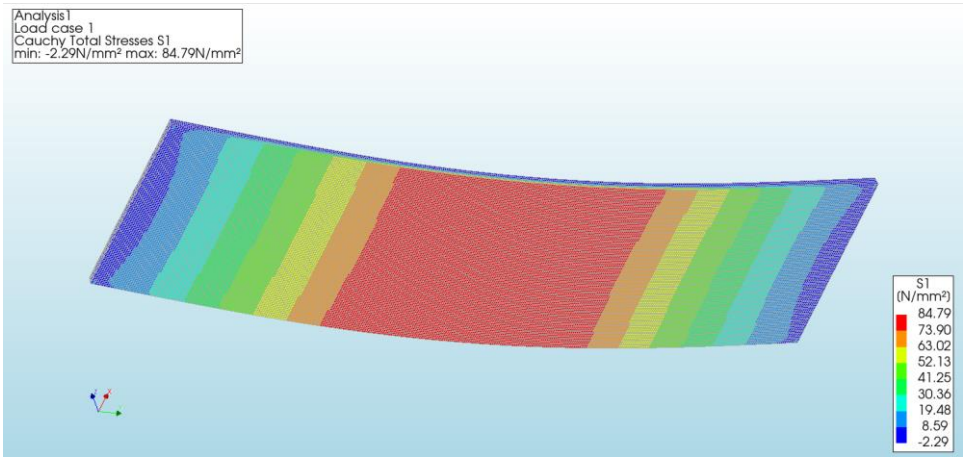

- Tensile principal stress at place of initiation of failure: 84 N/mm^2

case	case id	case value	element	node	layer	X [mm]	Y [mm]	Z [mm]	S1 [N/mm^2]
Load cas...	1	0	3268	567	1	100	156	4.44089e-16	84.4089
Load cas...	1	0	3284	567	1	100	156	4.44089e-16	84.4042

Shallow – 1

Loads: 320N + Global self-weight

Deformations (as seen from above):

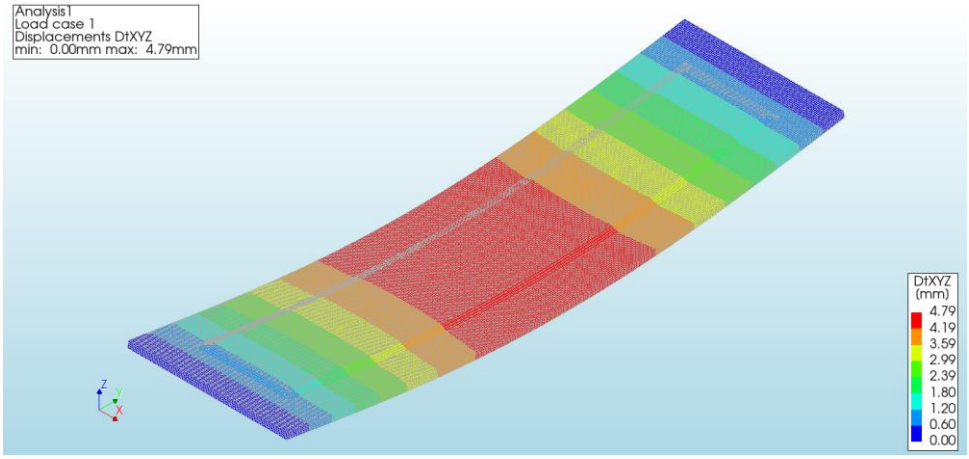

- Deformation at place of loading: 7.12mm

case	case id	case value	node	X [mm]	Y [mm]	Z [mm]	DtXYZ [mm]
Load cas...	1	0	1	0	225	3.89	7.12318
Load cas...	1	0	2	0	125	3.89	7.12548
Load cas...	1	0	3	100	225	3.89	7.12318
Load cas...	1	0	4	100	125	3.89	7.12548

Tensile principal stresses (as seen from below):

Note: Numerical peak stresses occurring at infinitely-small areas are discarded.

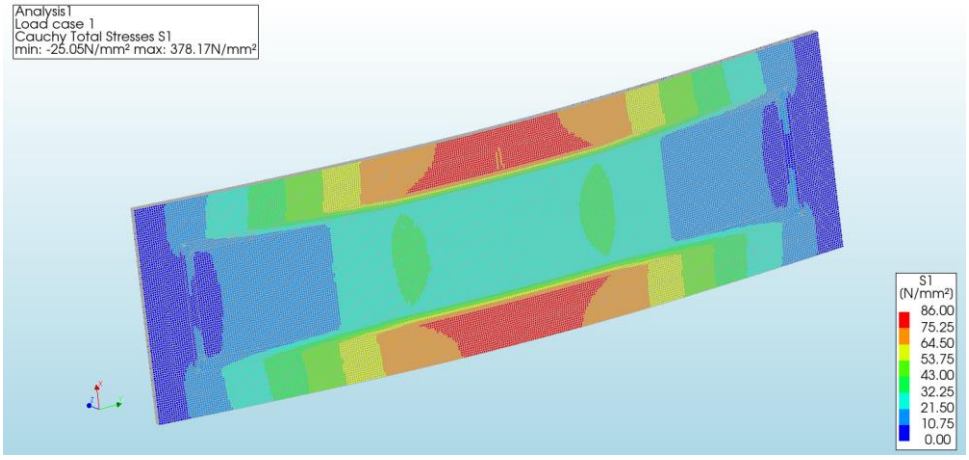

- Tensile principal stress at place of initiation of failure: 73 N/mm^2

case	case id	case value	element	node	layer	X [mm]	Y [mm]	Z [mm]	S1 [N/mm^2]
Load cas...	1	0	2865	1506	1	100	131	-4.44089e-16	73.2582
Load cas...	1	0	2881	1506	1	100	131	-4.44089e-16	73.4711

Shallow – 2

Loads: 179N + Global self-weight

Deformations (as seen from above):

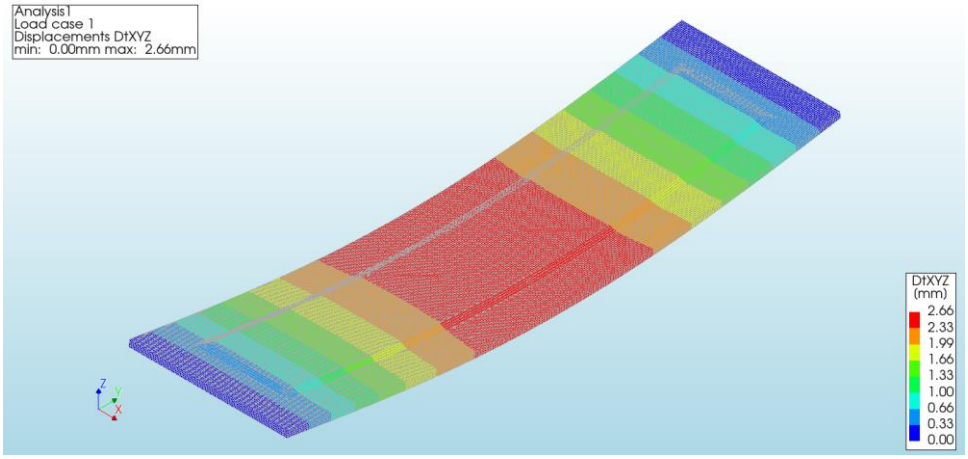

- Deformation at place of loading: 2.37mm

case	case id	case value	node	X [mm]	Y [mm]	Z [mm]	DtXYZ [mm]
Load cas...	1	0	1	74.53	125	5.76	2.36739
Load cas...	1	0	2	25.47	125	5.76	2.36732
Load cas...	1	0	3	74.53	225	5.76	2.36639
Load cas...	1	0	4	25.47	225	5.76	2.36637

Tensile principal stresses (as seen from below):

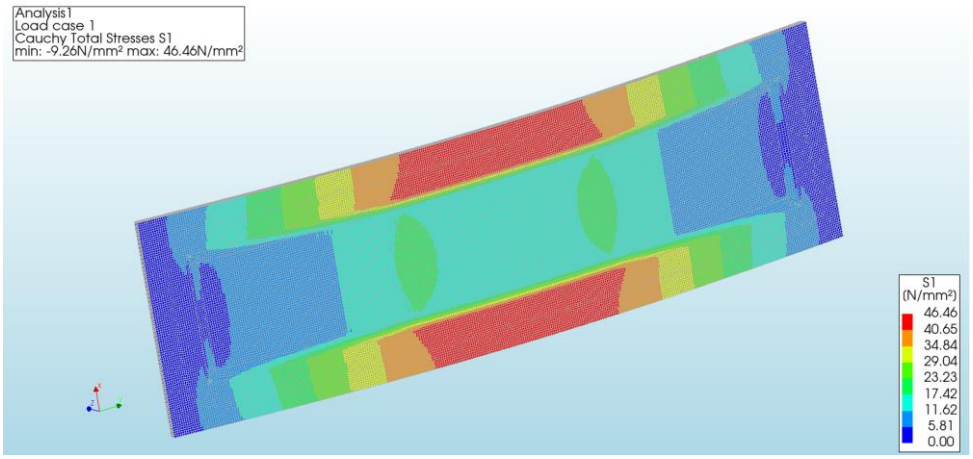

- Tensile principal stress at place of initiation of failure: 42 N/mm^2

case	case id	case value	element	node	layer	X [mm]	Y [mm]	Z [mm]	S1 [N/mm^2]
Load cas...	1	0	3180	1527	1	100	150	0	42.349
Load cas...	1	0	3196	1527	1	100	150	0	42.3727

Shallow – 3

Loads: 250N + Global self-weight

Deformations (as seen from above):

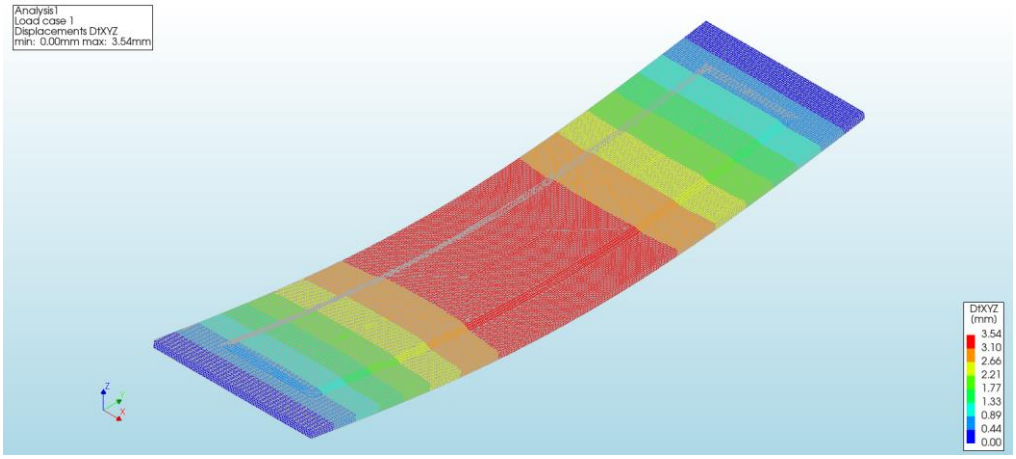

- Deformation at place of loading: 3.15mm

case	case id	case value	node	X [mm]	Y [mm]	Z [mm]	DtXYZ [mm]
Load case 1	1	0	1	74.3455	225	5.87	3.15348
Load case 1	1	0	2	25.6545	225	5.87	3.1535
Load case 1	1	0	3	74.3455	125	5.87	3.15537
Load case 1	1	0	4	25.6545	125	5.87	3.15536

Tensile principal stresses (as seen from below):

Note: Numerical peak stresses occurring at infinitely-small areas are discarded.

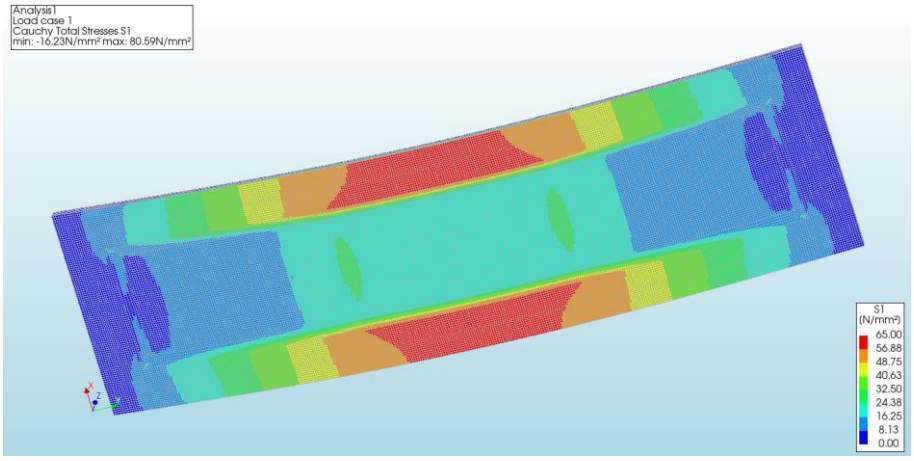

- Tensile principal stress at place of initiation of failure: 56 N/mm^2

case	case id	case value	element	node	layer	X [mm]	Y [mm]	Z [mm]	S1 [N/mm^2]
Load case 1	1	0	2916	1511	1	100	134	0	56.2261
Load case 1	1	0	2932	1511	1	100	134	0	56.3539

Shallow – 4

Loads: 353N + Global self-weight

Deformations (as seen from above):

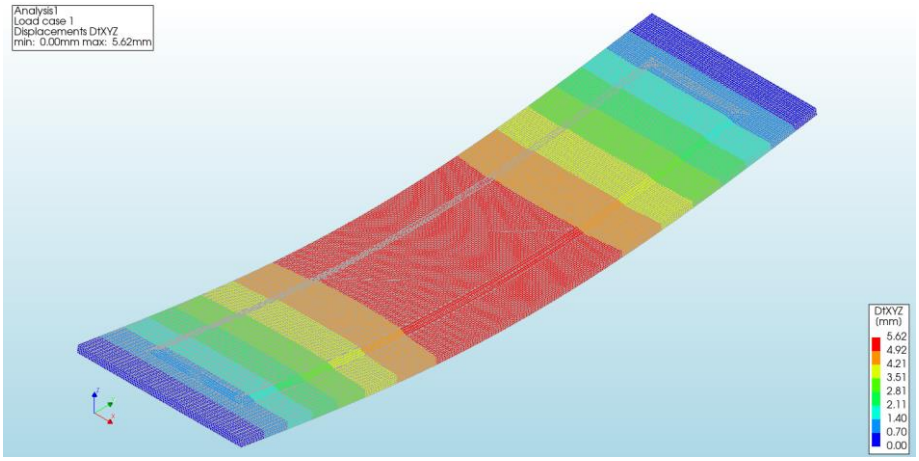

- Deformation at place of loading: 5.00mm

case	case id	case value	node	X [mm]	Y [mm]	Z [mm]	DtXYZ [mm]
Load case 1	1	0	1	74.4543	225	5.57	4.99856
Load case 1	1	0	2	25.5457	225	5.57	4.99859
Load case 1	1	0	3	74.4543	125	5.57	5.00161
Load case 1	1	0	4	25.5457	125	5.57	5.00156

Tensile principal stresses (as seen from below):

Note: Numerical peak stresses occurring at infinitely-small areas are discarded.

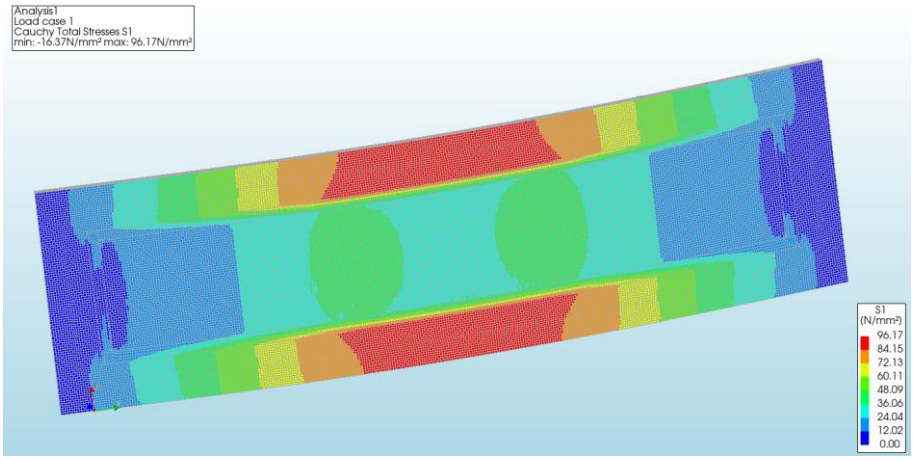

- Tensile principal stress at place of initiation of failure: 84 N/mm^2

case	case id	case value	element	node	layer	X [mm]	Y [mm]	Z [mm]	S1 [N/mm^2]
Load case 1	1	0	1456	1509	1	100	132	0	84.22
Load case 1	1	0	1464	1509	1	100	132	0	84.4461

Shallow – 5

Loads: 380N + Global self-weight

Deformations (as seen from above):

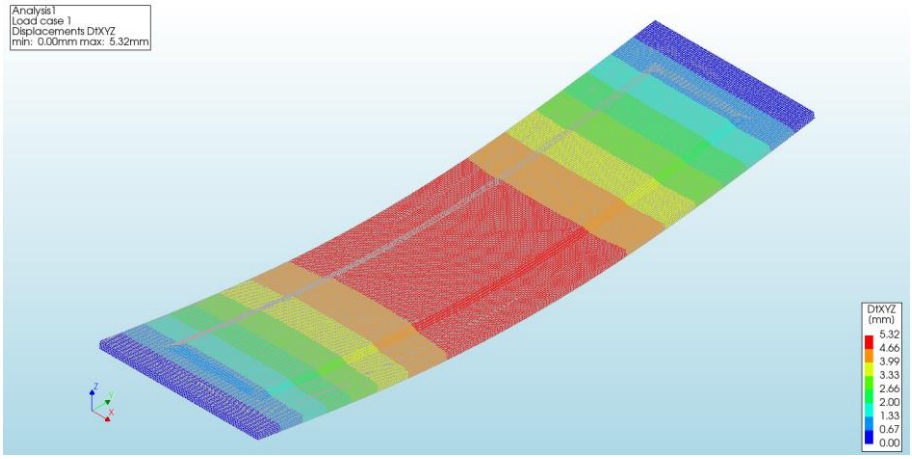

- Deformation at place of loading: 4.74mm

case	case id	case value	node	X [mm]	Y [mm]	Z [mm]	DtXYZ [mm]
Load case 1	1	0	1	74.6144	225	5.88	4.73638
Load case 1	1	0	2	25.3856	225	5.88	4.73638
Load case 1	1	0	3	74.6144	125	5.88	4.73956
Load case 1	1	0	4	25.3856	125	5.88	4.7396

Tensile principal stresses (as seen from below):

Note: Numerical peak stresses occurring at infinitely-small areas are discarded.

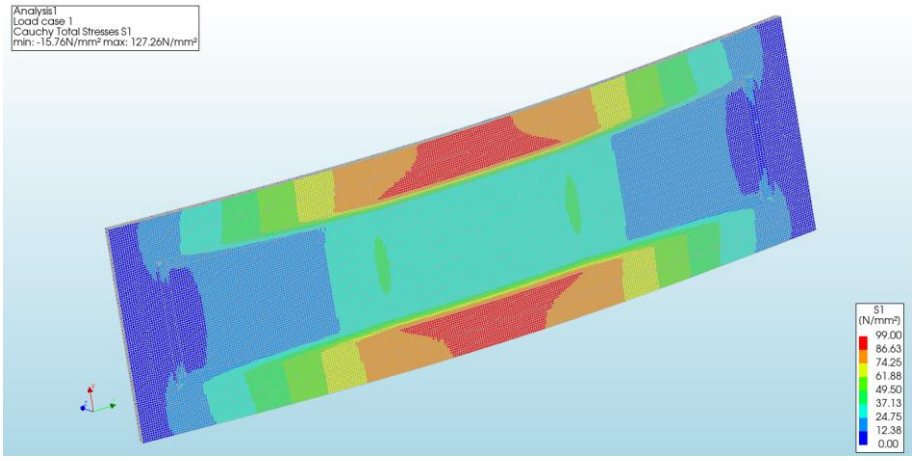

- Tensile principal stress at place of initiation of failure: 80 N/mm^2

case	case id	case value	element	node	layer	X [mm]	Y [mm]	Z [mm]	S1 [N/mm^2]
Load case 1	1	0	1358	1496	1	100	119	0	79.8337
Load case 1	1	0	1366	1496	1	100	119	0	80.2864

Shallow – 6

Loads: 390N + Global self-weight

Deformations (as seen from above):

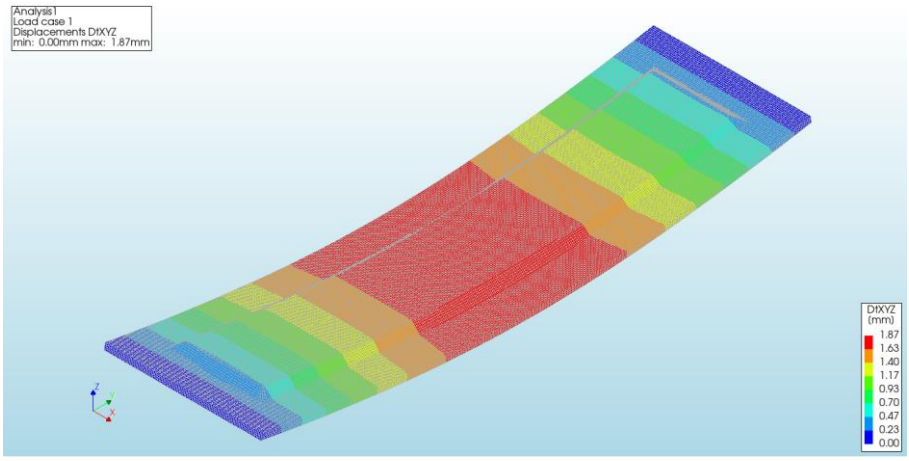

- Deformation at place of loading: 1.67mm

case	case id	case value	node	X [mm]	Y [mm]	Z [mm]	DtXYZ [mm]
Load case 1	1	0	1	74.2257	225	8.73	1.66481
Load case 1	1	0	2	25.7743	225	8.73	1.6648
Load case 1	1	0	3	74.2257	125	8.73	1.66713
Load case 1	1	0	4	25.7743	125	8.73	1.66711

Tensile principal stresses (as seen from below):

Note: Numerical peak stresses occurring at infinitely-small areas are discarded.

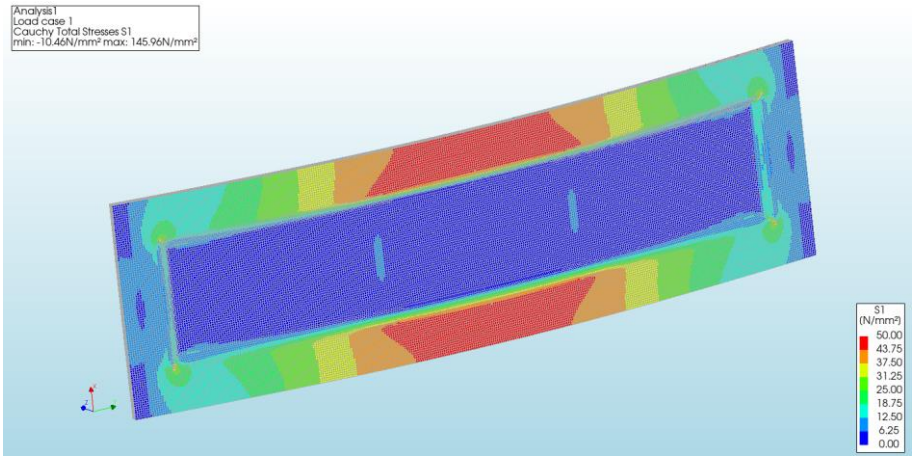

- Tensile principal stress at place of initiation of failure: 35 N/mm^2

case	case id	case value	element	node	layer	X [mm]	Y [mm]	Z [mm]	S1 [N/mm^2]
Load case 1	1	0	1187	1482	1	100	98	0	34.5194
Load case 1	1	0	1195	1482	1	100	98	0	34.8729

Shallow – 7

Loads: 1001N + Global self-weight

Deformations (as seen from above):

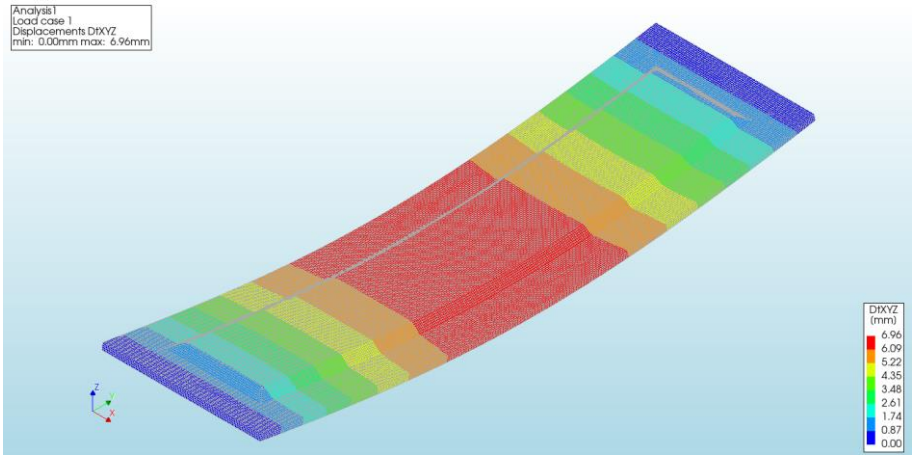

- Deformation at place of loading: 6.20mm

case	case id	case value	node	X [mm]	Y [mm]	Z [mm]	DtXYZ [mm]
Load case 1	1	0	1	74.1472	125	7.65	6.20491
Load case 1	1	0	2	25.8528	125	7.65	6.20462
Load case 1	1	0	3	74.1472	225	7.65	6.19652
Load case 1	1	0	4	25.8528	225	7.65	6.19653

Tensile principal stresses (as seen from below):

Note: Numerical peak stresses occurring at infinitely-small areas are discarded.

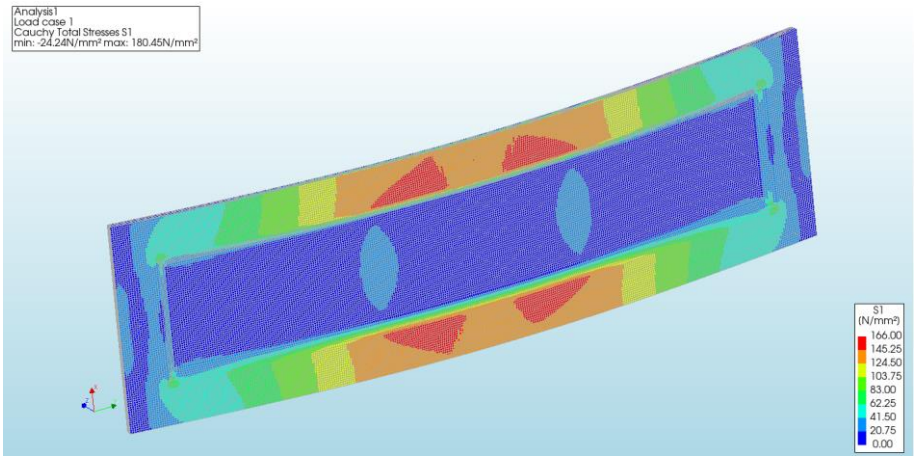

- Tensile principal stress at place of initiation of failure: 144 N/mm^2

case	case id	case value	element	node	layer	X [mm]	Y [mm]	Z [mm]	S1 [N/mm^2]
Load case 1	1	0	2576	1521	1	100	140	0	144.375
Load case 1	1	0	3023	1521	1	100	140	0	144.517

Shallow – 8

Loads: 497N + Global self-weight

Deformations (as seen from above):

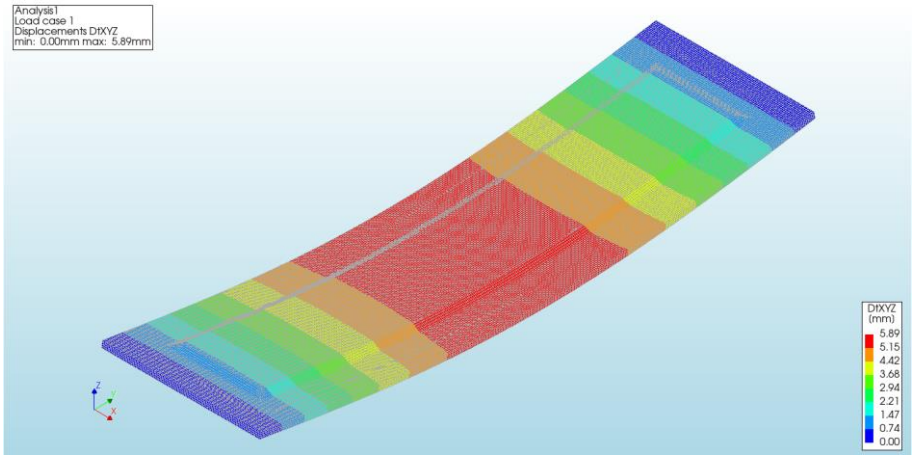

- Deformation at place of loading: 5.25mm

case	case id	case value	node	X [mm]	Y [mm]	Z [mm]	DtXYZ [mm]
Load case 1	1	0	1	74.4663	225	6.29	5.24308
Load case 1	1	0	2	74.4663	125	6.29	5.24797
Load case 1	1	0	3	74.4663	225	6.29	5.24308
Load case 1	1	0	4	74.4663	125	6.29	5.24797

Tensile principal stresses (as seen from below):

Note: Numerical peak stresses occurring at infinitely-small areas are discarded.

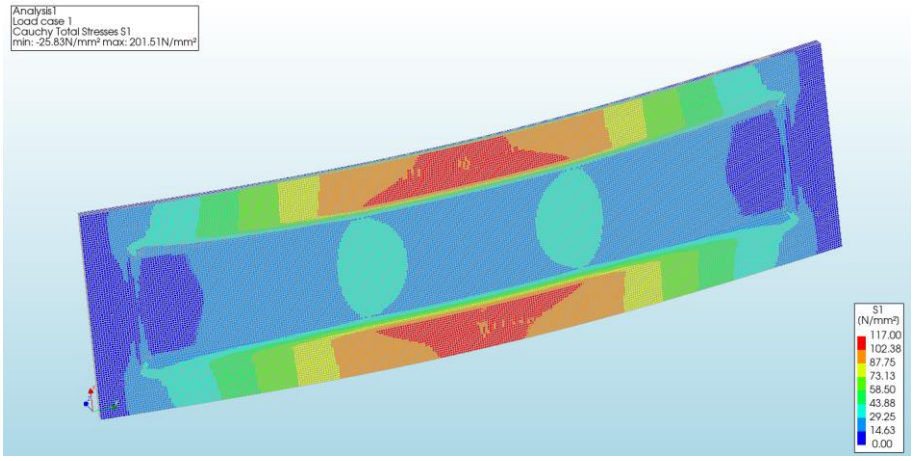

- Tensile principal stress at place of initiation of failure: 63 N/mm^2

case	case id	case value	element	node	layer	X [mm]	Y [mm]	Z [mm]	S1 [N/mm^2]
Load case 1	1	0	1021	1458	1	100	77	0	62.6136
Load case 1	1	0	1029	1458	1	100	77	0	63.4572

Shallow – 9

Loads: 443N + Global self-weight

Deformations (as seen from above):

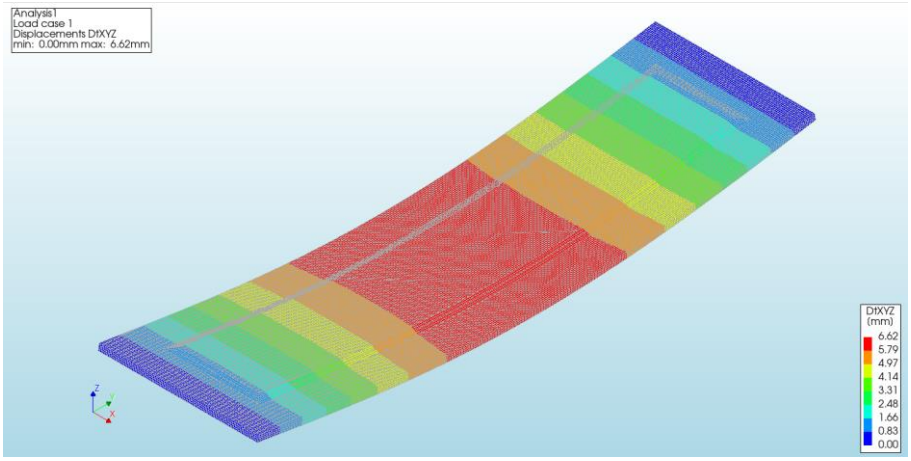

- Deformation at place of loading: 5.89mm

case	case id	case value	node	X [mm]	Y [mm]	Z [mm]	DtXYZ [mm]
Load case 1	1	0	1	74.4282	225	5.72	5.89261
Load case 1	1	0	2	25.5718	225	5.72	5.89267
Load case 1	1	0	3	74.4282	125	5.72	5.89516
Load case 1	1	0	4	25.5718	125	5.72	5.89568

Tensile principal stresses (as seen from below):

Note: Numerical peak stresses occurring at infinitely-small areas are discarded.

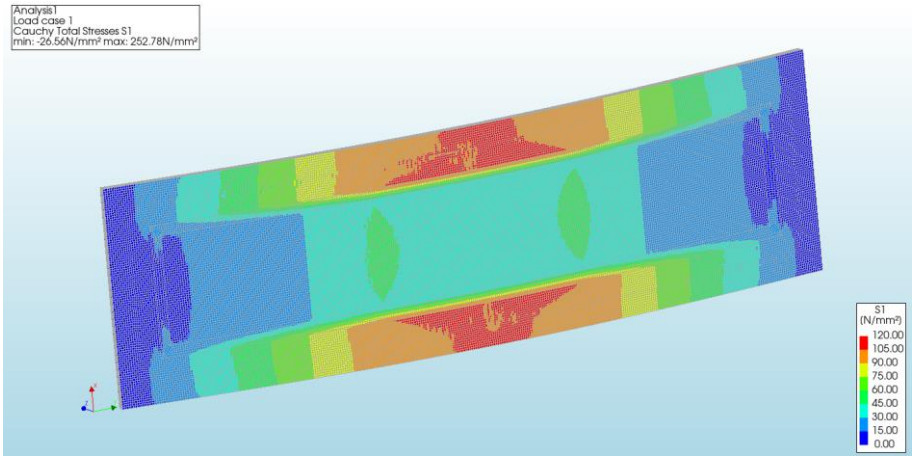

- Tensile principal stress at place of initiation of failure: 102 N/mm^2

case	case id	case value	element	node	layer	X [mm]	Y [mm]	Z [mm]	S1 [N/mm^2]
Load case 1	1	0	2908	1510	1	100	133	0	102.135
Load case 1	1	0	2924	1510	1	100	133	0	102.391

Shallow – 10

Loads: 300N + Global self-weight

Deformations (as seen from above):

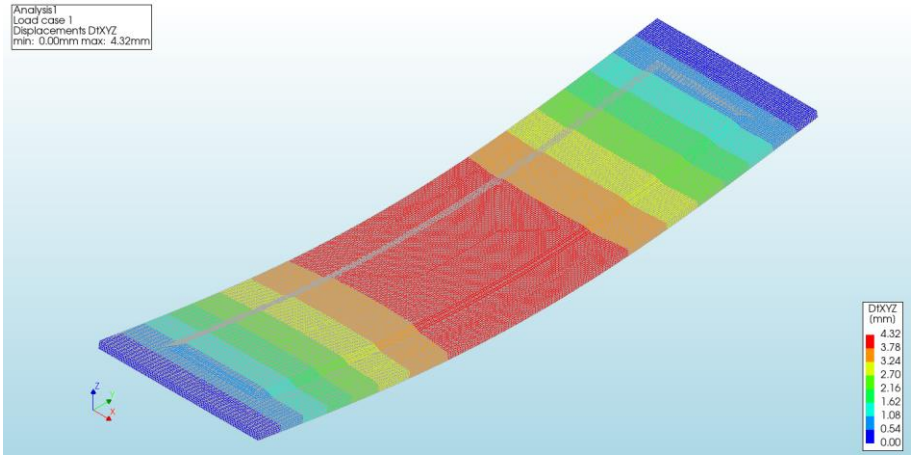

- Deformation at place of loading: 3.84mm

case	case id	case value	node	X [mm]	Y [mm]	Z [mm]	DtXYZ [mm]
Load case 1	1	0	1	74.7067	125	5.81	3.84514
Load case 1	1	0	2	25.2933	125	5.81	3.84561
Load case 1	1	0	3	74.7067	225	5.81	3.84362
Load case 1	1	0	4	25.2933	225	5.81	3.8437

Tensile principal stresses (as seen from below):

Note: Numerical peak stresses occurring at infinitely-small areas are discarded.

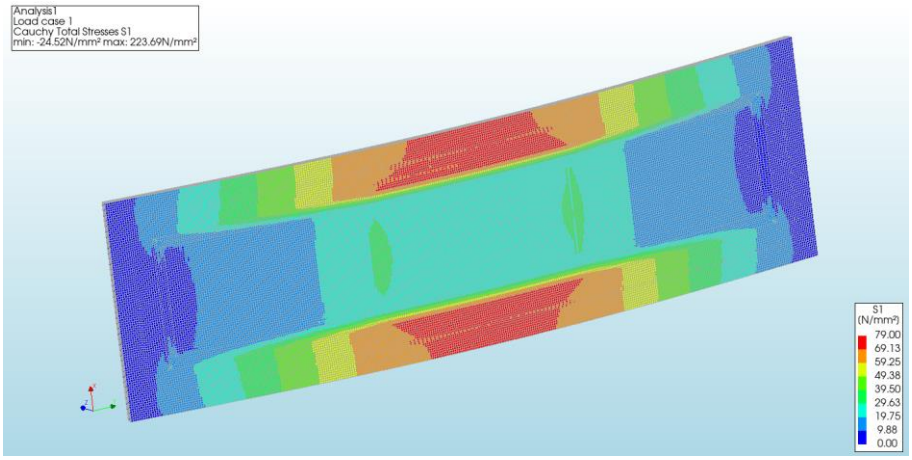

- Tensile principal stress at place of initiation of failure: 65 N/mm^2

case	case id	case value	element	node	layer	X [mm]	Y [mm]	Z [mm]	S1 [N/mm^2]
Load case 1	1	0	1364	1497	1	100	120	0	64.3848
Load case 1	1	0	1372	1497	1	100	120	0	64.7303

Deep - 1

Loads: 899N + Global self-weight

Deformations (as seen from above):

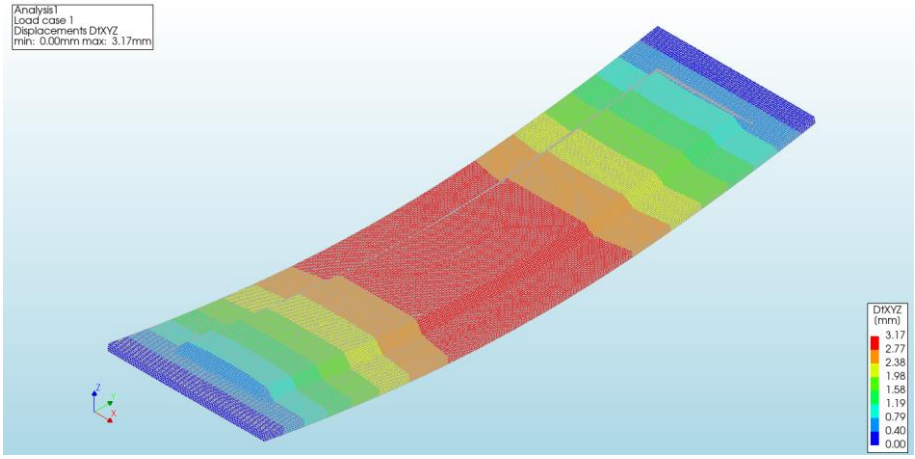

- Deformation at place of loading: 2.82mm

case	case id	case value	node	X [mm]	Y [mm]	Z [mm]	DtXYZ [mm]
Load case 1	1	0	1	73.7161	225	9.8	2.81871
Load case 1	1	0	2	26.2839	225	9.8	2.81856
Load case 1	1	0	3	73.7161	125	9.8	2.82379
Load case 1	1	0	4	26.2839	125	9.8	2.82366

Tensile principal stresses (as seen from below):

Note: Numerical peak stresses occurring at infinitely-small areas are discarded.

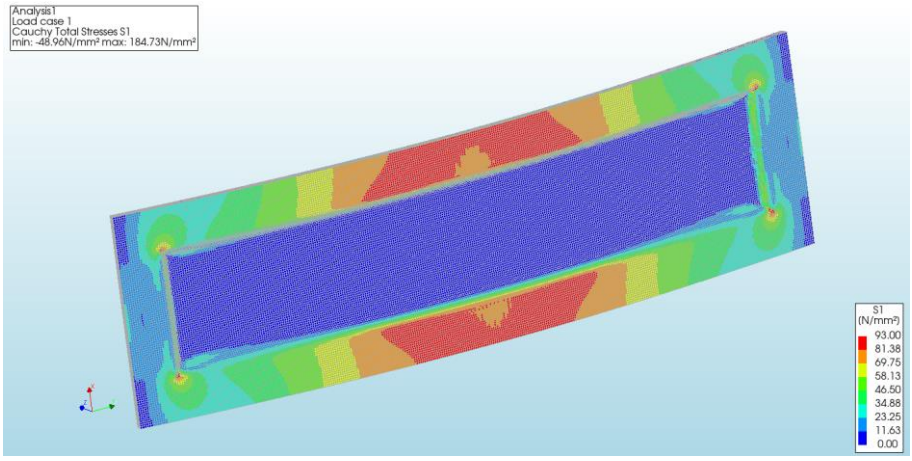

- Tensile principal stress at place of initiation of failure: 82 N/mm^2

case	case id	case value	element	node	layer	X [mm]	Y [mm]	Z [mm]	S1 [N/mm^2]
Load case 1	1	0	3577	1557	1	100	175	0	81.6384
Load case 1	1	0	3578	1557	1	100	175	0	81.6373

Deep - 2

Loads: 400N + Global self-weight

Deformations (as seen from above):

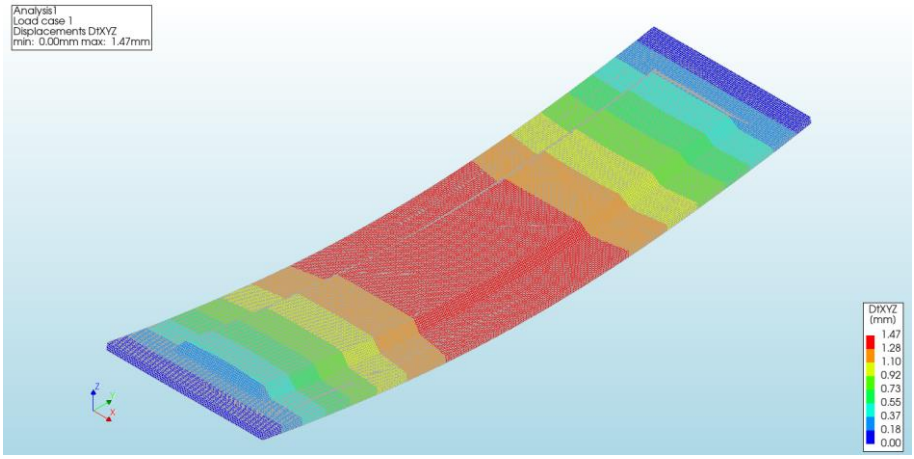

- Deformation at place of loading: 1.31mm

case	case id	case value	node	X [mm]	Y [mm]	Z [mm]	DtXYZ [mm]
Load case 1	1	0	1	73.4787	225	9.7	1.30551
Load case 1	1	0	2	26.5213	225	9.7	1.30554
Load case 1	1	0	3	73.4787	125	9.7	1.30796
Load case 1	1	0	4	26.5213	125	9.7	1.30793

Tensile principal stresses (as seen from below):

Note: Numerical peak stresses occurring at infinitely-small areas are discarded.

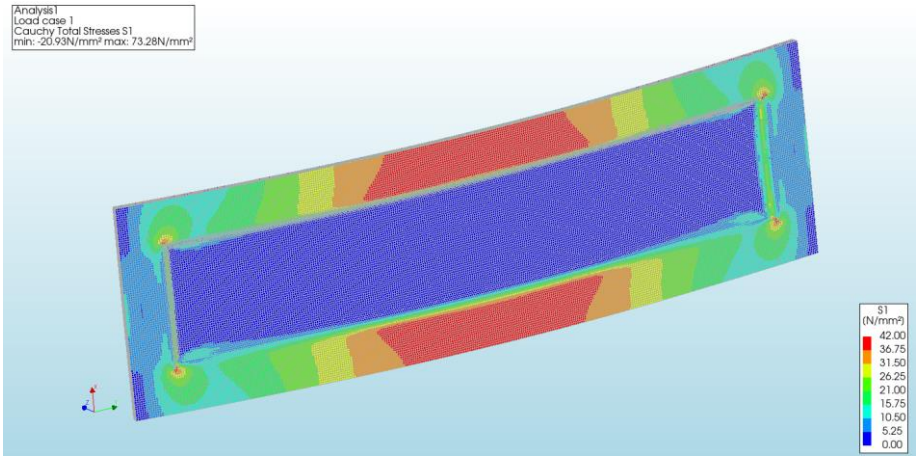

- Tensile principal stress at place of initiation of failure: 37 N/mm^2

case	case id	case value	element	node	layer	X [mm]	Y [mm]	Z [mm]	S1 [N/mm^2]
Load case 1	1	0	3068	1526	1	100	144	0	37.4766
Load case 1	1	0	3084	1526	1	100	144	0	37.4841

Deep - 3

Loads: 459N + Global self-weight

Deformations (as seen from above):

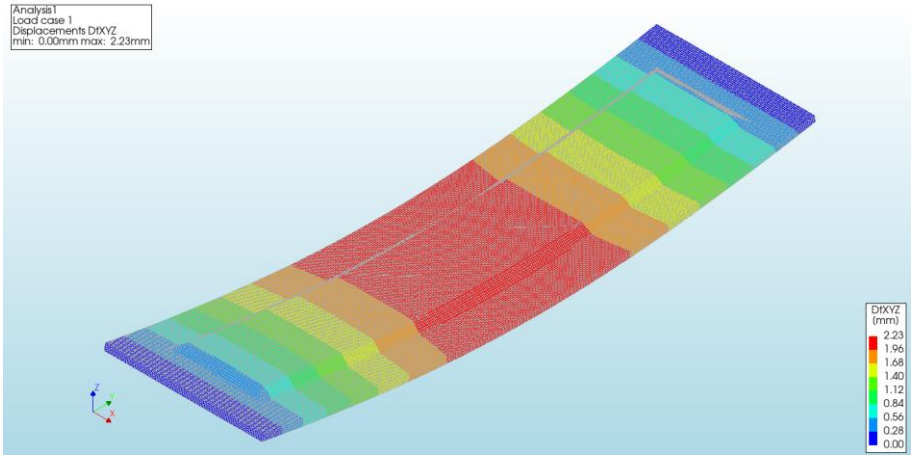

- Deformation at place of loading: 1.99mm

case	case id	case value	node	X [mm]	Y [mm]	Z [mm]	DtXYZ [mm]
Load case 1	1	0	1	73.4276	225	8.75	1.98914
Load case 1	1	0	2	26.5724	225	8.75	1.98916
Load case 1	1	0	3	73.4276	125	8.75	1.99203
Load case 1	1	0	4	26.5724	125	8.75	1.99199

Tensile principal stresses (as seen from below):

Note: Numerical peak stresses occurring at infinitely-small areas are discarded.

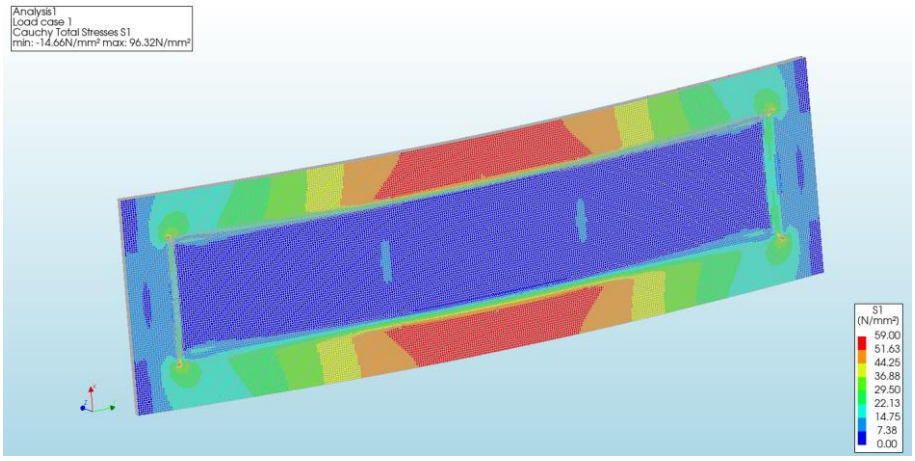

- Tensile principal stress at place of initiation of failure: 52 N/mm^2

case	case id	case value	element	node	layer	X [mm]	Y [mm]	Z [mm]	S1 [N/mm^2]
Load case 1	1	0	1530	1517	1	100	135	0	51.6818
Load case 1	1	0	1538	1517	1	100	135	0	51.7668

Deep - 4

Loads: 453N + Global self-weight

Deformations (as seen from above):

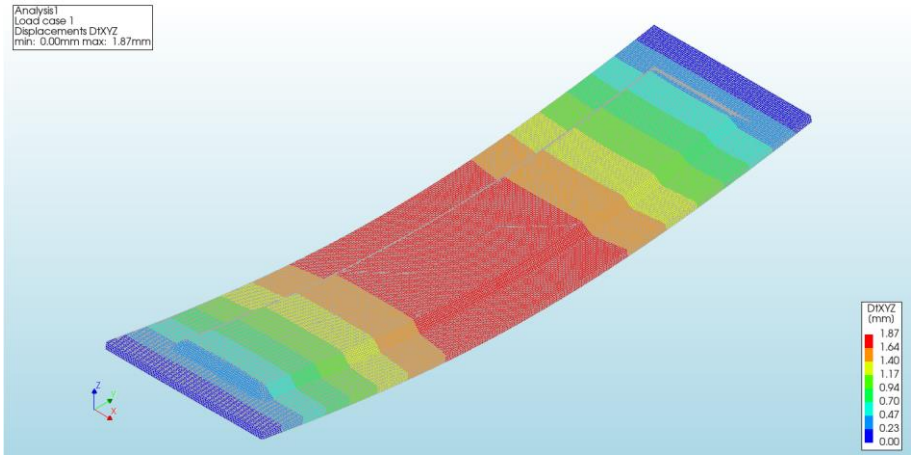

- Deformation at place of loading: 1.67mm

case	case id	case value	node	X [mm]	Y [mm]	Z [mm]	DtXYZ [mm]
Load case 1	1	0	1	74.3754	225	9.19	1.66944
Load case 1	1	0	2	25.6246	225	9.19	1.66933
Load case 1	1	0	3	74.3754	125	9.19	1.67197
Load case 1	1	0	4	25.6246	125	9.19	1.67198

Tensile principal stresses (as seen from below):

Note: Numerical peak stresses occurring at infinitely-small areas are discarded.

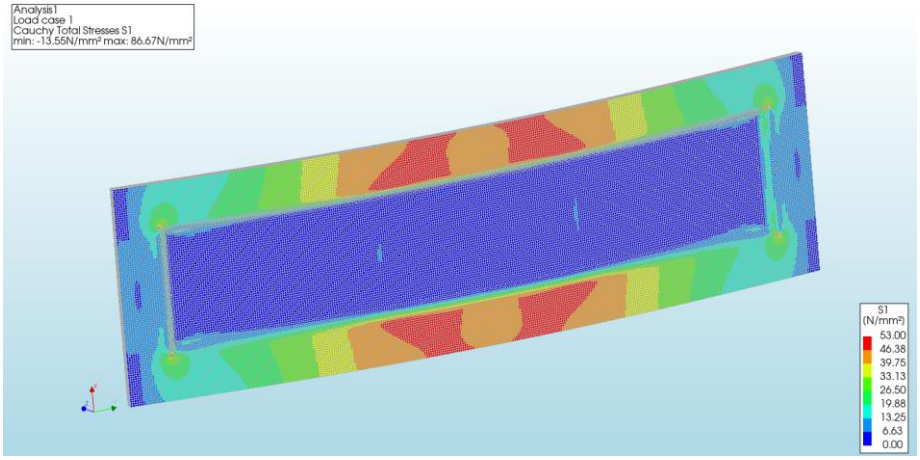

- Tensile principal stress at place of initiation of failure: 46 N/mm^2

case	case id	case value	element	node	layer	X [mm]	Y [mm]	Z [mm]	S1 [N/mm^2]
Load case 1	1	0	1729	1550	1	100	164	0	46.3899
Load case 1	1	0	1735	1550	1	100	164	0	46.3832

Deep - 5

Loads: 472N + Global self-weight

Deformations (as seen from above):

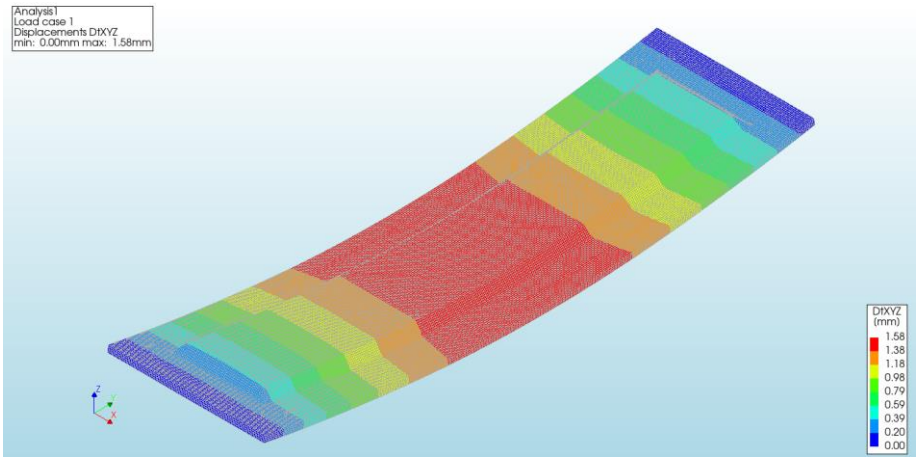

- Deformation at place of loading: 1.40mm

case	case id	case value	node	X [mm]	Y [mm]	Z [mm]	DtXYZ [mm]
Load case 1	1	0	1	73.5665	225	10.04	1.39911
Load case 1	1	0	2	26.4335	225	10.04	1.39914
Load case 1	1	0	3	73.5665	125	10.04	1.40173
Load case 1	1	0	4	26.4335	125	10.04	1.4018

Tensile principal stresses (as seen from below):

Note: Numerical peak stresses occurring at infinitely-small areas are discarded.

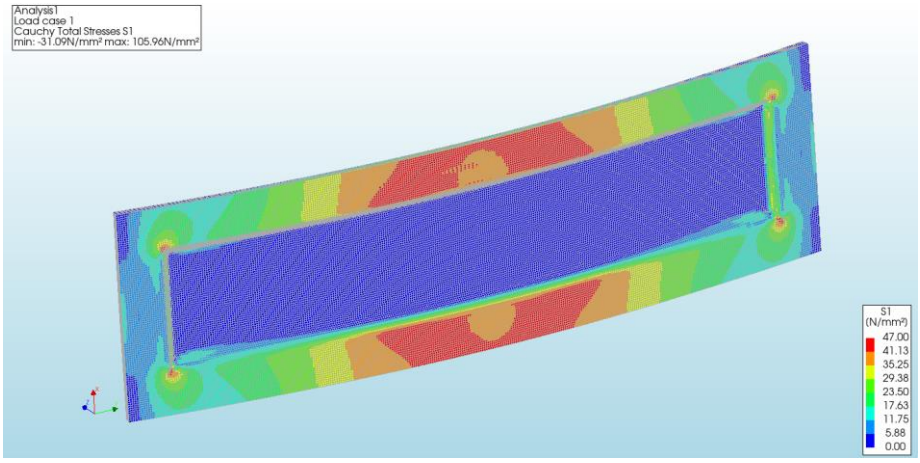

- Tensile principal stress at place of initiation of failure: 38 N/mm^2

case	case id	case value	element	node	layer	X [mm]	Y [mm]	Z [mm]	S1 [N/mm^2]
Load case 1	1	0	1307	1503	1	100	115	4.44089e-16	37.8174
Load case 1	1	0	1315	1503	1	100	115	4.44089e-16	38.0824

Deep - 6

Loads: 418N + Global self-weight

Deformations (as seen from above):

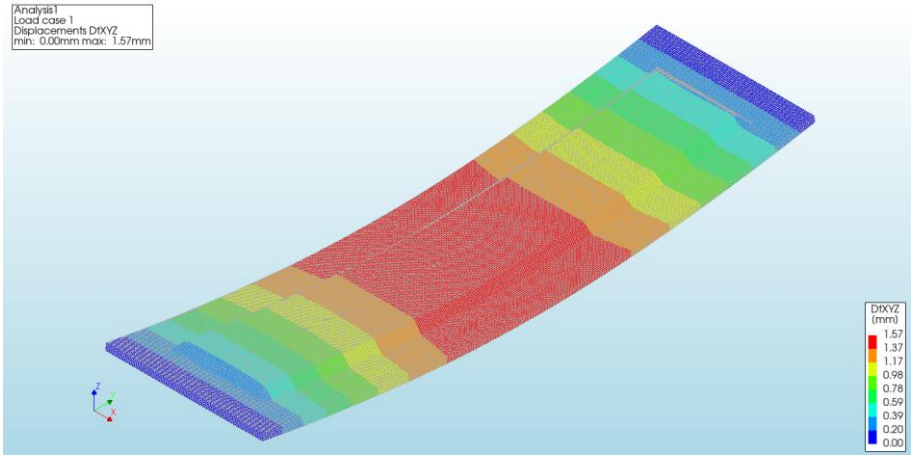

- Deformation at place of loading: 1.39mm

case	case id	case value	node	X [mm]	Y [mm]	Z [mm]	DtXYZ [mm]
Load case 1	1	0	1	73.7731	225	9.59	1.39304
Load case 1	1	0	2	26.2269	225	9.59	1.39311
Load case 1	1	0	3	73.7731	125	9.59	1.39558
Load case 1	1	0	4	26.2269	125	9.59	1.39565

Tensile principal stresses (as seen from below):

Note: Numerical peak stresses occurring at infinitely-small areas are discarded.

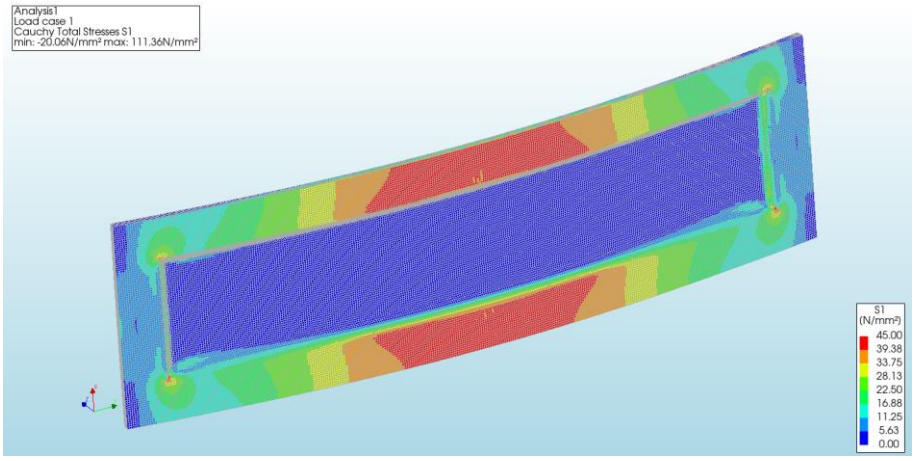

- Tensile principal stress at place of initiation of failure: 36 N/mm^2

case	case id	case value	element	node	layer	X [mm]	Y [mm]	Z [mm]	S1 [N/mm^2]
Load case 1	1	0	1283	1496	1	100	112	-4.44089e-16	35.5257
Load case 1	1	0	1291	1496	1	100	112	-4.44089e-16	35.8005

Deep - 7

Loads: 590N + Global self-weight

Deformations (as seen from above):

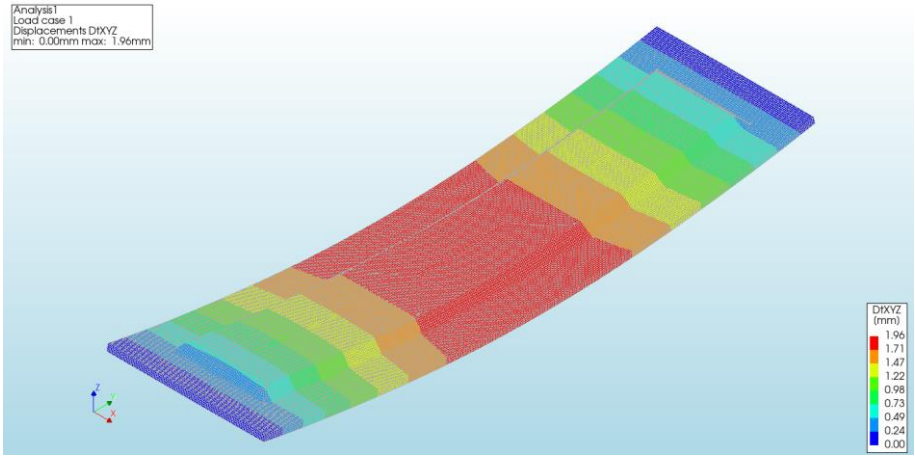

- Deformation at place of loading: 1.74mm

case	case id	case value	node	X [mm]	Y [mm]	Z [mm]	DtXYZ [mm]
Load case 1	1	0	1	73.2701	225	10.12	1.7347
Load case 1	1	0	2	26.7299	225	10.12	1.7347
Load case 1	1	0	3	73.2701	125	10.12	1.73801
Load case 1	1	0	4	26.7299	125	10.12	1.73767

Tensile principal stresses (as seen from below):

Note: Numerical peak stresses occurring at infinitely-small areas are discarded.

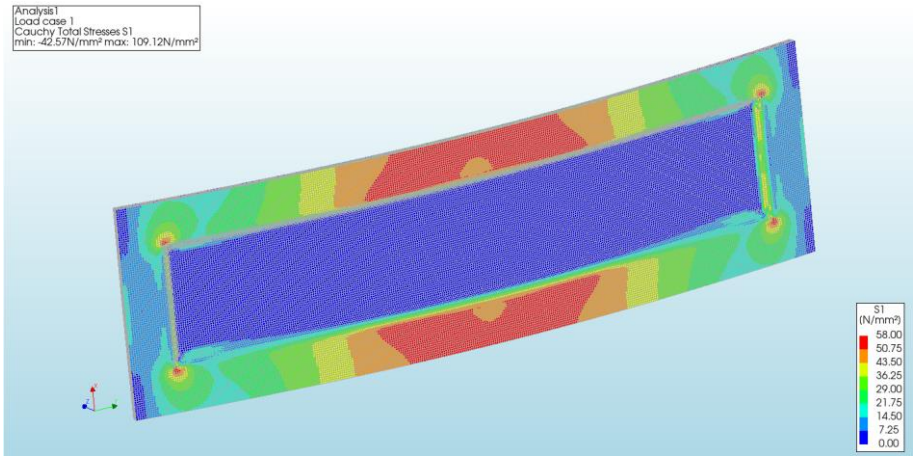

- Tensile principal stress at place of initiation of failure: 51 N/mm^2

case	case id	case value	element	node	layer	X [mm]	Y [mm]	Z [mm]	S1 [N/mm^2]
Load case 1	1	0	1676	1547	1	100	159	-4.44089e-16	51.1611
Load case 1	1	0	1684	1547	1	100	159	-4.44089e-16	51.1446

Deep - 8

Loads: 483N + Global self-weight

Deformations (as seen from above):

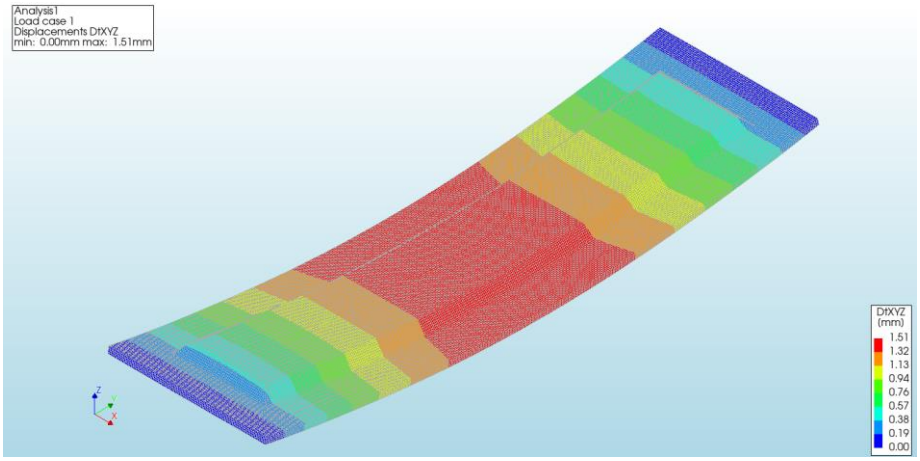

- Deformation at place of loading: 1.34mm

case	case id	case value	node	X [mm]	Y [mm]	Z [mm]	DtXYZ [mm]
Load case 1	1	0	1	73.2146	225	10.36	1.33789
Load case 1	1	0	2	26.7854	225	10.36	1.33768
Load case 1	1	0	3	73.2146	125	10.36	1.34084
Load case 1	1	0	4	26.7854	125	10.36	1.34035

Tensile principal stresses (as seen from below):

Note: Numerical peak stresses occurring at infinitely-small areas are discarded.

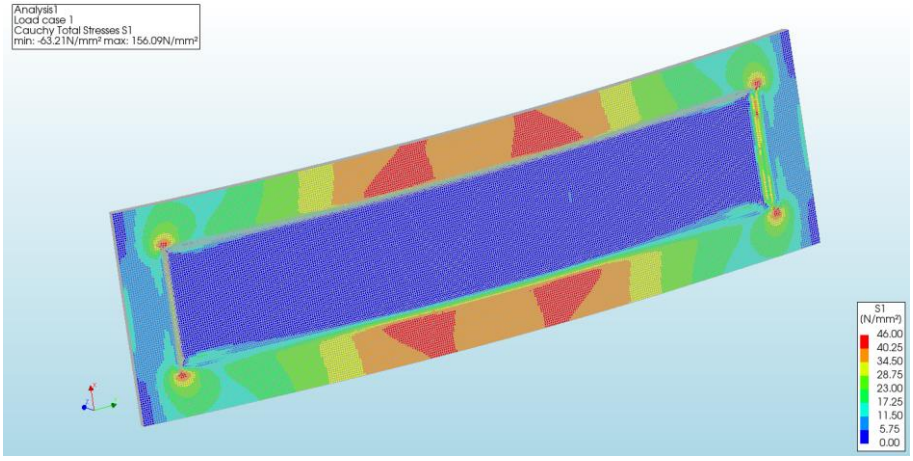

- Tensile principal stress at place of initiation of failure: 40 N/mm^2

case	case id	case value	element	node	layer	X [mm]	Y [mm]	Z [mm]	S1 [N/mm^2]
Load case 1	1	0	1507	1523	1	100	137	0	40.151
Load case 1	1	0	1515	1523	1	100	137	0	40.192

Deep - 9

Loads: 663N + Global self-weight

Deformations (as seen from above):

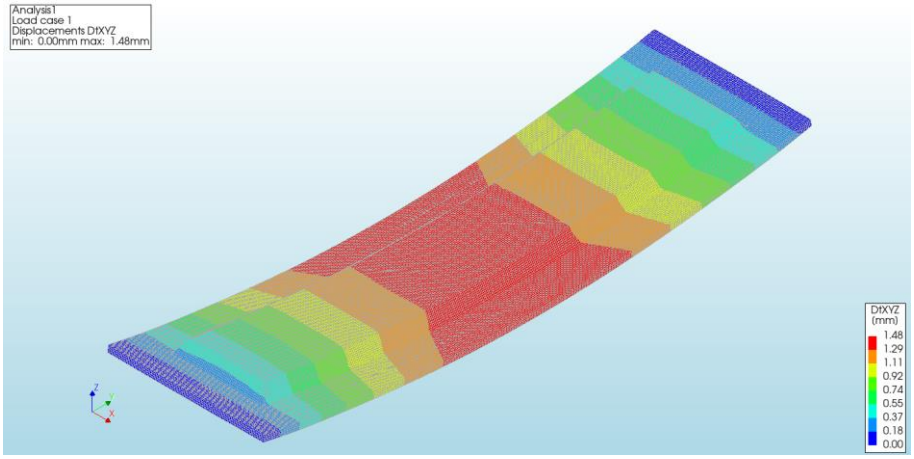

- Deformation at place of loading: 1.28mm

case	case id	case value	node	X [mm]	Y [mm]	Z [mm]	DtXYZ [mm]
Load case 1	1	0	1	73.4527	225	12.11	1.27519
Load case 1	1	0	2	26.5473	225	12.11	1.27422
Load case 1	1	0	3	73.4527	125	12.11	1.27829
Load case 1	1	0	4	26.5473	125	12.11	1.27754

Tensile principal stresses (as seen from below):

Note: Numerical peak stresses occurring at infinitely-small areas are discarded.

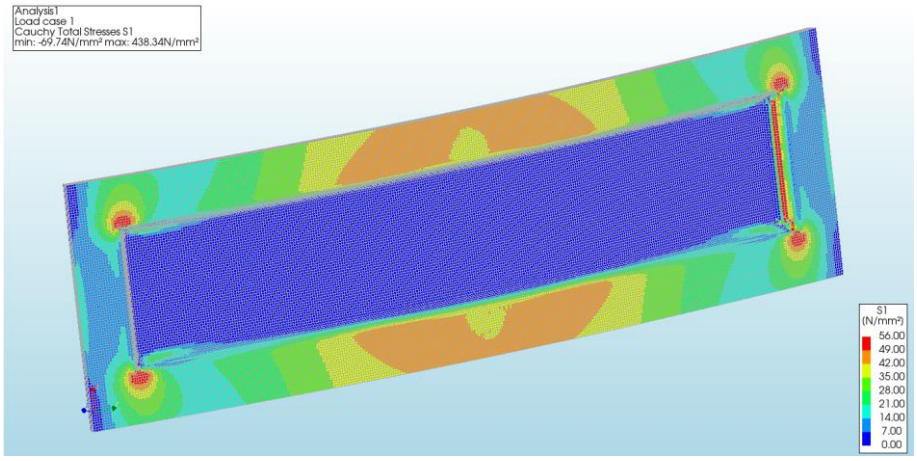

- Tensile principal stress at place of initiation of failure: 48 N/mm^2

case	case id	case value	element	node	layer	X [mm]	Y [mm]	Z [mm]	S1 [N/mm²]
Load case 1	1	0	14202	36655	1	84.1326	19.8698	0	46.9534
Load case 1	1	0	14971	36655	1	84.1326	19.8698	0	47.5287
Load case 1	1	0	17609	36655	1	84.1326	19.8698	0	48.8154
Load case 1	1	0	17739	36655	1	84.1326	19.8698	0	49.4064

Deep - 10

Loads: 1111N + Global self-weight

Deformations (as seen from above):

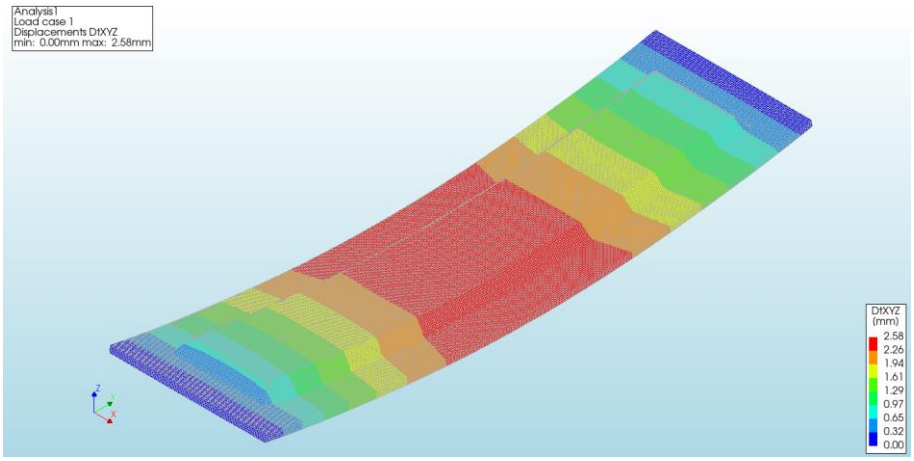

- Deformation at place of loading: 2.29mm

case	case id	case value	node	X [mm]	Y [mm]	Z [mm]	DtXYZ [mm]
Load case 1	1	0	1	73.8718	225	11.51	2.28728
Load case 1	1	0	2	26.1282	225	11.51	2.28696
Load case 1	1	0	3	73.8718	125	11.51	2.29246
Load case 1	1	0	4	26.1282	125	11.51	2.29209

Tensile principal stresses (as seen from below):

Note: Numerical peak stresses occurring at infinitely-small areas are discarded.

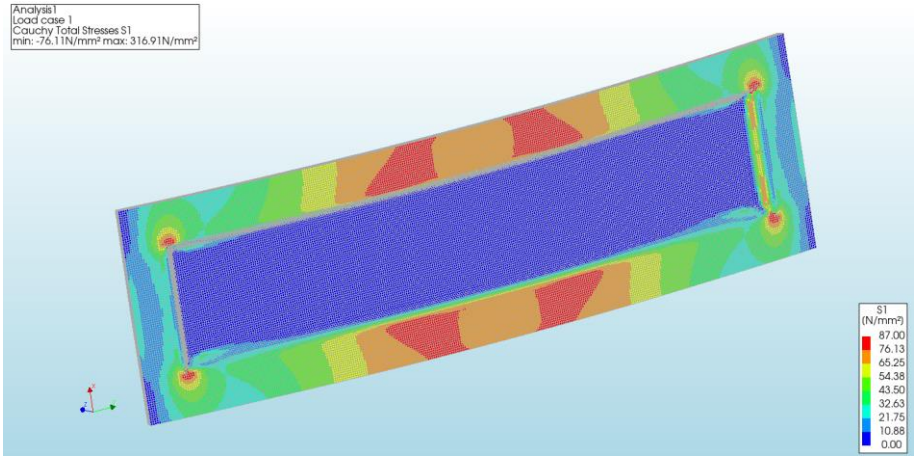

- Tensile principal stress at place of initiation of failure: 76 N/mm^2

case	case id	case value	element	node	layer	X [mm]	Y [mm]	Z [mm]	S1 [N/mm^2]
Load case 1	1	0	3360	1550	1	100	157	0	76.1579
Load case 1	1	0	3376	1550	1	100	157	0	76.1297